N ° d'ordre : 201XREN1E0XX

Année 2015

Thèse / Université de Rennes 1
sous le sceau de l'Université Européenne de Bretagne
pour le grade de
Docteur de l'Université de Rennes 1
Mention : Physique
École Doctorale : Sciences de la Matière
présentée par

Trung-Hiên NGUYEN
préparée à l'unité de recherche Foton CNRS UMR 6082
Équipe Systèmes Photoniques
U.F.R. S.D.L.M.

Theoretical and experimental study of optical solutions for analog-to-digital conversion of high bit-rate signals

Thèse soutenue à Lannion
le 19/11/2015
devant le jury composé de :

Liam BARRY
Professeur, Dublin City University / *Rapporteur*
Dominique DALLET
Professeur, Université de Bordeaux INP-ENSEIRB-MATMECA/ *Rapporteur*
François HORLIN
Professeur, Ecole Polytechnique de Bruxelles / *Examinateur*
Jean-Pierre CANCES
Professeur, XLim, Université de Limoges / *Examinateur*
Jean-Pierre HAMAIDE
Docteur, BELL LABS, Alcatel-Lucent / *Examinateur*
Michel JOINDOT
Professeur émérite, Université de Rennes 1 / *Invité*
Pascal SCALART
Professeur, Université de Rennes 1 / *Invité*
Jean-Claude SIMON
Professeur émérite, Université de Rennes 1 / *Directeur de thèse*
Olivier SENTIEYS
Directeur de Recherche, INRIA / *Co-directeur de thèse*
Mathilde GAY
Ingénieur de Recherche, CNRS-Foton / *Encadrante*

To my parents, Trung Hai and Thuy Ngan

To my younger brother, Trung Kien

ACKNOWLEGDEMENT

First and foremost, I would like to greatly thank my supervisors Prof. Jean-Claude Simon, Prof. Olivier Sentieys and Dr. Mathilde Gay for giving me the opportunity to work on this stirring topic. I highly appreciate their generous helps, immense knowledge and extraordinary supports to make this thesis a reality. I am sincerely grateful to Mathilde for her countless inspiring discussions both in the research and in the administrative business.

I would like to show my sincere gratitude to the members of my thesis jury for their acceptance to be the reviewers and examiners of my thesis.

I owe a great deal of thanks to Prof. Pascal Scalart and Prof. Michel Joindot for all their support regarding signal processing, general communication theory, corrections of the thesis, especially the work with FIR filtering based equalization. Special thanks to Dr. Laurent Bramerie, who is always patient with all my questions and gave me some precious great tips in the laboratory. Many thanks to Dr. Fausto Gomez-Agis, who gave me some deep experimental lessons that I could ever have learnt from any course.

I would like to express a deep acknowledgment to Prof. Christophe Peucheret for the insightful help and explanation pedagogy. I am very fortunate to have Sébastien Lobo, Eric Borgne for their technical support. Thank you so much! I gained lots of experience in the summer-time working with Art O'Hare whom I would like to thank a lot.

I especially thank the French government, President of the University of Rennes 1 and FOTON laboratory for supporting my work.

I would have never forgotten the great supports and the gentleness of colleagues in the laboratory for creating such a delighting working atmosphere and for the amusing time. Thanks a lot to Aurelien Lebreton for any Latex problems, to Maxime Baillot for the amazing endless French stories, to Arnaud Carer for demystifying the hardware complexity calculation, to Kevin Lenglé, Luiz Anet-Neto and every people in the lab that I could not list here for their helps, encouragement and funny chats. Thank you very much, Marie-Claire Renelle, Carole Perrot, Vincent Chevrette, Christian Sauquet, Françoise Toupin, Julien Corazza, and the former and present people in ENSSAT staff to make every administrative business faster and easier than ever.

To the former and present Vietnamese community in Lannion, I warmly thank all of them for their friendship and countless helps. Especial gratefulness to PTITers – the brothers and teachers, Thanh-Nam Nguyen, Sy-Dat Le, Quang-Vinh Nguyen, who supports me since the beginning day abroad not only in the daily life but also in the study. Thank you so much *ma petite Morlaisienne* for the support and understanding with sometimes long working days.

Last and most important, I would like to express my deepest gratitude to my family for their endless love, care and encouragement. I would not have been able to get where I am today without you. To my parents and younger brother, I would like to dedicate this thesis.

Lannion, France

November 2015

Contents

Contents vii

List of Figures xi

List of Tables xvii

INTRODUCTION 1

I CONTEXT OF THE STUDY: EVOLUTION OF HIGH BIT RATE OPTICAL TRANSMISSION SYSTEMS 5

1 Very high bit rate transmission systems 7
- 1.1 Optical fiber channel . . . 7
- 1.2 Evolution of modulation formats: from intensity modulation to M-QAM signal 10
  - 1.2.1 On-off keying (OOK) and amplitude shift keying (ASK) signal . . . 11
  - 1.2.2 Phase shift keying (PSK) signal . . . 12
  - 1.2.3 Quadrature amplitude modulation (QAM) . . . 12
- 1.3 State-of-the-art of very high bit rate transmission systems . . . 13

2 Bi-dimensional modulation format signal generation and detection 16
- 2.1 Signal generation . . . 16
  - 2.1.1 Phase modulator (PM) . . . 16
  - 2.1.2 Mach-Zehnder modulator (MZM) . . . 17
  - 2.1.3 Inphase/Quadrature (IQ) modulator . . . 18
- 2.2 Optical coherent receiver . . . 19
- 2.3 Digital signal processing . . . 21
  - 2.3.1 Front-end correction . . . 22
  - 2.3.2 Equalization . . . 23
  - 2.3.3 Carrier frequency offset compensation . . . 24
  - 2.3.4 Carrier phase noise estimation . . . 26
  - 2.3.5 Other compensations: STR, CD, PMD, nonlinearities compensation 28
- 2.4 Metrics for the quality evaluation of reconstructed signal . . . 31
  - 2.4.1 Q-factor . . . 31
  - 2.4.2 Error vector magnitude (EVM) . . . 33
  - 2.4.3 Optical signal-to-noise ratio (OSNR) . . . 34

3 A crucial element of the receiver: the analog-to-digital converter 36
3.1 Limitation of high bit rate transmission systems . . . 36
3.2 Principle of ADC track and hold . . . 37
3.3 Quantization . . . 38
3.4 Performance of an ADC . . . 39
3.4.1 Metrics for performance measurement . . . 40
3.4.2 Upper bounds for ADC performance limitation . . . 42
3.5 State-of-the-art of the electronic ADCs . . . 44
3.6 Some solutions to push ADC speed for real-time DSP . . . 45

4 Conclusion 51

II LINEAR OPTICAL SAMPLING FOR HIGH BIT RATE SIGNAL MONITORING 53

1 Introduction to optical sampling 55
1.1 LOS-based optical signal detection . . . 56
1.2 LOS-based monitoring application . . . 58

2 Linear optical sampling technique 60
2.1 Principle of linear optical sampling based on 90° optical hybrid . . . 60
2.2 State-of-the-art of linear optical sampling . . . 62
2.3 Some parameters impacting the optical sampling system specifications . . . 64
2.3.1 Pulsed-LO parameters . . . 64
2.3.2 ADC ENOB . . . 65
2.4 Possible pulsed-LO for LOS . . . 65

3 Proposed scheme for linear optical sampling based monitoring 67
3.1 Pulsed-LO source . . . 67
3.1.1 Optical frequency comb generator source . . . 67
3.1.2 Mode-locked laser source . . . 70
3.2 Coherent detector . . . 71
3.3 ADCs used in our LOS . . . 71
3.4 Additional DSP algorithms . . . 72
3.4.1 Transceiver impairments compensation . . . 72
3.4.2 Algorithms for samples synchronization and representation . . . 73
3.5 Evaluation of proposed LOS-based monitoring scheme with different signals 75
3.5.1 Optimization of LOS detection chain . . . 75
3.5.2 NRZ-OOK signal . . . 77
3.5.3 NRZ-QPSK signal . . . 78
3.5.4 16-QAM signal . . . 78
3.5.5 Problem statement and some hypothesis . . . 78

4 Analysis of limitations in proposed LOS-based monitoring system 82
4.1 Impacts of ADC parameters . . . 82
4.1.1 Motivation . . . 82
4.1.2 Experimental scheme for the study . . . 84
4.1.3 Numerical model . . . 85

4.1.4 Results and discussion . . . 86
4.1.5 Experimental ADC ENOB characterization . . . 94
4.2 Impact of pulsed-LO parameters . . . 96
4.2.1 Impact of pulsed-LO signal-to-noise ratio . . . 96
4.2.2 Impact of pulsed-LO timing jitter . . . 96
4.2.3 Impact of pulsed-LO extinction-ratio . . . 97
4.2.4 Experimental study of pulsed-LO extinction ratio impact . . . 98

5 Conclusion 105

III DIGITAL SIGNAL PROCESSING FOR HIGH BIT RATE SIGNAL TRANSMISSION 107

1 IQ imbalance compensation in optical fiber communications 109
1.1 State of the art of IQ imbalance compensations in optical communications . 109
1.2 First proposed method: IQ imbalance compensation based on MSEM . . . 111
1.2.1 Principle and analytical study of MSEM . . . 112
1.2.2 Numerical study of the proposed method . . . 114
1.2.3 Experimental study of the proposed method . . . 116
1.3 Second proposed method: Joint IQ imbalance compensation and equalization 119
1.3.1 Analysis of the joint method proposal . . . 120
1.3.2 Robustness of joint algorithm in the presence of ASE noise (experimental case) . . . 125
1.3.3 Robustness of joint algorithm in the presence of chromatic dispersion (numerical case) . . . 128

2 Carrier recovery in optical coherent communications 131
2.1 State of the art of feedforward carrier recovery (FFCR) . . . 131
2.1.1 Feedforward CFO compensation . . . 131
2.1.2 Feedforward CPE . . . 132
2.2 Carrier recovery based on circular harmonic expansion . . . 132
2.2.1 Theoretical analysis of the method . . . 134
2.2.2 Proposed improved CHE algorithm for CR . . . 137
2.2.3 Algorithm validation . . . 138

3 DSP application to all-optical signal regeneration in coherent systems 148
3.1 Context of the study . . . 148
3.1.1 Presentation of the device . . . 149
3.1.2 Principle of the power limiter . . . 149
3.2 Demonstration of phase preservation of the power limiter . . . 150
3.2.1 Experimental setup . . . 151
3.2.2 Results and discussions . . . 152
3.3 Demonstration of NPN reduction in optical coherent transmission systems . 156
3.3.1 Experimental setup . . . 156
3.3.2 Results and discussions . . . 158

4 Conclusion 160

CONCLUSION **161**

IV **167**

Appendices **168**

A Expected value calculation of modified received QPSK signal in MSEM algorithm for IQ imbalance compensation **169**

B Variance calculation of modified received QPSK signal in MSEM algorithm for IQ imbalance compensation **171**

C Angle differential coding and decoding for $M-$QAM signal **173**
C.1 Square $M-$QAM 173
C.2 Cross $M-$QAM 176

D Energy of square $M-$QAM **179**

E Energy of cross $M-$QAM **181**

List of publications **183**

Bibliography **187**

List of symbols and abbreviations **215**

List of Figures

I.1 Examples of (a) a point-to-point optical fiber transoceanic link; (b) optical fiber network - workhorse of the Internet (after Ref. [21]). 9
I.2 Examples of (a) OOK and (b) 4-ASK constellation diagrams. 11
I.3 Examples of PSK constellation diagrams for (a) BPSK and (b) QPSK signal. 12
I.4 Examples of QAM constellation diagrams for (a) square M-QAM (16-, 64-QAM) and (b) cross M-QAM (32-, 128-QAM) signals. 13
I.5 (a) The experimentally achieved single-channel bit rates (single-carrier, single-polarization, electronically multiplexed expressed by green circles), symbol rates in digital coherent detection (expressed by purple squares), and aggregate per-fiber capacities (triangles) using wavelength-division multiplexing (WDM; red), polarization-division multiplexing (PDM; blue), and space-division multiplexing (SDM; yellow) during the past and estimation for future. (b) Evolution of experimentally achieved per-polarization spectral efficiencies in single- (red) and dual-polarization (blue) experiments. (adopted from [18]). 14
I.6 (a) Phase modulator structure and (b) the possible transition on the IQ plane. 17
I.7 (a) Mach-Zehnder modulator (MZM) structure. (b) MZM transfer characteristics. (c) Modulated positions on the IQ plane for an OOK modulation. 18
I.8 (a) IQ modulator structure. (b) Relation of IQ modulator on IQ plane. (c) Example of 4 possible states on the constellation with transitions. . . 18
I.9 Classification of the coherent detection with (a) homodyne detection, (b) intradyne detection and (c) heterodyne detection. 19
I.10 General structure of dual-polarization, dual-quadratures coherent receiver. $S_{x(y)}$ corresponds to the *x(y)*-polarization. PBS: polarization beam splitter; TIA: trans-impedance amplifier; LPF: low-pass filter; ADC: analog-to-digital converter. 20
I.11 Structure of 90° optical hybrid. 20
I.12 Basic blocks in digital signal processing procedure. 22
I.13 Examples of QPSK constellations in (a) the ideal case, (b) the distorted case under the IQ imbalance impact. 22
I.14 Equalizer block diagram. The FFE, DFE are often clocked at a half of symbol duration ($T_B/2$) and a symbol duration (T_B), respectively. (reproduced from Ref. [83]) 25
I.15 Diagram for the CFO compensation, reproduced from Ref. [85]. 25
I.16 Block diagram for the carrier phase estimation of QPSK signal based on Virtebi-Viterbi algorithm. 27

I.17 (a) Feedforward and (b) feedback structures for the symbol timing recovery. NCO: numerical control oscillator; ADC: analog-to-digital converter. . . . 28
I.18 A 2×2 MIMO filter in an adaptive equalizer structure. 30
I.19 Example of the probability density functions of the corresponding NRZ-OOK signal. 32
I.20 Example of EVM calculation in IQ plane. 34
I.21 Error probability versus OSNR for QPSK (4-QAM) signal at the different symbol rates. 35

I.22 General analog-to-digital converter block diagram (after Ref. [127]). . . . 37
I.23 Time-domain response of an ideal (instantaneous and accurate) T/H circuit. 37
I.24 Example of uniform quantization with 8 possible output levels. 39
I.25 μ-law transformation at different μ values. 39
I.26 Example of a quantization waveform (dash line) with 3-bits for one period T of a sinusoidal signal (dash line) and its corresponding quantization error (lower waveform). 41
I.27 Maximum achievable NOBs as the function of the sampling rate limited by either thermal noise or aperture jitter or comparator ambiguity or Heisenberg uncertainty. 44
I.28 (a) SAR; (b) flash; (c) pipeline; (d) serial/ripple; (e) folding/interpolating and (f) time-interleaved architectures of the high-speed ADCs (reproduced from [138]). 47
I.29 Architecture for doubling ADC sampling rate. f_s = sampling rate of combined ADC inputs (after Ref. [138]). 48
I.30 Classification of photonic ADCs based on the electrical and optical implementation in the sampling and quantization stages (after Ref. [10]). . . . 49
I.31 ADC ENOB as the function of analog input frequency. The dashed lines denote the loci of aperture jitter values. Circle symbols: electronic ADC performance taken from Ref. [185]; Star symbols: optical sampling-based photonic ADCs demonstrated in Ref. [184]. 50

II.1 (a) Schematically optical sampling by mixing a short pulse train with optical signal. (b) Optical sampling gate classification based on linear and nonlinear effects. (c) Typical applications of optical sampling in optical fiber communications. NOLM: nonlinear optical loop mirror; EAM: electro-absorption modulator; MZM: Mach-Zehnder modulator; UNI: ultrafast nonlinear interferometer; SOA: semiconductor optical amplifier; PPLN: periodically poled Lithium Niobate. 56
II.2 Principle of LOS based signal detection in parallel configuration (after Ref. [12]). 57
II.3 Schematically temporal alignment of pulsed-LOs and signal in parallel structure with four optical samplers (R_B is the baud rate (symbol rate)) (Ref. [12]). 57
II.4 General principle of LOS technique for signal monitoring. 58

II.5 90° optical hybrid based optical sampling setup. 60

II.6 Setup for proposed linear optical sampling. MZM: Mach-Zehnder modulator. T_{SD} is much greater than data rate. 68

II.7 (a) Configuration for generation of 714 MHz pulsed-LO from an optical frequency comb generator based on a doubly-resonant electro-optic modulator [217]. (b) Temporal form of pulsed-LO after the repetition rate down-conversion and (c) its corresponding spectrum. 69
II.8 Spectrum of NRZ-OOK signal superimposed to that of pulsed-LO. PSD: power spectrum density. 70
II.9 (a) Temporal forms of pulsed-LO at the output of MLL and (b) its corresponding spectrum. 70
II.10 ADCs used in LOS based on a FPGA mezzanine card (FMC). 72
II.11 Examples of 10 Gb/s NRZ-OOK signal eye diagrams (a) before, (b) after equivalent-time samples reconstruction and (c) with re-alignment algorithm. 74
II.12 Calculated SNR versus input pulsed-LO powers. 75
II.13 Examples of CW representations (acted as data under test in LOS) on complex plane with 2 output I and Q components (a) without and (b) with using the electrical amplifiers before DSPs. The insets show the CW representation after DSPs. 76
II.14 Calculated SNR of reconstructed CW signal using LOS-based monitoring technique with 100 iterations. 77
II.15 (a) I and Q components; and the corresponding (b) constellation and (c) eye diagram of raw data of 10 Gbit/s NRZ-OOK signals acquired by linear optical sampling technique. 78
II.16 Constellations of 10 Gbit/s NRZ-OOK signals after (a) IQ imbalance compensation, (b) CFO compensation, (c) CPE operation and (d) the corresponding represented eye diagram. 79
II.17 (a) Constellations of 10 Gbit/s NRZ-QPSK signals and (b) the corresponding represented eye diagram. 79
II.18 (a) Eye diagram and (b) constellation of the 10 Gbaud 16-QAM signal. . 80
II.19 Comparison of the proposed prototype to the available optical sampling oscilloscope in laboratory with 1 ps resolution, for 10 Gbaud NRZ-OOK and NRZ-QPSK signals. 80

II.20 Illustration of LOS-based monitoring of a sinusoidal signal and of the parameters influencing its performance. 83
II.21 Experimental (a)(b) and numerical (c)(d) 10 Gbaud NRZ-OOK signals eye diagrams for a limited-BW of 3 GHz with integration times of (a)(c) 0.4 ns and (b)(d) 0.6 ns. 87
II.22 Evolutions of Q-factors as a function of integration times with (a) numerical and (b) experimental data. BW is set to 3 GHz. 88
II.23 Experimental and numerical 10 Gbaud NRZ-QPSK signals eye diagrams and corresponding constellations (in the insets) with a limited-BW of 3 GHz and integration times of (a)(c) 0.4 ns (b)(d) 0.6 ns. 89
II.24 Evolutions of EVMs as a function of integration time with (a) numerical and (b) experimental data. BW is set to 3 GHz. 89
II.25 Experimental and numerical eye diagrams of 10 Gbaud NRZ-OOK signals with 0.4 ns integration time and limited-BWs of (a)(c) 1 GHz (b)(d) 3 GHz, respectively. 90
II.26 Q-factor as a function of limited-BWs obtained from (a) experimental and (b) numerical data. 91

II.27 Experimental and numerical eye diagrams and corresponding constellations (in the insets) of 10 Gbaud NRZ-QPSK signals with 0.4 ns integration time in cases of limited-BWs of (a)(c) 1 GHz (b)(d) 3 GHz. 92
II.28 Impact of limited-BW on the 10 Gbaud NRZ-QPSK signals evaluated by the EVM metric with (a) experimental and (b) numerical data. 92
II.29 Dependence of (a) Q-factor for NRZ-OOK signal, (b) EVM for NRZ-QPSK signal on the ADC ENOB. 93
II.30 Setup for ADC ENOB characterization. 94
II.31 Evolution of calculated ENOB as the function of input signal power (a) without and (b) with electrical amplifier. 95
II.32 Examples of OOK and QPSK eye diagrams with different pulsed-LO OSNRs: a) 10 dB, b) 20 dB and c) 30 dB. 97
II.33 Simulated NRZ-OOK eye diagrams (a) without jitter and with jitter of (b) 600 fs; (c) 1.2 ps; (d) 3 ps and (e) 5 ps. 98
II.34 Impact of different pulsed-LO extinction-ratios of a) 100 dB; b) 20 dB; and c) 15 dB on the reconstructed OOK (first row) and QPSK (second row) signals. 99
II.35 Setup for modeling and characterizing the impact of ER_{LO} in linear-optical sampling. 100
II.36 Temporal traces for the signal under test and the pulsed-LO with delay $\tau = 0$. $ER_{S(LO)}$ is the extinction-ratio of the SUT (pulsed-LO). T_S and T are the repetition rate and the pulse time-slot, respectively. 100
II.37 Analytical prediction of $\overline{I(\tau)}$, with $ER_{LO} = 20$ dB, validated by experimental data. 102
II.38 ER_{out} evolution as a function of ER_{LO} for the different values of ER_S. . 104

III.1 Analytical prediction of the estimated phase imbalance values for different pre-defined phase imbalance values using the proposed MSEM method and their corresponding estimated phase error. 114
III.2 Numerical calculation the proposed metric, SNR_r, as the function of the variable added phase ϕ_{var} at the $-15°$ phase imbalance. 115
III.3 Estimated phase imbalance under the impact of AWGN. Dashed lines: predefined phase imbalances of 10°, 20° and 30°. Solid lines: estimate phase imbalance by using the algorithm. 116
III.4 Experimental setup for characterizing the quadrature imbalance compensation in a QPSK coherent system. 116
III.5 Experimental QPSK constellations at 12 dB OSNR: (a) without IQ imbalance, (b) with IQ imbalance of 17°, (c) recovered using the GSOP method, (d) recovered using the proposed MSEM method. 117
III.6 BER measurement as a function of OSNR (in 0.1 nm) for phase misalignments of 0° and 17° without any correction and with compensation using the GSOP and MSEM methods. 118
III.7 EVM calculation under the impact of IQ imbalance without (w/o) and with compensation by the GSOP and MSEM methods. 119
III.8 IQ imbalance compensators for (a), (b) the transmitter imbalance and (c), (d) the receiver imbalance. 122
III.9 (a) Conventional butterfly structured-FIR filters. (b) Proposed adaptive FIR filters. (c) IQ compensator structure. 123

III.10 (a) Schematic of DSP blocks for the received samples. (b) Second-order loop filter structure. (c) Convergence of the estimated phase imbalance. . 126
III.11 BER measurement versus received power for 10° phase imbalance. 128
III.12 Experimental power penalty at a BER of 10^{-3} versus phase imbalance. Solid lines: fitted curves corresponding to the measured values, represented with symbols. 128
III.13 BER versus OSNR under the impacts of chromatic dispersion and IQ imbalance. Solid lines: no IQ imbalance and with compensation. Dotted lines: with IQ imbalance of 20° and with compensation. Dashed lines: with IQ imbalance of 20° and without compensation. 129
III.14 Influence of ADC ENOB (6 and 4 bits for the I and Q components, respectively) on the calculated BER in systems with IQ imbalance. 130

III.15 Joint blind CR configuration based on CHE-ML using the first nonzero harmonic component. The insets show the 32-QAM constellations at each stages with SNR = 21 dB, $\Delta\nu \cdot T_B = 10^{-5}$, and normalized CFO of 0.025; LUT: lookup table. 138
III.16 Schema used in the simulations for characterizing the carrier recovery algorithms. 139
III.17 Examples of normalized spectra of 16- and 32-QAM signals with the CFOs of 0.25 GHz (first column) and 0.5 GHz (second column), respectively, using (a) circular harmonic expansion frequency offset estimation (CHEFOE); (b) Viterbi-Viterbi monomial frequency offset estimation (VVMFOE); (c) 4-th power methods. 140
III.18 Average and STD values of the CFO estimation error as the function of the number of symbols, N, used for the FFT operation of (a) 16-QAM and (b) 32-QAM signals. 141
III.19 CFO estimation error versus normalized linewidth for (a) 16-QAM and (b) 32-QAM signals. CFOs/ FFT block lengths for 16- and 32-QAM are set to 0.5 GHz/ 2^9 and 0.25 GHz/ 2^{10}, respectively. The 4-th power method for 32-QAM is not plotted due to the error worse than 30 MHz. 141
III.20 Mean and STD of the estimation errors for 16-QAM in a FFT interval. . 142
III.21 Calculated BER versus the block length for the first CPE step of (a) 16-QAM and (b) 32-QAM with the signal SNRs corresponding to 1 dB penalty at the BER of 10^{-3}. Normalized linewidths, $\Delta\nu \cdot T_B$, of 10^{-4} and 10^{-5} in the first and second rows of 16-QAM, respectively. Normalized linewidths, $\Delta\nu \cdot T_B$, of 10^{-5} and 10^{-6} in the first and second rows of 32-QAM, respectively. 143
III.22 Calculated BER versus laser linewidth for (a) 16-QAM and (b) 32-QAM signals and the SNRs of 1 dB penalty at the FEC threshold of 10^{-3}. . . . 144
III.23 Calculated BER versus laser linewidth for (a) 64-QAM and (b) 128-QAM signals and the SNRs of 1 dB penalty at the FEC threshold of 10^{-3}. . . . 145

III.24 (a) Device structure and (b) scanning electron microscope picture of the fabricated component. (c) Measured transmission of the cavity (resolution 0.01 nm). 150
III.25 (a) Principle of the power limiter function. (b) Example of the transmission function. 151
III.26 Experimental setup for power-limitation of a 20-Gbit/s QPSK signal. . . 151

III.27 Experimental constellation diagrams for OSNR at the receiver of 13 dB: (a) Reference without additional noise. (b) Degraded signal with additional noise. (c) Regenerated signal through the nanocavity. Amplitude distributions of (d) the degraded signal and (e) the regenerated signal. . . 153
III.28 Impact of the limiter on the phase (for OSNR at the receiver of 13 dB). (a) Phase histogram of the degraded signal. (b) Phase histogram of the regenerated signal. (c) Evolution of the standard deviation of the phase with the imposed amplitude noise level. 154
III.29 BER curves of the power-limiter for 20-Gbit/s QPSK (for artificial amplitude noise level SNR_{est}=9.8 dB). 155
III.30 Evolution of the BER as a function of the amplitude noise level for a 20 Gbit/s QPSK signal with and without power limitation (for an OSNR at the receiver of 10 dB). 156
III.31 Experimental setup for evaluation of NPN reduction in coherent optical transmission link. 157
III.32 Constellations and phase distributions at a transmitted OSNR of 18 dB for (a), (d): back-to-back; (b), (e): 100 km transmission without intensity limitation, and (c), (f): 100 km transmission with intensity limitation. . . 158
III.33 BER curves back-to-back and after transmission without and with intensity limitation for input OSNR values of 18 dB and 33 dB. 159
III.34 BER versus input OSNR (P_{rec} = -20 dBm). 159

C.1 (a) Angle differential multi-stage encoding scheme for 4-, 16-, 64-QAM. (b) Multi-stage decoding scheme of angle differential square $M-$QAM receiver. 175
C.2 BER calculation of square $M-$QAM (16-, 64- and 256-QAM) using Gray mapping and differential encoding. 176
C.3 Bits to symbol assignment of 32-QAM using the first 2 bits for differential encoding of the quadrant and Gray mapping the other bits. 177
C.4 BER calculation of cross $M-$QAM (32- and 128-QAM) using Gray mapping and differential encoding. 177

D.1 Examples of the first quadrants for square (16- and 64-QAM) $M-$QAM. 179

E.1 Examples of the first quadrants for cross (32- and 128-QAM) $M-$QAM. . 181

List of Tables

I.1 Reported transmission at very high bit rate and SEs. 15

I.2 Available electronic high-speed ADCs. 46
I.3 Summary of several typical developed photonic ADCs with respect to their classes. 50

II.1 Summary of commercial products for the measurement and characterization of advanced modulation format signals. 63

II.2 The achievable specifications for several key parameters of 90° optical hybrid. 71

III.1 Some typical IQ imbalance compensation proposed in single carrier optical coherent communication systems. 111
III.2 Summary of operations used in two IQ imbalance compensation algorithms (GSOP and MSEM). 119
III.3 Hardware complexity and computational effort for various IQ imbalance compensation methods. 125

III.4 Some typical works on feedforward carrier recovery in optical communications. 133
III.5 Optimum results of block lengths for 1 dB penalty at the hard FEC limit of 10^{-3} for the first CPE step. 143
III.6 Normalized linewidth tolerance for 1 dB penalty at the hard FEC limit of 10^{-3} for various CPE methods. 146
III.7 Hardware and computational complexity for different CPE methods. . . . 146
III.8 Example of calculated hardware complexity for different CPE methods with 16-QAM signal. 147

C.1 Rule for mapping two bits to differential angle. 173

INTRODUCTION

At present, a vast increase in the number of mobile devices (i.e. laptops, tablets, mobile phones, etc.) and a huge simultaneously Internet-user connections to different applications (i.e. Facebook, Twitter, Youtube, etc.) result in a plentiful network capacity. In order to keep up with the recent exponential growth in the capacity and the required bandwidth, the performance of current networks needs to be increased and new technologies are required to reduce the cost per bit. In this scenario, optical fiber communications and associated technologies have become the indispensable solutions, both in the short-haul and long-haul transmission, to attain a very high data rate and to maximize the quality and the reachable distance [1]. For instance, the invention of the erbium-doped fiber amplifiers (EDFA), at the end of 1980s, led to a dramatic breakthrough in design of optical transmission lines [2]. In the mid-1990s, a dramatic increase in the capacity was achieved by EDFA-amplified wavelength division multiplexing (WDM) technology (from 2.5 to 10 Gb/s per channel) [3]. Since 2005 (the end of Internet Bubble), the much slower increase in capacity resulted in the new technological challenges with the required 100 Gb/s (or higher) channel bit rate. Thanks to the offered possibilities of the high speed digital circuits, the coherent detection in conjunction with the bi-dimensional modulation formats and DSP have become the attractive solution to achieve the high spectral efficiency, high overall bit rate per wavelength. For example, the first commercial coherent system at 40 Gb/s has been proposed by Nortel in 2008 [4]. The commercial standard for 100 Gb/s transmission recommends to use the coherent detection of a DP-QPSK signal [5].

In contrast to the intensity modulated signal and direct detection, the coherent detection gives more sensitivity as well as tolerance against impairments during the transmission. Moreover, the received signal in coherent detection is proportional to the electrical fields of the optical signals, resulting in the possibility of electronic compensation for the linear or possibly nonlinear impairments. For example, the chromatic dispersion (CD) and the polarization mode dispersion (PMD) can be fully compensated for by the adaptive electronic filters [6]. For these reasons, coherent detection and subsequent digital signal processing (DSP) have revolutionized the way that telecommunication systems designers and researchers dealt with fiber impairments and other limitations occurring in the transmission. As much electronic signal processing is carried out in optical coherent systems (compared to previous direct detection optical systems), the sufficient available bandwidth

of electrical components and the high speed analog-to-digital converters (ADCs - available up to 70 GS/s [7]) are compulsory. In the case of increasing more the data rate, the technical challenges are now transferred to the electrical domain where the ADC is the bottleneck. In order to work with 100 Gb/s and beyond, the development of faster ADCs and suitable algorithms used in DSPs are still the challenging issues.

To cope with the ADC bandwidth limitation, a number of either electronic or optical-assisted solutions have been proposed. The former can be achieved by combining some electronic ADCs in which each ADC is responsible for converting a part of signal (separated by spectrum filtering) [8]. This technique, named as digital bandwidth interleaving (DBI), has been recently demonstrated for an ADC prototype with 240 GS/s sampling rate and 100 GHz bandwidth [9]. However, high electronic ADC sampling rate requires a tight control of clock jitter to be able to sample at precisely defined times. To overcome this issue, the optical-assisted ADCs have gained more and more attention in recent years [10]. Among the optical-assisted solutions, the optical sampling, especially linear optical sampling, has been shown as a very promising alternative to surpass the ADC bandwidth limitation. The principle of the linear optical sampling has been given and proof-of-concept demonstrated in 2003 [11]. Since then, a lot of works used this technique, either for optically sampling a high bit-rate optical signal or for signal monitoring, have been carried out. For instance, an aggregate optical sampling of 112 GHz applied in a 610-km long transmission of 56 Gbaud QPSK has been demonstrated by using only 20 GHz and 50 GS/s electrical ADCs [12] with the parallel structure. The highest bit rate monitoring up to 640 Gb/s was reported in [13, 14]. The first application for the detection of high bit-rate signal concerns the oversampling and synchronous technique, whereas the second application for signal monitoring relates to the undersampling and asynchronous technique. It is also to be noted that the first application requires some coherent receivers and high speed ADCs, while the second application needs only one coherent receivers and low speed ADCs.

At present, the parallelization experiment for the first optical sampling application is temporarily not possible to carry out in our laboratory. Moreover, the required DSP for parallel processing seems to be extremely difficult. For this reason, the second optical sampling application has been chosen to be studied during my PhD. The PhD work has been conducted thanks to the collaboration of the "Fonctions Optiques pour les Technologies de l'informatiON" laboratory (FOTON - strong experimental expertise in the field of new photonic devices at high bit rate) and "Computing Architectures with embedded RecoNfigurable resources" laboratory (CAIRN IRISA/INRIA - expertise in the field of digital signal processing and integrated circuit design). This thesis has been carried out at the "Ecole Nationale Supérieure des Sciences Appliquées et de Technologie" (ENSSAT) and supported by the Ministère de l'Enseignement Supérieur et de la Recherche.

In the same time that my PhD work has started, the laboratory has been involved in the OCELOT project that investigates the possibility of linear optical sampling techniques

for the visualization (in terms of eye diagram and constellation) of optical signals. I had the opportunity to contribute to the OCELOT project (supported by French government) in this context. This project aimed at developing the linear optical sampling of very high bit rate (superior to 100 Gb/s) optical signals with bi-dimensional modulation formats, especially optical phase shift keying signal ($M-$PSK) or optical quadrature amplitude modulation signal ($M-$QAM), in order to extract amplitude and phase information and display them in a constellation diagram. The following objectives have been pointed out during the PhD work

- Contribution to the generation of the optical bi-dimensional modulation format signals such as QPSK, 16-QAM.
- Contribution to the implementation of a prototype setup for linear optical sampling: characterization of proposed scheme in terms of optical and electrical parts; optimization of the setup chain; validation of the proposed linear optical sampling scheme.
- Development of DSP algorithms: to enable the linear optical sampling prototype to work with more complex modulation format signals; suitable for high speed optical communications; adaptable to the real-time processing requirements.
- Application of developed DSPs for a specific transmission system experiment, consisting to process the bi-dimensional modulation format signals in an all-optical regenerative laboratory transmission system.

The studies and the results achieved during this PhD work are structured in three parts that are outlined as follows

Part I: In this part, some solutions proposed to deal with the huge increase of the network capacity will be briefly introduced. More particularly, the basics of the optical transmission channel along with the evolution of modulation formats are firstly presented. The trend of using bi-dimensional modulation format signals and coherent detection as well as the advent in high speed DSP has opened the door to the strong increase of the network capacity. An overview of main records of capacity, spectral efficiency and optical reach that can be found in the literature is then reported. Then, the hardware (transmitter and receiver devices) and software (digital signal processing) tools for the transmission of bi-dimensional modulated signals will be presented. Additionally, different metrics allowing the evaluation of the received signal quality will be also discussed. The last part of the chapter finally focuses on one critical element of the receiver: the analog to digital converter (ADC), whose limited bandwidth imposes limitations of current systems. This crucial component will be described in terms of structures, main functions, metrics for the performance measurements. Finally, several solutions to push the ADC speed will be introduced in either electrical or optical domains.

Part II: This part will firstly introduce a short overview of optical sampling in which my study about linear optical sampling (LOS) technique is pointed out. Thanks to the use of low cost components compared to current commercialized products, LOS is shown as a promising technique for monitoring very high bit rate complex optical signals. In the second part of this chapter, the LOS technique will be discussed in terms of principle, major characterization parameters and pulsed-local oscillator (pulsed-LO) requirements. In the third part, the prototype built in the laboratory will be described and validated with various kinds of optical signals (such as NRZ-OOK, NRZ-QPSK, 16-QAM). Due to the imperfection of reconstructed signals, various assumptions in order to improve the signal quality will be investigated in the last part of this chapter. More specifically, the influence of the ADC parameters (integration time, bandwidth, ENOB) in this technique will be comprehensively studied for some important parameters that may be helpful for the system design. Then, the impact of the pulsed- LO parameters (such as the timing jitter, the OSNR and the extinction ratio of the LO-source) in the current configuration will finally be studied in detail.

Part III: Some of the developed DSPs for LOS application in previous chapters actually can be adapted to high bit rate optical coherent transmission where DSP is an indispensable part. As stated earlier, the linear and possibly nonlinear impairments can be completely compensated for, thanks to the help of DSP. In this chapter, three kinds of linear impairments, namely the IQ imbalance, the carrier frequency offset (CFO) and the laser phase noise, will be studied in the context of optical coherent communications. State-of-the-art of such compensations will be also given. Several proposals for these impairments compensation will also be introduced and validated by both numerical and experimental studies. More specifically, two new solutions for the IQ imbalance compensation, based on the introduction of a new metrics and the integration with the equalizer, will be proposed and validated with different kinds of signal. After that, the algorithm for carrier recovery (both CFO compensation and carrier phase estimation (CPE)) will be investigated in next parts of this chapter. The carrier recovery algorithm, based on the circular harmonic expansion (CHE), focuses on the notable interest on feedforward structure, facilitating the real-time processing implementation. Some additional improved algorithms will also be assessed to be integrated with CHE method to achieve the better carrier recovery performance for $M-$QAM signals. Finally, the developed DSP tools will be applied in an all-optical regenerative coherent transmission system where the nonlinear phase noise (NPN) is mitigated using a photonic-crystal-based power limiting function. This innovative solution is shown to preserve the phase of the signal and is hence compatible with phase encoded modulation formats; it is experimentally validated with QPSK signal showing the effectiveness of the proposed power limiter. Some perspectives and future work will also be discussed.

Part I

CONTEXT OF THE STUDY: EVOLUTION OF HIGH BIT RATE OPTICAL TRANSMISSION SYSTEMS

The larger capacity, lower attenuation and immunity to electromagnetic interference make the optical fiber more attractive in both long-haul and short-haul broadband transmission compared to the copper counterparts. For example, 54 Tb/s optical fiber transmission over 9150 km was reported in Ref. [15]. Since the early 2000's, the research in optical fiber communications has been becoming remarkable due to the requirements in increasing the capacities of the new interactive bandwidth-hungry services such as online gaming, video on demand (VoD), high definition (HD) 3D television, etc. The overall traffic on backbone networks has been growing exponentially about 30% to 60% per year [16]. According to the recent statistics of Cisco [17], the global Internet Protocol (IP) traffic will increase at a compound annual growth rate of 21% from 2013 to 2018. It is also pointed out that the annual global IP traffic will exceed the Zettabyte (10^{21} bytes) threshold in 2016. More specifically, global IP traffic will reach 1.1 Zettabytes per year, equivalent to approximately 1 billion Gigabytes per month in 2016.

In this part, we introduce briefly some solutions that are proposed to deal with this huge increase of the network capacity. Generality on the optical transmission channel is first introduced together with the evolution of modulation format in order to allow the transport of large capacities. An overview of main records of capacity, spectral efficiency and distance that can be found in the literature is then reported. In the second section of the part, the hardware (transmitters and receivers devices) and software (digital signal processing) tools for the transmission of bi-dimensional modulated signals are presented as well as the different metrics allowing the evaluation of the received signal quality. The last section of the part finally focuses on one critical element of the receiver, knowing the analog to digital converter.

1. Very high bit rate transmission systems

In the past, the development in the reduction of optical fiber losses and the invention of fiber doped optical amplifiers enabled the use of wavelength-division multiplexing (WDM) technology that allows different wavelength channels to be densely located (i.e. 50 GHz spacing enabling nearly 160 channels on the C- and L-bands), enhancing the use of available bandwidth. This technology allowed for a time to cope with the increase of bandwidth demand and to solve the saturation network issues. However, WDM was initially employed for intensity modulation/direct detection (IMDD) that has been quickly limited in capacity. The increase of overall capacity growth was first managed by the use of time-division multiplexing (TDM) techniques. However, the use of TDM solutions for 100 Gb/s or higher leaded to limitations in terms of spectral efficiency (SE) and propagation impairment [18]. This limited the potential of IMDD for very high bit rate transmission systems. In contrast to the IMDD systems, the systems using advanced modulation formats yield an improvement in capacity and an increase in SE. Indeed, advanced modulation formats signals, exploiting not only the amplitude but also the other signal domains (i.e. phase, state of polarization (SOP)) to encode the electrical data onto an optical carrier, improve noise and nonlinearity tolerance thanks to the more optimum allocation of symbols on a constellation diagram. The constellation diagram is a two-dimensional diagram on a complex plane allowing the visualization of both signal amplitude and phase. Furthermore, the combination of coherent detection and digital signal processing (DSP) allow to mitigate main fiber impairments and to demodulate bi-dimensional modulated signals. This evolution of optical communications towards modulation formats that are commonly used in the radio communication domain was made possible thanks to the advents in signal generation (integrated IQ modulator), detection (integrated 90° hybrid) and of DSP implementation (clock speed of silicon chips, enabling the convergence of the silicon chip speed with optical line-rates [19].

1.1 Optical fiber channel

Optical fiber has become the primary transport medium for wide area network (WAN), metro area network (MAN), local area network (LAN), especially in long-haul transoceanic

transmission. The most advanced laboratory systems have demonstrated total capacities up to Petabits per second [20]. Moreover, the Internet growth has driven the push for ever faster fiber optic transport networks. Fig. I.1(a) shows an example of the simplest optical link, which is a point-to-point configuration, normally applied for the transoceanic transmission. The transmitter (Tx) is usually a laser (*C*- and/or *L*-band) and the data signals are imprinted onto the optical carrier by either direct or external modulation. The signal transmitted in the optical fiber is regularly amplified to compensate for the attenuation. At the receiver side (Rx), the optical signal is photodetected. Another picture of current optical network is presented in Fig. I.1(b), in which 100 Gb/s at client line interface can be achieved thanks to the optical fiber transmission and WDM technique. The optical network structure can be separated into three levels based on the transmission distance such as the access network (up to 100 km), metro-regional (from 100 to 800 km) and long-haul transmission (superior to 800 km). A lot of components and interface standards are used in both central offices (CO) and client sides to adapt the requirements of modern network (i.e. high speed, low power consumption, compactness). The success of optical fiber deployment is due to its low loss (around 0.2 dB/km in the 1550 nm wavelength window) and the bit rate independence of its loss compared to other counterparts (i.e. coaxial cable).

During transmission, the fiber degradation effects (linear and nonlinear effects) can lead to a strong reduction of the transmission system performance, especially when increasing the bit rate. Most of the fiber degradations are caused by (i) fiber attenuation; (ii) chromatic dispersion (CD); (iii) polarization mode dispersion (PMD) (referred to as linear effects); (iv) Kerr nonlinearities (mentioned as nonlinear effects). When attenuation is dominant, the optical amplifiers can be used to compensate for, albeit at the cost of additional noise (amplified spontaneous emission - ASE noise). When the channel bit rate is increased to 40 Gb/s, the CD leads to the rapid signal degradation in terms of amplitude and possibly phase information. CD indeed leads to a broadening of the optical pulses due to group velocity dispersion between frequencies causing the inter-symbol interference (ISI). Additionally, PMD, coming from random imperfections and asymmetries of fibers, leads to different group velocities between polarization modes [22] which can cause randomly spreading of optical pulses. Similar to CD, PMD becomes more critical in the >40 Gb/s transmission systems leading to the requirement of compensation.

In this thesis, only the linear impairments generated during the transmission along the optical fiber are considered. However, it is necessary to understand the nonlinearities origin that may be observed during the work. The most important Kerr effect causing the nonlinear response is due to the intensity dependence on the refractive index. Normally the optical signal propagation in fiber is described by the nonlinear Schrodinger equation (NLSE) in which the evolution of the complex optical field $E(z,t)$ is as follows [23]

$$\frac{\partial E}{\partial z} = -\frac{\alpha_p}{2}E - j\frac{\beta_2}{2}\frac{\partial^2 E}{\partial t^2} + j\gamma\left|E\right|^2 E. \tag{I.1}$$

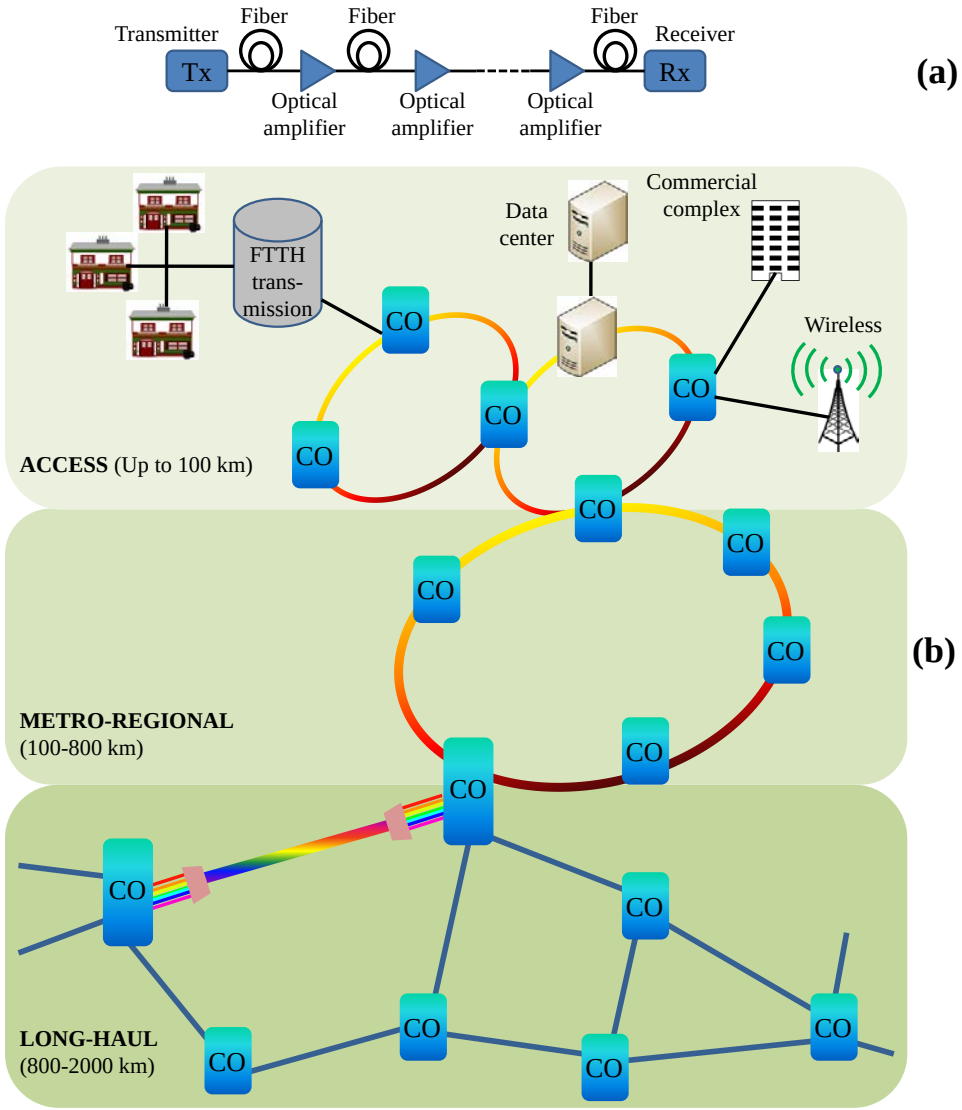


Figure I.1: Examples of (a) a point-to-point optical fiber transoceanic link; (b) optical fiber network - workhorse of the Internet (after Ref. [21]).

The first and second right hand side (RHS) terms represent the attenuation and CD, respectively, as aforementioned. The last term denotes the nonlinear contribution proportional to the optical signal power and Kerr nonlinearity coefficient (γ in $W^{-1}km^{-1}$). As previously stated, the variation of fiber refractive index $n(z,t)$ depending on the signal power $P(z,t) = |E(z,t)|^2$ can be expressed by

$$n(z,t) = n_L + n_{NL}\frac{P(z,t)}{A_{eff}}, \tag{I.2}$$

where n_L, n_{NL} and A_{eff} are the conventional, nonlinear refractive index and optical mode effective area (fiber core area), respectively. Additionally, the relation between the nonlin-

earity coefficient and the nonlinear refractive index is given by

$$\gamma = \frac{2\pi}{\lambda} \cdot \frac{n_{NL}}{A_{eff}}. \tag{I.3}$$

Kerr effects include three major contributions depending on the transmission contexts such as the self-phase modulation (SPM), cross phase modulation (XPM) and four wave mixing (FWM) [24]. For SPM, it causes phase variation depending on the power variation over time. Particularly, for intensity modulated signal, SPM creates the instantaneous frequency variations resulting in the generation of new frequencies and the enlargement of the signal spectrum. In WDM systems, this spectrum enlargement can generate a spectral overlap between the adjacent channels leading to the dramatic degradation of optical signals, especially when combined to the CD effect. In the multi-channel system, XPM usually occurs due to the power fluctuations of neighboring channels leading to the signal phase shift and amplitude fluctuation on the current propagating channel. The third effect is FWM in which the interaction of two or more propagating wavelengths at high power generates some new frequencies, resulting in impairments of adjacent channels in wavelength multiplexed systems.

In the very high bit rate transmission (superior to 100 Gb/s), the signal degradation due to both linear and nonlinear effects is very critical and limits the optical reach. Many solutions for such problems have been proposed so far by using either optical solutions or DSP. DSP is now attractive thanks to its low cost and will be discussed in the following sections. All-optical signal processing, however, brings the advantage of real-time and very fast processing without requirements of extra optical-electronic-optical conversion step. An example of optical function for all-optical processing is shown in the last part of this thesis.

1.2 Evolution of modulation formats: from intensity modulation to *M*-QAM signal

Many properties of the optical carrier can be used to modulate the information data, for example the amplitude, the phase or the frequency as in the radio domain [25]. Moreover, the state of signal polarization can be exploited to carry the information, resulting in doubling the spectral efficiency (SE) [26]. SE can be linked to the data rate as $SE \sim R_b/R_B = \log_2 M$, in which R_b is the bit rate, R_B is the baud rate or modulation rate (roughly equal to the physical bandwidth) and M is the number of symbols in a modulated alphabet.

In order to increase the achievable bit rate on a single-wavelength channel, a large number of optical data channels (i.e. OOK signal) with a very short duty cycle were bit-interleaved to form the higher bit rate. Very high bit rates have been demonstrated in the 1990's and the beginning of 2000's years using this solution [27]. The data bit rate can be further increased by multiplexing several wavelength channels. Nevertheless, the use of very short pulses in these techniques results in a spectrum broadening or an increase of nonlinear

impairments, leading to the limited multiplexed-channels.

Another solution to increase the capacity is to use the bi-dimensional modulation format that allows carrying several bits per symbol. Data bit can be encoded on the amplitude or phase (amplitude shift keying (ASK) or phase shift keying (PSK)) of optical waves. This allows the increase of overall data bit rate as well as the spectral efficiency while remaining the modulation rate. The phase modulation format is less sensitive to the nonlinear effect than the amplitude modulation format because of its constant intensity. However, when the number of symbols increases, the effect of ASE and phase noise are more critical.

An alternative solution is to combine the amplitude and phase modulation in a bi-dimensional modulation formats forming the quadrature amplitude modulation (QAM) formats. If the same number of symbols compared to PSK modulation format is used, the QAM modulation format gives a better tolerance to the ASE and phase noise than the PSK.

These three kinds of modulation formats are detailed in the following section. It is to notice that there are some additional solutions to increase the capacity and notably multiple-carriers modulation formats, such as orthogonal frequency division multiplexing (OFDM) [28]. These solutions are not discussed in my work.

1.2.1 On-off keying (OOK) and amplitude shift keying (ASK) signal

OOK is historically the most widely used modulation format in optical communication as well as in commercial systems thanks to its simplicity in both generation and detection. OOK consists of 2 levels which are low and high levels representing bit 0 and bit 1, respectively. Fig. I.2(a) presents the OOK constellation diagram. The constellation diagram is the representation of modulated signal in a complex plane with two-dimensional components (in-phase (I) and quadrature (Q)). Due to only one bit per symbol, high SE cannot be done with OOK signal. More than 2 amplitude levels can be used to improve SE forming ASK signal. Fig. I.2(b) shows an example of a 4-ASK constellation that has 4 different amplitude levels along the I component.

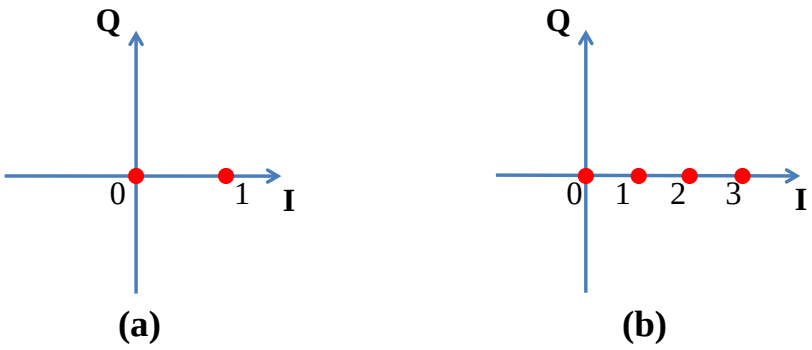


Figure I.2: Examples of (a) OOK and (b) 4-ASK constellation diagrams.

1.2.2 Phase shift keying (PSK) signal

The phase term of optical carrier can be used to modulate the information forming the PSK signal. The binary PSK (BPSK) is the simplest form of PSK signal which uses two states of phase to code the information data with the constellation shown in Fig. I.3(a). Although this modulation format combines 1 bit/symbol as in an OOK signal, its average signal energy (required for a given error probability, in the presence of the same noise spectral density for both modulations) is reduced by a factor of 2 compared to the OOK signal, thanks to the placement of symbol points on the constellation. When four states of phase are used to modulate the information, quadrature phase shift keying (QPSK) signal is achieved (Fig. I.3(b)). QPSK modulation enabling to carry 2 bits/symbol has been widely studied for radio as well as fiber optical communications [29]. This modulation format increases the SE by a factor of 2 compared to BPSK. It is noted that more than four states of phase can be used to modulate M-PSK signal ($M > 4$) allowing to carry more than 2 bits/symbol. However, for a fixed average energy in the constellation diagram, the spacing between the constellation points becomes small leading to the increase of error probability at the detection.

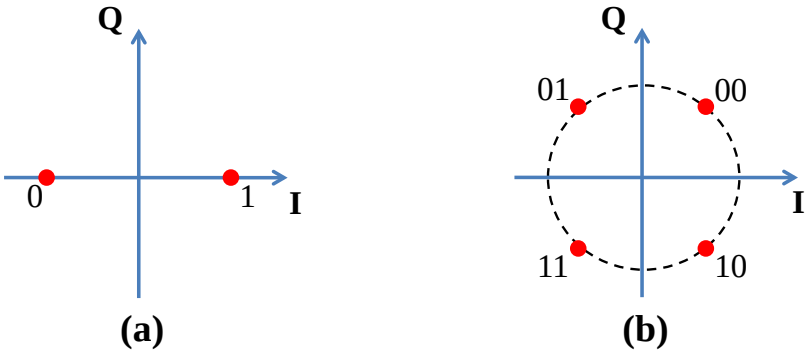


Figure I.3: Examples of PSK constellation diagrams for (a) BPSK and (b) QPSK signal.

1.2.3 Quadrature amplitude modulation (QAM)

To be able to increase the SE while keeping the appropriate minimum distance between the constellation points, the combination of ASK and PSK are used to carry the information on both amplitude and phase components. This modulation format, called QAM, has been recently introduced in fiber optical communication [30]. The placement of QAM constellation points can be symmetric or asymmetric over the abscissa and ordinate axis of the IQ plane. The combination of ASK and PSK generates the equidistant-phase QAM, however at the cost of sensitivity to additive white Gaussian noise (AWGN) [25]. The most common placement used in optical communications is symmetric and on the square grids with equal vertical and horizontal spacing, constituting of 2 forms of square and cross M-QAM constellations (Fig. I.4). Fig. I.4(a) shows the examples of square constellation diagrams for

16-QAM and 64-QAM signals that provide 4 bits/symbol and 6 bits/symbol, respectively. Examples of cross constellation diagrams for 32-QAM and 128-QAM signals are presented in Fig. I.4(b), allowing to carry 5 bits/symbol and 7 bits/symbol, respectively. Other higher QAM modulation formats, i.e. 1024-QAM, or recently 2048-QAM, have been experimentally investigated over a single fiber transmission link up to 150 km [31, 32]. The square and cross M-QAMs are studied in the rest of thesis and mentioned as M-QAM in brief.

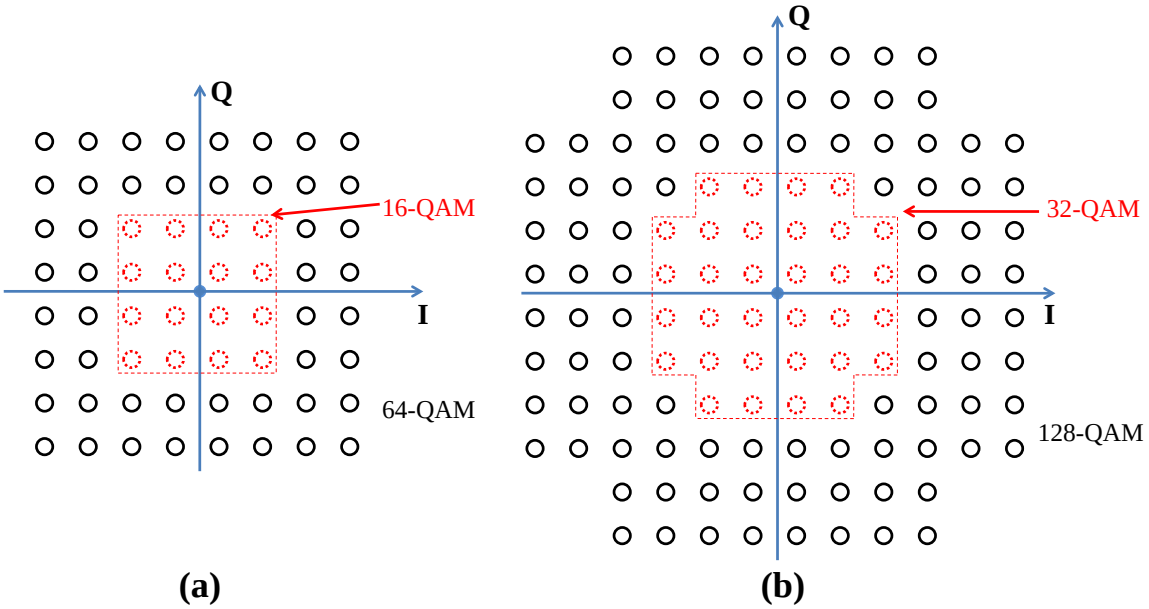


Figure I.4: Examples of QAM constellation diagrams for (a) square M-QAM (16-, 64-QAM) and (b) cross M-QAM (32-, 128-QAM) signals.

1.3 State-of-the-art of very high bit rate transmission systems

The evolution of optical transmission systems has considerably changed in the last three decades in terms of capacity, reach and structure of networks. From 622 Mb/s single span fiber in 1980's to the invention of erbium doped fiber amplifier (EDFA) in 1990's allowing the use of multi span fibers, the study on the largest optical system capacity is still a hot topic devoting remarkable research efforts. The system capacity defined as a product of system bandwidth (BW) and SE is doubled every year in 1990's [33]. Particularly, the first 1.8 Tb/s transmission over a distance of 7000 km using full C-band was reported in 1999 [34]. Before 2002, the transmission records were achieved with OOK signal and Raman-assisted EDFAs to extend the usable BW (i.e. C+L-band). Since 2002, the advent of bi-dimensional modulation formats to obtain higher SE provides the improvement of total capacity. Starting with only phase modulation [35], signal modulation gradually changed to a combination of amplitude, phase and polarization states. Thanks to the remarkable point of advancements in digital coherent technology that the optical and electronic bandwidths

had met [18], the optical communications had to move from physics toward communication engineering to further increase SEs and overall capacities. Before 2010, two main approaches to exploit the large bandwidth of the optical fiber, called WDM and/or TDM [36] were used to push the optical channel capacity up to Tb/s [37].These techniques consider a number of n independent data flows (or sub-rate channels), having a bit rate of R bit/s, being multiplexed to create a data rate of $n \cdot R$ bit/s. Comparing to WDM, TDM is limited by the available electronic bandwidth. Thanks to the recent achievement in high speed oscilloscopes (e.g. 160 GS/s and 65 GHz bandwidth), the experimental test of the electrical TDM limit has been recently demonstrated with up to 110 Gbaud PDM-QPSK signal per channel over 3600 km length [38]. In combination to WDM, it was shown to reach a channel capacity of 8.8 Tb/s.

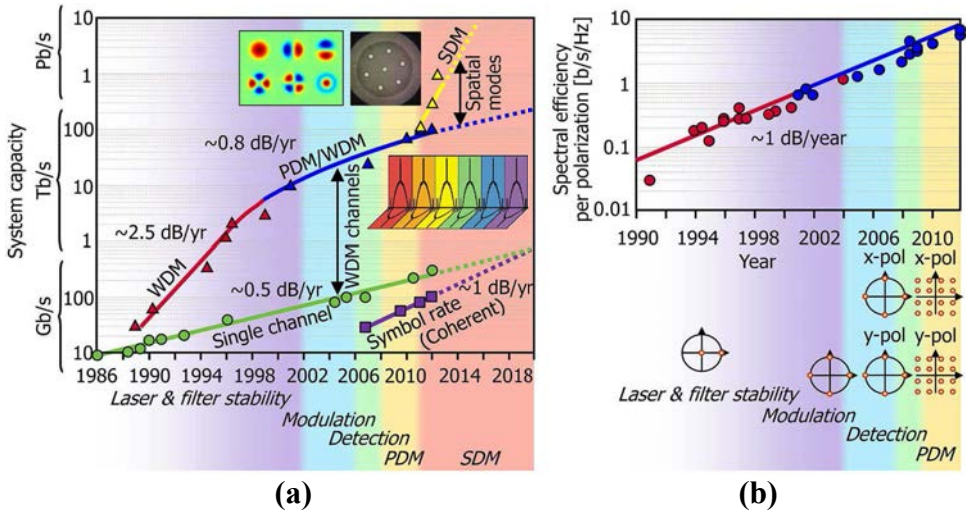


Figure I.5: (a) The experimentally achieved single-channel bit rates (single-carrier, single-polarization, electronically multiplexed expressed by green circles), symbol rates in digital coherent detection (expressed by purple squares), and aggregate per-fiber capacities (triangles) using wavelength-division multiplexing (WDM; red), polarization-division multiplexing (PDM; blue), and space-division multiplexing (SDM; yellow) during the past and estimation for future. (b) Evolution of experimentally achieved per-polarization spectral efficiencies in single- (red) and dual-polarization (blue) experiments. (adopted from [18]).

Fig. I.5, after Ref. [18], presents the evolution of the already reported single-channel bit rates, SEs and aggregate per fiber capacities. More specifically, in Fig. I.5(a), the achieved single-channel bit rates (single carrier, single polarization, electronically multiplexed) are presented in circle symbols with almost reachable limitation in 2012. To increase the aggregation per fiber capacities, the experiments with wavelength-, polarization-, and most recently space-division multiplexing (WDM, PDM, SDM) are summarized in triangle symbols. For example, the record of 1.01 Pb/s transmission over 52 km low-crosstalk one-ring-structured 12-core fiber was obtained with a SE of 91.4 b/s/Hz and 32-QAM signal [20]. Based on the statistics in Fig. I.5(b), it can be observed that the SEs is increased

Table I.1: Reported transmission at very high bit rate and SEs.

Refs.	SE (b/s/Hz)	Capacity (Tb/s)	Distance (km)	Mod. format	Bit rate/ channel (Gb/s)	No. of channels	FEC overhead	Channel spacing (GHz)	No. of core
[63]	2	8	9000	QPSK	112	80	7%	50	1
[33]	3.6	22	6860	QPSK	112	198	7%	25	1
[49]	4	13.8	10181	8QAM-OFDM	120.5	115	20%	25	1
[57]	5.2	25	5530	16QAM	128	250	23%	20	1
[64]	6.1	30.58	7230	half 4D-16QAM	133.12	286	28%	17	1
[65]	11	1.44	495.2	256-IPM-OFDM	480	3	38.35%	100	1
[62]	18	18	1705	QPSK	600	30	20%	33	6
[66]	53.6	120.7	204	32QAM	115	180	20%	12.5	7
[61]	247.9	2.1	40.4	32QAM	105	20	20%	12.5	12

by almost 1 dB per year (expressed in dB as in Ref. [16]). The various techniques for achieving the SEs (higher than 2 b/s/Hz) have been investigated such as spectral shaping [39, 40], Nyquist WDM [41, 42, 43, 44, 45], orthogonal frequency division multiplexing (OFDM) [46, 47, 48, 49, 50, 51], optical superchannels [52, 53, 54], tight optical filtering with multi symbol detection using maximum *a posteriori* probability (MAP) detection [55, 56] or maximum likelihood sequence estimation (MLSE) [33], coded modulation [57, 58, 15] and SDM [59, 60, 61, 62].

Tab. I.1 lists some recent achievable high SEs and reachable transmission distances thanks to the advent of coherent technologies. Because of a huge research reported every year, we rather try to give some examples corresponding to each proposed technique for the increase of SEs. Despite a lot of parameters, the order in this table is chosen based on the increase of SEs.

2. Bi-dimensional modulation format signal generation and detection

Coherent transmission tools were developed during this work both for hardware (operating the transmitters and receivers) and software (mainly for DSP). This section aims at presenting main tools for signal generation and detection.

2.1 Signal generation

To be able to emulate random data signals in laboratory and simulations, either pseudo random binary sequences (PRBS) or De Bruijn sequences [67] can be used. Due to the available used PRBS in our equipments, we utilize the PRBS for simulation and other software-defined experiments. Actually, a PRBS is a deterministic periodic signal with a long period. When observed over a relative small time window (compared to its period), this PRBS appears as a random sequence. The comparison of the received and transmitted sequences allows the determination of the BER.

The electrical signal, emulated by PRBS, is carried on the optical carrier with different modulation formats by the means of external modulators. In optical fiber communications, external modulators are widely used to reproduce the electrical signal onto the optical one. Moreover, the combination between different kinds of modulators can bring different kinds of modulation formats. In this subsection, the three most popular modulators, called phase modulator (PM), MZM and IQ modulators are described.

2.1.1 Phase modulator (PM)

Fig. I.6 shows a typical structure of a PM. A PM consists of a waveguide (often made of Lithium Niobate, $LiNbO_3$) with two stacked electrodes. This modulator is based on the Pockels effect [68] in which the refractive index of the material is changed when applying an electrical field. The change of refractive index leads to the phase shift

$$\Delta\phi\left(t\right) = \pi\frac{V\left(t\right)}{V_\pi}, \tag{I.4}$$

in which $V(t)$, V_π are the applied voltage and half-wave voltage (leading to π phase shift) of

the modulator, respectively. More details on the PM parameters could be found in Ref. [69]. Fig. I.6(b) shows an example of a possible transition of the modulated signals on the IQ plane.

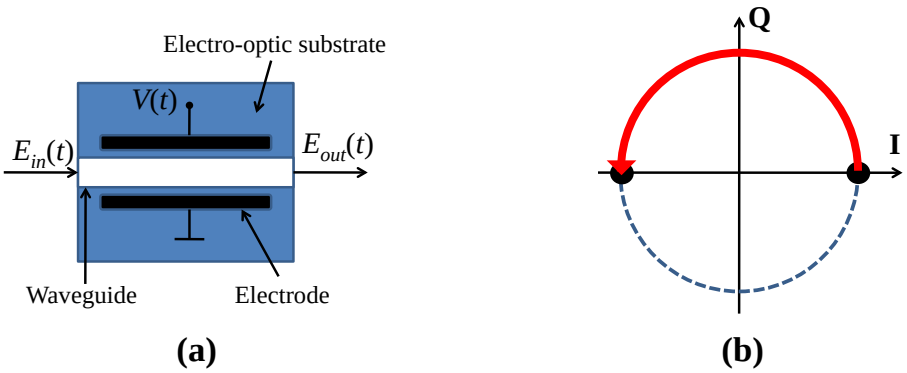


Figure I.6: (a) Phase modulator structure and (b) the possible transition on the IQ plane.

2.1.2 Mach-Zehnder modulator (MZM)

A MZM is structured as in Fig. I.7(a) where the input electrical field is split and recombined after the phase shifts of ϕ_1 and ϕ_2 in two arms of modulator. Supposing that the coupling ratio of the MZM is perfect, the output field can be obtained as follows [70]

$$\frac{E_{out}(t)}{E_{in}(t)} = \frac{1}{2}\left(e^{-j\Delta\phi_1(t)} + e^{-j\Delta\phi_2(t)}\right) = \cos\left[\frac{\pi\left(V_2(t) - V_1(t)\right)}{2V_\pi}\right] e^{-j\frac{\pi(V_2(t)+V_1(t))}{2V_\pi}}, \tag{I.5}$$

where $V_i(t)$ is the voltage applied to the two branches of the MZM, $i = 1, 2$. The MZM is often worked in push-pull operation (or chirp-free mode) in which case $V_1(t) = -V_2(t)$. At this operation, the MZM output field and power transfer characteristics are written as

$$\frac{E_{out}(t)}{E_{in}(t)} = \cos\left[\frac{\pi\left(V_2(t) - V_1(t)\right)}{2V_\pi}\right] = \cos\left[\frac{\pi\Delta V(t)}{2V_\pi}\right], \tag{I.6}$$

$$\frac{P_{out}(t)}{P_{in}(t)} = \cos^2\left[\frac{\pi\Delta V(t)}{2V_\pi}\right]. \tag{I.7}$$

Fig. I.7(b) shows the MZM transfer characteristic. Depending on the modulation formats, different operating points are chosen. For example, in intensity modulation with NRZ-OOK signal, the operating point (OP) point (or quadrature point), is set at $V_\pi/2$. And the modulator is driven by an applied voltage $\Delta V(t) = V_\pi$, resulting in the output power P_{out} ranging between P_{in} and 0. The possible modulated signal on the constellation by the MZM is illustrated in Fig. I.7(c).

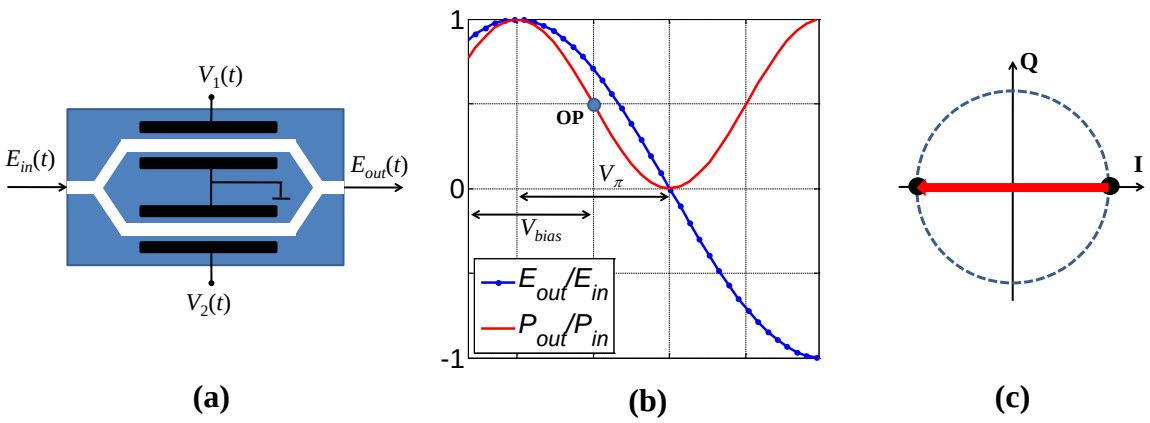


Figure I.7: (a) Mach-Zehnder modulator (MZM) structure. (b) MZM transfer characteristics. (c) Modulated positions on the IQ plane for an OOK modulation.

2.1.3 Inphase/Quadrature (IQ) modulator

An IQ modulator is constructed with 2 MZMs and a PM, as shown in Fig. I.8(a). This structure allows to reach every possible point on the IQ plane (Fig. I.8(b)) based on the driving electric signals and bias voltages.

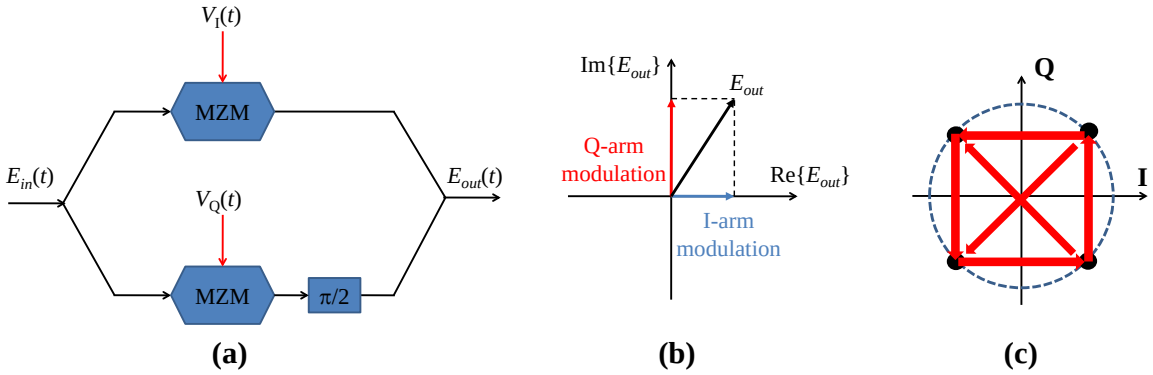


Figure I.8: (a) IQ modulator structure. (b) Relation of IQ modulator on IQ plane. (c) Example of 4 possible states on the constellation with transitions.

The input electrical field is separated into two arms. The upper arm, called I-arm, consists of a push-pull mode MZM driven by $V_I(t)$, whereas the lower arm, called Q-arm, cascades another push-pull mode MZM and a PM with theoretically fixed phase shift value of $\pi/2$. Note that this phase shift in an actual device can be slightly different from $\pi/2$, causing the IQ phase imbalance. The influence of this impairment on system performance is investigated and dealt with by DSP. In the simulation, the coupling ratio is assumed to be perfect and the couplers introduce no phase shift. After the interference, the output electric field is given by

$$E_{out}(t) = E_{in}(t)\left[\frac{1}{2}\cos\left(\frac{\pi V_I(t)}{2V_\pi}\right) + j\frac{1}{2}\cos\left(\frac{\pi V_Q(t)}{2V_\pi}\right)\right]. \tag{I.8}$$

Fig. I.8(c) presents an example of QPSK signal modulation by the IQ modulator with the 4 possible states on the constellation. The transitions corresponding to each state are also shown. By pre-defining the driving electrical signals (e.g. multi amplitude signals) and appropriate bias points, more complicate modulation formats can be generated. For instance, to be able to generate the 16-QAM signals, two electrical 4-PAM signals are used to drive two arms of IQ modulation at the bias null as in QPSK generation case. As a consequence, 16 states on the constellation are achieved.

2.2 Optical coherent receiver

Based on the frequency difference between the signal (S) and local oscillator (LO), coherent detection is divided into 3 categories as shown in Fig. I.9. If the carrier frequencies of S and LO are identical, the homodyne detection corresponds to Fig. I.9(a). However, it is very difficult to achieve this detection in the actual transmission systems due to the requirement of LO frequency and phase locked to the signal. Fig. I.9(b) presents the intradyne detection with a relative small frequency difference between S and LO. With the advent of DSP, this frequency offset can be compensated in the detected signal. The last category of coherent detection is heterodyne detection (Fig. I.9(c)), in which there is a large frequency offset between S and LO, compared to the bandwidth of modulating signal. The diverse degrees of coherent reception (amplitude, phase, polarization) have been introduced in many works [71]. A general structure of dual-polarization and dual-quadratures coherent receiver is represented in Fig. I.10. The input signal and LO are passed to a polarization beam splitter (PBS) to separate the x- and y-polarizations. Considering only x-polarization (the principle is similar for y-polarization), the data signal E_{Sx} and LO fields E_{LOx} are coupled into a 90° optical hybrid-unit where they are split and cross-combined, producing four output interference terms. These four outputs are detected in balanced photodiodes. The summation of signals coming from each pair of balanced photodiodes gives the beating of signal and LO fields and allows to remove the quadratic terms of detection. The two outputs, called the in-phase and quadrature components, are filtered and amplified. Finally, these components are quantized and digitally processed.

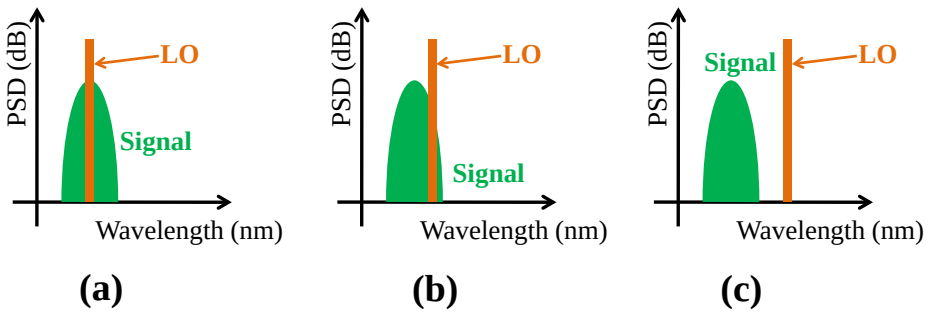


Figure I.9: Classification of the coherent detection with (a) homodyne detection, (b) intradyne detection and (c) heterodyne detection.

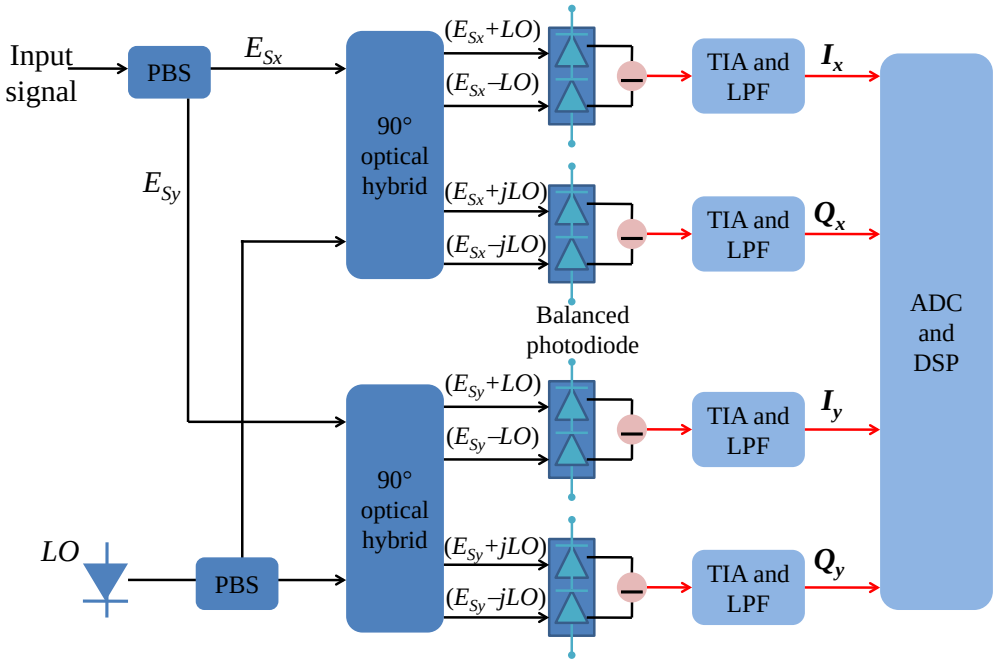


Figure I.10: General structure of dual-polarization, dual-quadratures coherent receiver. $S_{x(y)}$ corresponds to the $x(y)$-polarization. PBS: polarization beam splitter; TIA: trans-impedance amplifier; LPF: low-pass filter; ADC: analog-to-digital converter.

In this work, we focus on single polarization study only. Consequently, the fields of signal and LO will be denoted E_S and E_{LO}, respectively, for simplicity. We will describe a bit more in detail the 90° optical hybrid in next section.

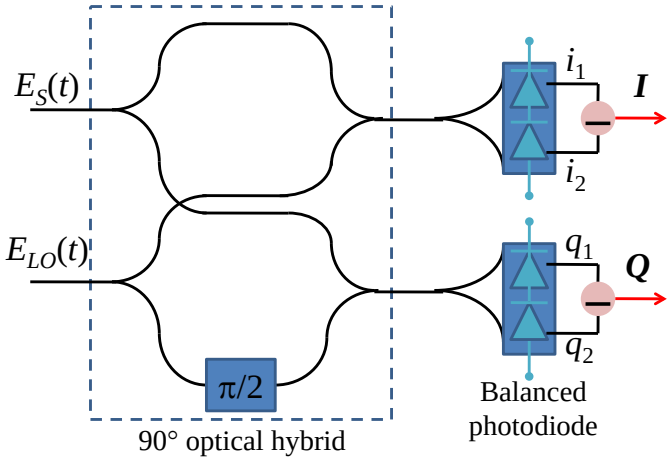


Figure I.11: Structure of 90° optical hybrid.

Fig. I.11 shows the basic diagram of a 90° optical hybrid. The local oscillator source and input signal are assumed to be in the same polarization. The four photocurrents generated by the photodetectors are proportional to

$$i_1 = |E_S + E_{LO}|^2 \sim |E_S|^2 + |E_{LO}|^2 + 2\Re\{E_S E_{LO}^*\}, \tag{I.9}$$

$$i_2 = |E_S - E_{LO}|^2 \sim |E_S|^2 + |E_{LO}|^2 - 2\Re\{E_S E_{LO}^*\}, \tag{I.10}$$

$$q_1 = |E_S + j \cdot E_{LO}|^2 \sim |E_S|^2 + |E_{LO}|^2 + 2\Im\{E_S E_{LO}^*\}, \tag{I.11}$$

$$q_2 = |E_S - j \cdot E_{LO}|^2 \sim |E_S|^2 + |E_{LO}|^2 - 2\Im\{E_S E_{LO}^*\}. \tag{I.12}$$

The resulting voltage levels of the real and imaginary parts are enhanced by the balanced photodetection process, which perform the $(i_1 - i_2)$ and $(q_1 - q_2)$ operations to form the I and Q components. This process in coherent detection brings an advantage (i.e. high sensitivity, reduced shot noise) compared to the direct detection [72] (used quadratic detection of electric field). Finally, the I and Q voltage components are given as follows

$$I \sim 4\Re\{E_S E_{LO}^*\}, \tag{I.13}$$

$$Q \sim 4\Im\{E_S E_{LO}^*\}. \tag{I.14}$$

The two optical components are changed to electrical domain by a couple of balanced photodiodes with large bandwidth (e.g. 15 GHz). Thanks to this large bandwidth, the signals can be considered as undistorted and the shot noise is assumed to be small enough to be ignored in some simulation works.

2.3 Digital signal processing

Two states of polarization (SoP) are assumed to be well split, so a similar DSP is then used for each SoP. DSP is generally carried out step-by-step as indicated in Fig. I.12. Firstly, the front-end impairments caused by DC offset and/or IQ imbalance are compensated. The carrier recovery, composed of carrier frequency offset (CFO) compensation and carrier phase estimation (CPE), is then carried out to compensate the impacts of laser phase noises and frequency difference either at the transmitter or at the receiver. Finally, some metrics, i.e. estimated signal-to-noise ratio (SNR), Q-factor, error vector magnitude (EVM) (as defined in section 2.4), are calculated to be able to quantitatively characterize the signal quality. For signal transmission or evaluation of new algorithms (work in Part III), an equalizer is inserted into the DSP procedure, more specifically after front-end correction, to remove the ISI effect and potential CD compensation.

Due to two slightly different approaches in next parts, several key DSP functions are discussed in the following subsections. Other compensations that may be raised during the work are briefly summarized in Section 2.3.5 for future research. Note that, the following discussed DSPs are applied to homodyne and intradyne detections.

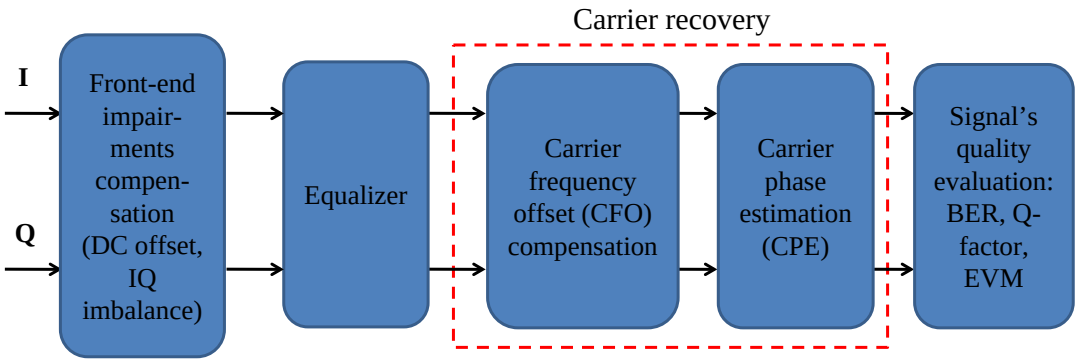


Figure I.12: Basic blocks in digital signal processing procedure.

2.3.1 Front-end correction

In the first step of DSP, the algorithm performs DC offset compensation and the corrections of specific optical front-end errors, knowing the gain and/or phase imbalance between the I and Q components. Particularly, in an optical bi-dimensional modulation format transmission system, the I and Q components of the optical field (namely $r_I(t)$ and $r_Q(t)$, respectively) achieved in the receiver, should result from the signal projection on an orthogonal basis. However, hardware implementation imperfections such as incorrect bias-points settings in the modulator, imperfect splitting ratio of couplers, photodiodes responsivities mismatch and misadjustment of polarization splitters in the optical coherent receiver can create amplitude and phase imbalance, known as quadrature imbalance (or IQ imbalance), which destroys the orthogonality of the received signal [73]. Fig. I.13(a) shows an example of ideal QPSK constellation, whereas Fig. I.13(b) presents a QPSK constellation under the impact of IQ imbalance. This IQ imbalance, if not compensated, could induce BER degradation.

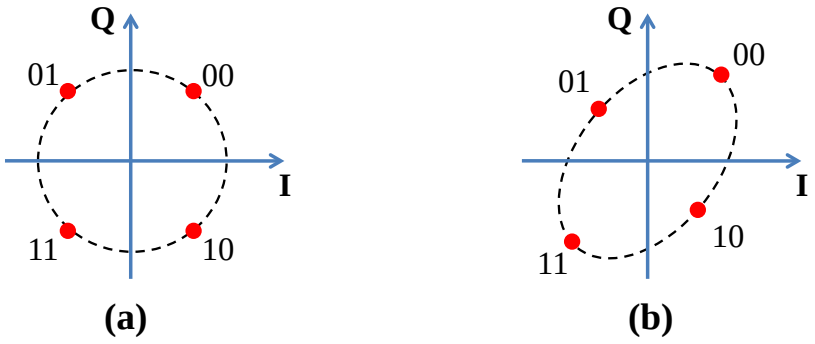


Figure I.13: Examples of QPSK constellations in (a) the ideal case, (b) the distorted case under the IQ imbalance impact.

Assuming the received I and Q components of the signal optical field under the IQ

imbalance impact, the DC offset is firstly compensated as follows

$$r_I(t) = r_I(t) - \mathbf{E}\{r_I(t)\}, \tag{I.15}$$

$$r_Q(t) = r_Q(t) - \mathbf{E}\{r_Q(t)\}, \tag{I.16}$$

where $\mathbf{E}(\cdot)$ is the ensemble average operator. The most common used IQ imbalance compensation is Gram-Schmidt orthogonalization procedure (GSOP) [74]. In this method, the correlation coefficient, ξ, is firstly calculated by

$$\xi = \mathbf{E}\{r_I(t) \cdot r_Q(t)\}. \tag{I.17}$$

After that, the GSOP transformation is carried out, resulting in two following orthogonal components with the normalized energy values [74]

$$I_{GSOP}(t) = \frac{r_I(t)}{\sqrt{P_I}}, \tag{I.18}$$

$$Q'(t) = r_Q(t) - \frac{\xi \cdot r_I(t)}{P_I}, \tag{I.19}$$

$$Q_{GSOP}(t) = \frac{Q'(t)}{\sqrt{P_Q}}, \tag{I.20}$$

in which P_I and P_Q are the average energies of the I and Q components, calculated as $P_I = \mathbf{E}\{r_I^2(t)\}$ and $P_Q = \mathbf{E}\{Q^2(t)\}$. Furthermore, some other IQ imbalance compensation techniques have been published such as the ellipse correction method [75], constant modulus algorithm based compensation [76], statistical properties of received signals [77], or the maximum signal-to-noise ratio estimation based method [78] proposed during this work: this technique will be presented in detail in Part III.

2.3.2 Equalization

An equalizer is widely used to remove the ISI effect caused by the bandwidth limitation in backplanes and dispersion in optical fibers. In theory, ISI can be explained by the effect of neighboring symbols on the current one. The effect of past symbols is called pre-cursor ISI, while that of future symbols is named as post-cursor ISI. Despite the ISI can come from various phenomena, the same equalization can be applied to compensate for all phenomena leading to ISI.

For a limited ISI (short normalized impulse response (compared to the symbol period) of a channel, L), the optimum detector for a data sequence recovery under the ISI is the maximum likelihood sequence detector (MLSD) [79]. The computational complexity growing exponentially with L makes the MLSD implementation impractical, especially with large L.

In such cases, the sub-optimal methods called feedforward and decision feedback equalizations (FFE and DFE) are utilized.

a) Feedforward equalization (FFE)

The upper part of Fig. I.14 shows an example of FFE which is equivalent to a linear transversal finite impulse response (FIR) filter, consisting of adjustable tap coefficients with time delay τ between adjacent taps. If $\tau = T_B$, where T_B is the symbol duration, the FFE is called a symbol-spaced equalizer. If $\tau < T_B$ the FFE is a fractionally-spaced equalizer, this kind of equalizer brings the advantage of avoiding aliasing [80]. The equalizer coefficients can be dynamically updated and calculated using algorithms designated to satisfy the system criteria such as data-aided (DA) or non-data-aided (NDA) algorithms (typically constant modulus algorithm (CMA), least mean square (LMS) combined to directed-decision (DD)). Finally, the FFE output is a summation of the input signal with its delayed and weighted versions. However, the FFE equalizer noise amplification results in poor SNR on some channels (i.e. channel with deep spectral valleys) [81]. To overcome this problem, the decision-feedback equalizer (DFE) is used, employing previous decisions to eliminate the ISI caused by previous symbols on the current symbols without noise enhancement [82].

b) Decision feedback equalization (DFE)

A DFE consists of the FFE, a clock decision element and a feedback filter, as shown in Fig. I.14 [83]. Normally, without feedback equalizer, FFE taps are set to cancel both pre- and post-cursors ISI. As far as the DFE is activated, the FFE requirements can be relaxed. For example, the FFE is a fractionally-spaced equalizer having the coefficients set to remove the pre-cursor ISI, whereas the feedback filter is a symbol-spaced FIR one responsible to cancel the post-cursor ISI. Therefore, the required number of taps in the DFE can be less than that in the single FFE for the same ISI to get the similar performance. LMS based on the minimum mean square error (MMSE) criteria is often used to update the coefficients in this case. However, the number of taps is usually the trade-offs among performance, power and area consumption, implementation possibility. More details about equalization could be found in Ref. [81].

2.3.3 Carrier frequency offset compensation

In the intradyne detection with a free-running LO, the carrier frequency offset (CFO) between the transmitted laser and the LO is inevitable. The LO frequency can be directly controlled by an analog feedback loop, at the cost of the increased complexity and the ineffectiveness, to remove the CFO. Fortunately, the DSP approaches can compensate for the CFO, for example the compensation in frequency domain [84] or Leven's algorithm [85] in time domain based on M^{th}-power operation with the limited estimation range to $\pm R_B/2M$, where R_B is the baud rate (symbol rate). Several efforts to improve the estimation range and the estimator quality have been reported in Ref. [86, 87] with more implementation

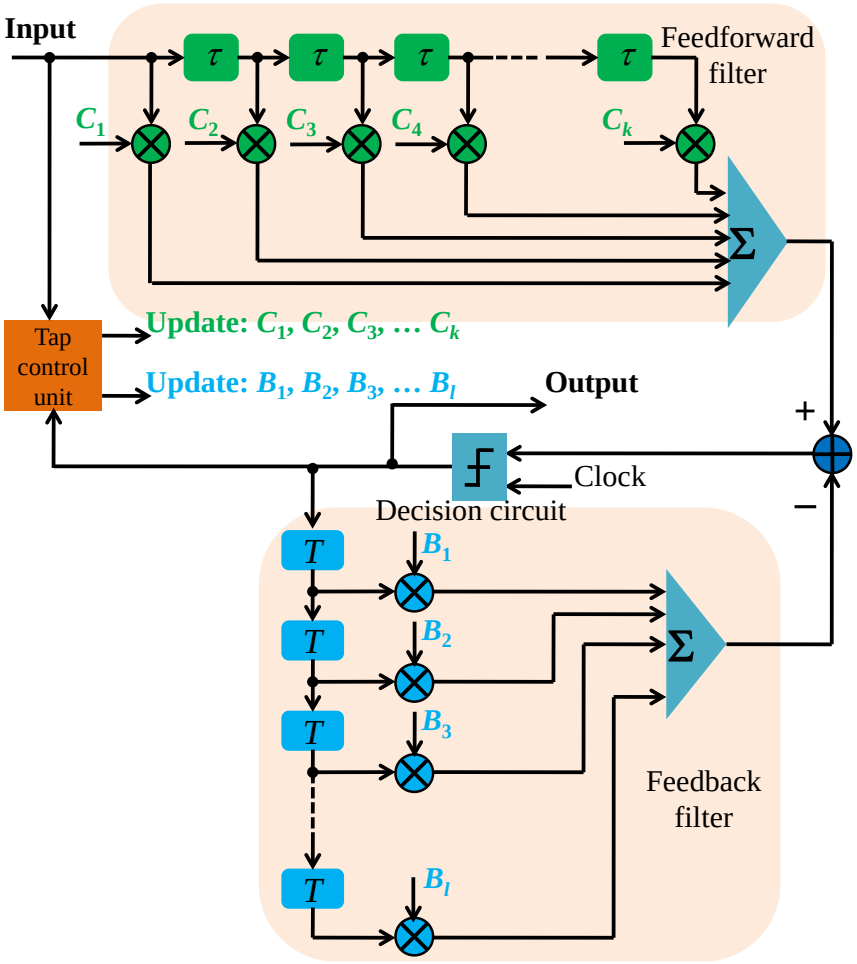


Figure I.14: Equalizer block diagram. The FFE, DFE are often clocked at a half of symbol duration ($T_B/2$) and a symbol duration (T_B), respectively. (reproduced from Ref. [83])

complication. Thanks to the recent advances in distributed feedback (DFB) laser, the temperature-stabilized wavelength locker accuracy is of ±1.25 GHz [88], the Leven's algorithm was shown to be sufficient to accommodate for such a range of frequencies.

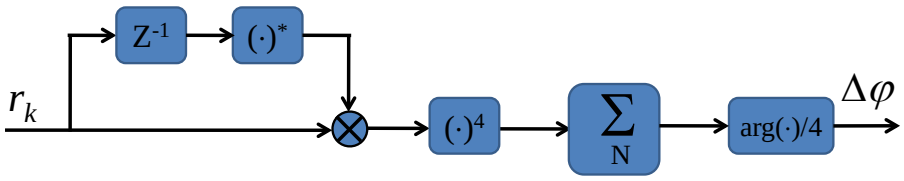


Figure I.15: Diagram for the CFO compensation, reproduced from Ref. [85].

Assuming that the frequency offset, Δf, between the transmitted laser and the LO is slowly drifting, the phase shift $\Delta\varphi$ between two consecutive samples r_k and r_{k+1}, caused by

CFO, is given by

$$\Delta\varphi = 2\pi \cdot \Delta f \cdot T_S, \tag{I.21}$$

in which T_S is the sampling time. Because the phase shift is also impacted by the laser phase noise, the phase shift caused by CFO should be estimated over a large number of samples, i.e. 500 samples as in Ref. [85]. Once estimated the CFO value, the following accumulated phase offset is subtracted from each symbol s_k to correct the CFO effect

$$\varphi_k = k \cdot \Delta\varphi \cdot T_S. \tag{I.22}$$

Fig. I.15 presents the block diagram of Leven's algorithm [85]. The current symbol is firstly multiplied with the complex conjugate of the previous symbol, resulting in a new complex number whose phase is the phase difference between two consecutive symbols. Then, any information encoded onto the signal phase should be removed by M^{th}-power operator (for $M-$PSK signals). The resulting complex numbers are summed up over a large number of samples, which is equivalent to the average operation. Finally, the phase component of the resulting summation is divided by M to get the estimated phase difference between two consecutive symbols. The symmetric and square $M-$QAM was shown to sufficiently provide the CFO estimation by 4^{th}-power operator [89]-[90] associated with the fast Fourier transform (FFT) analysis. It should be noted that the number of samples used to estimate the CFO can be reduced significantly by adding an extra step for fine searching such as Gradient-descent algorithm [90] or chirp Z transformation [91].

2.3.4 Carrier phase noise estimation

Like CFO compensation, the carrier phase noise estimation (CPE) can be done with the help of DSP allowing the free running LO in the intradyne detection. Assuming that the CFO was pre-compensated, the received samples, r_k, can be expressed in polar coordinate as follows

$$r_k = \rho_k \cdot \mathrm{e}^{j\theta_k}, \tag{I.23}$$

where ρ_k and θ_k are the amplitude and phase components of the received samples. The phase components after CFO compensation consists of the modulated signal phase φ_m, and the laser induced phase noise φ_n, with $\theta_k = \varphi_m + \varphi_n$.

To accommodate the requirements of equivalent time processing, the feedforward structures are of interest. For M-PSK signals, the well-known Viterbi-Viterbi algorithm [92] is used to compensate for the laser phase noise. Taking QPSK as an example, the modulated signal phase φ_m can take one of four values $\{\pi/4, 3\pi/4, 5\pi/4, 7\pi/4\}$. The Viterbi-Viterbi algorithm, whose block diagram is depicted in Fig. I.16, firstly strips off the data modulated

phase by the 4^{th}-power operation, resulting in the simply four-times phase noise quantity in the phase component

$$r_k^4 \sim \rho_k^4 \cdot \mathrm{e}^{j4\varphi_n(k)}. \tag{I.24}$$

The phase noise is then estimated over a number of samples, called block length. It is an important parameter depending on the property of the laser phase noise and the residual frequency offset. It is shown that the block length from 5 to 10 is optimized for 10 Gbaud QPSK signal [93]. After that, the estimated phase value is divided by 4 to undo the 4^{th} power operation. Finally, this value is subtracted from the phase of received samples to recover the information data. The similar operation can be carried out for M-PSK signal by the M^{th} power operation, however, at the expense of M-fold ambiguity. This problem can be solved by using differential encoding [94].

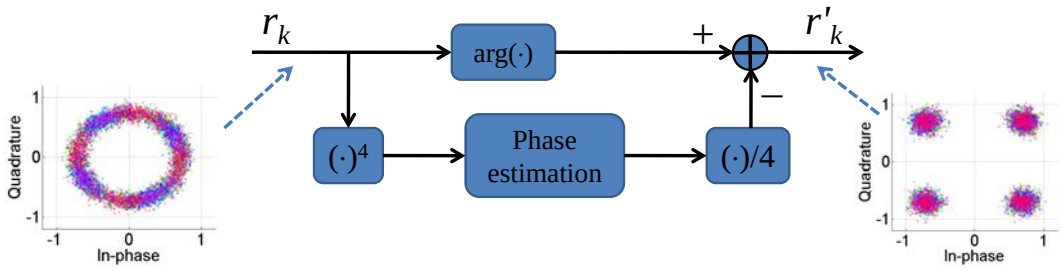


Figure I.16: Block diagram for the carrier phase estimation of QPSK signal based on Virtebi-Viterbi algorithm.

For M-QAM signal, the symbols are not distributed with equal angles on the constellation, and therefore the Viterbi-Viterbi algorithm does not operate properly. It is shown that the monomial nonlinear transformation provides a good estimator for phase noise estimation [95] in this case. This estimator modifies amplitude and phase components of the received samples through nonlinear operators

$$r'_k = \rho_k^n \cdot \mathrm{e}^{j \cdot l \cdot \theta_k}, \tag{I.25}$$

with $n, l = 1, 2, ..., M$. More details could be found in Ref. [95]. It is noted that the received symbols are distorted dominantly by either the amplified spontaneous emission (ASE)-LO beat noise or the shot noise of the LO in real transmission system [96]-[97] that could influence the performance of carrier phase estimation. Moreover, the laser phase noise follows a Wiener process and a Wiener filter can be applied for better compensation [98].

2.3.5 Other compensations: STR, CD, PMD, nonlinearities compensation

Symbol timing recovery (STR)

In order to get the samples with optimal SNR and phase representation, a symbol timing recovery (STR) should be carried out prior to the subsequent DSP algorithm. Various methods have been proposed involving the combination of a timing phase estimator and a digital interpolator. In general, they can be grouped into two types consisting of feedforward STRs (Fig. I.17(a)) and feedback STRs (Fig. I.17(b)). The former is referred to as a well-known square-and-filter (or square law nonlinearity) proposed by Oerder and Meyr (O&M) [99] and a Lee estimator [100]; whereas the latter often uses the algorithms proposed by Gardner [101] and Godard [102]. Among them, O&M algorithm normally requires 4 samples per symbol for the operation, while the others need only 2 samples per symbol. For real-time implementation, the feedforward structure is always of interest because of block-by-block data processing and having no feedback delay. The aforementioned algorithms play the main roles for timing error detector (TED) blocks providing the input data for the filter blocks. These filters update the phase estimation of current symbol based on the timing error signal and the previous symbol's phase estimation. The filter output is responsible for controlling the interpolator that could be cubic or piecewise-parabolic types with Farrow structure for the convenient on-line computation [103]-[104].

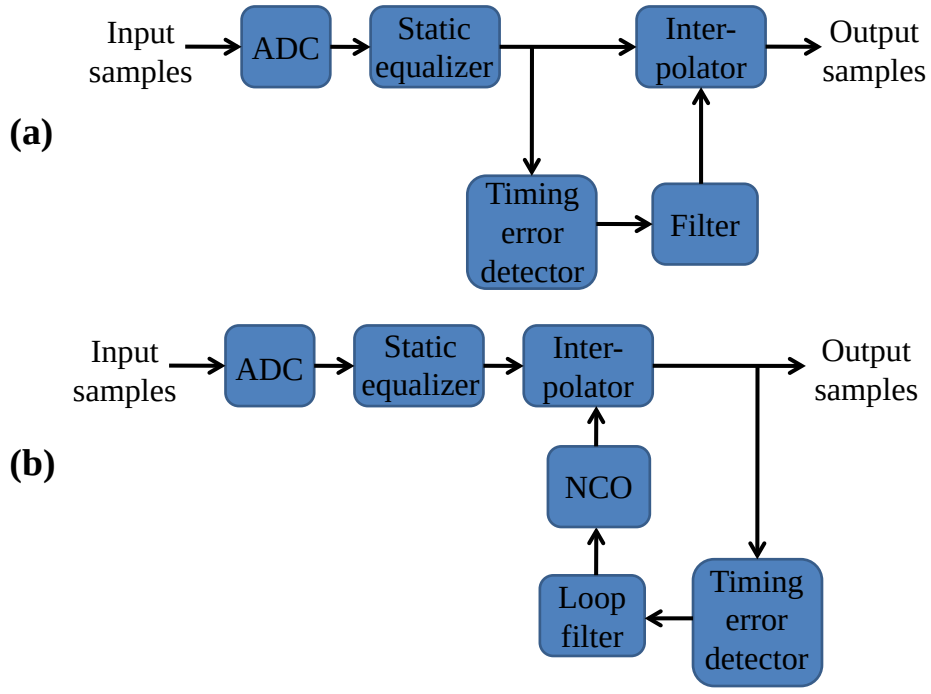


Figure I.17: (a) Feedforward and (b) feedback structures for the symbol timing recovery. NCO: numerical control oscillator; ADC: analog-to-digital converter.

Chromatic dispersion (CD) compensation

In the absence of fiber nonlinear impairments, this effect can be simply compensated by a linear filtering with an inverse transfer function of optical fiber. Moreover, this filter can be implemented either in time domain or in frequency domain [6]. It is to notice that the channel dispersion inherent by the particularity of fiber optic communications is deterministic on the contrary to the time-varying channel in radio communications.

a) Frequency domain CD compensation

Frequency domain response of the optical fiber when keeping the linear part of the nonlinear Schrodinger equation has the following form [105]

$$H\left(z,\Delta\omega\right)=\exp\left(-j\frac{D\lambda_0^2 z}{4\pi c}\Delta\omega^2\right), \tag{I.26}$$

in which λ_0 is the optical carrier wavelength, D is the dispersion parameter (usually expressed in $ps/nm/km$), $\Delta\omega$ is the difference between the pulsation of interest and ω_0, z is the distance of propagation, c is the speed of light. By multiplying the phase conjugate of this response to the fast Fourier transform (FFT) of the signal, CD can be compensated.

b) Time domain CD compensation

FFT operation normally requires more computational effort than the calculation in time domain. By calculating the inverse Fourier transform of equation (I.26), an impulse response liked approximate solution is presented as follows [6]

$$\begin{aligned} N_c &= 2\cdot\left\lfloor\frac{|D|\lambda_0^2 z}{2cT_S^2}\right\rfloor+1 \\ -\left\lfloor\frac{N}{2}\right\rfloor &\le k\le\left\lfloor\frac{N}{2}\right\rfloor \\ a_k &= \sqrt{\frac{jcT_S^2}{D\lambda_0^2 z}}\exp\left(-j\frac{\pi cT_S^2}{D\lambda_0^2 z}k^2\right) \end{aligned}. \tag{I.27}$$

This solution indicates the parameters for designing a FIR filter, in which N_c is the number of taps (if an odd number of taps is considered), k is the tap index, a_k is the $k-$th tap coefficients and T_S is the sampling period.

Polarization mode dispersion (PMD)

In contrast to CD, PMD is a time-varying phenomenon due to the variation of the fiber SoP. This effect can be therefore adaptively compensated for [6]. An adaptive equalizer realized in a multiple input multiple output (MIMO) butterfly structure (Fig. I.18) can be separated into 3 parts: the FIR filter banks composed of 4 FIR filters with the 4 corresponding coefficient-sets (namely $h_{XX}, h_{XY}, h_{YX}, h_{YY}$); a memoryless nonlinear estimator for the error, $e_{X(Y)}$, estimation and a device for updating the filter coefficients [106] based on the calculated errors. Each output is an arbitrary combination of the input signals enabling the deconvolution of the signal from the channel and separating the two SoP sources. It is also noted that the required filter taps number in this structure is generally small and this FIR

filter can compensate for the PMD and the residual CD. Usually, the LMS based equalizer is used. Compared to other adaptation algorithms such as recursive least square (RLS), least square, or Kalman filter, the LMS is more attractive in high speed transmission thanks to its high stability, rapid convergence and relatively less computational effort. Moreover, a decision-directed (DD) based LMS equalizer is used instead of using CMA or radius directed algorithm (RDA) due to its simplicity and rapid convergence. More information about the updated rules can be read in Ref. [107].

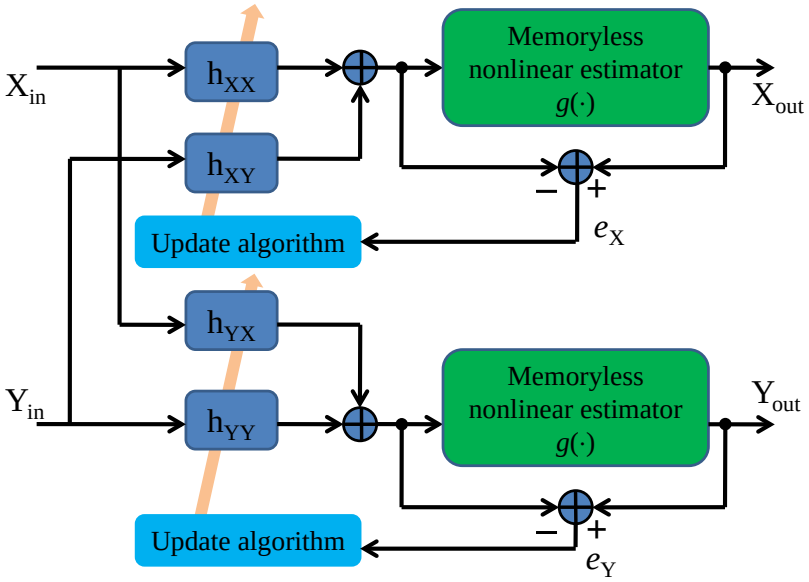


Figure I.18: A 2×2 MIMO filter in an adaptive equalizer structure.

Nonlinearities compensation

The signal propagation experiences both linear and nonlinear effects, resulting in the signal degradation. If nonlinear impairments compensation has been not implemented yet in deployed systems, DSP based nonlinear equalizers have been proposed in the last few years and notably the lumped nonlinear post compensation [108, 109], the maximum-likelihood sequence estimation (MLSE) or Volterra series based equalizers [110, 111]. These methods however require a very high computational complexity. Another idea is based on digital backward propagation (DBP) for the compensation of fiber deterministic impairments [112]. The general principle of this method is to emulate the propagation into a fictive fiber with negative dispersion and nonlinearity coefficients. Thanks to the DBP, the maximum reached distance can be increased from up to 70%, however, its performance is still limited in WDM system where XPM is normally dominant [113]. More details on this method can be found in [114, 115, 116].

2.4 Metrics for the quality evaluation of reconstructed signal

To quickly assess the performance of a high speed link or receiver, the eye diagram and constellation diagram are generally used. Based on them, several metrics to characterize the signal quality can be extracted such as the jitter, eye opening, SNR, error vector magnitude (EVM), Q-factor, bit error ratio (BER) ... In the following subsections, some frequently-used metrics in this thesis are discussed.

2.4.1 Q-factor

Quality factor (Q-factor) and BER are widely used and possibly interchangeable with each other. BER is the ratio between the number of received error bits (modified by the noise and interference) and the total number of transferred bits during the measured time interval. The symbol detection is realized by the decision circuits. Considering the NRZ-OOK signal as an example, the voltage with respect to the measured photocurrent at a sampling time is compared to a threshold voltage. If the signal voltage is superior (inferior) to the threshold voltage, the received symbol is detected as 1 (0). In the case where signal fluctuations due to noise are critical, the voltage of symbol 1 at the transmitter can be modified to be smaller than the threshold voltage and vice versa, leading to errors in the detection. In analytical calculation, the error probability is usually used. When BER is obtained over a sufficient long sample sequence, this measured BER can be approximately the error probability.

The error probability can be calculated as follows [23]

$$P_e = P_1 \cdot P\left(0/1\right) + P_0 \cdot P\left(1/0\right), \tag{I.28}$$

where $P_{1(0)}$ is the probability that the symbol 1 (0) is transmitted. $P(0/1)$ denotes the conditional probability of receiving the symbol 0 when the symbol 1 is sent, whereas $P(1/0)$ presents the conditional probability of receiving the symbol 1 when transmitting the symbol 0.

Assuming the equi-probabilities in the transmission of symbols 1 and 0, the error probability is represented by

$$P_e = \frac{1}{2} \cdot \left[P\left(0/1\right) + P\left(1/0\right)\right]. \tag{I.29}$$

Considering the noise in the optical transmission system as an additive white Gaussian noise (AWGN), the probability density functions (PDFs) of symbols 1 and 0 can be expressed by the following relation

$$p_1\left(u\right) = \frac{1}{\sqrt{2\pi}\sigma_1} e^{-\frac{(u-\mu_1)^2}{2\sigma_1^2}}, \tag{I.30}$$

$$p_0\left(u\right) = \frac{1}{\sqrt{2\pi}\sigma_0} e^{-\frac{(u-\mu_0)^2}{2\sigma_0^2}}, \tag{I.31}$$

where μ_i and σ_i, $i = 0, 1$, are the mean and standard deviation of the Space (symbol 0) and Mark (symbol 1) level distributions, respectively. Fig. I.19 presents an example of PDFs for 2 levels of NRZ-OOK signal, in which V^{th} is the optimum decision threshold. The optimum decision threshold minimizing the error probability is specified by

$$V^{th} = \frac{\mu_0\sigma_1^2 - \mu_1\sigma_0^2 + \sigma_1\sigma_0\sqrt{(\mu_1-\mu_0)^2 + 2(\sigma_1-\sigma_0)^2\ln(\sigma_1/\sigma_0)}}{\sigma_1^2-\sigma_0^2}. \tag{I.32}$$

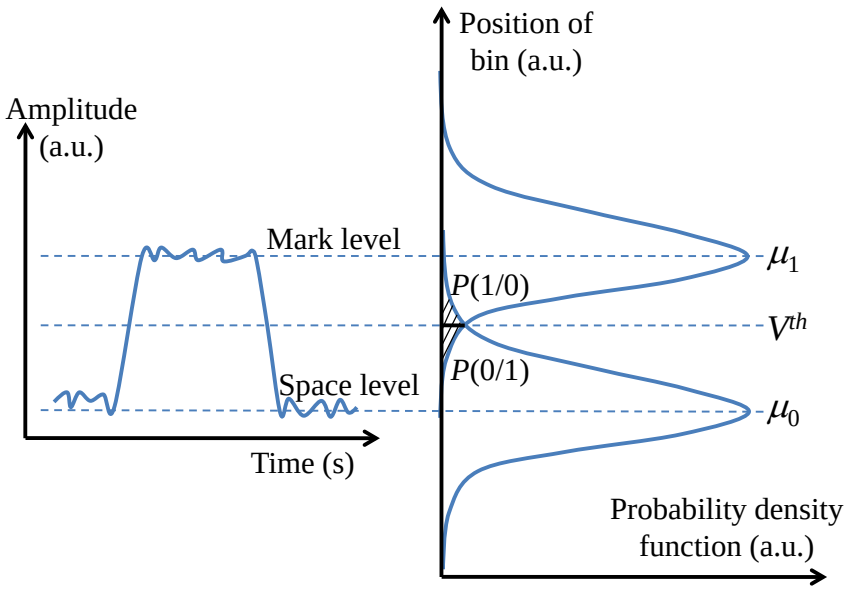


Figure I.19: Example of the probability density functions of the corresponding NRZ-OOK signal.

The conditional error probabilities are then calculated as

$$P(1/0) = \int_{V^{th}}^{+\infty} p_0(u)\,du = \frac{1}{2}erfc\left(\frac{V^{th}-\mu_0}{\sqrt{2}\sigma_0}\right), \tag{I.33}$$

$$P(0/1) = \int_{-\infty}^{V^{th}} p_1(u)\,du = \frac{1}{2}erfc\left(\frac{\mu_1-V^{th}}{\sqrt{2}\sigma_1}\right). \tag{I.34}$$

Substituting (I.33) and (I.34) into (I.29), the error probability is represented by

$$P_e = \frac{1}{4}\left[erfc\left(\frac{V^{th}-\mu_0}{\sqrt{2}\sigma_0}\right) + erfc\left(\frac{\mu_1-V^{th}}{\sqrt{2}\sigma_1}\right)\right]. \tag{I.35}$$

Assuming that $\ln(\sigma_1/\sigma_0) \to 0$, the optimum decision threshold is given by

$$V^{th} = \frac{\sigma_0\mu_1 + \sigma_1\mu_0}{\sigma_0+\sigma_1}. \tag{I.36}$$

The arguments of each $erfc$ function in (I.35) become identical and give the definition of Q-factor

$$\frac{V^{th} - \mu_0}{\sigma_0} = \frac{\mu_1 - V^{th}}{\sigma_1} = Q. \tag{I.37}$$

Q-factor is usually expressed in dB, Q_{dB} [117], from (I.36) and (I.37), the Q-factor is given by

$$Q_{dB} = 20 \log_{10} \left(\frac{\mu_1 - \mu_0}{\sigma_1 + \sigma_0} \right). \tag{I.38}$$

It is noted that error probability is bijectively linked to Q-factor in an OOK transmission system corrupted by AWGN by substituting the (I.38) into (I.35). BER (measured over a long acquisition) in this system is approximately to error probability, the following relation is then achieved

$$BER = \frac{1}{2} erfc \left(\frac{Q}{\sqrt{2}} \right). \tag{I.39}$$

The Q-factor metric is often established for the OOK transmission systems, however, this method cannot be simply used for QAM signals. A recent work [118] analytically derives the relationship between Q-factor and BER for PAM signals albeit at the complexity and computational effort.

2.4.2 Error vector magnitude (EVM)

The popular EVM metric is also utilized to evaluate the reconstructed constellation deviation of bi-dimensional modulation format signals compared to the reference one. As given in Ref. [119], EVM can be expressed mathematically as

$$EVM_{RMS} = \sqrt{\frac{1}{N} \sum_{r=1}^{N} \left(|I_{ideal,r} - I_{measure,r}|^2 + |Q_{ideal,r} - Q_{measure,r}|^2 \right)}, \tag{I.40}$$

where N is total number of measured symbols. $I_{ideal(measure),r}$ and $Q_{ideal(measure),r}$ are the normalized voltages of ideal (measured) in-phase and quadrature components, respectively, for the r^{th} symbol.

Fig. I.20 shows an example of EVM calculation, in which the error vector presents the deviation of the measured symbol comparing to the ideal symbol. The magnitude of this error vector provides the information of how many the deviation is. In case the received optical field is perturbed by AWGN only, the EVM can be translated to the BER and to the optical signal-to-noise ratio (OSNR, as discussed below) [120], providing a useful tool for the characterization of bi-dimensional modulation format.

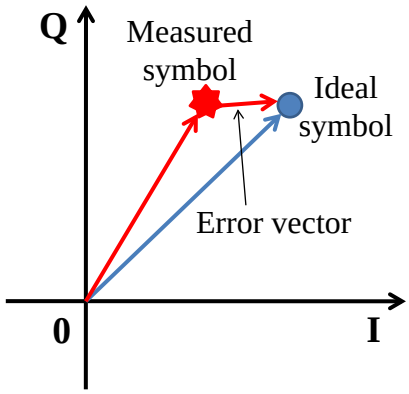


Figure I.20: Example of EVM calculation in IQ plane.

2.4.3 Optical signal-to-noise ratio (OSNR)

To characterize the optical signal, optical signal-to-noise ratio (OSNR) is usually used instead of signal-to-noise ratio (SNR). The OSNR is defined as the ratio of optical signal power and optical noise power in the bandwidth of interest, measured in both polarizations [121]

$$OSNR = \frac{P_s}{2 \cdot N_0 \cdot B_{ref}}, \tag{I.41}$$

where P_s is the average optical signal power summed over all states of polarization, N_0 presents the power spectral density of the optical noise in one state of polarization. Usually the reference bandwidth is chosen as $B_{ref} = 12.5$ GHz (equivalent to $\Delta\lambda_{ref} = 0.1$ nm).

Moreover, the SNR of an AWGN channel is defined by

$$SNR = \frac{E_s}{N_0}, \tag{I.42}$$

in which N_0 presents the power spectral density of AWGN noise, and $E_s = P_s \cdot T_B$ denotes the energy per symbol. Note that, P_s in this case is the average power of the modulated symbol and is assumed to be similar when transmitting on the optical channel. $T_B = 1/R_B$ represents the symbol period, where R_B is the baud rate (symbol rate).

In some cases, we use the following SNR definition [122] to quickly assess the SNR value regardless of the calculation of the noise power spectral density

$$SNR_x = \frac{\mu_x}{\sigma_x}, \tag{I.43}$$

where x is the data under test. μ_x and σ_x denote the mean and standard deviation of x, respectively. In this case, the SNR of x represents the standard deviation of the data under test compared to its mean value being calculated [122].

Assuming AWGN noise in the radio frequency domain and in the optical domain are

equivalent, the OSNR and SNR are linked by the following relationship

$$OSNR = \frac{R_B}{2B_{ref}} SNR. \tag{I.44}$$

Another metric, SNR_b - called SNR per bit, is commonly used. If $m = log_2(M)$ is the number of encoded bits on one symbol, the SNR can be expressed as $SNR = m \cdot SNR_b$. SNR per bit is useful because it directly indicates the power efficiency of the system regardless of modulation type, error correction coding or signal bandwidth. Finally, the relationship in (I.44) can be represented as follows

$$OSNR = \frac{mR_B}{2B_{ref}} SNR_b. \tag{I.45}$$

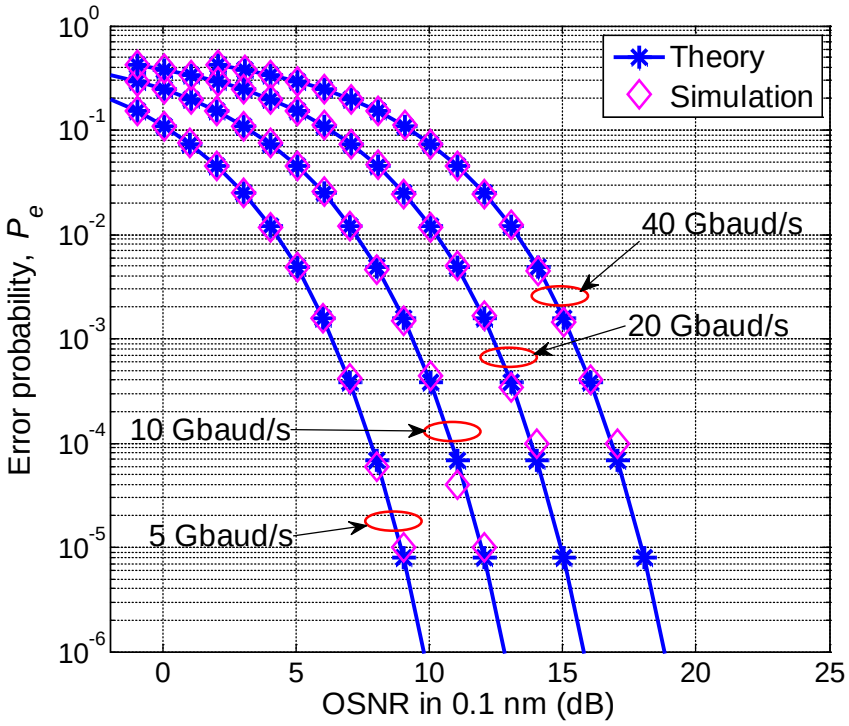


Figure I.21: Error probability versus OSNR for QPSK (4-QAM) signal at the different symbol rates.

Fig. I.21 presents the evolution of error probability versus OSNR of QPSK (4-QAM) signals at different symbol rates. The analytical curve [123, 25] shows a good agreement with the simulated one. It should be noted that the relationship between OSNR and SNR still holds as long as the noise is AWGN [120].

3. A crucial element of the receiver: the analog-to-digital converter

Bi-dimensional modulation format generation techniques, coherent detection in combination to high speed electronics for DSP can encode information on the four optical domains such as amplitude, phase, polarization, and wavelength per spatial mode. More importantly, advances on material and device fabrication both in electrical domain (i.e. complementary metal-oxide-semiconductor (CMOS)) and in optical domain (i.e. devices with higher non-linearities and higher efficiencies), and photonic integrated circuits (PICs) technologies are the major keys for the future network [124, 125], in which 400 Gigabit Ethernet (IEEE P802.3bs) is under discussion and will be standardized in early 2017 [126]. However, one must solve a number of technological bolts by the means of photonic solutions, because the electronic solutions for analog signal processing developed for radio-communications are limited in bandwidth and in amplitude resolution. The heart of the present work concerns the analog-to-digital conversion (ADC) as it is a key element of coherent receivers. The study about the high-speed ADC is hence very important for high-performance receivers. The combination of numerical and optical signal processing could indeed solve a part of the challenge of new modulation formats bolts.

3.1 Limitation of high bit rate transmission systems

The requirement of high-speed ADC in coherent receivers is a main limitation for very high bit rate optical transmission systems. An ADC transforms a continuous signal into a discrete or digital signal by four distinct functions including filtering, track-and-hold (T/H) or sampling, quantization and digital coding (Fig. I.22) [127]. The analog signal, $x(t)$, is firstly filtered by a bandlimited low-pass filter (range of $0 \leq f_x \leq f_B$) to avoid aliasing. After sampling and digitizing the analog signal to the discrete-amplitude ensembles, the digital processor generates the digital code for each discrete value. We will describe a little further on the T/H and the quantization stages in the following parts as they are the most important functions in ADC. More details about two other stages can be referred to Ref. [127].

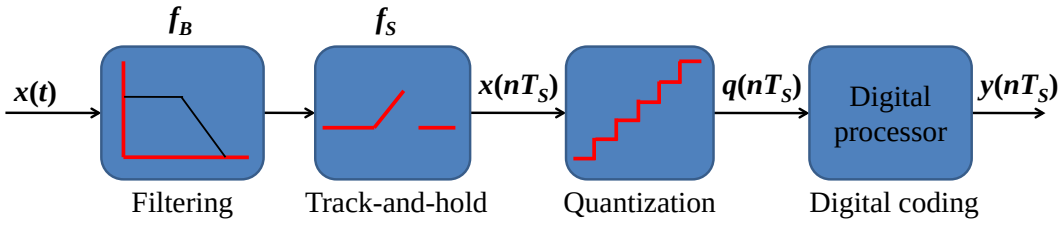


Figure I.22: General analog-to-digital converter block diagram (after Ref. [127]).

3.2 Principle of ADC track and hold

The key element for high sampling rates in ADCs is the T/H in which the CMOS technology is a main-stream technology because of its low power dissipation design and on-chip DSP capability. Due to the available fast T/H, the signal can be further down-sampled and processed by interleaved ADC cores where the clock distribution is now the limiting factor [128]. For this limitation, SiGe technology provides a major advantage associated with bandwidth and gain, making the integration of automatic gain control/trans-impedance amplifiers (AGC/TIAs) possible in real applications. However, to meet the requirements of up to Tb/s transmission systems, the use of optical functions to improve the ADCs performance could be of interest.

The T/H is a controlled analog circuit that tracks the input signal (during the sample mode) and holds it (during the hold mode) to an instantaneous value of signal at the time when switching from the sample mode to the hold mode. An example of time-domain response of an ideal T/H circuit is represented in Fig. I.23. The functionality of T/H is to continuously sample the input signal and to hold this sample value constant as long as it takes for the ADC to achieve its digital representation. T/H is crucial in high-resolution ADC [129].

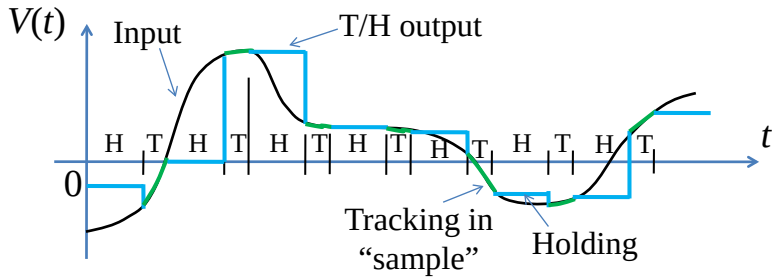


Figure I.23: Time-domain response of an ideal (instantaneous and accurate) T/H circuit.

One of the most important performance metrics of T/H circuit is the *acquisition time*. It is defined as the time starting from the switching time (from the hold mode to sample mode) to the moment that a new sample is readily taken [130]. The maximum achievable sampling rate of ADC is also linked to the acquisition time. Other performance metrics of T/H circuit, such as aperture delay and jitter, hold mode settling time, droop rate due

to signal leakage, pedestal error, gain deviation, dynamic range and nonlinearities are not addressed in this study for simplicity.

3.3 Quantization

Quantization stage is carried out after the sampling (T/H) stage in an ADC. Quantization refers to the process whereby the continuous amplitude values are transformed into a finite set of discrete values. Depending on the classification of associated quantizer step-size, several methods for the quantization are introduced. The method, called uniform quantizers, accomplishes the digitization process using 2^b equal quantization steps to be able to obtain b-bits resolution. Other methods (for example, μ-law, A-law) attempt to modify the step-size as a function of the input signal's PDF (power density function).

For uniform quantization (Fig. I.24), if the signal is in a finite range of (x_{min}, x_{max}), the quantization step-size, Δ, can be deduced by dividing the entire data range by $L = 2^b$ equal intervals

$$\Delta = \frac{x_{\max} - x_{\min}}{L}. \tag{I.46}$$

The index of quantized value is calculated by

$$INT\left(x\right) = \left\lfloor \frac{x - x_{\min}}{\Delta} \right\rfloor, \tag{I.47}$$

where $\lfloor a \rfloor$ is the floor function returning to the largest integer less than or equal to a. Based on this index, the quantized value is hence given by

$$F\left(x\right) = INT\left(x\right) \cdot \Delta + \Delta/2 + x_{\min}. \tag{I.48}$$

The quantized value is finally mapped to a specific digital code representing for an input signal level. This uniform quantization is only optimal for a uniformly distributed signal. However, real signals (i.e. speech, music) are more concentrated near zero region where human ear is more sensitive to quantization errors. This problem can be overcome by using non-uniform quantization by which the quantization interval is smaller near zero. For instance, μ-law transforms the signal before applying the uniform quantizer as follows

$$y = F_\mu\left(x\right) = x_{\max} \frac{\log\left[1 + \mu \frac{|x|}{x_{\max}}\right]}{\log\left(1 + \mu\right)} \operatorname{sgn}\left(x\right), \tag{I.49}$$

where μ is the compression parameter, $sgn(\cdot)$ is the signum function. The quantized value can then be transformed back using inverse μ-law

$$x = F_\mu^{-1}\left(y\right) = \frac{x_{\max}}{\mu}\left(10^{\frac{\log(1+\mu)}{x_{\max}}|y|} - 1\right) \operatorname{sgn}\left(y\right). \tag{I.50}$$

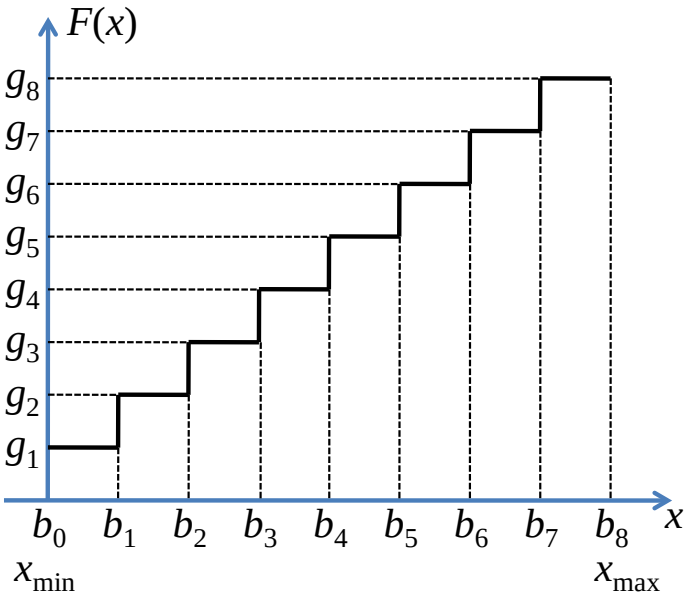


Figure I.24: Example of uniform quantization with 8 possible output levels.

The basic idea behind μ-law companding is to improve the signal-to-quantization noise and distortion ratio at low signal levels by a logarithmic transformation [131]. Fig. I.25 shows an example of μ-law companding at different μ value. It is observed that the low signal levels are expanded proportionally to the increase of μ value and vice versa. In our study, uniform quantizers are used to match to the experimental device.

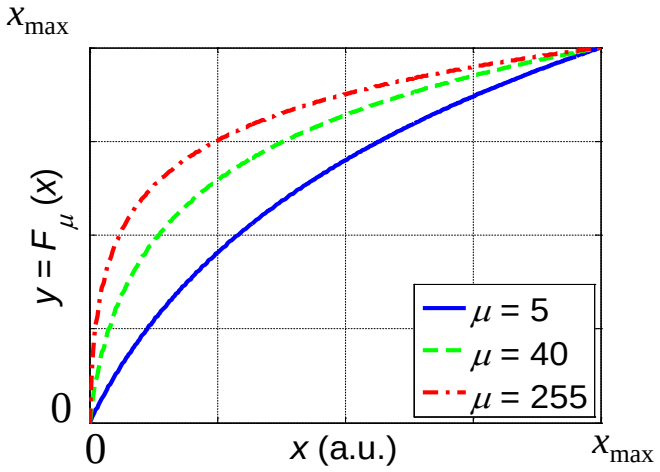


Figure I.25: μ-law transformation at different μ values.

3.4 Performance of an ADC

ADCs are the critical components in digital systems, as their performance have great impact on the system bandwidth, accuracy and signal SNR. Despite the various ADCs, their overall

performance can be characterized by a relatively small number of parameters, as introduced in the following subsections.

3.4.1 Metrics for performance measurement

a) Sampling rate

A periodic impulse train is normally used to sample a continuous time signal at regular intervals to sample the signal. Moreover, the Nyquist theorem stated that to be able to recover the signal from the discrete-time waveform, the sampling rate (called Nyquist rate) should be equal to or greater than twice the bandwidth of the analog signal. In other words, the larger the signal bandwidth is, the higher the required ADC sampling rates should be.

b) Resolution

The signal amplitude is usually sampled and quantized by the mean of dividing the full-scale voltage (V_{FS}) into 2^b quantization levels, where b denotes the number of resolution bits in the ADC [127]. To characterize precisely the ADC resolution, a frequently used parameter is the effective number of bits (ENOB), which refers to the actual dynamic range or the noise performance of the ADC.

c) Effective number-of-bit (ENOB)

Fig. I.26 shows an example of the sinusoidal wave and the corresponding time-discrete representation by a 3-bit (8-level) quantization. The difference between the analog signal and its digitized amplitude level corresponds to the quantization noise (also represented on the graph). Quantization leads to a loss of information by going away from the analog curve at some points. If Δ is the smallest quantization step (or the least significant bit (LSB)), the quantization error should be within the range $[-\Delta/2, \Delta/2]$. The SNR parameter in the presence of only quantization noise is called the signal to quantization noise ratio (SQNR). In the next step, the analytical closed-form for the relationship between SQNR and ENOB is derived. The analog input to the ADC is assumed to be a sinusoidal signal, $x(t) = A \cdot sin(\omega_0 t + \phi)$, where A, ω_0, ϕ are the amplitude, angular frequency and initial phase of the signal. The input full-scale amplitude V_{FS} is divided into $L = 2^b$ uniform levels, and the signal amplitude can be expressed as $A = 1/2 \cdot L \cdot \Delta$.

The root mean square (rms) value of the input signal can be represented by [132]

$$A_{rms} = \frac{A}{\sqrt{2}} = \frac{L \cdot \Delta}{2\sqrt{2}} = \frac{\Delta \cdot 2^b}{2\sqrt{2}}. \tag{I.51}$$

Note that, the quantization error, e, is assumed to be uniformly distributed over the

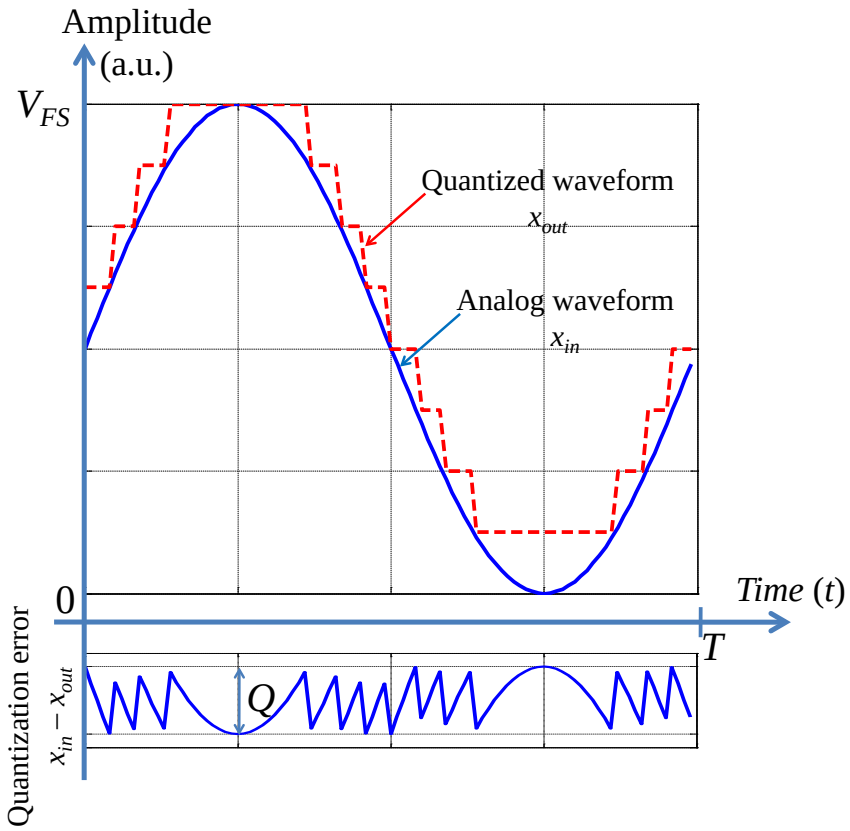


Figure I.26: Example of a quantization waveform (dash line) with 3-bits for one period T of a sinusoidal signal (dash line) and its corresponding quantization error (lower waveform).

interval $[-\Delta/2, \Delta/2]$. By this way, the mean-square value of e is given by

$$E_{ms} = \int_{-\Delta/2}^{\Delta/2} \frac{1}{\Delta} e^2 de = \frac{\Delta^2}{12}. \tag{I.52}$$

The rms quantization error, e_{rms}, is therefore deduced by $e_{rms} = \sqrt{E_{ms}} = \Delta/\sqrt{12}$. The rms SQNR for an ideal b-bit converter is as follows

$$SQNR = \frac{A_{rms}}{e_{rms}} = \sqrt{3/2} \cdot 2^b. \tag{I.53}$$

In the logarithmic representation, the SQNR has the following form

$$SQNR\,(\text{dB}) = 6.02 \cdot b + 1.76. \tag{I.54}$$

Inspection of (I.54) shows increasing the number of bits by 1 results in 6 dB improvement of SQNR. In practice, there are many other noise sources causing the SNR degradation of the ADC. These noises can be modeled as additive white Gaussian noise (AWGN) and counted as an equivalent quantization noise when evaluating the SNR [127]. Assuming the

input signal is filled in the full-scale range of the ADC, a well-known formula of the effective number of bits, ENOB, can be defined by [133]

$$ENOB = \frac{SNR\,(\mathrm{dB}) - 1.76}{6.02}. \tag{I.55}$$

The ENOB is one of the most important specifications of the ADC that is normally used to characterize the ADC performance [134]. To simulate the effect of ENOB on the digitized signal, the quantization noise is modeled as AWGN noise with zero mean and its variance of $\Delta^2/12$ [132].

d) Figure of merit (FOM) and power dissipation

A figure-of-merit, *FOM*, is widely used for the investigation of power efficiency in relation to resolution and speed in the ADC performance analysis. It is defined as [135]

$$FOM = \frac{2^{ENOB} \cdot f_S}{P_{diss}}, \tag{I.56}$$

where f_S is the sampling rate and P_{diss} presents the power dissipation. If T/H block is assumed the most power consuming part and the input signal supplies the power to charge the T/H capacitance, the power dissipation of such an ADC can be derived by [136]

$$P_{diss} = k \cdot \Theta \cdot f_S \cdot 10^{(6b+1.76)/10}, \tag{I.57}$$

in which $k = 1.38 \cdot 10^{-23}$ J/K is Boltzmann's constant and Θ is temperature in Kelvin. Furthermore, the SNR and spurious-free dynamic range (SFDR) metrics are also used to characterize the dynamic performance of ADCs for high speed applications. More information about these metrics can be found in Ref. [127].

3.4.2 Upper bounds for ADC performance limitation

The reduction of quantization noise can be achieved by increasing the ADC resolution bit number. However, the noises may come from various internal and external sources, setting the noise floor of the ADC. To fully utilize the available SNR, the quantization step is chosen so that the quantization noise is equal to the noise floor level. In this section, we discuss four major factors limiting the maximum achievable bit number, which are the thermal noise, aperture jitter, comparator ambiguity and Heisenberg uncertainty. The design criteria derived in Ref. [127], can be applied to both electronic and optic ADCs.

In practice, the various noise sources, i.e. the thermal noise, shot noise, ..., can contribute to the noise level at the input of an ADC that can be seen as an equivalent thermal resistor, R_{eq}. Considering that the thermal noise is the dominant contribution to the noise floor, the maximum achievable number of bit (NOB) can be deduced by [127]

$$NOB = \log_2 \left(\frac{V_{FS}^2}{6 \cdot k \cdot \Theta \cdot R_{eq} \cdot f_S} \right)^{-1/2} - 1, \tag{I.58}$$

where V_{FS} and f_S are the full-scale voltage and the sampling rate of the ADC, respectively.

Jitter is the uncertainty in sampling time caused by the phase noise of the sampling clock or of the input signal. Aperture jitter or timing jitter, τ_a is defined as the standard deviation of the timing offset between the practical sampling time and the ideal one. This leads to the sample error in amplitude. Assuming that the aperture jitter is an uncorrelated Gaussian random process and the main contribution to the noise floor, the maximum NOB is limited by [127]

$$NOB = \log_2\left(\frac{1}{\pi \cdot \tau_a \cdot f_S}\right). \tag{I.59}$$

It should be recalled that the quantization is performed by comparing the analog input to different reference levels made of the comparator followed by the logic circuits. The comparator is primarily an amplifier and a regenerator [127] whose growing time causes ambiguity errors to the logic circuits if it is not sufficiently fast. The regeneration time is sometimes mentioned as the speed of the comparator. This time is proportional to the unit current gain of transistor in the comparator, f_T, which is determined by the transistor technology and the interconnection capacitance. The NOB limitation due to the dominant ambiguity error can be calculated by [127]

$$NOB = \frac{\pi \cdot f_T}{6.93 f_S} - 1.1. \tag{I.60}$$

Three aforementioned limitations are specified by the current technologies. Moreover, the physical limitation, called Heisenberg uncertainty, acts as the upper-bound limitation. More specifically, the energy and time cannot be measured with an infinite accuracy at the same time, which can be expressed as [127]

$$\Delta E \cdot \Delta t \geq \hbar/2, \tag{I.61}$$

in which ΔE is the uncertainty of energy that is the smallest resolvable energy for the ADC (or 0.5 LSB). Δt denotes the half of the sampling period. Moreover, $\hbar = h/2\pi$ is of about $1.055 \cdot 10^{-34}$ J·s, where h is the Planck constant. Assuming that $V_{FS} = 1$V and the input resistance $R = 50\Omega$, the NOB-sampling rate product can be evaluated as follows

$$2^{NOB} \cdot f_S \leq 4.86 \cdot 10^{15}. \tag{I.62}$$

Fig. I.27 illustrates the maximum achievable NOB when either thermal noise or aperture jitter or comparator ambiguity or Heisenberg uncertainty overwhelms. It can be observed that the increase of the sampling rate is proportional to the decrease of the achievable NOB. More specifically, in the low sampling rate region, the NOB of ADCs is limited by the equivalent thermal noise. For instance, 1000 Ω resistor restricts the maximum NOB to 15 bits at the sampling rate of about 10 MS/s. Moreover, the aperture jitter limited from 0.1 ps to 1 ps specifies the sampling rate in the range of 10 MS/s to 100 MS/s. ADCs'

sampling rates above 100 MS/s are limited by the comparator ambiguity. For example, the ADC sampling rate of 10 GS/s using the comparator with f_T of 100 GHz gives a NOB of about 3 bits.

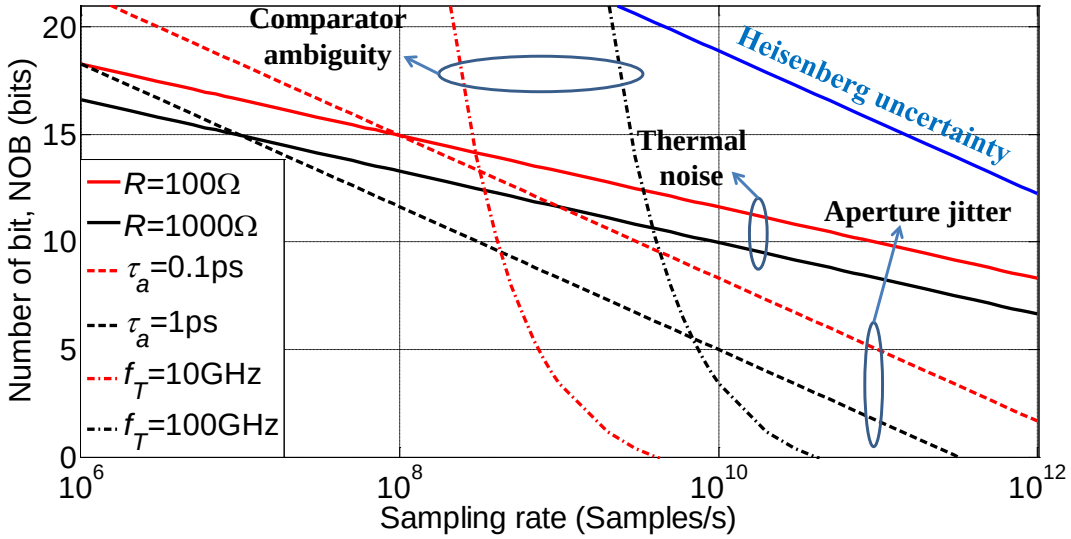


Figure I.27: Maximum achievable NOBs as the function of the sampling rate limited by either thermal noise or aperture jitter or comparator ambiguity or Heisenberg uncertainty.

3.5 State-of-the-art of the electronic ADCs

Several works have been carried out for revisiting the state-of-the-art of ADCs with both experimental and commercial converters [137, 135, 138]. It was shown that the ADCs performance have improved significantly since 2000s in terms of aperture uncertainty (jitter) and power dissipation. More specifically, the jitter value has reduced from nearly 1 ps in 1998 [139] to less than 100 fs recently [140]. Moreover, the figure of merit (FOM) was reported to be improved by an order of magnitude [135]. Thanks to progress in the application-specific integrated circuit (ASIC) technology for ADCs fabrication, 130-nm CMOS-BiCMOS has been migrated to 28-nm CMOS providing a 20-fold increase in throughput and gate count [138]. This trend brings a great advantage to the early realization stages of coherent systems [141] and to further high bit rate coherent transmission. For instance, a 100 Gb/s transmission on a single carrier was recently demonstrated [142, 143].

In terms of ADC architecture, the high-speed ADC cores are constituted of successive approximation registers (SAR), flash, pipeline, serial/ripple, folding/interpolating and time-interleaved stages. These architectures are conceptually shown in Fig. I.28. The choice of topology depends on several criteria when setting up a system, for example, SAR and multistage flash are suitable for lower power operation, whereas the parallel structure (time-interleaved) is better for high-sample rate converters. Fig. I.28(a) shows the diagram of a successive approximation register (SAR) ADC implementing a binary search algorithm. A

bit by bit processing from the MSB down to the LSB is decided by a single high speed, high accuracy comparator that is the limiting factor on the ADC operating speed. Fig. I.28(b) presents a flash ADC which is the fast architecture thanks to a large bank of comparators. However, the increase of ADC resolution is proportional to the number of comparators. Moreover, the power consumption of flash ADC is higher than that of SAR ADC due to the requirement of extra conversion circuitry. Fig. I.28(c) illustrates a parallel structure of a pipelined ADC where each stage processes one to several bits. The advantages of this architecture are the increases of throughput, less complexity and lower power consumption than flash architecture. The drawbacks are the trade-off between the power consumption and latency; moreover, the area for implementing this structure is greater than that for SAR ADC. Fig. I.28(d) shows an architecture of a serial or ripple ADC in which the T/H circuit holds the input signal constant during the conversion with N stages. Each stage creates a bit output and a residue output that is the input for the next stage. This architecture is simpler and yields a lower complexity than the flash one since the number of amplifiers and flip-flops is equal to the resolution. However, it is strongly affected by the propagation delay through each stage. Fig. I.28(e) presents the structure of the folding ADC that reduces the required area, complexity and power dissipation due to the reuse of comparators, the use of M-times folding circuit and interpolation. Fig. I.28(f) shows architecture of a time-interleaved ADC using a set of N sub-ADCs (normally the SAR ADCs) such that the total throughput is N times the sample rate of each sub-ADC. This architecture is suitable for the implementation of high speed ADC (above 10 GS/s) [144]. However, the requirements of calibration circuits for offset, gain mismatch and timing skew between the sub-ADCs are the challenge for this structure. More details about the electronic ADCs can be found in Ref. [145]. The state-of-the-art of high-speed ADCs with sample rates above 1 GS/s are summarized in Tab. I.2 based on the order of increasing sampling rate.

It is clearly observed that the limited ADC sampling rate below 70 GS/s is the bottleneck for very high-speed optical coherent transmission system. The next section is aiming at summarizing some available techniques for the realization of high speed ADCs.

3.6 Some solutions to push ADC speed for real-time DSP

Although there is always a trade-off between the sampling speed and the ADC resolution, increasing the ADC speed is feasible by either electronic or optical-assisted solutions.

a) Electronic solution

The effective sample rate and bandwidth of an ADC can be increased by combining several ADCs. Fig. I.29 shows an example to double the ADC sampling rate by filtering the spectrum of the input signal from 0 to $f_S/2$ to split it into two halves. In fact, this scheme is used in the high-end real-time sampling oscilloscopes [8] enabling to sample the signals with 80 GS/s and 30 GHz bandwidth, and possibly up to 120 GS/s and 45 GHz bandwidth

Table I.2: Available electronic high-speed ADCs.

Ref.	**Process technology**	**Architecture**	**Maximum sampling rate (GS/s)**	**Resolution (bits)**	**Power dissipation (W)**	**Year**
[146]	130-nm CMOS	TI	1	11	0.25	2006
[147]	npn bipolar	FL, DEC	2	10	6.5	2005
[148]	GaAs HBT	IF	3	8	5.5	2006
[149]	Bipolar hybrid	TI	4	8	39	1991
[150]	GaAs HBT	IF	6	6	6	2006
[151]	180-nm CMOS	TI	20	8	9	2003
[152]	130-nm SiGe BiCMOS	FL	22	5	3	2006
[144]	90-nm CMOS	TI/SAR	24	6	1.2	2008
[153]	130-nm SiGe BiCMOS	FL	25	5	4.8	2008
[154]	SiGe HBT/BiCMOS	SRC	30	6	2	2009
[155]	180-nm SiGe BiCMOS	FL	35	4	4.5	2009
[156]	65-nm CMOS	TI/SAR	40	6	1.5	2010
[157]	SiGe BiCMOS	TI	40	4	n/a	2010
[158]	65-nm CMOS	TI/SAR	56	8	n/a	2010
[7]	28-nm CMOS	TI/SAR	55-70	8	n/a	2013

FL: flash; IF: interpolating/folding; SRC: serial ripple converter; TI: time-interleaved; DEC: digital error correction; n/a: information not available.

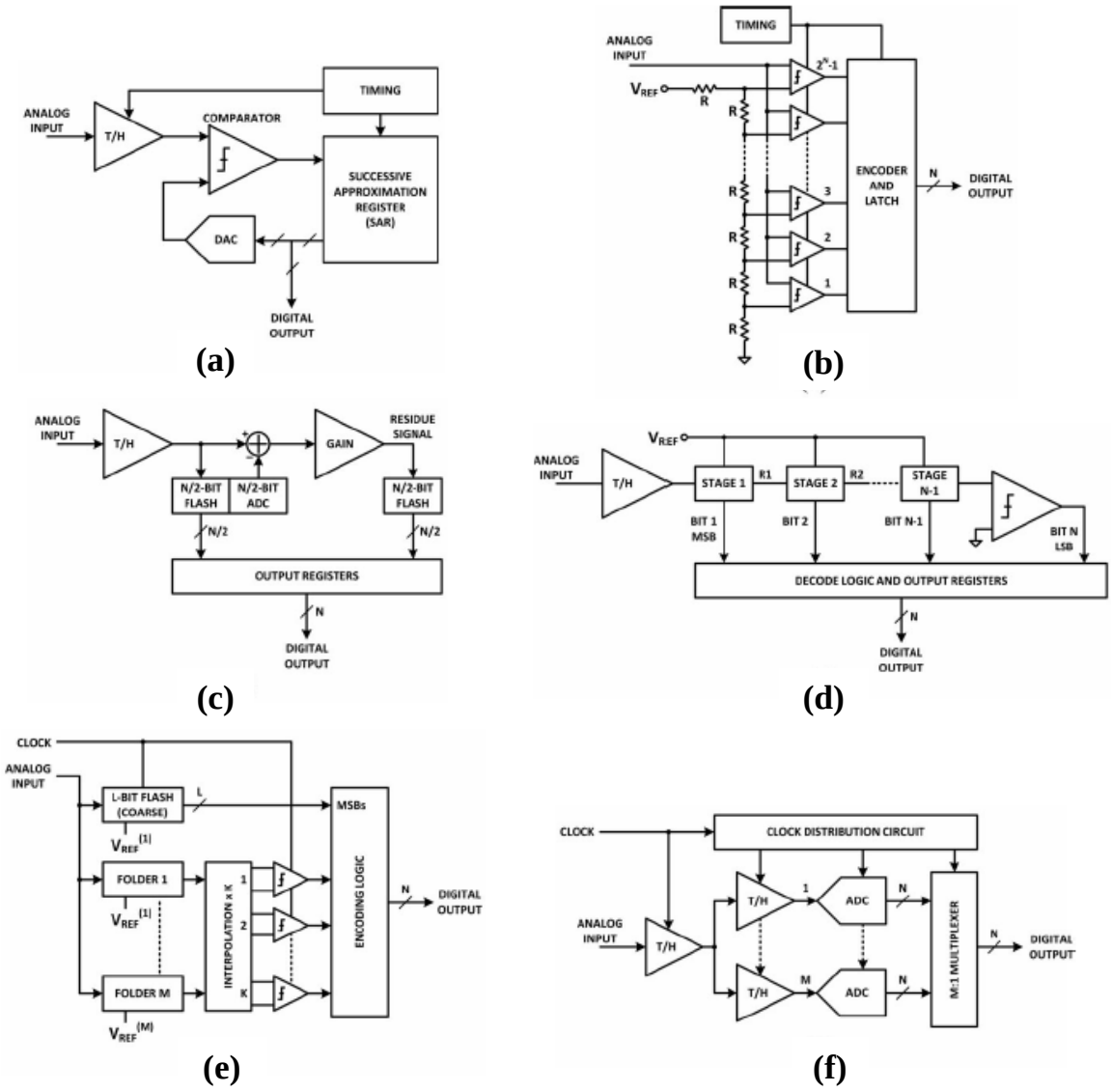


Figure I.28: (a) SAR; (b) flash; (c) pipeline; (d) serial/ripple; (e) folding/interpolating and (f) time-interleaved architectures of the high-speed ADCs (reproduced from [138]).

with a prototype in Ref. [159]. In this way, the first half of the signal spectrum from 0 to $f_S/4$ is quantized by a first ADC, whereas the second one is firstly down-converted to baseband through a mixer and then digitized by a second ADC. The two digitized outputs are recombined in the DSP part for a digital representation of the analog input signal. This technique, called digital bandwidth interleaving (DBI), has been recently demonstrated for a sampling rate up to 240 GS/s and a bandwidth of 100 GHz [9].

b) Photonic solution

High electronic ADC sampling rate requires a tight control of clock jitter to be able to sample at precisely defined times. This jitter and the comparator ambiguity limit ADC sampling rate and ENOB, especially at high input signal frequency. To break this bottleneck,

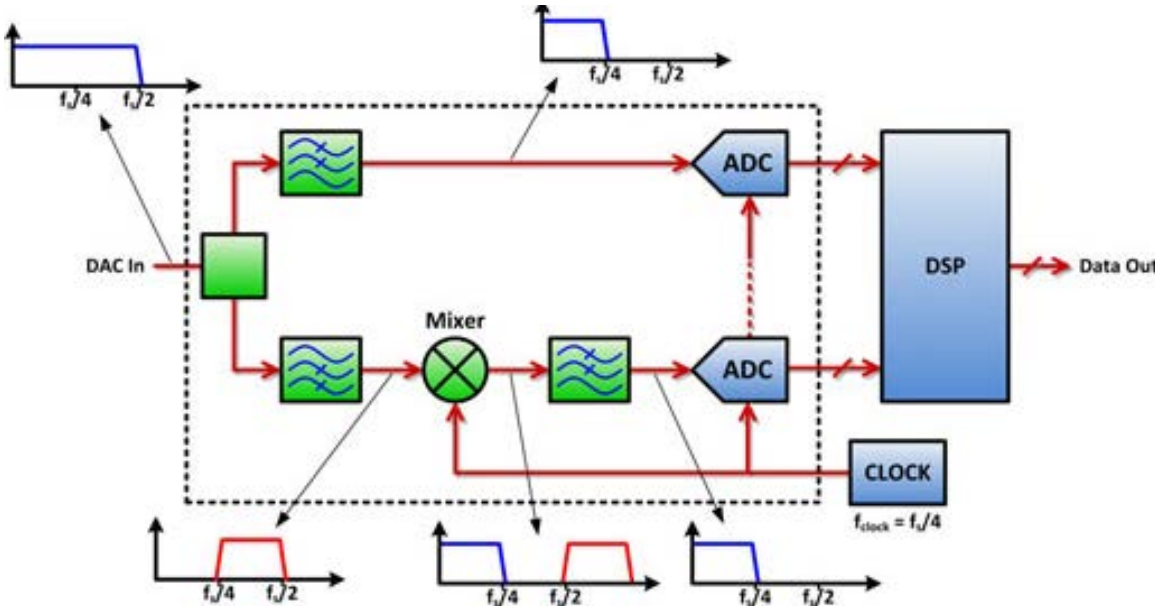


Figure I.29: Architecture for doubling ADC sampling rate. f_s = sampling rate of combined ADC inputs (after Ref. [138]).

photonic ADCs have gained more and more attention in recent years [10]. Photonic ADCs surpass their electronic counterparts in their significant high-speed capability [160, 161, 162]. Fig. I.30 summarizes 4 typical classes of photonic ADCs [10] composed of photonic assisted, photonic sampled, photonic quantized, photonic sampled and quantized ADCs. Particularly, some researchers have proposed hybrid photonic ADCs that combine optical sampling and electronic quantization techniques [163, 164], or electronic sampling and optical quantization techniques [165, 166]. All optical ADCs have been proposed in Ref. [167, 168]. Also, the fourth class of photonic ADC, called photonic assisted ADC, uses optics to overcome the limitation of electronics while keeping electronic sampling and quantization. For the photonic-assisted ADCs, the interests were focused on the time-stretched photonic ADCs with an amazing sampling rate of 10 TS/s and 4.5 bits ENOB for the digitization of 95 GHz tone [169]. The idea behind this technique is the use of significant dispersion on chirped optical pulses to temporally enlarge a wideband input signal, enabling to digitize this signal with slower commercial electronic ADCs. For the photonic quantizers and fully-optical ADCs, notable efforts have been made with the sampling rate up to 160 GS/s and ENOB of about 4 bits. For example, an optical quantizer has been reported in Ref. [166] for a 1.25 GHz input signal with the sampling rate of 40 GS/s and ENOB of 3.6 bits. Recently, a resolution enhancement scheme has been proposed and possibly combined to optical sampling, enabling the tera-samples/s ADC with up to 8 bits resolution [170]. Tab. I.3 presents the summary of some typical photonic ADCs associated with their classes up to date in order of increasing the sample rate. More details about these classifications are mentioned in Ref. [10].

The photonic ADC class studied in this thesis is based on the optical sampling and

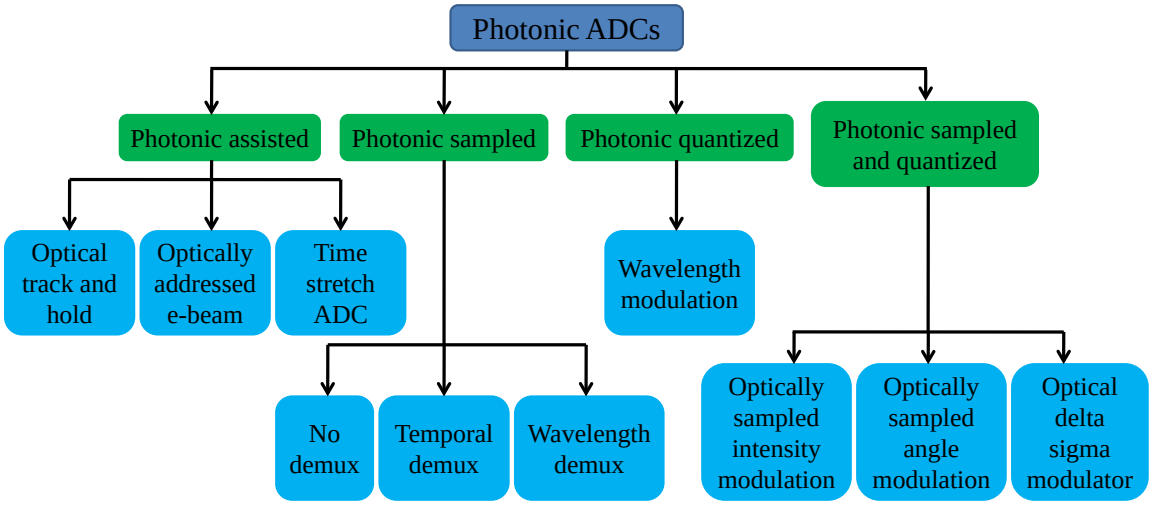


Figure I.30: Classification of photonic ADCs based on the electrical and optical implementation in the sampling and quantization stages (after Ref. [10]).

electronic quantization, thanks to the advancements in ultra-short, stable optical pulse generation. The ultra-short laser pulses, having a jitter of several hundreds fs or less, and a repetition rate widely varied from MHz to GHz, are well realized in the laboratory and already commercialized [177, 178, 179]. Ultra-short pulses provide a useful tool for many applications in such physical, chemical, biological domains or in engineering. Particularly, short pulses used in optical sampling bring a good solution to solve the measurement bandwidth limitation; for example, the sampling pulse with of 1 ps duration allows an optical bandwidth of a sampling system up to 300 GHz [180]. Moreover, the optical pulse has small timing jitter in comparison to electrical pulse, which is an important requirement in a sampling system, thanks to its high phase stability. Last but not least, the compact size and low energy consumption of optical pulse sources are now assured thanks to the advent of silicon photonics, and electronic-photonic integration technologies [181, 182, 183] that are very valuable for building a compact measurement device. Recently, the optical sampling assisted ADC is integrated on chip thanks to the rapid development of silicon photonics technology and demonstrated with a record 7 bits ENOB for sampling a 41 GHz signal [184]. This accuracy corresponds to a timing jitter of 15 fs that is at least 5 times better as compared to the existing electronic ADCs today.

Fig. I.31 presents a plot of ENOB as a function of input signal frequency. Since it is initiated in 1999 [133], it has been updated with the blue dots showing the electronic ADCs performance [185], and the red stars presenting the recent optical sampling assisted ADCs [184]. Thanks to the great advantage and progress in optical sampling technique, we will explore in the next part for the linear optical sampling technique that is of interest in various applications nowadays.

Table I.3: Summary of several typical developed photonic ADCs with respect to their classes.

Ref.	Maximum sampling rate (GS/s)	ENOB (bits)	Class	Input test signal frequency (GHz)	Year
[164]	0.505	8.2	PS	0.25	2001
[161]	10	6.0	PS	101.01	2014
[171]	10	4.0	PQ	10	2011
[172]	10	5.0	PSQ	10	2012
[173]	10	7.0	PSQ	10	2013
[166]	40	3.6	PQ	1.25	2006
[174]	80.64	n/a	PS	10.08	2005
[175]	100s	3.0	PSQ	n/a	2012
[176]	120	3.5	PA	20	2003
[169]	10000	4.5	PA	95.3	2007

PA: photonic assisted; PS: photonic sampled; PQ: photonic quantized; PSQ: photonic sampled and quantized.

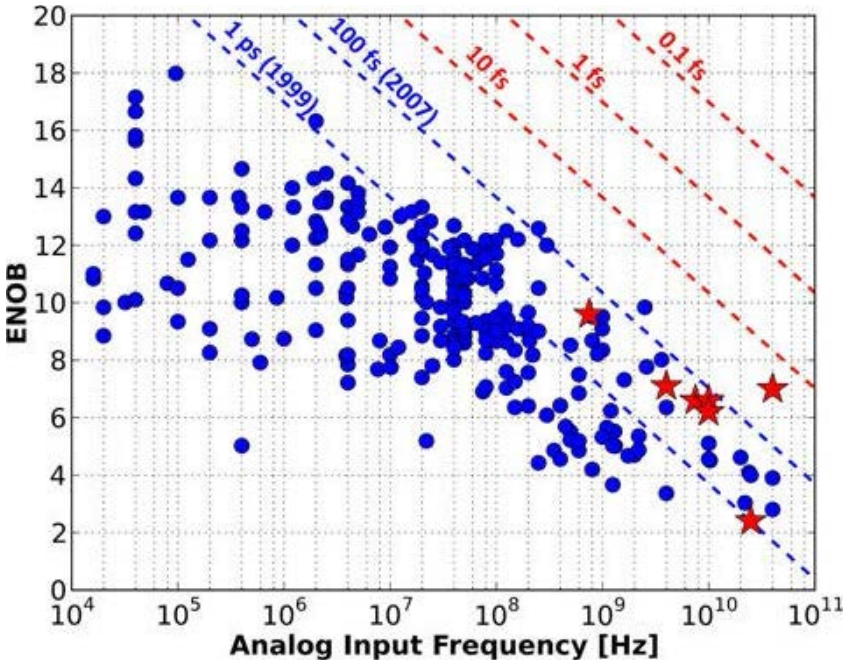


Figure I.31: ADC ENOB as the function of analog input frequency. The dashed lines denote the loci of aperture jitter values. Circle symbols: electronic ADC performance taken from Ref. [185]; Star symbols: optical sampling-based photonic ADCs demonstrated in Ref. [184].

4. Conclusion

In this part, we firstly introduced the state-of-the-art of very high bit rate transmission systems. The trend of using bi-dimensional modulation format signals and coherent detection as well as the advent in high speed DSP has opened the door to adapt the strong increase in network capacity. The coherent detection technique and the selected DSPs are discussed in details with an emphasis on our contribution during the study. The limitation of current systems is due to the limited bandwidth of electronic devices at both transmitter and receiver sides. The crucial limited component at the receiver which is the ADC, was presented in terms of structures, main functions, metrics for the performance measurement. Finally, several solutions to push the ADC speeds proposed in either electrical or optical domains have been briefly summarized. Based on this observation, one objective of my work focused on the investigation of optical sampling technique as a solution to assist speed of ADC. This study is detailed in next part of the manuscript.

Part II

LINEAR OPTICAL SAMPLING FOR HIGH BIT RATE SIGNAL MONITORING

Nowadays, the requirements of direct measurement and monitoring of ultra-fast signal in the time domain are rapidly increasing for various applications such as very high bit-rate communication, biophotonics, sensing, dynamic characterization, testing of new materials, etc. In optical communications, the conventional sampling techniques (i.e. photodetector combined with electrical sampling) provide powerful tools for possibly resolving signals up to 100 Gb/s [186]. In the mid 1990's, optical sampling became the solution for higher bandwidths and demonstrations up to 640 Gb/s were performed [187, 188, 13]. In these techniques, optical signals are sampled at low repetition rate by means of an ultrafast optical gate. After that, the optical samples are converted to the electrical signal and digitized by an appropriate ADC. Based on optical sampling technique, the high bandwidth requirement in conventional sampling can be relaxed and the major measurement limitation in optical sampling is transferred to the optical sampling gate and to the sampling source.

In this part, I firstly present a short overview of optical sampling in which my study about linear optical sampling (LOS) technique is pointed out. LOS technique is then discussed in terms of principle, major characterization parameters and pulsed-local oscillator (pulsed-LO) requirements. In the third section, the prototype built in the laboratory is described and validated with various kinds of optical signals (such as NRZ-OOK, NRZ-QPSK, 16-QAM). Diverse hypothesis in order to improve the signal quality are investigated in the last section of this part. More specifically, the influence of the ADC parameters in this technique is comprehensively assessed for some important parameters that may be helpful for the system design. Then, the impact of the pulsed- LO parameters (such as the timing jitter, the OSNR and the extinction ratio of the LO-source) in the current configuration are finally studied in details.

1. Introduction to optical sampling

Various kinds of optical sampling techniques are summarized in Ref. [180]. An optical sampling operation is schematically presented in Fig. II.1(a) where the input optical signal and a short pulsed sampling signal enter through an optical sampling gate to generate the samples. Regarding the optical sampling gate, either linear or nonlinear effects can be utilized as schematized in Fig. II.1(b). The nonlinear effect can be exploited through the second-order susceptibility ($\chi^{(2)}$, i.e. sum frequency generation (SFG), difference frequency generation (DFG)) or from the third-order susceptibility ($\chi^{(3)}$, i.e. four wave mixing (FWM), cross-phase modulation (XPM), parametric amplification). The materials able to generate such nonlinearities can be fiber-based (nonlinear optical loop mirror (NOLM), parametric amplifier), semiconductor-based (electro-absorption modulator (EAM), ultrafast nonlinear interferometer (UNI)), or crystal-based (periodically poled Lithium Niobate (PPLN)). The efficiency of the non linear effect is the main limiting factor of these techniques. Alternatively, linear optical sampling gate involves coherent detection as an optical gate: it is in this case sensitive to the electric field and keeps the information both on the amplitude and on the phase of the sampled signal. For this reason, our interest is concentrated on linear optical sampling (LOS) by using coherent detection.

In optical fiber communications, there are two typical applications of optical sampling, knowing the high bit-rate signal detection and the signal monitoring (Fig. II.1(c)).

In the first application, the high bit-rate signal is oversampled and the sampling rate is specified by the pulsed-LO repetition rate. In this method, the optical sampling needs to be synchronized with the pulsed-LO to achieve at least two samples per symbol, according to Nyquist theorem. However, when the data rate is increased, the synchronization may be difficult and the electrical ADC sampling rate is the main limitation in this application. The requirements of electrical ADC can be relaxed by either increasing the encoded bits per transmitted symbol or using the LOS in combination to parallel processing. The former solution makes the system less tolerant to amplified spontaneous emission (ASE) noise and nonlinear impairments occurring during the transmission. The latter solution has become an attractive solution since 2008 [189].

In the second application, the signal is usually undersampled as the sampling rate is much lower than data signal rate, allowing to relax requirements on the bandwidth of the opto-electronic conversion and of the ADC. In this application, the sampling rate should not

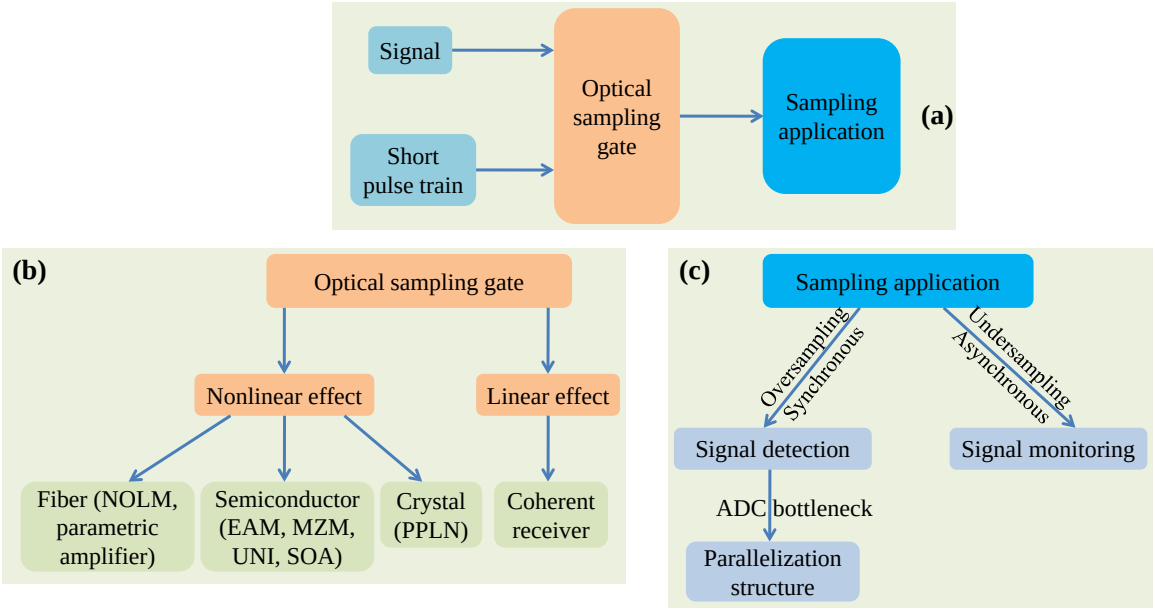


Figure II.1: (a) Schematically optical sampling by mixing a short pulse train with optical signal. (b) Optical sampling gate classification based on linear and nonlinear effects. (c) Typical applications of optical sampling in optical fiber communications. NOLM: nonlinear optical loop mirror; EAM: electro-absorption modulator; MZM: Mach-Zehnder modulator; UNI: ultrafast nonlinear interferometer; SOA: semiconductor optical amplifier; PPLN: periodically poled Lithium Niobate.

be an integer fraction of the data rate so that all samples, after a long sampling operation, can be gathered to reconstruct the data signal waveform. To do this, the asynchronous or software-synchronized methods [188] can be used to reconstruct the monitored signal. This undersampling operation brings the advantage of using low speed detection components, at the cost of more effort in post-processing.

The principles of both LOS-based detection and LOS-based monitoring will be discussed in the following paragraphs, although only the second application will be thoroughly studied in this thesis.

1.1 LOS-based optical signal detection

The key idea behind this technique is to duplicate the signal samples into several tributaries thanks to LOS operation, in order to detect, digitize and process them in parallel. The required photodetector bandwidth, ADC speed and DSP rate are hence effectively decreased thanks to parallel processing configuration. This technique is briefly named as parallel-LOS hereafter.

Fig. II.2 presents the principle of LOS based signal detection in parallel structure with one polarization state for simplicity. In this figure, N parallel optical samplers are plotted, in which the incoming optical signal and the pulsed-LO are also split into N branches.

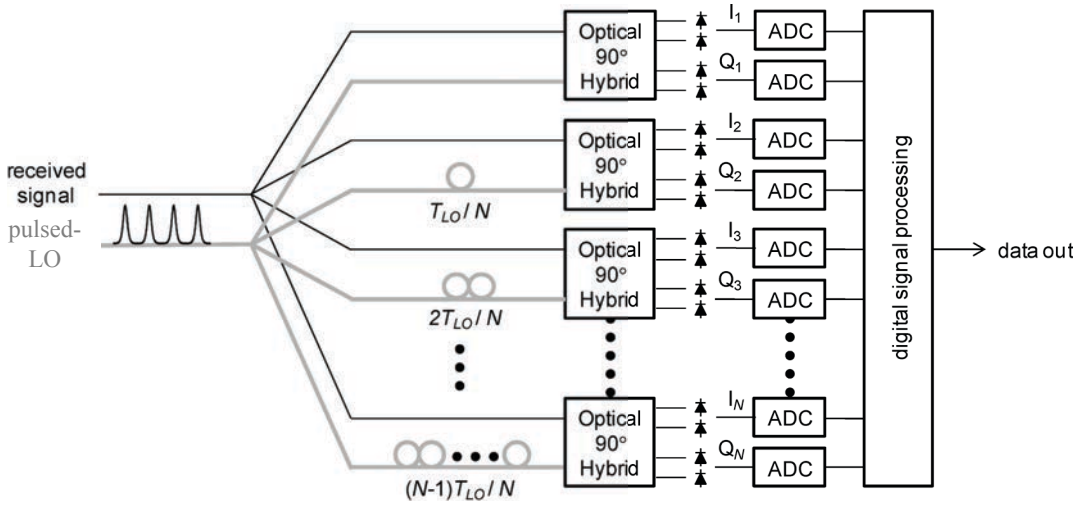


Figure II.2: Principle of LOS based signal detection in parallel configuration (after Ref. [12]).

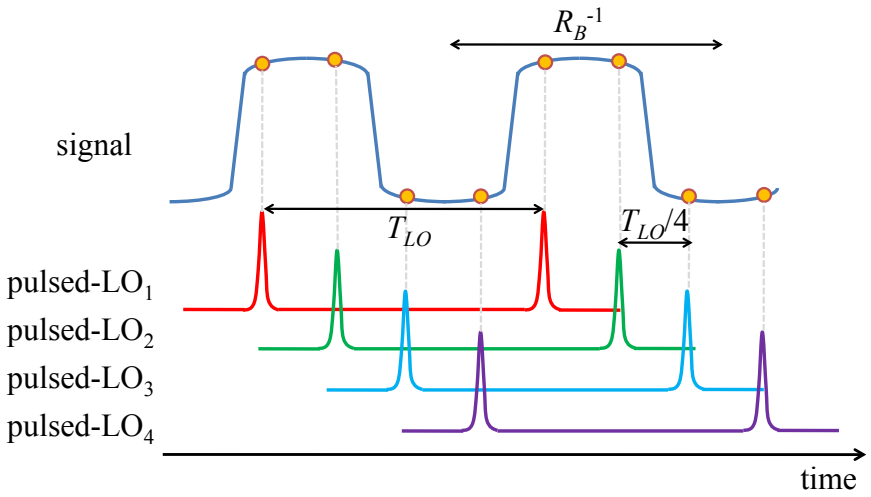


Figure II.3: Schematically temporal alignment of pulsed-LOs and signal in parallel structure with four optical samplers (R_B is the baud rate (symbol rate)) (Ref. [12]).

In the $n-$th branch, the pulsed-LO is delayed by τ_n to make an equidistant time-domain sampling, where $\tau_n = \frac{(n-1)T_{LO}}{N}$, T_{LO} denotes the time period between sampling pulses and $n = 1, ..., N$. The temporal alignment of pulsed-LOs in comparison to signal position is shown in Fig. II.3 for a configuration with $N = 4$ optical samplers. Signal under test and pulsed-LOs are then mixed into N parallel coherent receivers (90° optical hybrid combined with balanced photodiodes). The output photocurrents, I_n and Q_n, contain parts of the I and Q components at time instants $t_{n,k} = \tau_n + k \cdot T_{LO}$, with $k = 0, 1, 2, ...$ These output photocurrents are then digitized by $2N$ parallel electrical ADCs. Finally, the impairments compensation and carrier recovery are electronically carried out.

1.2 LOS-based monitoring application

The concept of LOS based on a coherent receiver has been proposed since 2003 [11]. This technique involves a pulsed-LO whose repetition rate is much smaller than that of the signal to be analyzed in order to undersample the signal under test and to reconstruct the eye diagram and constellation diagram.

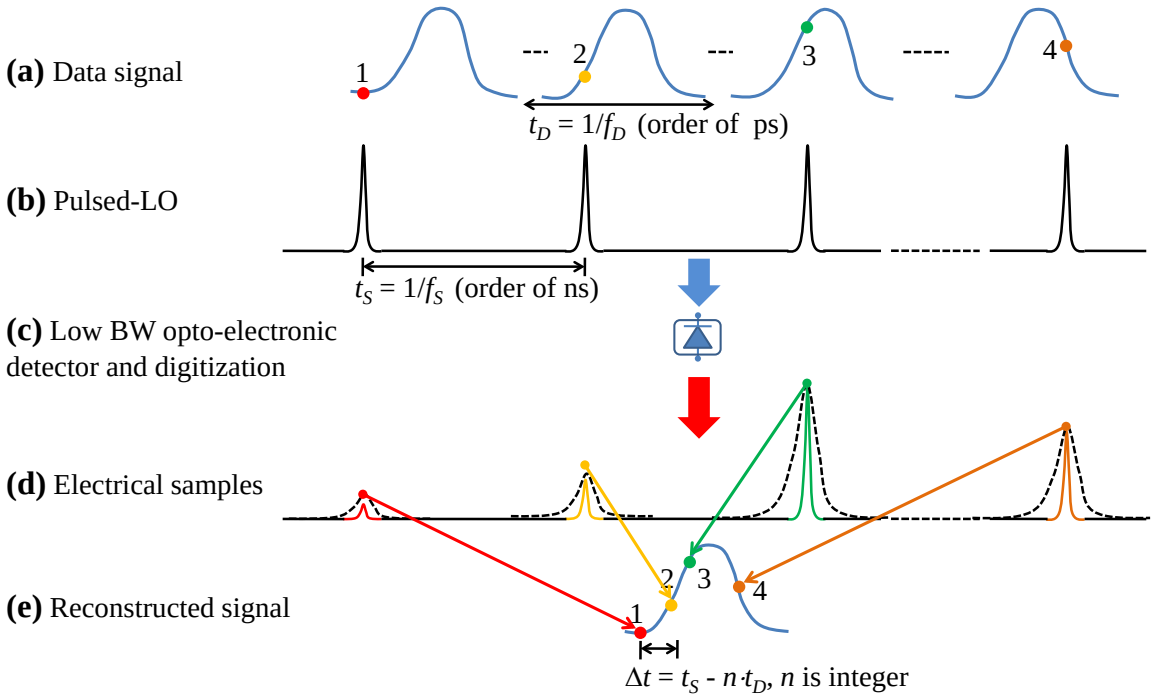


Figure II.4: General principle of LOS technique for signal monitoring.

Fig. II.4 presents an example of LOS technique for high bit-rate signal monitoring, in which a hundred Gb/s RZ-OOK signal is schematically plotted, resulting in a bit slot duration in order of several ps. This optical signal is sampled by a pulsed optical source (namely the pulsed-LO), whose pulse width should be as short as possible as the sampling resolution depends on that parameter. The pulsed-LO repetition rate should also be small in order to relax the speed of opto-electronic conversion and of electronic signal processing. After detection, the gathered electrical samples hence constitute an image of the analyzed signal with an enlarged time-scale. The signal can then be amplified in a trans-impedance amplifier before being digitized by a low cost, low speed ADC. Finally, the eye diagram of the optical signal can be reconstructed based on software synchronization [190, 188].

My PhD work is partly dedicated to the investigation of linear optical sampling techniques for the visualization (in terms of eye diagram and constellation) of optical signals. I had the chance to contribute to the OCELOT project (supported by French government) in this context. This project aims at developing the linear optical sampling of very high bit rate (superior to 100 Gb/s) optical signals with bi-dimensional modulation formats, especially

optical phase shift keying signal ($M-$PSK) or optical quadrature amplitude modulation signal ($M-$QAM), in order to extract amplitude and phase information and display them in a constellation diagram. The two major obstacles, identified and considered in the project, refer on one hand to the pulsed-local oscillator (pulsed-LO) used for LOS, and on the other hand to the acquisition and processing of the sampled and digitized signals matching end users requirements about real time measurement and analysis. The pulsed-LO must provide short (fewer than 5 ps), stable (timing jitter $<$ 200 fs) pulses, with relatively low average power ($>$ -3 dBm) but also low pulse rate (hundreds of MHz), in order to fit the economical requirement of simple implementation and reduced cost. Digital acquisition board (ADC) is designed with digital signal processing (DSP) integrated circuits (field programmable gate array - FPGA) enabling the end display of the constellation diagram. Robust and fast algorithms are also required. The next section is focused on the linear optical sampling technique: after introducing the principle and state of the art of realizations using this technique, the prototype developed during my work is described and validated.

2. Linear optical sampling technique

2.1 Principle of linear optical sampling based on 90° optical hybrid

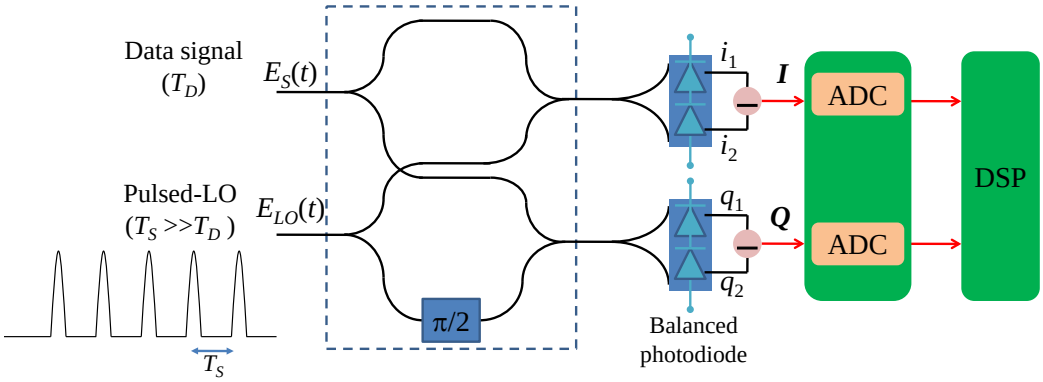


Figure II.5: 90° optical hybrid based optical sampling setup.

The schematic diagram of linear optical sampling based on 90° optical hybrid is shown in Fig.II.5. In LOS technique, an ultra-short pulse train (generally a mode-locked laser) is used as a pulsed-LO in the coherent detection scheme. In this setup, the coherent receiver plays the role of the sampling gate. At the photodiodes outputs, the optical data signal field, $\varepsilon_S(t)$, beats with the pulsed-LO field, $\varepsilon_{LO}(t)$, with a 90° phase difference between *ad hoc* beating terms outputs, allowing to access to amplitude and phase terms of the signal field as it will be shown below on the writing of resulting photocurrents. Moreover, two balanced photodiodes are used in order to suppress the quadratic terms of the photocurrent and keep only the beating part. The resulting two signals, knowing the in-phase (I) and quadrature (Q) components, will constitute the real and imaginary part of the sampled signal.

The complex electric fields of data signal and pulsed-LO are written as [191]

$$\varepsilon_S(t) = E_S(t)e^{-j\omega_0 t}, \tag{II.1}$$

and

$$\varepsilon_{LO}(t) = \sum_N E_{LO}(t - NT_S)e^{-j\omega_0(t-NT_S)+jN\phi+j\phi_0}, \tag{II.2}$$

where E_S and E_{LO} are the envelopes of data and pulsed-LO, respectively. T_S is the period of the pulsed-LO, ω_0 is the optical carrier angular frequency and $N\phi + \phi_0$ is the relative phase between the analytic signal and the carrier for pulse N. Both photodetectors of upper arms are assumed to have the same impulse response $h(t)$. Therefore, the electric currents after photo-detection at ports i_1 and i_2 are

$$\begin{aligned} i_1 &= \tfrac{R}{2}\left\{|\varepsilon_S(t)|^2 + |\varepsilon_{LO}(t)|^2 + 2\Re\left[\varepsilon_S(t)\varepsilon^*_{LO}(t)\right]\right\} \otimes h(t), \\ i_2 &= \tfrac{R}{2}\left\{|\varepsilon_S(t)|^2 + |\varepsilon_{LO}(t)|^2 - 2\Re\left[\varepsilon_S(t)\varepsilon^*_{LO}(t)\right]\right\} \otimes h(t). \end{aligned} \tag{II.3}$$

The resulting current I after balanced detection for the in-phase interference term is given by

$$\mathrm{I} = i_1 - i_2 = 2R\Re\left\{\varepsilon_S(t)\varepsilon^*_{LO}(t)\right\} \otimes h(t), \tag{II.4}$$

where $\Re$ is the real-part operator. The symbol $\otimes$ and $*$ represent the convolution and complex-conjugated operations, respectively. R represents the photodiode responsivity and $h(t)$ is assumed to be constant during the integration time. Therefore, the I can be represented as

$$\mathrm{I}(NT_S) = 2R\cos(\omega_0 NT_S + N\phi + \phi_0)\Re\left\{\int_{-\infty}^{\infty} E_S(t)E^*_{LO}(t - NT_S)dt\right\}. \tag{II.5}$$

Similarly, the quadrature interference term can be obtained as follows

$$\mathrm{Q}(NT_S) = 2R\sin(\omega_0 NT_S + N\phi + \phi_0)\Im\left\{\int_{-\infty}^{\infty} E_S(t)E^*_{LO}(t - NT_S)dt\right\}, \tag{II.6}$$

where $\Im$ denotes the imaginary-part operator. Finally, the two quadrature optical samples expressed in (II.5) and (II.6) are summed in a post-detection process to get the field of the sampled signal

$$S_N = \mathrm{I} + j\mathrm{Q} = 2R \cdot e^{j(\omega_0 NT_S + N\phi + \phi_0)} \cdot \int_{-\infty}^{\infty} E_S(t)E^*_{LO}(t - NT_S)dt. \tag{II.7}$$

The equivalent intensity of the sampled data signal is given by

$$I(NT_S) = 4R^2\left|\int_{-\infty}^{\infty} E_S(t)E^*_{LO}(t - NT_S)dt\right|^2. \tag{II.8}$$

In summary, a sampling event yields a complex sample which is proportional to the correlation of the fields of data signal and pulsed-LO $\int_{-\infty}^{\infty} E_S(t)E^*_{LO}(t - NT_S)dt$. In contrast to the nonlinear sampling techniques [192, 193, 194, 195] using the gated temporal

intensity for representing the data signal, the linear sampling technique can be considered as an instrument for of optical electric field diagnostics [196]. Considering the fields in the frequency domain, $\tilde{E}_S$ and $\tilde{E}_{LO}$, the quantity $\int_{-\infty}^{\infty} E_S(t)E_{LO}^*(t-NT_S)dt$ can be re-written as follows

$$\int_{-\infty}^{\infty} E_S(t)E_{LO}^*(t-NT_S)dt = \int_{-\infty}^{\infty} \tilde{E}_S(\omega)\tilde{E}_{LO}^*(\omega)\cdot e^{jN\omega T}d\omega. \tag{II.9}$$

If pulsed-LO has a constant spectral density and phase over the data spectrum range, the measured electrical samples presented in (II.9) can be reformulated as

$$S_N = 2R\cdot e^{j(\omega_0 NT_S+N\phi+\phi_0)}\cdot E_S(NT_S)\tilde{E}_{LO}^*(0). \tag{II.10}$$

Inspection of (II.10) shows that the temporal field of the data waveform $E_S(NT_S)$ can be obtained by the linear optical sampling technique with infinite time resolution for signals with limited spectra [196]. In practice, it is sufficient to choose the spectrum of pulsed-LO few times larger than that of data signal. From (II.8) and(II.10), it can be observed that the linear optical sampling can be sensitive to the optical data phase and is yielding the temporal intensity samples of the data signal, by using a sampling pulse with flat phase and amplitude spectra over the data signal spectrum.

2.2 State-of-the-art of linear optical sampling

Linear optical sampling (LOS) based on a coherent receiver has been firstly proposed by a group of Bell labs [11]. This technique, proposed for signal monitoring, explored a very low repetition rate pulsed-LO (10 MHz) to undersample the signal under test up to 640 Gb/s and to reconstruct the eye diagrams and constellation diagrams [197, 196, 191]. In 2009, a NTT group has proposed a dual-channel LOS to monitor the intensity and frequency modulation of 10 Gb/s gain-switched laser diode pulses and 160 Gb/s optical time division multiplexing signals [198]. The bi-dimensional signal constellation and waveform monitoring (i.e. 66 Gbaud 16-QAM signal) was also demonstrated by a group of Chalmers University of Technology [199]. By using a 1 GHz pulsed-LO, the sampling up to 107 Gbaud PDM-QPSK signals has been recently reported [200].

Since 2008, the idea of using LOS for signal detection has been proposed by a University of Central Florida group [189, 201]. In this work, they reported on the transmission of 10 Gb/s BPSK signals over 220 km standard SMF using 10 GS/s ADCs. The university of Tokyo group [202, 203, 14] has shown the proof-of-concept experiment for parallel optical sampling with 160 Gbaud QPSK and 8-PSK signals transmitted over 80-km SMF. The time-domain sampling was carried out on each 10 Gbaud tributary. In 2011, the Heinrich-Hertz-Institute (HHI) group experimentally reported on an aggregate optical sampling of

Table II.1: Summary of commercial products for the measurement and characterization of advanced modulation format signals.

Provider	Detection methods	Referent model	Baud rate measurement (Gbaud)	Price (k$)	Phase sensitivity
Agilent	Continuous (real-time or time-equivalent) coherent detection or very fast photodiode in combination to electronic sampling	Optical modulation analyzer (OMA) N4391A and N4392B	28 or 56	150 or 350	No
Tektronix (Optametra for optical part)		OM4106B/D coherent lightwave signal analyzer	28 or 56	>170	No
TeledyneLecroy (Optametra for optical part)		Labmaster 10Zi-100GHz-DS	56 or 100	>250	No
Southern photonics		IQ scope	28 or 56	50→ 170	No
EXFO	LOS based nonlinear interaction (or coherent detection)	Optical modulation analyzer (OMA) PSO-100	80 or 100	>120	Yes (limited)
		Optical modulation analyzer (OMA) PSO-200	80 or 100	>300	Yes
Aragon photonics	Complex spectral analysis	BOSA phase OCSA	No limit [1]	100→ 170	Yes
Apex technologies		AP2441B/ AP2443B OCSA	No limit		Yes

112 GHz applied in a 610-km long transmission of 56 Gbaud QPSK by using 20 GHz and 50 GS/s electrical ADCs.

Some of the techniques used in previously cited works gave rise to commercial products. In general, three kinds of measurement are often used based on (i) oversampling technique (i.e. the use of coherent detection or very fast photodiode in combination to very fast electrical oscilloscope) (ii) under-sampling technique (i.e. the use of low repetition rate pulsed-LO combined with coherent detection or direct detection and low speed photodiode followed by an ADC), or (iii) complex spectrum analyzer. Tab. II.1 summarizes some available solutions for characterization of optical signals.

[1] In the sense that the considered range corresponds to the optical response of physical nonlinear phenomena.

2.3 Some parameters impacting the optical sampling system specifications

As in general optical sampling systems, the LOS system performance can be characterized by different parameters such as temporal resolution, wavelength range, sensitivity, dynamic range, etc. [180]. These characteristics are directly impacted by the configuration parameters of optical and electrical parts in the LOS system. More specifically, sampling pulse width and timing jitter, the typical parameters of the optical pulsed-LOs, have a significant influence on the temporal resolution. Effective number of bit (ENOB) of ADC, the typical parameters of the electrical part, specifies the accuracy of sample values having a strong impact on the dynamic range. Furthermore, the phase noise and sampling pulse repetition rate also have an influence on the phase measurement of the LOS system. The following discussion gives more detail on the configuration parameters.

2.3.1 Pulsed-LO parameters

Pulse width

One of the most important parameters in optical sampling system is the full-width at half maximum (τ_{FWHM}) of the pulsed-LO which is associated with the temporal resolution. The bandwidth of the sampling system (B) is indeed related to the LO spectral bandwidth as it will determine the bandwidth at which the beating can occur. For instance, for a Gaussian pulse width of 1.5 ps, with a spectral bandwidth B given by the relationship $B{\cdot}\tau_{FWHM} = 0.44$ (known as Fourier-transform-limited), the corresponding sampling system bandwidth is of about 300 GHz. A chirp pulsed-LO can provide a better relationship (between the bandwidth and the FWHM) than Fourier-transform-limited. However, the chirp should be minimized or compensated for in LOS system [204] to avoid the phase measurement error.

Timing jitter

Along with LO pulse width, timing jitter plays an important role in the optical sampling system in order to visualize the high bit-rate signal eye diagram because it will lead to noise on the reconstructed signal as seen later in the document. The overall timing jitter should be as low as possible and is depending on the particular configuration of the sampling system. For example, in synchronous sampling system, the timing jitter is directly specified by the jitter of the clock recovery and of the pulsed-LO, whereas in a software-synchronized sampling system, the algorithmic jitter has a major impact on the overall timing jitter. A typical value for optical sampling jitter is in the order of hundred femtoseconds.

Phase noise

For the characterization of advanced modulation format signals, in which the signal

phase characterization is important, the phase noise of the pulsed-LO will directly impact the phase of the reconstructed signal. The large phase noise can lead to the uncompensated phase rotation of the reconstructed signal. Phase noise is associated to laser linewidths (the repetitive pulsed LO spectrum is constituted of numerous individual lines) and the expected value of laser linewidths in the optical sampling system is fewer than a hundred of kHz.

Repetition rate

The pulsed-LO repetition rate will directly impact the ADC and photodiodes bandwidth requirements as two successive detected samples should not interfere. However, the lower bound of repetition rate is specified by the coherence length of the light source (depending on the laser linewidth) [205]. If the coherent length is not guaranteed, it may lead to impossibility to compensate for phase noise in acquired samples. Therefore, there is a trade-off between the pulsed-LO repetition rate and the laser phase noise that must be carefully considered in optical sampling system design.

Carrier frequency detuning with the signal under test

Carrier frequency detuning is defined as the offset between data optical carrier frequency and the pulsed-LO center frequency. This leads to a phase rotation that may not be compensated by algorithms if too large. In order to optimize the beating of pulsed-LO and signal under test, the center frequencies of these two sources should be as close as possible. The tunability of the pulsed-LO in the wavelength range of the signal is hence an important issue. A non-tunable pulsed-LO will also lead to a reduction of the system sensitivity whenever the wavelength center of the signal is far from that of the pulsed-LO.

2.3.2 ADC ENOB

ENOB can cause amplitude error in the reconstructed signal due to the quantization noise. ENOB is linked to the dynamic range of the optical sampling system, as it will determine the possibility to discriminate two levels of the quantized amplitude.

2.4 Possible pulsed-LO for LOS

To satisfy the previously discussed requirements, the pulsed-LO repetition rate should be as small as possible to relax the detection bandwidth constraint. MHz-repetition rate pulsed-LO can be achieved by a directly modulated gain-switched laser diode (or distributed feedback laser, DFB) [206, 207, 208, 209, 210]. However, the requirements of a stabilized circuit to reduce the timing jitter and the necessity for pulse compression to get sub-picosecond pulses make this solution difficult to implement. Although the passively mode-locked lasers (MLL) were used in [196, 211] with potential low short-term jitter and phase noise, the long-term drift in the repetition rate of these lasers, due to the variable cavity length, limits their use since the natural repetition rate varies with time.

Possible solutions to alleviate this constraint consist of using a cavity-less source which consists of a CW laser modulated by two RF-driven modulator stages (intensity and phase modulation) and an optimized length of dispersion-compensated fiber to produce pulses as short as 5 ps [212, 213]. The pulses can then be subsequently compressed down to the sub-picosecond regime using an additional compression stage [214]. This solution however requires high optical and electrical powers. Another solution is to use actively mode-locked lasers, like monolithic lasers [215] or very-short external-cavity lasers [216] that deliver pulses as short as 1 ps with a highly-stable repetition frequency and sufficiently low jitter. Nevertheless, both solutions provide repetition frequencies greater than 2.5 GHz, which implies the use of expensive photodetectors (larger bandwidth) and ADCs featuring at least 5 GS/s per channel. The solution proposed in my work is described in the next paragraph.

3. Proposed scheme for linear optical sampling based monitoring

Fig. II.6 shows the proposed setup of LOS. It is based on the typical LOS structure as the one introduced earlier: the signal to be analyzed and the pulsed-LO (presented in Section 3.1) enter a coherent detector (presented in Section 3.2). Note that polarization controllers are here inserted at both inputs of the receiver to select one polarization in a first step. The study with 2 polarization inputs could be explored in future work. The two ADC cards synchronized to the sampling source are presented in Section 3.3. Finally, some algorithms of prime importance to ensure the equivalent time operation of the LOS are introduced in Section 3.4 as a complement to the DSPs required for advanced modulation format signals analysis (mentioned in Section 2.3 of Part I). Finally, the validation of our LOS with different signals is shown in Section 3.5. The originality of our setup comes from the pulsed-LO source which is based on the use of a 10 GHz short pulse train whose repetition rate is decreased down to a few hundred of MHz using an external modulator as depicted in Fig. II.6. This method, which is further described in Section 3.2, allows to take advantage both of the limited required bandwidths at receiver when low repetition rate sources are used, and of good laser quality (low timing jitter, low phase noise, good long time stability) of higher repetition rate sources.

3.1 Pulsed-LO source

The pulsed source used in this work was either a 11 GHz pulse source from an optical frequency comb generator (OFCG, which setup will be discussed later) based on a doubly-resonant electro-optic modulator [217] or a semiconductor mode locked laser (MLL) with pulse repetition rate of 10 GHz [218]. In order to reduce the required speed of ADC cards, the pulse repetition rate is externally reduced to 714 MHz by electrically optically gating the pulses with a Lithium Niobate ($LiNbO_3$) Mach-Zehnder modulator (MZM), as depicted in Fig. II.6.

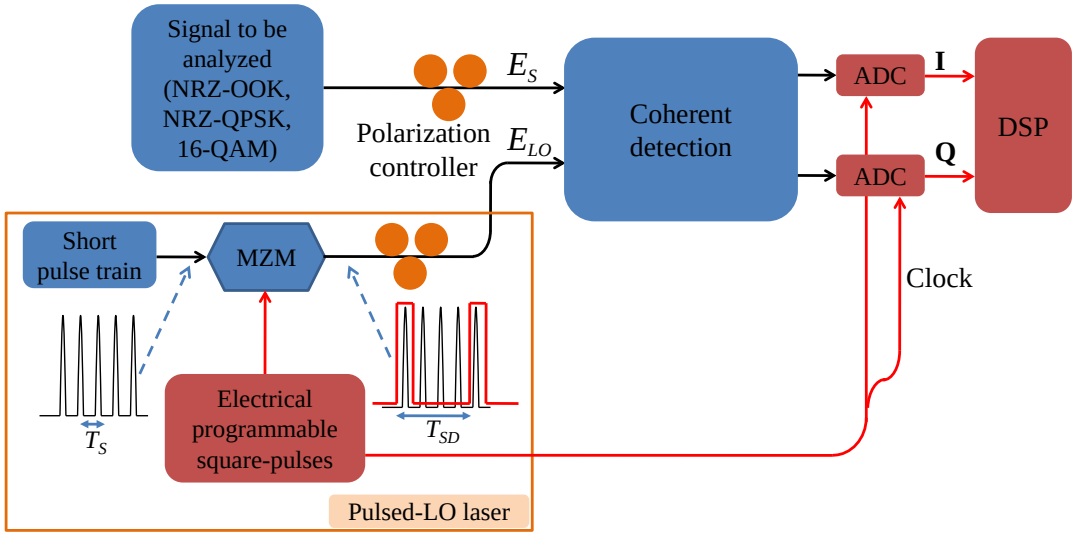


Figure II.6: Setup for proposed linear optical sampling. MZM: Mach-Zehnder modulator. T_{SD} is much greater than data rate.

3.1.1 Optical frequency comb generator source

The commercial OFCG source is based on the modulation of a continuous wave (CW) laser into a conventional Fabry-Perot cavity including a high-speed electro-optic phase modulator. The resulting resonant enhanced modulation of this device can lead to short pulse generation providing that the modulation frequency applied to the phase modulator is close to (or to a multiple of) the free spectral range of the cavity [217, 219]. Due to the use of an external CW laser, this solution is largely wavelength tunable (tens of nm). Moreover, a very low timing jitter was reported in Ref. [217] (between 6 fs and 94 fs). Short Lorentzian pulses (a few ps) are finally obtained resulting in the optical power spectrum with a double-side exponentially-decaying shape; the particularity of this source is that adjacent pulses have phase shift of 180° [217] as schematically plotted in subsets of Fig. II.7(a) and illustrated by different colors (red and green).

The configuration for the generation of this short pulse train is shown in Fig. II.7(a). The CW laser is amplified by a polarization-maintaining (PM) erbium-doped fiber amplifier (EDFA) and coupled into the cavity. The RF driving signal of the cavity is 5.712 GHz which is twice the free spectral range (FSR) of the cavity. The repetition rate of the output pulse train is twice the RF frequency, resulting in 11.4 GHz pulse repetition rate. Isolators are inserted before and after the resonant cavity to avoid any reflection.

In our particular case, the repetition rate of the pulsed source is reduced using an external modulator as displayed in the introduction of Section 3. In this aim, the signal is firstly amplified by another EDFA before passing through a Mach Zehnder Modulator (MZM) which is driven by a programmable electrical pulse generator. 100 ps square pulses at 714 MHz are generated in order to select one pulse over sixteen of the pulsed source through the MZM. As the MZM has a finite extinction ratio, the 15 eliminated pulses

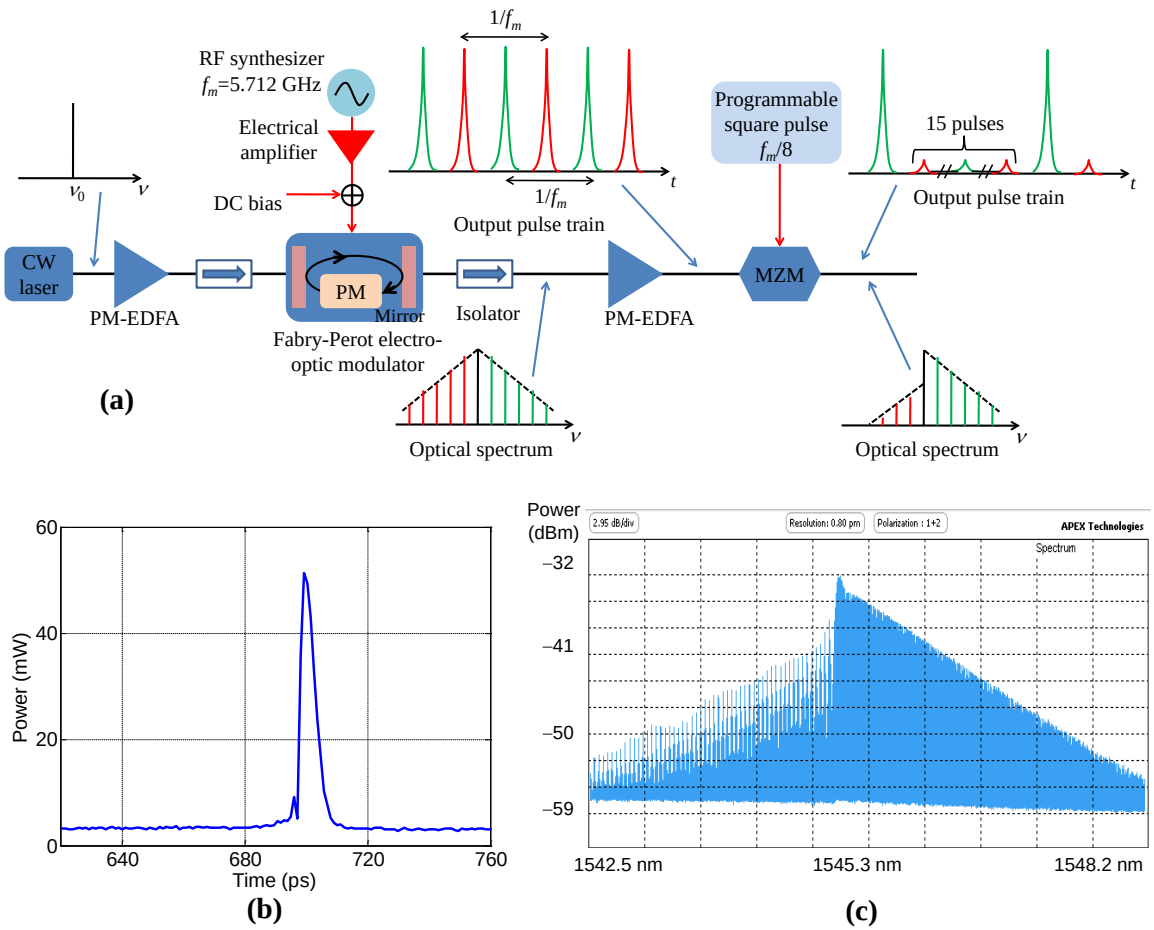


Figure II.7: (a) Configuration for generation of 714 MHz pulsed-LO from an optical frequency comb generator based on a doubly-resonant electro-optic modulator [217]. (b) Temporal form of pulsed-LO after the repetition rate down-conversion and (c) its corresponding spectrum.

are still present with an attenuation corresponding to the MZM extinction ratio (typically 20 dB). The consequence of such a particularity will be investigated later on.

A consequence of this repetition rate down-conversion, in the particular case of this source presenting a phase shift between adjacent pulses and for an even down-conversion ratio (here 16), is that the spectrum becomes asymmetric because one sideband of the spectrum (lower sideband in our case) is attenuated as it corresponds to removed pulses of the down-conversion. Fig. II.7(b) shows a measured temporal form after the repetition rate down-conversion. A pulse width of 5 ps is measured; residual adjacent pulses are 10 dB below. The corresponding optical spectrum is plotted in Fig. II.7(c) showing the exponential decay and the attenuation of one side of the spectrum.

For LOS operation, the LO wavelength is adjusted in such a manner that the spectrum of the signal to be analyzed is superimposed with the exponential decay part of the LO spectrum with both signal carriers as close as possible to each other. A typical spectrum of

both signals is represented in Fig. II.8. As described in [11], the LO spectrum should be as flat as possible in order to optimize the beating of the signal and the LO. Our pulsed-LO is not optimum from this point of view with its exponential decay shape. However, its slope of about 6 dB/nm allows a good superposition of both spectra.

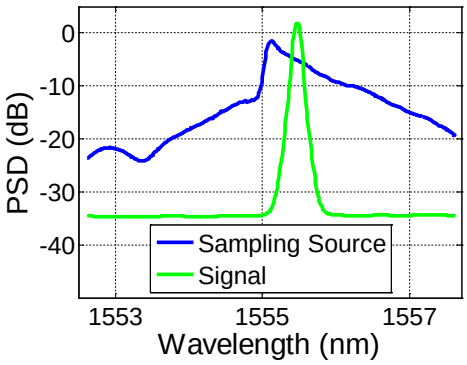


Figure II.8: Spectrum of NRZ-OOK signal superimposed to that of pulsed-LO. PSD: power spectrum density.

3.1.2 Mode-locked laser source

For the MLL, the wavelength tuning range is about 70 nm. The tunable mode-locked laser (TMLL) is composed of a 1.5 μm diode laser (InP-BH laser) being placed in an external cavity [216]. One facet of the laser is antireflection coated and coupled via a gradient index (GRIN) rod lens to a grating, whereas the other facet is bombarded with the special ions (i.e. $^{15}N^{2+}$ ions) to create a fast saturable absorber. This laser facet and the grating represent the resulting laser cavity [220]. The repetition rate is between 9.8 GHz and 10.8 GHz. Timing jitter was reported to be smaller than 200 fs. Moreover, the average output power exceeds -5 dBm. Fig. II.9(a) shows the temporal waveforms at the MLL output using active mode-locking. The pulse-width is about 4 ps measured by an optical sampling oscilloscope (OSO). Fig. II.9(b) presents the corresponding spectrum of this pulse source. The repetition rate is down-converted from 10.6 GHz to 667 MHz using the same method as for the OFCG source.

As a conclusion, two pulsed-LOs were used in my linear optical sampling experiment: both are hundreds of MHz in repetition rate (714 MHz and 667 MHz) with a few ps pulse duration; both are wavelength tunable (the OFCG more easily as its tunability is that of a commercially available tunable CW laser); both have low timing jitter with better performances on the OFCG (timing jitter below 100 fs) also resulting in lower phase noise in this source. Despite of the expected better results using the OFCG source, some of the studies were performed with the MLL in the following as it was the only one available from the start of my work.

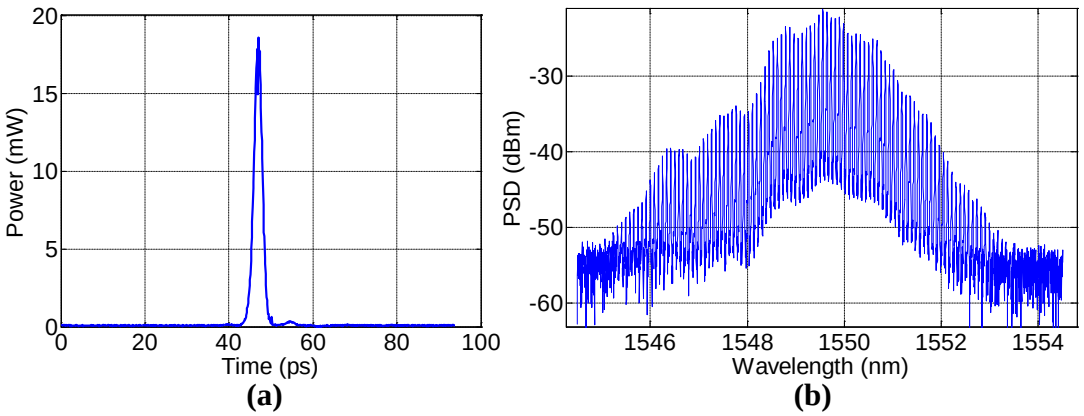


Figure II.9: (a) Temporal forms of pulsed-LO at the output of MLL and (b) its corresponding spectrum.

3.2 Coherent detector

A commercial coherent detector is used [221] including a 90° optical hybrid and a couple of balanced photodiodes. The device operates over a wide wavelength range between 1527 nm and 1607 nm. A small phase imbalance (±5°) between the I and Q components is specified. The excess insertion loss (or the ideal intrinsic loss from any input to any output) is smaller than 2 dB, whereas the optical return loss (the ratio between the input power and the reflected power) is greater than 30 dB. The balanced photodiodes have a bandwidth of 15 GHz. Photodiodes are followed by transimpedance amplifiers integrated into the device, leading to photocurrent amplification together with voltage conversion. As it will be characterized in Section 3.5.1, the gain of these amplifiers can saturate when the photocurrent is too high, leading to a signal degradation. Tab. II.2 summarizes some typical specifications of this coherent receiver.

Table II.2: The achievable specifications for several key parameters of 90° optical hybrid.

Parameter	**Unit**	**Specification**
Wavelength range (C+L band)	nm	1527 - 1607
Phase difference	degree	90 ± 5
Excess insertion loss (any input to any output)	dB	<2.0
Insertion loss difference (between any two conjugate outputs)	dB	<0.5
Optical return loss	dB	>30

3.3 ADCs used in our LOS

ADC used in the setup is based on a commercially available FPGA mezzanine card (FMC) with four channels of 1.25 GS/s. The card provides 8-bit per channel. Moreover, the configuration of ADC card enables simultaneous sampling of 4, 2, or 1 channel at a maximum sampling rate of 1.25 GS/s, 2.5 GS/s, or 5 GS/s, respectively. The sampling clock can be supplied by either an external coax connection or an internal clock source (optionally locked to an external reference). The clock tree enables cascading multiple boards for phase locked sampling. Additionally a trigger input for customized sampling control is also available. After calibration, the voltage offset of this card is ±50 mV and the phase mismatch is about ±14 ps. An image of the ADC cover is shown in Fig. II.10. Our FPGA card has a hardware memory allowing block length of each acquisition in the order of several thousand of samples which are then transferred to a computer through an Ethernet cable for the subsequent DSP treatment.

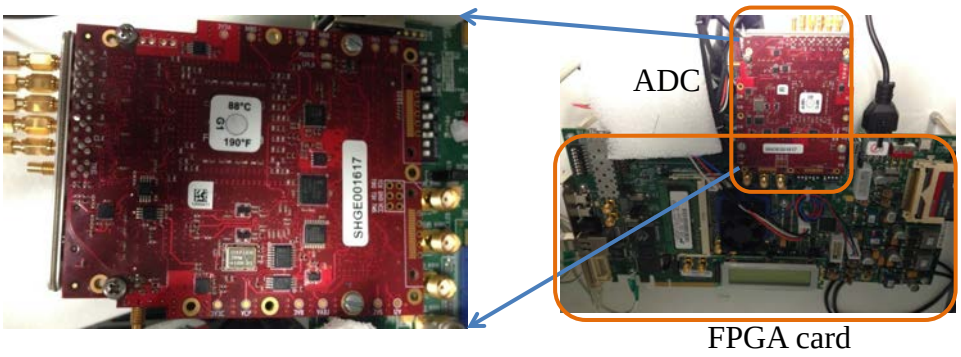


Figure II.10: ADCs used in LOS based on a FPGA mezzanine card (FMC).

The ADC ENOB is 8-bits. However it is to notice that this number of bit is obtained when the input voltage corresponds to its maximum range (which is called the full-scale range of the ADC); if the signal voltage is lower than its full-scale range, then the number of bits for the signal quantization will be smaller. As it will be described later in the manuscript, the signal voltage has to be optimized at the input of the ADC for an optimal quantization.

3.4 Additional DSP algorithms

Based on the DSP described in Section 2.3 of Part I, the suitable algorithms used for the LOS are discussed in the following subsections with some additional algorithms developed for this project.

3.4.1 Transceiver impairments compensation

Because a software synchronization is used, the requirements for DSP algorithms are stringent to be able to display the amount of processed samples in a very short time (i.e. 8192 processed samples per second (equivalent refresh speed of 1 Hz)). More specifically, the feedforward algorithms are preferable and require less computational efforts. Besides, several complex computations such as square root, trigonometric functions can be relaxed thanks to software processing. The GSOP method [74] is selected for front-end impairment compensation, the carrier frequency offset (CFO) is compensated based on the Leven's algorithm [85]. The feedforward carrier phase estimation (CPE) is used for the phase noise compensation; particularly, the well-known Viterbi-Viterbi algorithm [92] is used for $M-$PSK signals and its monomial version [222] is used for $M-$QAM signals.

3.4.2 Algorithms for samples synchronization and representation

Up to this stage, the impairments caused by the non-ideal coherent receiver, the laser frequency offset and the laser phase noise are compensated for. It should be reminded that our concern in DSP is for the time equivalent sampling technique. Due to the asynchronous under-sampling operation based on the time equivalence, some additional DSPs in software synchronization are required for the received samples after the impairments compensation.

a) Equivalent-time samples reconstruction

In under-sampling technique, the data signal $E_D(t)$ with a period T_D is sampled with a period T_S much larger than T_D. As the data signal period is not a multiple of the sampling source period, we have the following relation

$$T_S = nT_D + \delta T, \tag{II.11}$$

in which n is a positive integer and δT denotes a fraction of T_D. To be able to display the eye diagram of the sampled signal, it is necessary to estimate the fractional part, δT. Fig. II.11(a) shows an example of NRZ-OOK eye diagram if no algorithm for samples reconstruction is applied, or the fractional part is unknown. There have been several methods proposed for the calculation of δT based on the periodogram analysis [223, 188].

The periodogram $S_m(f)$ is defined as the discrete Fourier transform of the m^{th}-power set of sampled data, s_k, with m being an integer depending on the modulation properties of data signals ($m = M, 2, 4$ for $M-$PSK, OOK, $M-$QAM, respectively)

$$S_m(f) = \frac{1}{N}\left|\sum_{n=0}^{N-1} s_k^m \cdot \mathrm{e}^{2j\pi nf}\right|^2, \tag{II.12}$$

where N is the data block length. By locating the maximum value in the periodogram, $\max(S_m(f))$, corresponding to index value f_{max}, the symbol period can be detected. More

particularly, to be able to plot the signal along N_P periods, the normalized abscissa of each sampled data can be expressed as [224]

$$t(n) = \left(n \cdot \frac{f_{\max}}{N} \right) \bmod N_P, \tag{II.13}$$

where *mod* is the *modulo* operator. However, due to the frequency resolution of $S(f)$, the estimated maximum value is proportional to $1/N$. The estimation error becomes critical when the block length is small. To reduce this error, the optimization technique based on Newton algorithm is used thanks to its fast convergence

$$f_{\max}(k+1) = f_{\max}(k) + \mu \cdot \left[\left. \frac{\partial S}{\partial f} \right|_{f_{\max}(k)} \Big/ \left. \frac{\partial^2 S}{\partial f^2} \right|_{f_{\max}(k)} \right], \tag{II.14}$$

in which μ is the step size. The estimation error is now reduced to $1/N^3$. Fig. II.11(b) presents the eye diagram of NRZ-OOK signal after applying the periodogram search algorithm for two bits time-slot. A clear reconstructed eye diagram is observed indicating the effectiveness of the algorithm. However, the misalignment of the output eye diagram can make the signal quality evaluation difficult if we superpose many acquisitions and this issue is dealt with in the following part.

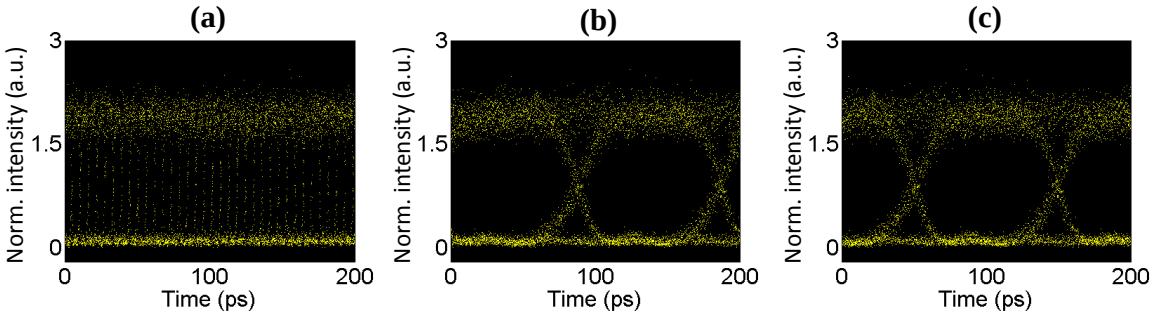


Figure II.11: Examples of 10 Gb/s NRZ-OOK signal eye diagrams (a) before, (b) after equivalent-time samples reconstruction and (c) with re-alignment algorithm.

b) Algorithm for the alignment of eye diagram

Because the incoming signal is under-sampled at an unknown starting position, the equivalent time eye diagram is generally not symmetric. This leads to difficulties in qualifying the reconstructed time-equivalent eye diagram in long persistence time, for example, in terms of Q-factor, error vector magnitude (EVM) calculations (as shown later on) due to the lack of the fundamental parameters of the eye diagram. The fundamental parameters including the one level, zero level, crossing times, crossing amplitudes, are achieved by some aforementioned methods based on the histogram analysis [225, 226].

In order to reconstruct a symmetrical eye diagram, the misaligned eye diagram from the previous steps is shifted by a certain equivalent time. This shifted equivalent time is

determined with respect to the equivalent symbol period using a proper determination of the crossing points position. To do this, the intensity average value is firstly calculated by

$$A_{mid} = \frac{1}{N}\sum_{k=1}^{N}|s_k|^2. \tag{II.15}$$

This calculation is more accurate with the increase of samples number. Then the samples having the intensity inside the range of $[A_{mid} - \rho \times A_{mid}, A_{mid} + \rho \times A_{mid}]$ are selected for the histogram analysis, where ρ specifies the percentage of selected intensity and it can be chosen to sufficiently remove the low and high levels in the eye diagram, i.e. 10%. The first crossing time corresponding to the biggest appearance of the selected samples is specified by the index (equivalent time) of the position in histogram having the maximum value. After retrieving this index, the eye diagram is circularly shifted by amount of $\lfloor N/P - A_{mid} \rfloor$ samples, where $\lfloor \cdot \rfloor$ is the operator rounding to the nearest integer. As a consequence, the eye diagram should be well aligned (Fig. II.11(c)).

3.5 Evaluation of proposed LOS-based monitoring scheme with different signals

This section shows some results that validate the aforementioned prototype for monitoring NRZ-OOK, NRZ-QPSK and 16-QAM signals. The goal of this section is to present the full picture of the signals in terms of constellation and eye diagrams. In this validation, the OFCG source is used as the pulsed-LO mainly because of its low timing jitter.

3.5.1 Optimization of LOS detection chain

In order to characterize the suitable range of input powers to the coherent detection, the setup in Fig. II.6 is used in a simple configuration. Particularly, the input signal is a continuous wave laser (CW) having a fixed power of -1 dBm. The pulsed-LO power is varied in a wide range from -10 dBm to 6 dBm. It should be reminded that the output photocurrents are amplified by the integrated transimpedance amplifiers (TIAs) in the coherent receiver. The bias voltages of these TIAs are also not changed (i.e. 1.2 V), providing a constant gain for the photocurrents. In the next step, the SNR of the reconstructed CW intensity is calculated (as defined in Section 2.4.3 of Part I) as a function of the pulsed-LO powers.

Fig. II.12 presents the calculated SNR, SNR_{CW} (ratio between the mean of reconstructed CW intensity and its corresponding standard variation), corresponding to different input pulsed-LO powers. In the low pulsed-LO power region (below -2 dBm), the calculated SNR increases with the increase of the pulsed-LO power. When the pulsed-LO power reaches -1 dBm, the SNR is remained at 10.6 dB up to 3 dBm of pulsed-LO power. The SNR decreases when the pulsed-LO power is increased further. This degradation is due to the saturation effect of the transimpedance amplifiers integrated in the coherent receiver.

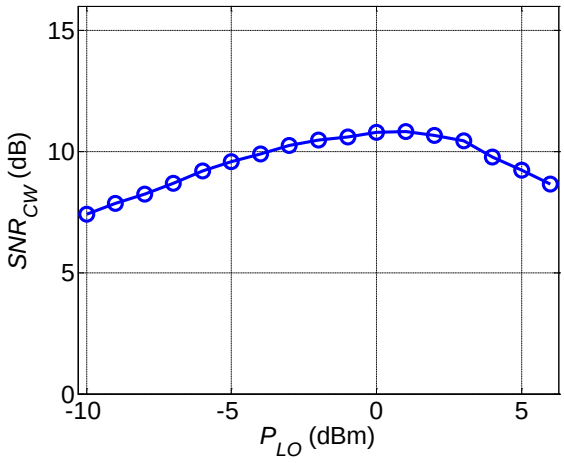


Figure II.12: Calculated SNR versus input pulsed-LO powers.

By optimizing the pulsed-LO input power to the coherent receiver, it is hence possible to reach a SNR_{CW} of 10.6 dB.

However, the limitation of optical input power in front of the coherent receiver (to avoid coherent receiver saturation) also limits the signal level at the input of the ADCs, which cannot work in its full range operation anymore. In order to work with the full range of ADC, the electrical amplifiers are inserted between the coherent receiver and the ADCs. In this setup, we compare the calculated SNR of the reconstructed CW signal without and with using the electrical amplifiers. For a fair comparison, the input signal and pulsed-LO powers are set to -1 dBm and 2 dBm, respectively. The TIA voltage is also fixed. Fig. II.13 presents the reconstructed signal in the complex plane in the cases without electrical amplifiers (Fig. II.13(a)) and with electrical amplifiers (Fig. II.13(b)). Here, no DSP is applied to the acquired I and Q components. Without using the electrical amplifiers, the magnitude of the samples is in the range of (-20, 20) for both I and Q components. The corresponding calculated SNR in this case is 10.6 dB. By using the electrical amplifiers, the magnitude range of the I and Q components is expanded to (-100, 100). As a result, the better calculated SNR of 11.7 dB is achieved. The CW representations on the complex plane after DSP in two cases are also plotted in the insets of Fig. II.13. Less variation of the reconstructed constellation state is observed in the case of using the electrical amplifiers.

Fig. II.14 presents the calculated SNR of reconstructed CW signal with 100 acquisitions. The average SNR_{CW} without using amplifier is only 10.4 dB whereas the average SNR with the help of amplifiers is increased to 11.6 dB. Note that, our amplifiers used in this experiment were not optimized in term of bandwidth (about 10 GHz), leading to more additional noise after amplification. It would be expected that the reconstructed signal quality would be better with electrical amplifiers having a bandwidth equal to the sampling rate (to remove out-of-band noise).

The detection chain was hence optimized with available equipments for our experiment. We then studied the reconstruction of different kinds of signals.

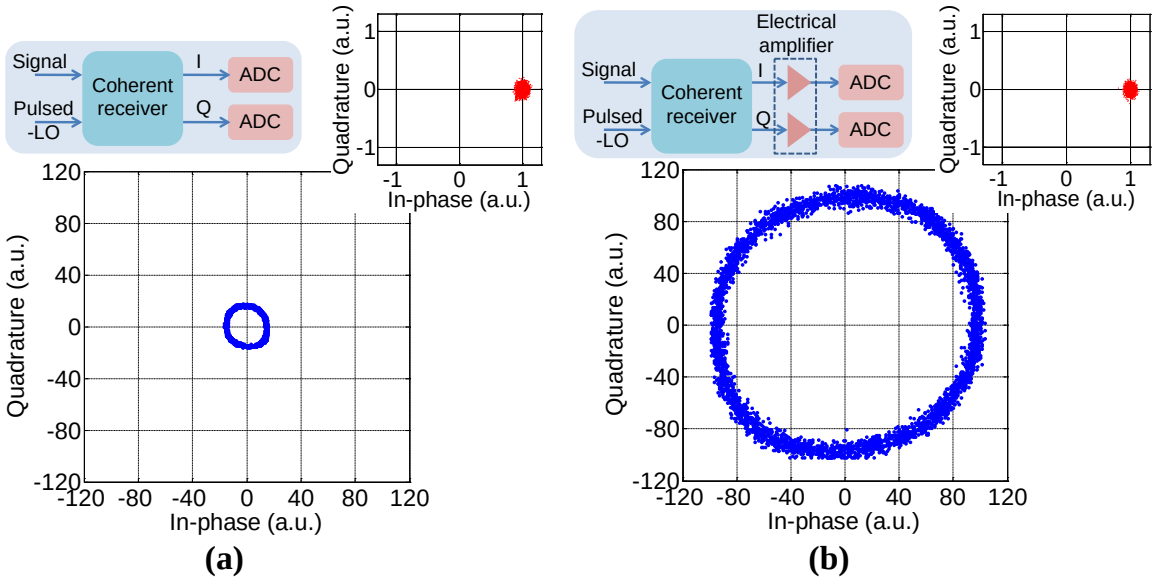


Figure II.13: Examples of CW representations (acted as data under test in LOS) on complex plane with 2 output I and Q components (a) without and (b) with using the electrical amplifiers before DSPs. The insets show the CW representation after DSPs.

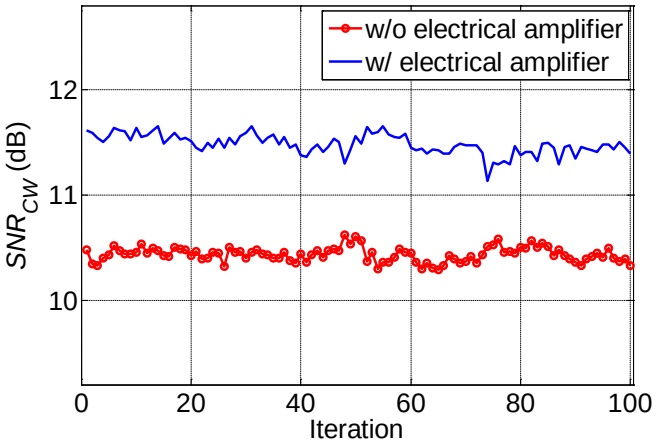


Figure II.14: Calculated SNR of reconstructed CW signal using LOS-based monitoring technique with 100 iterations.

3.5.2 NRZ-OOK signal

The most simple modulation format – NRZ-OOK signal at 10 Gbit/s is used for the first validation. Fig. II.15 shows the I and Q components as well as the corresponding constellation after the ADC acquisition. At this step, no DSP is applied leading to the distortion of the constellation, and no eye diagram can be displayed, owing to the impairments (i.e. IQ imbalance, CFO, laser phase noise).

By applying the DSP procedure, the constellation after DC offset and IQ imbalance compensation is represented in Fig. II.16(a), whereas Fig. II.16(b) and (c) present the constellation after CFO compensation and CPE operation, respectively. For eye diagram repre-

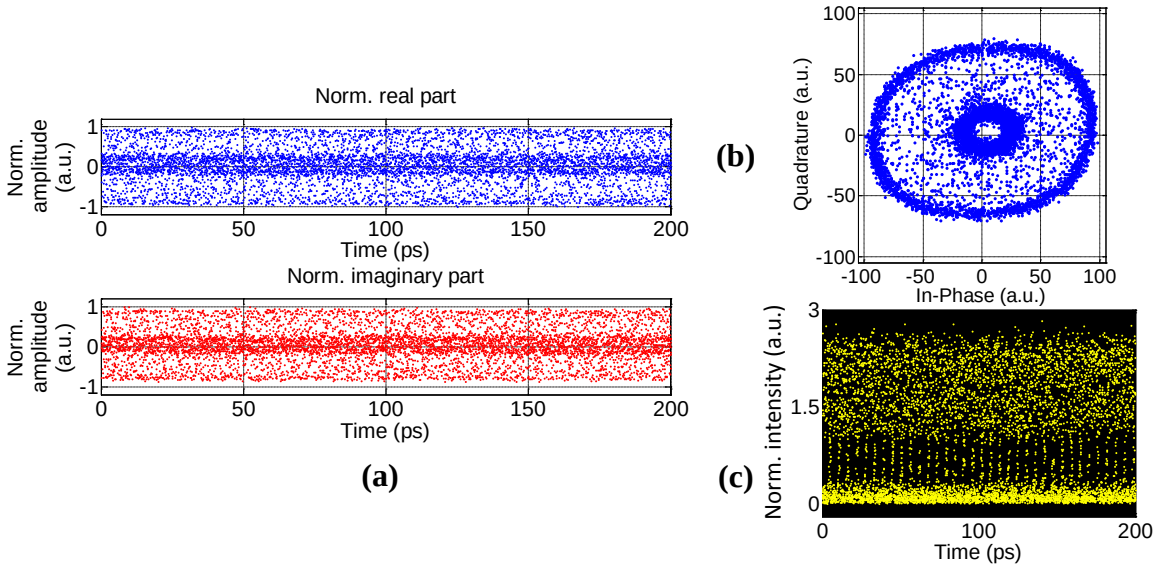


Figure II.15: (a) I and Q components; and the corresponding (b) constellation and (c) eye diagram of raw data of 10 Gbit/s NRZ-OOK signals acquired by linear optical sampling technique.

sentation, the algorithm presented in Section 3.4.2 is used to obtain the Fig. II.16(d). It can be observed that the constellation diagram is well represented with a horizontal line connecting two constellation spots due to the finite transition times of the modulator, whereas the eye diagram is also reconstructed with a quite noisy one-level. One of the reasons could come from the limited extinction ratio of sampling pulses, as discussed later in Section 4.2.4.

3.5.3 NRZ-QPSK signal

In the next step, a 10 Gbaud NRZ-QPSK signal is used. Fig. II.17 illustrates the constellation and eye diagrams of the NRZ-QPSK signal after the software synchronization. As expected, all signal information as well as the transition are fully represented, confirming the effectiveness and robustness of the prototype.

3.5.4 16-QAM signal

We further validate our prototype with a 10 Gbaud 16-QAM signal. Due to some issues related to the electrical generation parts (i.e. limited bandwidth, nonlinear electrical amplifiers), the signal source has not a very good quality; however, it allows us to validate the proposed prototype with upgraded DSPs for the advanced modulation format signals that is an extension of DSPs used in the QPSK signal case. Fig. II.18 presents the constellation and eye diagrams of acquired samples. Although the eye diagram is quite noisy due to the signal generation part, the constellation diagram is well constructed, confirming the functionality of the proposed prototype.

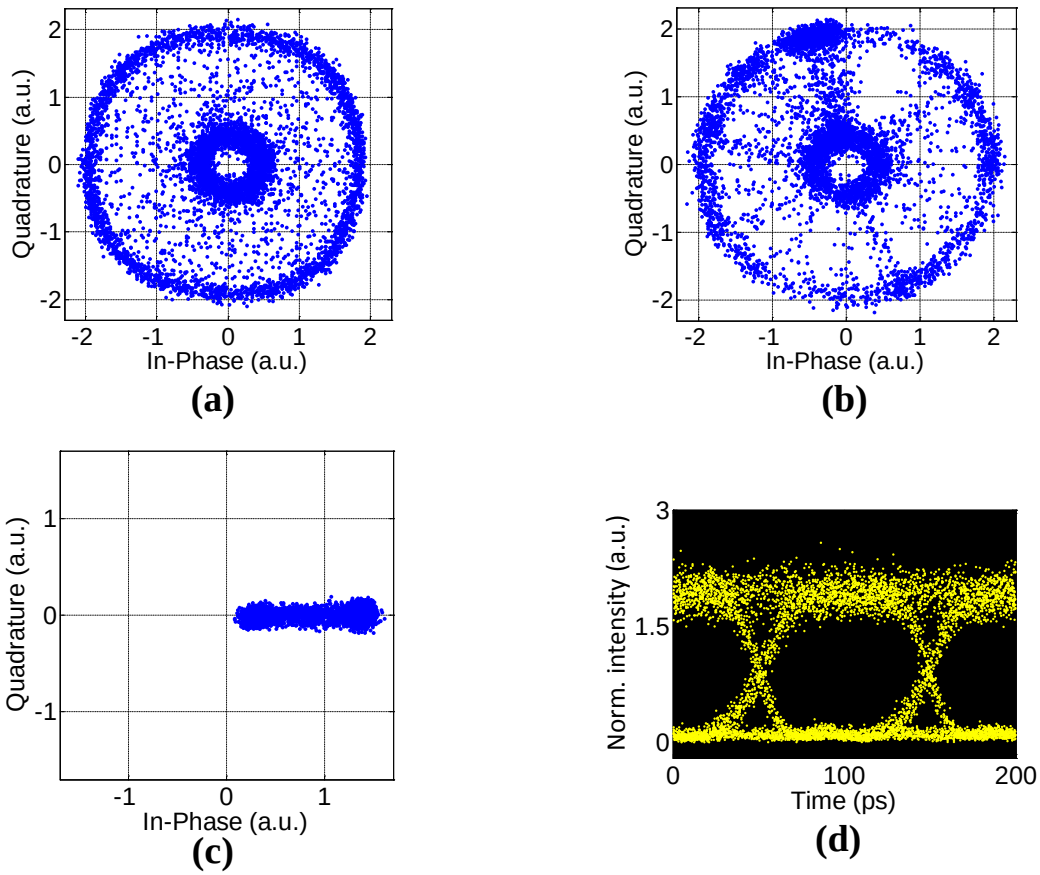


Figure II.16: Constellations of 10 Gbit/s NRZ-OOK signals after (a) IQ imbalance compensation, (b) CFO compensation, (c) CPE operation and (d) the corresponding represented eye diagram.

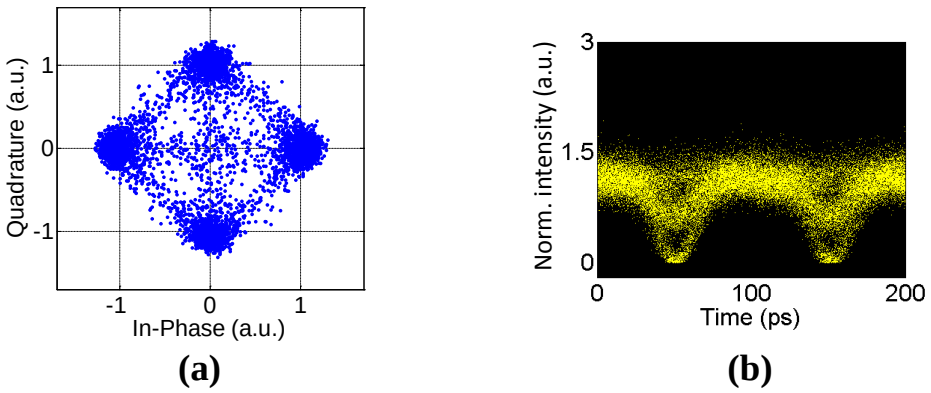


Figure II.17: (a) Constellations of 10 Gbit/s NRZ-QPSK signals and (b) the corresponding represented eye diagram.

3.5.5 Problem statement and some hypothesis

The achieved results are further compared to a commercial optical sampling oscilloscope (OSO). Note that this OSO does not provide the phase information as a constellation

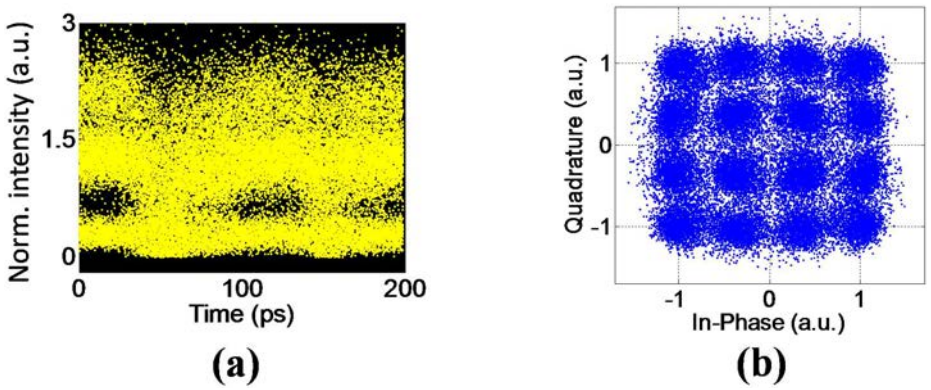


Figure II.18: (a) Eye diagram and (b) constellation of the 10 Gbaud 16-QAM signal.

diagram. Fig. II.19 summarizes these comparisons for both NRZ-OOK and NRZ-QPSK signals. In order to achieve a fair comparison, the same number of acquisition points (about 16000 samples) are acquired by both OSO and prototype test-bed. For the NRZ signal, it can be seen that the recovered signal is not so different except for an increase of amplitude noise on one-levels in the case of the LOS-based monitoring. Next paragraphs will aim at studying this effect. For QPSK signal, there is no noticeable difference on the eye diagram, while the constellation diagram is not available with our OSO. This is an encouraging result for signal monitoring and parallelization techniques.

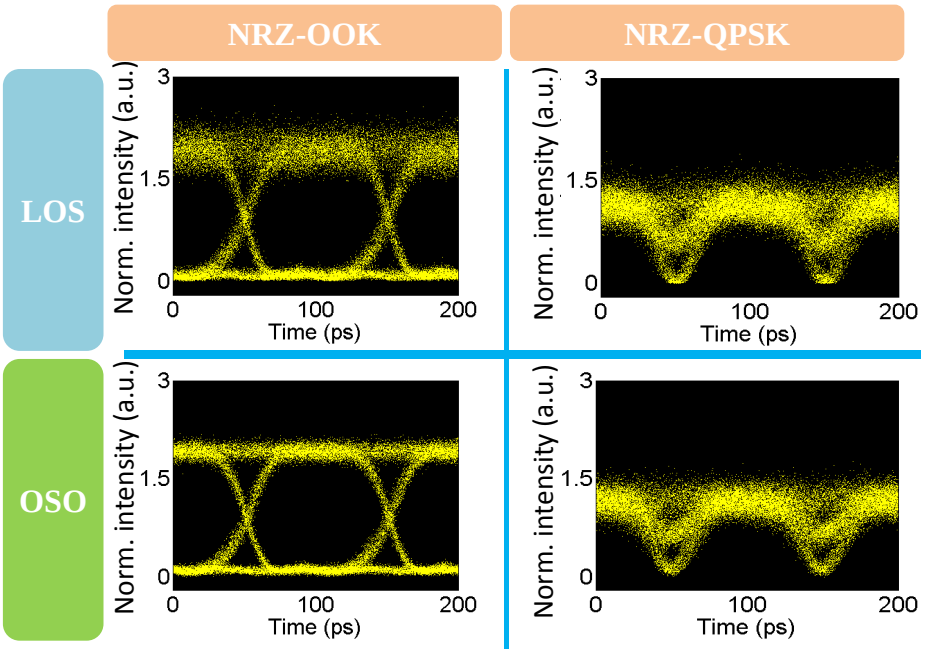


Figure II.19: Comparison of the proposed prototype to the available optical sampling oscilloscope in laboratory with 1 ps resolution, for 10 Gbaud NRZ-OOK and NRZ-QPSK signals.

The intensity variation, especially on one-level of the NRZ-OOK signal, can come from

the inter-symbol interference (ISI) or intensity noise inherent in current LOS-based monitoring setup. Several hypotheses concerning the impairments of either electrical or optical parts were proposed so far. More specifically, the following impairments in the system setup can generate the ISI and amplitude noise in the reconstructed signal

◇ Receiver bandwidth (photodiodes, ADC, etc.)

◇ ADC effective number of bits (ENOB)

◇ Signal-to-noise ratio of pulsed-LO

◇ Timing jitter of pulsed-LO

◇ Extinction-ratio of pulsed-LO

In order to identify which hypothesis causes the amplitude noise and ISI, some numerical and experimental works have been carried out and are reported in Section 4.

4. Analysis of limitations in proposed LOS-based monitoring system

In this section, the proposed LOS-based monitoring configuration has been studied for both optical and electrical parts. As far as the electrical part is concerned, the ADC parameters impacts are firstly studied in Section 4.1 in terms of limited-bandwidth, integration time and effective number of bits (ENOB). The most significant element in the optical part is the pulsed-LO that mostly influences the recovered signal quality. The impact of some typical pulsed-LO parameters is studied in Section 4.2. Particularly, the impacts of the pulsed-LO signal-to-noise ratio and jitter are numerically carried out in Sections 4.2.1 and 4.2.2, respectively, by using the developed numerical model. As the requirements (chirp, detuning frequency, etc.) of this source were fully studied in [204], we focus in this work on our particular case of the use of an external modulator to decrease the source repetition rate. The effect of the presence of residual sub-pulses on the sampling source resulting from the finite extinction ratio the modulator is particularly investigated in the last subsection.

4.1 Impacts of ADC parameters

The section starts with motivations highlighting the importance of this study on linear optical sampling. After that, a general scheme is described for characterizing the influence of various ADC parameters. A detailed numerical model and the experimental investigations are then introduced, before presenting the results.

4.1.1 Motivation

Fig. II.20 illustrates the operation of LOS-based monitoring of a simple sinusoidal signal (S) and the parameters influencing its performance. As mentioned in section 3, S is mixed with the pulsed-LO in a 90° optical hybrid. Normally, a low sampling rate ADC synchronized with the pulsed-LO is used to acquire the samples of the signal under test in the time-equivalent manner. The voltage envelope of the analog waveform (the mixing product between the signal and pulsed-LO) is qualitatively represented by the dashed-line with the effects of limited-bandwidth, integration time and quantization noise. Finally, online DSP

can be applied in order to display the eye and constellation diagrams of the signal under test.

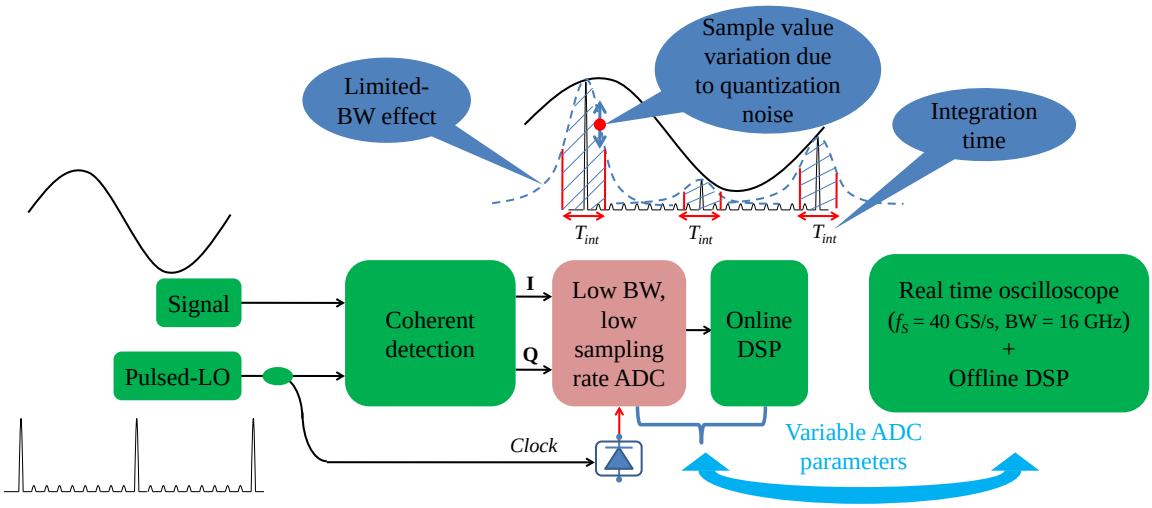


Figure II.20: Illustration of LOS-based monitoring of a sinusoidal signal and of the parameters influencing its performance.

The waveforms at the I and Q outputs of the receiver depend on the limited-bandwidth (BW) of the opto-electronic interfaces and ADCs (the resulting dashed line in Fig. II.20 which is a broadened version under the limited-BW effect). We name this bandwidth effect of both opto-electronic interfaces (i.e. photodiodes) and ADCs as "limited-BW" hereafter for simplicity. Because the system can be modeled as linear time invariant (LTI) system, the position of photodiode bandwidth (BW_{PD}) and ADC bandwidth (BW_{ADC}) can be interchangeable and the one with smaller bandwidth has much impact. To reduce the complexity of this investigation, the limited-BW is implicitly represented either the photodiode bandwidth or the ADC bandwidth in which the smaller bandwidth is accounted for. Since this bandwidth limitation can be modeled by a low pass filter (LPF), one key issue is to assess the impact of such a LPF. Moreover, the heart of the electrical part is the ADC, which is responsible for the digitization of the detected electrical signal after the photodiodes in order to allow digital post-processing. In particular, the track-and-hold (T/H) function of the ADC holds the signal sample value for some time before the digitization operation. In other words, it can be characterized by integrating the signal voltage during the acquisition time (i.e. the selected region inside the vertical red lines) [227]. Therefore, it is relevant to assess the impact of the integration time, T_{int}, on the quality of the output processed signals. Furthermore, the sample voltage (amplitude) at the output of the digitizer is affected by quantization noise, leading to the variation of sample value (i.e. small circle point in Fig. II.20) around its real value. This effect can be characterized by the ADC ENOB.

The impacts of these three factors (ENOB; integration time; limited-BW) are numerically and experimentally investigated in the following sections. Available and conceivable ADC for LOS analysis has typical (ENOB; BW_{ADC}; T_{int}) specification sets typically varying

between (8; 3 GHz; 0.2 ns) and (16; 125 MHz; 0.8 μs). In order to explore different values of these parameters, we use in our experiment the photodiodes with BW_{PD} = 15 GHz and a digital sampling oscilloscope (DSO) with a high bandwidth (16 GHz) and a high sampling rate (40 GS/s), in order to be able, at the DSP stage, to artificially vary the ADC parameters. On the other hand, DSO ENOB being fixed to 5.5, the impact of ADC ENOB will be only numerically studied.

4.1.2 Experimental scheme for the study

To investigate the impacts of the opto-electronic interfaces and ADC parameters, the scheme presented in Fig. II.6 is employed. This investigation is performed numerically and experimentally with 10 Gbaud NRZ-OOK and NRZ-QPSK signals. The performance is evaluated in terms of Q-factor and error vector magnitude (EVM) calculations. Although these metrics are frequently used in characterizing the optical transmission systems, they are used here for parameters evaluation. In fact, EVM allows comparing the received signal and the ideal one in terms of both amplitude and phase errors; it is a useful tool to characterize the phase error of the reconstructed signal due to laser phase noise. The signal and pulsed-LO were described in Section 3.1. One polarization is selected at both inputs of the receiver. After mixing in the 90° optical hybrid, the I and Q components at the output of the hybrid are first detected in a set of photodiodes (15 GHz BW), then acquired and digitized by the real-time DSO. It is also noted that the oscilloscope is triggered by a part of the pulsed-LO (photodetected by a large BW photodiode) to be able to synchronize the I and Q components in the post-processing. Thanks to the large photodiodes BW and high speed DSO used in experiments, the undistorted waveform is obtained: We are then able to emulate the operation on this waveform of devices (photodiodes, ADCs) with lower performances in order to study their impact on the reconstructed signal.

The acquisition of the I and Q components at the outputs of the coherent receiver using a very fast sampling oscilloscope can give information on their waveforms. However, this method requires one more step in DSP to perform the integral function, representing the equivalent acquisition of a lower sampling rate ADC card, namely ADC_{low} for simplicity, in the LOS-based monitoring system at 714 MHz sampling repetition rate. The integration time was discussed earlier in Section 3.2 of Part I), linked to the maximum sampling rate of ADC_{low}. In the prototype setup (Section 3), the ADCs can sample at up to 5 GS/s, equivalent to $1/(5 \cdot 10^9) = 0.2$ ns acquisition time. From this statement, the achieved results use 0.2 ns of the integration time as a benchmark for other evaluations in the LOS-equivalent experimental setup.

Because of the timing jitter effects both in high sampling rate oscilloscope and in pulsed-LO, the sampling times are not regularly spaced, leading to reduced accuracy of the DSP. To be able to detect the proper sampling positions, a part of the pulsed-LO is used not only to serve as trigger for the oscilloscope, but also to estimate the index corresponding to the

peak positions of the pulsed-LO. This method provides a sufficient means to synchronize the acquired data for post-processing, as shown in the following sections.

4.1.3 Numerical model

The receiver model is analyzed and simulated based on the analysis in Section 2.1. It should be reminded that only one polarization is selected after coherent detection. The following parts then focus on the models of signal source, pulsed-LO and ADC BW that were used in the experiments. In the following equations, the optical carrier frequency is omitted for simplicity and shortening the equations.

a) Pulsed-LO model

The signal emitted by the pulsed-LO is modeled as a train of Lorentzian-shaped pulses whose envelope of the electric field is defined as [228]

$$E_{LO}(t) = \sqrt{P_{LO}} \sum_{m=-\infty}^{\infty} \left[f(t - mT_S) + \frac{1}{\sqrt{ER_{LO}}} \sum_{l=1}^{k-1} f(t - mT_S - lT) \right], \tag{II.16}$$

where T_S and T are the periods of the pulsed-LO and the pulse time-slot, respectively. ER_{LO} denotes the limited extinction-ratio of the pulsed-LO, which is due to the pulse rate down conversion operation realized by an external intensity modulator with finite extinction ratio during the pulsed-LO signal generation. This extinction-ratio is set to 20 dB (corresponding to the current reported extinction-ratio of MZM used in experiments) in the following simulations. In eq. (II.16), k is the down-conversion rate, P_{LO} represents the pulsed-LO power, and the $f(t)$ is the Lorentzian waveform defined as follows

$$f(t) = \frac{1}{\left(1 + \left(\frac{t}{T_0}\right)^2\right)}, \tag{II.17}$$

in which T_0 is the half of the full-width at half maximum (FWHM) $T_0 = FWHM/2$.

b) Limited-BW model

The limited-BW is modeled by a 5^{th} order Bessel low pass filter (LPF). It is the mostly used model for ADC modeling [227]. It should be noted that other kinds of LPF models will be used in further studies. The frequency domain transformation is normally implemented by the fast Fourier transform (FFT). The general transfer function of a Bessel filter is

$$H(f) = \frac{B_m(0)}{A_m(f)}, \tag{II.18}$$

where $A_m(f)$ and $B_m(f)$ are the m^{th} order Bessel polynomials. For example, in our case the 5^{th} order Bessel filter transfer function has the following form

$$H(f) = \frac{b_6}{a_1 f^5 + a_2 f^4 + a_3 f^3 + a_4 f^2 + a_5 f^1 + a_6}, \tag{II.19}$$

where a_i, b_6 are the coefficients related to the predefined BW of filter, $i = 1, ..., 6$.

It should be noted that this LPF function is also applied to the experimental data acquired from the DSO, to be able to emulate the impact of the ADC BW. In the simulations, it is applied after coherent detection before carrying out the DSP.

c) Other hypothesis in simulation model

In the numerical study, only additive white Gaussian noise (AWGN) is used as the noise source for both signal and pulsed-LO for the proof-of-concept purpose and the qualitative comparison to the experiments. This AWGN source is used to emulate the ASE noise added to signal and pulsed-LO by the EDFAs. In experiments, other noise sources can disturb the signals both at transmitter and receiver sides and in both electrical and optical domain. However, the noise can be modeled as the AWGN, and the exact noise quantity in experiment needs to be further studied. Even though the parameters used in this simulation approach may not perfectly match those in the experiments, it provides a good means for the evaluation and validation of the experimental studies.

In particular, the AWGN noise is added to both signal and pulsed-LO to reach the OSNRs of 40 dB and 25 dB (in 0.1 nm), respectively, which are similar to those of the experiments. To obtain accurate representations of the signal and pulsed-LO, 128 points are used to represent one bit slot (equivalently, the sample rate of the simulation is set to 1280 GHz). Because the ratio between the data rate and the sampling repetition rate is always much greater than 1, as inherent to the LOS-based monitoring technique, the positions of the samples relatively to the bit slot must be different from bit to bit in order to allow the full reconstruction of the signal. Therefore, the timing re-scale is required for the simulated detection operation. In our case, a cubic interpolation method is applied to the signal, estimating the values of signal samples corresponding to those of pulsed-LO samples in the same time scale. It should be also noted that the extinction ratio of the pulsed-LO is set to 20 dB (a typical value of the MZM extinction-ratio) in our simulation.

4.1.4 Results and discussion

In LOS-based monitoring, the signal transition points are also captured in the reconstructed signals. However, these points are not taken into account in the metrics calculation. Particularly, the Q-factor is calculated over 47% of total samples in which the selected points from OOK eye diagram is ensured to exclude the transition points. In contrast, 31% of overall samples are retained after removing the transition points from QPSK eye diagram to calculate the EVM metrics, to empirically investigate our study.

a) Impact of integration time T_{int}

Firstly, the impact of the integration time is experimentally evaluated with NRZ-OOK and NRZ-QPSK signals. The results are then numerically compared to those obtained using the simulation model. A limited-BW of 3 GHz and an ENOB of 5 are used in the numerical

investigation; these parameters are also introduced in the DSP stage of the experimental investigation. As introduced in the motivations, an integration time of 0.2 ns is a minimum for low cost ADC cards that can be considered for LOS-based monitoring technique. This is the minimum value considered in our study.

Influence of integration time on NRZ-OOK signals

The first row of Fig. II.21 presents the experimental eye diagrams at the integration time of 0.4 ns (Fig. II.21(a)), and of 0.6 ns (Fig. II.21(b)), respectively. The second row of Fig. II.21 presents simulated eye diagrams for the same integration times of 0.4 ns (Fig. II.21(c)) and of 0.6 ns (Fig. II.21(d)). We clearly observe a degradation of the eye diagrams after increasing the integration times. This can be explained by the fact that a larger integration time leads to a larger number of integrated samples hence leading to more quantization noise.

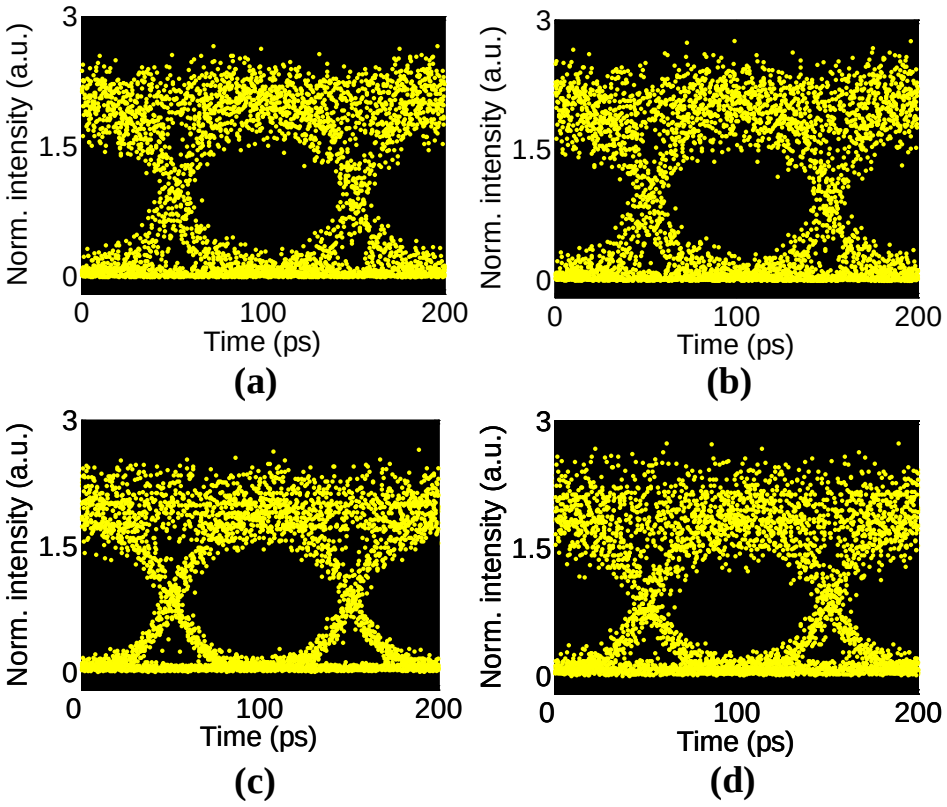


Figure II.21: Experimental (a)(b) and numerical (c)(d) 10 Gbaud NRZ-OOK signals eye diagrams for a limited-BW of 3 GHz with integration times of (a)(c) 0.4 ns and (b)(d) 0.6 ns.

Further processing enables to retrieve the numerical (Fig. II.22(a)) and experimental (Fig. II.22(b)) Q-factors as a function of the integration time. It confirms that the Q-factor degrades when the integration time increases. Despite the same number of samples are considered in both simulation and experiments, there are the different ASE noise and quantization noise (due to the unknown exact ENOB in experiments), between the experimental

and numerical data. The Q-factor values are then different in the two cases while the dependence of the Q-factor on the integration time remains qualitatively similar. Another reason for this quality degradation is due to the more contribution of sub-pulses inherent to the limited extinction ratio of pulsed-LO of 20 dB (further discussed in Section 4.2.4). When the integration time increases, the more presence of sub-pulses is contributed to the reconstructed signals, resulting in the deterioration of Q-factor.

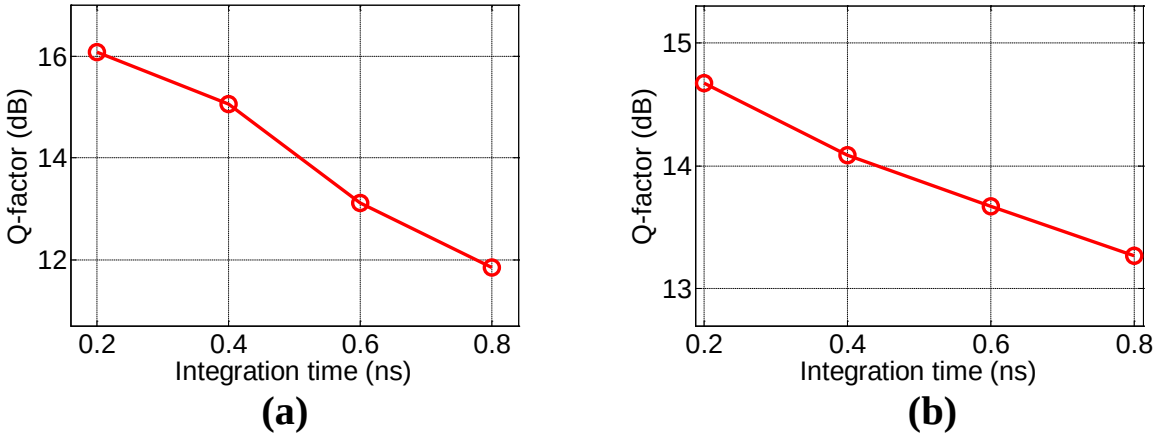


Figure II.22: Evolutions of Q-factors as a function of integration times with (a) numerical and (b) experimental data. BW is set to 3 GHz.

Influence of integration time on NRZ-QPSK signals

A similar evaluation is numerically and experimentally applied to a 10 Gbaud NRZ-QPSK signal, in particular, when 0.4 ns and 0.6 ns integration times are applied, resulting in the experimental eye diagrams shown in Fig. II.23(a) and (b), respectively. Using numerical data, reconstructed eye diagrams are represented in Fig. II.23(c) and (d), corresponding to integration times of 0.4 ns and 0.6 ns, respectively. In the same manner as for NRZ-OOK signal, a degradation of the eye diagram reconstruction is observed when the integration time is increased. This is also confirmed on the constellation diagrams (insets of Fig. II.23).

The EVMs increase with integration time, represented in Fig. II.24 for the numerical (Fig. II.24(a)) and experimental (Fig. II.24(b)) data, confirms this tendency. Since the more integration time is considered, the more noise and the more presence of sub-pulses are taken into account in the EVM calculation, resulting in the degradation of the reconstructed signal quality. As in the case of NRZ-OOK signals, the absolute values of EVM are different in the numerical and experimental evaluations. This is due to the different ASE noise contributions between the experimental and numerical data. However, the evolutions of the EVM agree qualitatively in both situations.

b) Impact of limited-BW

In the next step, the impact of the limited-BW is experimentally and numerically investigated with 10 Gbaud NRZ-OOK and NRZ-QPSK signals. A BW range of 0.5 to 5 GHz,

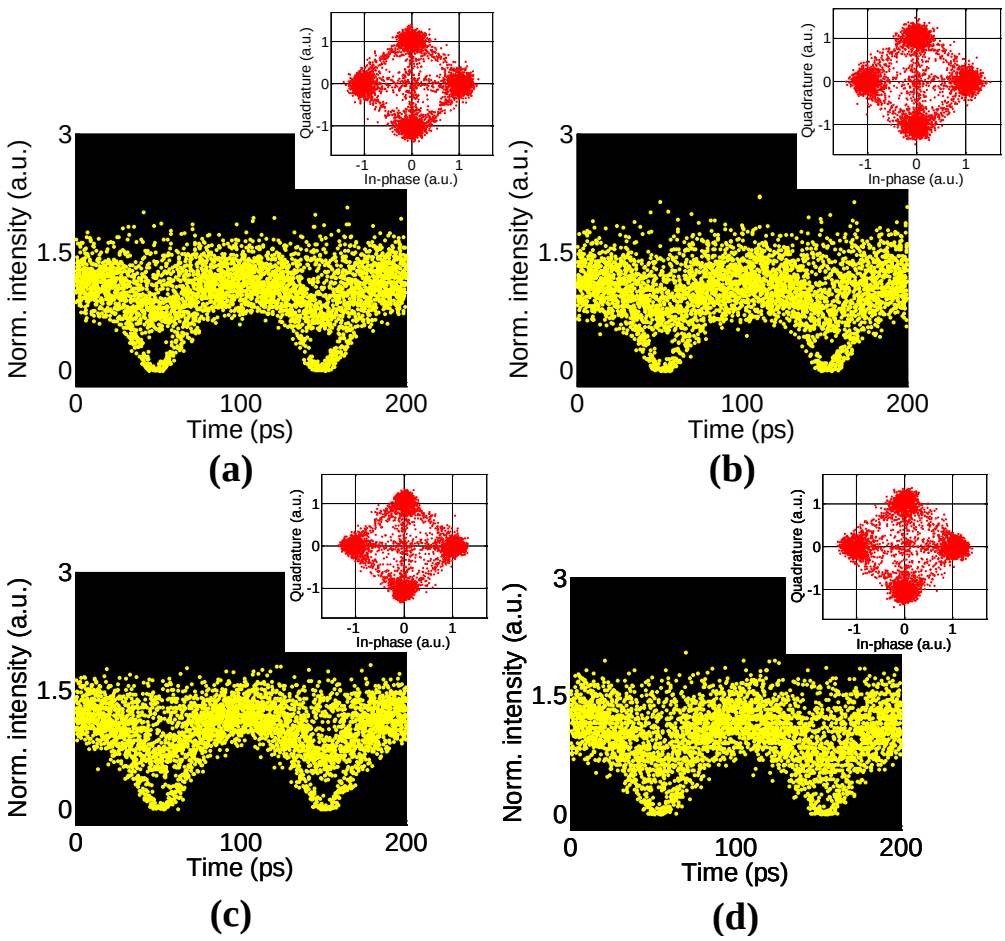


Figure II.23: Experimental and numerical 10 Gbaud NRZ-QPSK signals eye diagrams and corresponding constellations (in the insets) with a limited-BW of 3 GHz and integration times of (a)(c) 0.4 ns (b)(d) 0.6 ns.

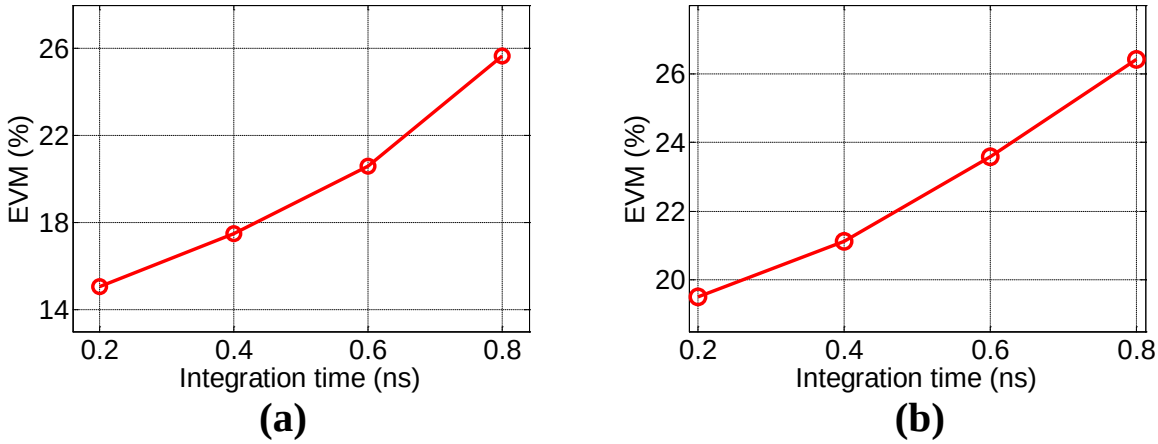


Figure II.24: Evolutions of EVMs as a function of integration time with (a) numerical and (b) experimental data. BW is set to 3 GHz.

the integration time of 0.4 and 0.6 ns and an ENOB of 5 are considered in this study. It should be reminded that the extinction-ratio of pulsed-LO of 20 dB is always presented.

Influence of limited-BW on NRZ-OOK signals

The first row of Fig. II.25 presents the experimental eye diagrams for a limited-BW of 1 GHz (Fig. II.25(a)), and of 3 GHz (Fig. II.25(b)), respectively. The second row of Fig. II.25 shows the simulated eye diagrams at the corresponding limited-BWs of 1 GHz (Fig. II.25(c)) and of 3 GHz (Fig. II.25(d)). It is observed that the eye opening is degraded when the BW is decreased. It can be intuitively understood by the fact that inter-symbol interference (ISI) will be introduced when the limited-BW is decreased. For a quantitative study, the Q-factor is used to evaluate the reconstructed NRZ-OOK signal quality under the impact of limited-BW.

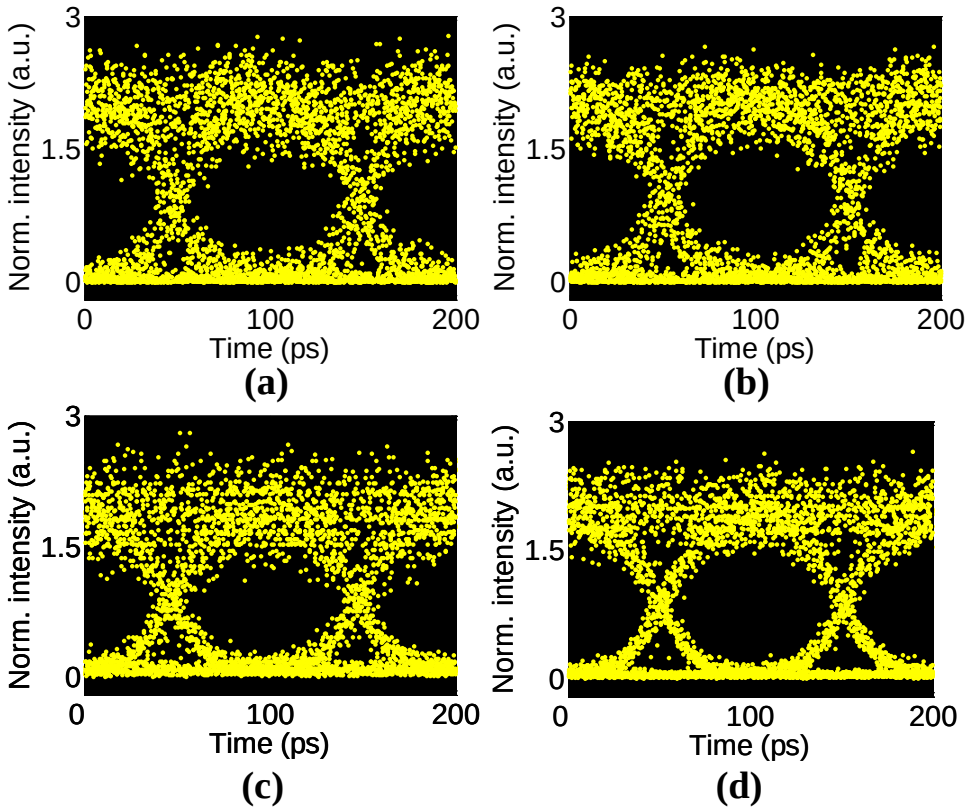


Figure II.25: Experimental and numerical eye diagrams of 10 Gbaud NRZ-OOK signals with 0.4 ns integration time and limited-BWs of (a)(c) 1 GHz (b)(d) 3 GHz, respectively.

Fig. II.26 presents the experimental (Fig. II.26(a)) and numerical (Fig. II.26(b)) Q-factor evolution with the BW for two integration times of 0.4 and 0.6 ns. In both cases, a BW of 2.5 GHz with 0.4 ns integration window gives a maximum Q-factor. It corresponds to the best compromise between ISI contribution (in the case of small BW) and additional noise (in the case of large BW). In the case of small BW, the Q-factor degrades rapidly (1.5 dB and 2.5 dB degradation in the experimental and numerical cases, respectively, when

the BW falls from 2 GHz to 0.5 GHz). It is due to the limited-BW leading to more ISI being introduced. In the case of high BWs, the Q-factor degradation due to additional noise integration is small (about 0.1 dB when the BW varies from 2.5 GHz to 5 GHz). For a 0.6 ns integration time, the maximum Q-factor is shifted back to a limited-BW of 2 GHz and evidently smaller than that with a 0.4 ns as in previous study. This shifted BW value is due to the dominant contributions of ASE noise and sub-pulses compared to the introduced ISI by the limited-BW. A similar evolution between the numerical and experimental data confirms the impact of limited-BWs on the signal reconstruction.

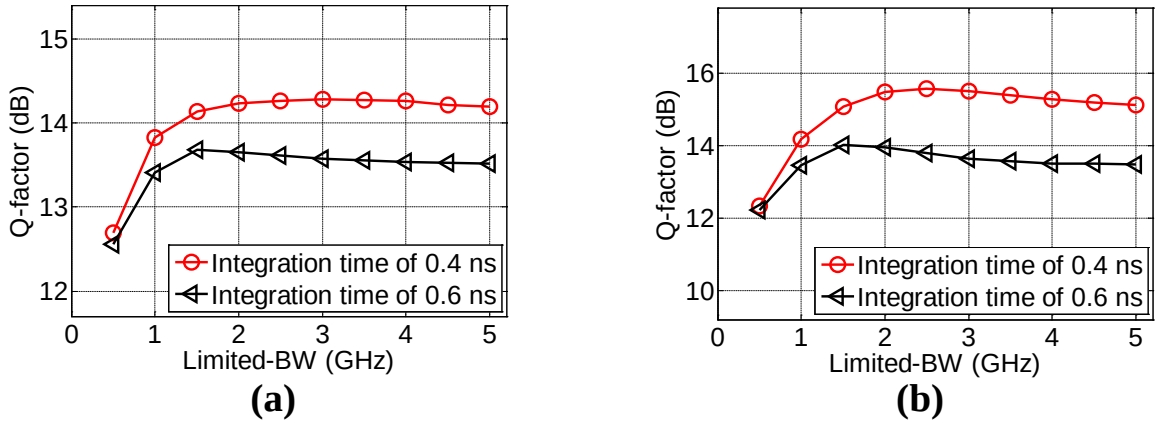


Figure II.26: Q-factor as a function of limited-BWs obtained from (a) experimental and (b) numerical data.

Influence of limited-BW on NRZ-QPSK signals

An investigation of the limited-BW impact on 10 Gbaud NRZ-QPSK signals is also numerically and experimentally carried out. Fig. II.27(a), (b) present the experimental eye diagrams for BWs of 1 GHz and 3 GHz, respectively. The numerical eye diagrams at 1 GHz and 3 GHz BWs are illustrated in Fig. II.27(c), (d). Once again, better eye diagram and constellations are observed with higher BW (insets of Fig. II.27).

Fig. II.28(a), (b) present the evolutions of the EVMs as a function of BW, calculated from experimental and numerical data, respectively. This confirms that larger EVM are obtained for low BW values, indicating the strong variation of the processed samples, because of ISI effect. For instance, with 0.4 ns integration time, the EVM starts reducing with an increase of limited-BW (10% and 7% reduction in experimental and numerical cases, respectively, when the BW increases from 0.5 GHz to 2 GHz). In the case of high BW (from 2 GHz to 5 GHz), the EVM metric is varied by less than 1% due to small additional noise integration in 0.4 ns. In a 0.6 ns integration time, as previously studied, the more variation is observed by the increase of EVM value due to the more integrated noise. However, the optimum EVM value in both cases is remained at 2 GHz bandwidth.

c) Impact of ADC ENOB

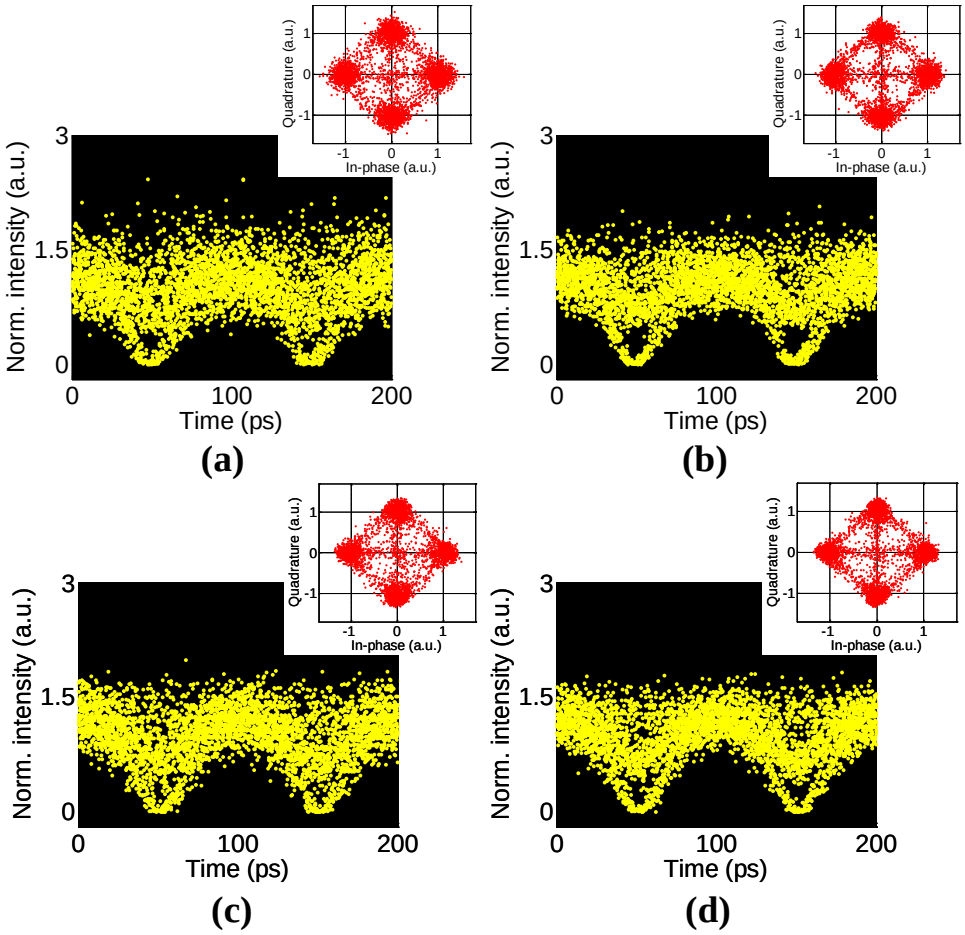


Figure II.27: Experimental and numerical eye diagrams and corresponding constellations (in the insets) of 10 Gbaud NRZ-QPSK signals with 0.4 ns integration time in cases of limited-BWs of (a)(c) 1 GHz (b)(d) 3 GHz.

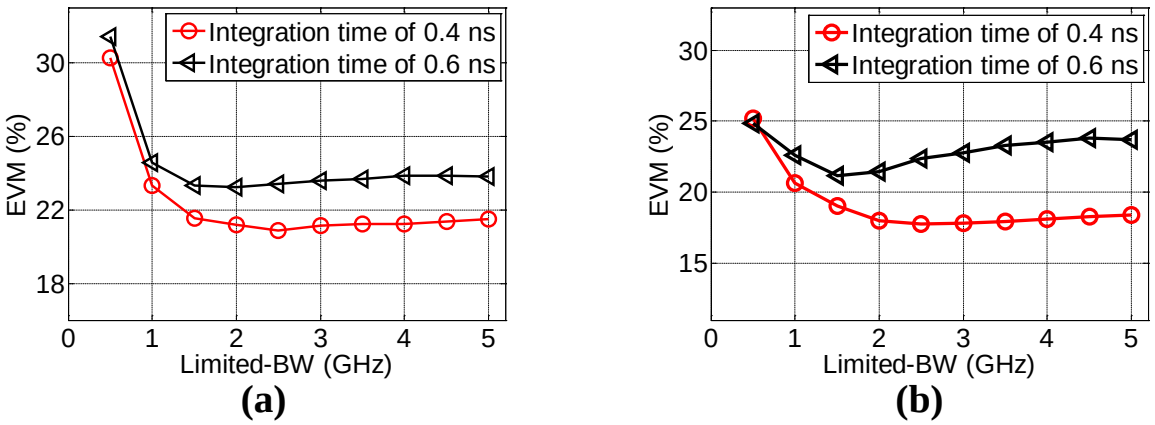


Figure II.28: Impact of limited-BW on the 10 Gbaud NRZ-QPSK signals evaluated by the EVM metric with (a) experimental and (b) numerical data.

Because the ENOB of the DSO cannot be changed experimentally, the impact of the ENOB on the signal reconstruction is only studied numerically. As seen in the previous studies, the numerical analysis gives a good idea of the trends, even if the absolute values are not perfectly in agreement with those obtained from the experiments. The raw data at the two outputs of the 90° optical hybrid are fed to the ADC model. To match with the devices available in the experiments, the limited-BWs of 1 GHz and 2 GHz are applied to the I and Q components before digitizing with variable ENOBs. The output data are processed with the same DSP procedure as before. It should be noted that the quantization error is generated as a normal (or Gaussian) distribution with the variance defined in Section 3.3 of Part I. To ensure proper statistical evaluations of the Q-factor and EVM, the calculations are repeated 50-times for each value of ENOB before taking the average values.

Fig. II.29(a), (b) present the evolutions of Q-factor and EVM as a function of ADC ENOB with different values of limited-BWs. For ENOB values smaller than 5 bits, a large variation of the samples is generated due to the big variance of quantization error, resulting in low Q-factors and high EVMs values. These metric values improve with the increase of the ENOB. When the ENOB is greater than or equal to 6 bits, there is no influence of the ENOB on the Q-factor and EVM regardless of the BW value. As a conclusion, an ENOB of 6 bits is found to be sufficient for negligible quantization noise in the linear optical sampling technique.

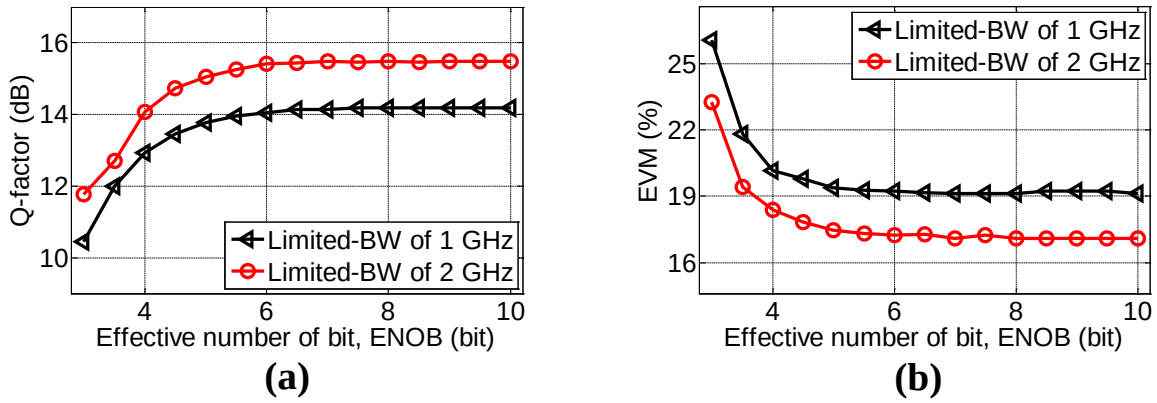


Figure II.29: Dependence of (a) Q-factor for NRZ-OOK signal, (b) EVM for NRZ-QPSK signal on the ADC ENOB.

Based on the specification of ADC card in Section 3.3, the ADC bandwidth and the ENOB are sufficient for the LOS-based monitoring setup. However, this specification is validated for all this ADC family, whereas the ADC parameters can be slightly different compared to the reported ones due to the imperfection in fabrication. Because the ENOB characterization is numerically evaluated, it is essential to experimentally assess this parameter of current ADC card. Next section is aimed at characterizing the ADC ENOB with a simple experiment.

4.1.5 Experimental ADC ENOB characterization

To characterize the ENOB of the ADC under test, a simple experimental setup as in Fig. II.30 is employed. The RF synthesizer provides a sinusoidal signal with tunable frequency. In this experiment, we compare two cases in which the RF signal is directly sent to the ADC (referred to as case 1) or the RF signal is electronically amplified before being sent to the ADC (named as case 2). A variable attenuator is inserted before the electrical amplifier allowing us to modify the ADC input power. Due to the maximum peak-to-peak ADC input value of 500 mV, another fixed attenuator is placed before the ADC to avoid any damage. The ADC is externally clocked at 714 MHz that is similar to the sampling rate used in LOS-based monitoring technique. The samples acquired by the ADC are then used in the frequency analysis and the ENOB calculation. In fact, there has been two methods to calculate the ENOB up to now. One processes in the time-domain by using the sine-fitting procedure to deduce the ENOB [229], whereas the other calculates ENOB based on frequency analysis [230]. In our case, we use frequency analysis to calculate ENOB because this analysis can provide more information (i.e. dynamic range, noise level, etc.). We firstly use one of four ADC channels for the ENOB calculation, i.e. channel B.

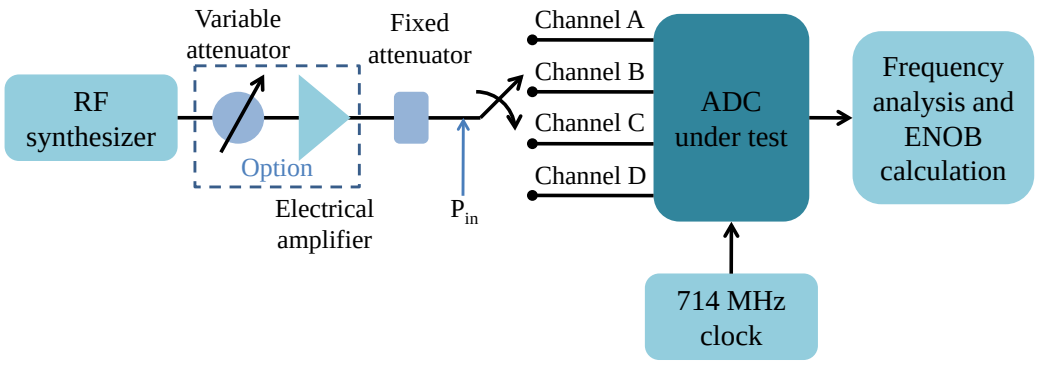


Figure II.30: Setup for ADC ENOB characterization.

Fig. II.31 presents the evolution of ENOB as the function of ADC input power without using an electrical amplifier (Fig. II.31(a), case 1) and with using the electrical amplifier (Fig. II.31(b), case 2). In this study, two RF frequencies (100 MHz and 89.25 MHz) are used in which one (89.25 MHz) is an integer fraction of the sampling frequency. It can be seen that the two RF signals show a similar evolution with negligible difference. In case 1, when the ADC input power is increased from -2 dBm to 10 dBm, the ENOB is also increased due to the improved SNR of the signal. From 10 dBm to 12 dBm input power, the ENOB is constant around 6 bits before decreasing with the increase of input power. It can be explained that the input power range of (10 - 12) dBm gives the best intrinsic SNR. When increasing the power, the RF synthesizer has to use an internal amplifier to get sufficient output power, resulting in more additional noise. As a consequence, the ENOB will be deteriorated. The idea behind case 2 is to quickly reach a constant output ENOB with

lower input power than in case 1. As shown in Fig. II.31, an input signal power of 6 dBm is required to achieve a constant ENOB value of about 5.6 bits. Actually, this ENOB value in case 2 is smaller than in case 1 due to the amplifier having a large bandwidth (more than 10 GHz), leading to more additional noise. However, it can be relaxed by using an amplifier with bandwidth of about 1 GHz that is close to sampling frequency. Unfortunately, it was not available at the time of the experiment. This ENOB is decreasing for signal power levels above 16 dBm.

The results in case 2 show that in the LOS-based monitoring experiment we can get a better reconstructed signal quality with low photodetected currents at the output of the I and Q components. By optimizing the electrical amplifier parameters (i.e. bandwidth, gain), we can obtain more dynamic range of the input signal even though the input power is small. The insets of Fig. II.31 present the spectra of 100 MHz RF signal in two cases. It can be observed that the dynamic range is improved by about 1 dB with an electrical amplifier regardless of the additional amplifier noise.

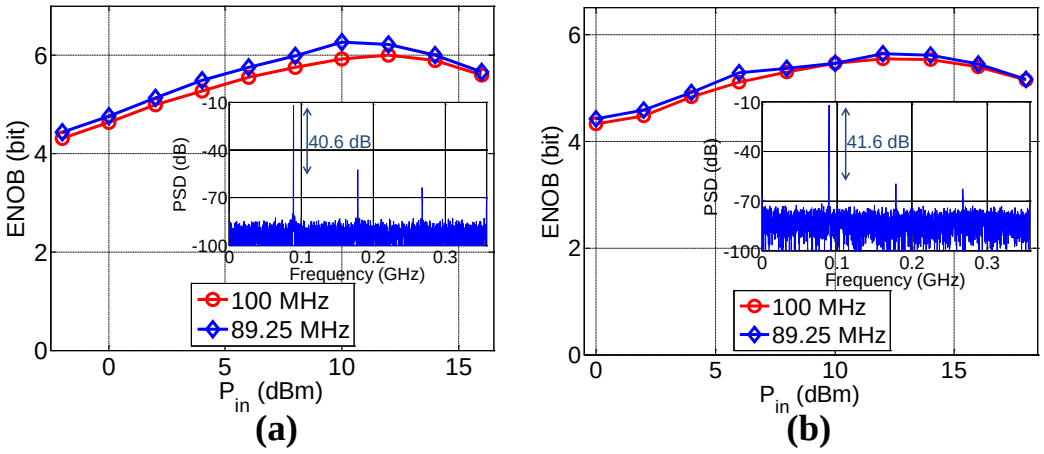


Figure II.31: Evolution of calculated ENOB as the function of input signal power (a) without and (b) with electrical amplifier.

As aforementioned in Section 4.1, an ENOB of 6 bits is sufficient to recover the signal in the LOS-based monitoring technique. Therefore, the impact of the ADC ENOB in current LOS-based monitoring configuration can be negligible as the optimum ADC ENOB values are 6.1 bits (Fig. II.31(a)) and 5.6 bits (Fig. II.31(b)). Up to this point, the electrical parameters of our LOS setup seem to be good enough to reconstruct the considered signal. These parameters do not seem to be the cause of the observed amplitude fluctuations of our reconstructed signals (i.e. Fig. II.19). In the following sections, we study if the LO source parameters can be at the origin of the reconstructed signal degradation. More precisely, the timing jitter, OSNR and extinction ratio properties are investigated.

4.2 Impact of pulsed-LO parameters

In order to evaluate what parameters of the LO could be at the origin of the observed reconstructed signal degradation, we firstly use the model developed in Section 4.1 to qualitatively evaluate the impact of different pulsed-LO parameters on the reconstructed signal. In each evaluation, if one parameter is studied, other parameters are set to perfect values. For instance, if the pulsed-LO signal-to-noise ratio is investigated, only the pulsed-LO signal-to-noise ratio is varied. No noise is added to the signal and no limited extinction ratio of pulsed-LO is generated. Based on these numerical investigations, the most likely cause for the signal degradation (observed in Section 3.5 for example) will be experimentally studied in Section 4.2. More specifically, the pulsed-LO extinction ratio is found to have a significant impact on the reconstructed signal. The analytical and additional numerical studies will be also carried out, in Section 4.2, to support the experimental finding.

4.2.1 Impact of pulsed-LO signal-to-noise ratio

We study here how the OSNR of the pulsed-LO can affect the reconstructed signal quality. In this aim, no noise is added to the signal and an extinction ratio of 100 dB is considered. Fig. II.32 presents the eye diagrams of simulated reconstructed OOK (first row) and QPSK (second row) signals using LOS for different pulsed-LO OSNRs of 10 dB (Fig. II.32(a)), 20 dB (Fig. II.32(b)) and 30 dB (Fig. II.32(c)) (measured in an optical bandwidth of 0.1 nm). The eye diagram opens when increasing the pulsed-LO OSNR especially on 1-levels (in the case of OOK). This observation is expected from the quadratic relation of (eq. II.8) involving the cross product between signal and noise: this beating term will be more important at higher input signal, meaning on 1-levels. The eye diagram degradation due to the OSNR limitation is thus similar to the one observed in our LOS experiment (i.e. in Fig. II.19). However, we have measured a pulsed-LO OSNR in 0.1 nm better than 25 dB (Fig. II.8); which leads to a very small eye diagram degradation according to our simulations. As a consequence, the pulsed-LO signal-to-noise ratio cannot fully explain the degradation of our reconstructed signal.

To understand the origin of the strong variations observed in our experiments, LO timing jitter is investigated in the following part.

4.2.2 Impact of pulsed-LO timing jitter

In this study, LO extinction ratio is 100 dB, and no noise is added on the signal and the LO. To be able to simulate the pulsed-LO timing jitter, a random shift of the sampling position is simulated. The random movement follows a Gaussian distribution. For 11.432 GHz pulse repetition rate (Section 3.1), each interval between two simulated samples corresponds to $1/(11.432 \cdot 10^9)/128 = 680$ fs. Fig. II.33 shows the simulated reconstructed eye diagrams of OOK signal for different timing jitters. Firstly, the eye diagram without jitter is plotted

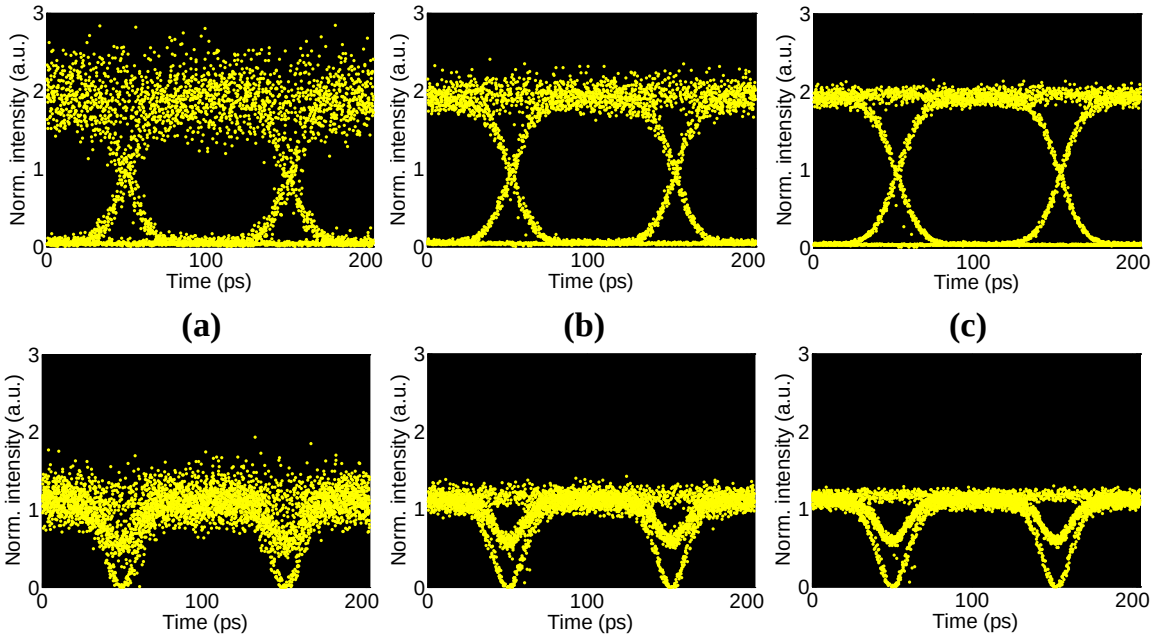


Figure II.32: Examples of OOK and QPSK eye diagrams with different pulsed-LO OSNRs: a) 10 dB, b) 20 dB and c) 30 dB.

in Fig. II.33(a). Then, the eye diagrams corresponding to a jitter of 600 fs (Fig. II.33(b)), 1.2 ps (Fig. II.33(c)), 3 ps (Fig. II.33(d)) and 5 ps (Fig. II.33(e)) are also presented. When the jitter increases, the eye diagram transition points get noisy. However, the noise at the 1-level does not seem to be significantly affected. Moreover, the required timing jitter to observe a significant degradation in this simulation is quite higher than the overall timing jitter of our setup which does not exceed 1 ps based on the reported jitter values of both optical and electrical parts.

Consequently, the cause of strong fluctuations on 1-levels of the reconstructed signal of our LOS (see Fig. II.19) should come from another parameter.

4.2.3 Impact of pulsed-LO extinction-ratio

In this part, we evaluate the impact of the limited extinction ratio of our LO on the reconstructed signal. The extinction-ratio (ER) of the pulsed-LO is defined as the ratio between the sampling pulse and the residual sub-pulses after the repetition rate down conversion. In these simulations, the signal and LO OSNR is assumed to add no noise and no timing jitter is considered. Fig. II.34 shows the eye diagrams of OOK signal (first row) and of QPSK signal (second row) for different pulsed-LO ERs of 100 dB (Fig. II.34(a)), 20 dB (Fig. II.34(b)) and 15 dB (Fig. II.34(c)). It can be observed that the variation of the reconstructed signal, especially on 1-level in OOK eye diagram, is increasing with the decrease of pulsed-LO ER, showing the significant impact of the pulsed-LO ER on the recovered signal. This point could explain our experimental results of Fig. II.19. Typical reachable extinction ratio of

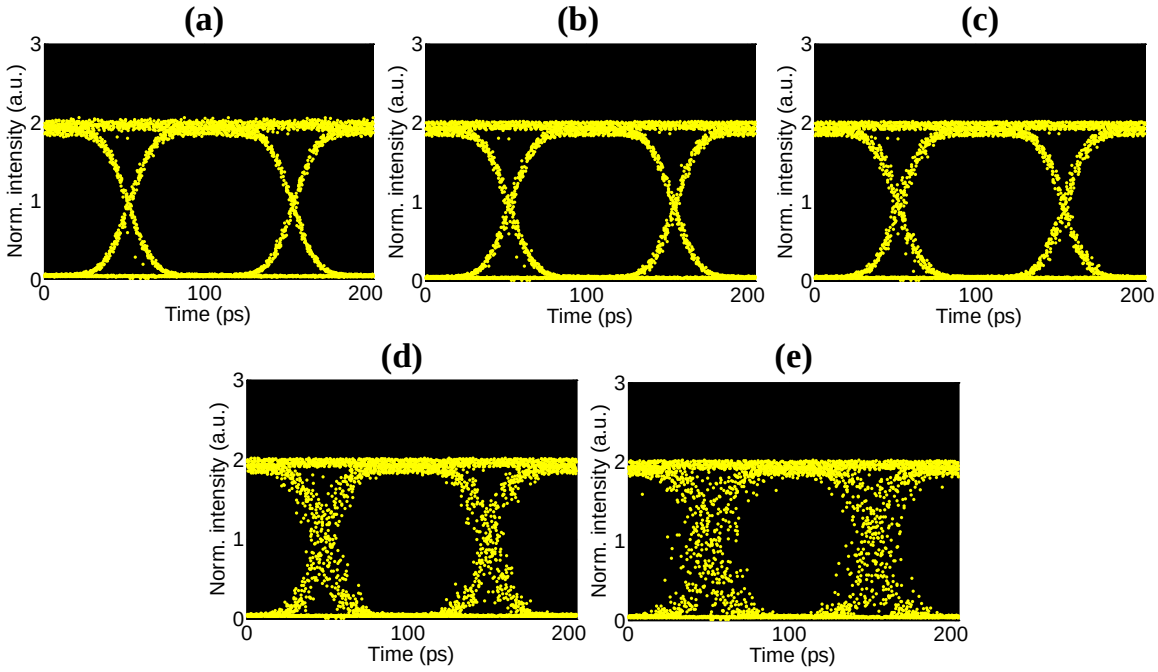


Figure II.33: Simulated NRZ-OOK eye diagrams (a) without jitter and with jitter of (b) 600 fs; (c) 1.2 ps; (d) 3 ps and (e) 5 ps.

the MZM is of the order of 20 dB which already leads to a noticeable degradation of the eye diagram. As a consequence, we think that our technique which consists of decreasing the LO repetition rate using a MZM in order to limit the required LOS detection bandwidth leads to a limitation of the reconstructed eye diagram quality.

Next study aims at quantifying the required LO extinction ratio in order to reconstruct properly the signal using LOS technique.

4.2.4 Experimental study of pulsed-LO extinction ratio impact

Investigated case

The considered scheme is represented in Fig. II.35. All the elements of the LOS-based monitoring described earlier are present. The only difference comes from the generation of the signal and of the LO. Indeed, in order to simplify the further analytical analysis, the particular case of synchronous and homodyne signals is considered. Homodyne means that the same laser is used for constructing the signal and the pulsed-LO. Synchronous means that each pulse of the LO will beat with the same portion of the signal. Consequently, in this particular case, an optical delay line is inserted in the LO branch in order to vary manually the delay between signal and LO and to be able to fully reconstruct the signal. We consider in this analysis that this approach is equivalent to the asynchronous case.

In this experiment, the 10 GHz MLL laser introduced in Section 3.1 was used as it was the only available LO source at the time of the experiment. The signal is split via an

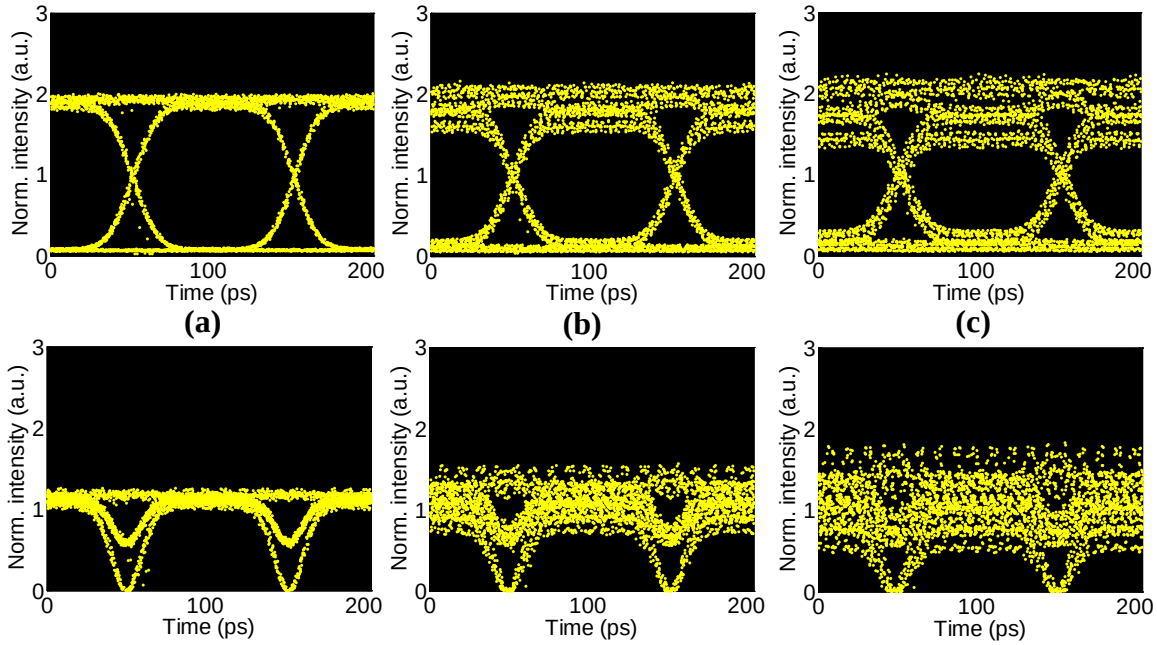


Figure II.34: Impact of different pulsed-LO extinction-ratios of a) 100 dB; b) 20 dB; and c) 15 dB on the reconstructed OOK (first row) and QPSK (second row) signals.

optical 50-50 coupler. One arm of the coupler constitutes the pulsed-LO whose repetition rate is reduced down to 660 MHz by means of an external modulator and a programmable electrical pulse train generating one "1" for each fifteen "0" as we do in previous LOS setup. Next, the sampling signal is amplified and filtered by an optical band-pass filter (OBPF) with 3-dB bandwidth of 5 nm. It then goes through an optical delay line (ODL) in order to vary the delay, τ, between signal and LO and it is finally coupled to the LO port of the 90° optical-hybrid. The second arm of the coupler constitutes the signal under test (SUT); it is modulated through a second MZM using the inverse data stream compared to the one modulating the LO. Electrical signals driving both modulators are synchronous. The signal is then amplified and filtered by an OBPF with 3-dB bandwidth of 0.25 nm in order to obtain a SUT pulse larger than the sampling pulse; the resulting pulse duration is 25 ps (at full width half maximum FWHM). Subsequently, the SUT is coupled into the S port of the 90° hybrid-unit. An example of the temporal traces of both signals is represented in Fig II.36, in which the SUT and the pulsed-LO have no delay with respect to each other ($\tau = 0$); the pulse time-slot of T and the repetition rate of T_S. The in-phase and quadrature output electrical terms at the I and Q ports are then sampled by an ADC card and followed by post-processing. By this way, we obtain variable (up to 20 dB) SUT and pulsed-LO extinction ratios (ER_S and ER_{LO}) by adjusting the modulators bias. We now can study the impact of ER_{LO} on the reconstructed signal (ER_{out}).

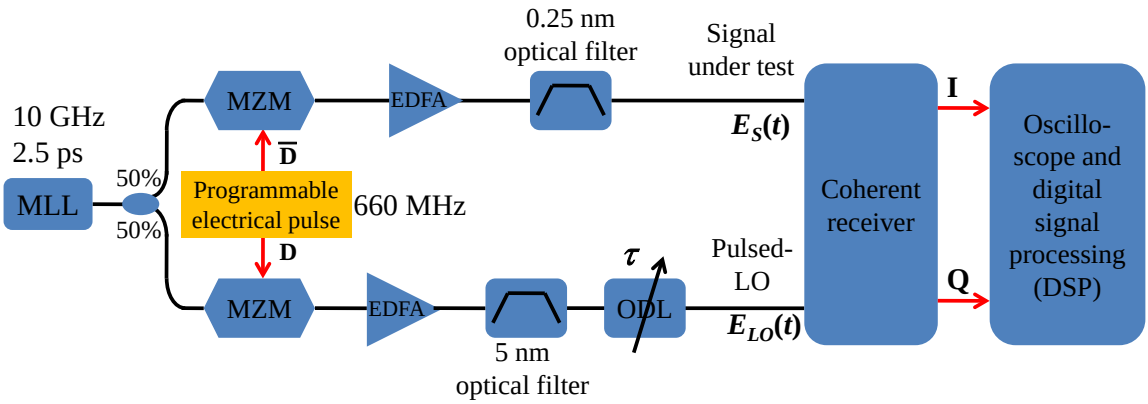


Figure II.35: Setup for modeling and characterizing the impact of ER_{LO} in linear-optical sampling.

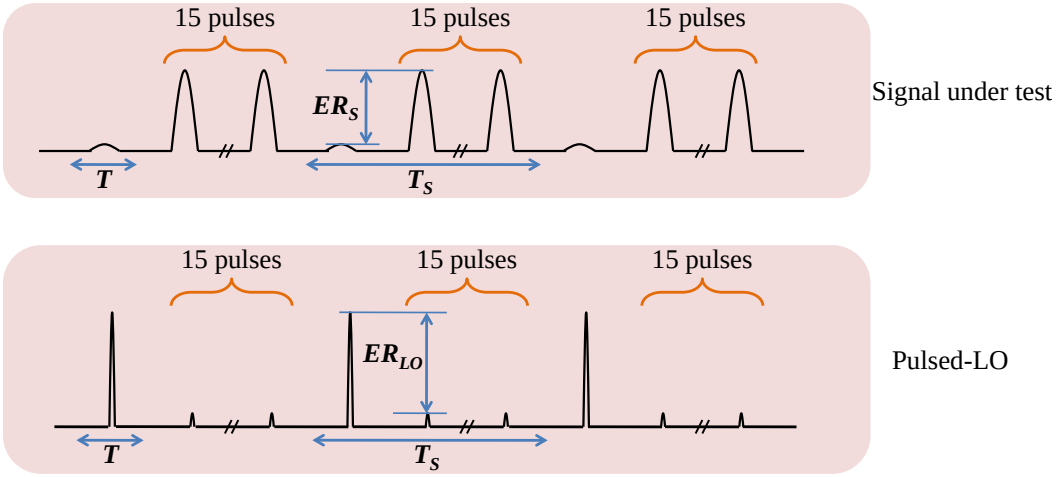


Figure II.36: Temporal traces for the signal under test and the pulsed-LO with delay $\tau = 0$. $ER_{S(LO)}$ is the extinction-ratio of the SUT (pulsed-LO). T_S and T are the repetition rate and the pulse time-slot, respectively.

Analytical analysis of the studied case

We calculate the resulting intensity of samples of this synchronous LOS by assuming that varying manually the time delay is equivalent to an asynchronous LOS. The analytical calculation of the sample intensity for a given delay allows us to find an expression of the output signal extinction ratio as a function of the input signal and LO extinction ratios.

In our theoretical study, noise effects are ignored. Following the formalism and assumptions employed in [11], the intensity of the reconstructed signal (as in (II.8)), including the filtering effects of the bandwidth-limited receiver and unit responsivity of photodiodes, is expressed as

$$I(t,\tau) = 4\left|\left[E_S(t)E_{LO}^*(t-\tau)\right] \otimes h(t)\right|^2, \tag{II.20}$$

where $h(t) = f_c \mathrm{sinc}(f_c t)$ is the impulse response (assumption of using rectangular filters)

of either photodiodes or ADCs (the one with lowest bandwidth).

We consider real signal and LO fields in this study for calculation simplifications. The corresponding amplitudes for the interacting signals are defined as

$$E_S(t) = \sum_{n=-\infty}^{\infty} \left[\sqrt{\frac{P}{ER_S}} f(t - nT_S) + \sum_{l_1=1}^{k-1} \sqrt{P} f(t - nT_S - l_1 T) \right], \tag{II.21}$$

$$E_{LO}(t) = \sum_{m=-\infty}^{\infty} \left[\delta(t - mT_S) + \sqrt{\frac{1}{ER_{LO}}} \sum_{l_2=1}^{k-1} \delta(t - mT_S - l_2 T) \right], \tag{II.22}$$

where $f(t)$ defines the pulse-shape of the amplitude envelope $|E_S(t)|$, index m and n indicate the number of periods T_S in the sampling train and the SUT respectively with $m = n = 0$ for one period of E_S and E_{LO}, while T defines the pulse time-slot. P is the peak power of the SUT and $k = T_S/T$ gives the total number of pulses within one period for E_S and E_{LO}. To simplify the analysis, one period of E_S and E_{LO} corresponding to $m = n = 0$ is used for the following calculation.

For this analysis, it is assumed that $f(t) = sech^2(t/T_1)$ with T_1 as the full-width at $1/e$ of the maximum of the intensity profile. By using (II.20), (II.21) and (II.22), the intensity of the low level at the delay τ can be expressed as

$$\begin{aligned} I^0(t,\tau) = {} & \tfrac{P}{ER_S T_c^2} \mathrm{sech}^2\left(\tfrac{\tau}{T_1}\right) \mathrm{sinc}^2\left(\tfrac{t}{T_c} - \tfrac{\tau}{T_c}\right) \\ & + \sum_{l=1}^{k-1} \tfrac{P}{ER_{LO} T_c^2} \mathrm{sech}^2(t - lT - \tau) \mathrm{sinc}^2\left(\tfrac{t}{T_c} - \tfrac{l}{(T_c/T)} - \tfrac{\tau}{T_c}\right), \end{aligned} \tag{II.23}$$

where $T_c = 1/f_c$. Considering the right-hand side of (II.23), the first term represents the magnitude of the symbol under test while the second one represents an additional contribution consisting of the product of neighboring symbols from the SUT with the corresponding sub-pulses of the pulsed-LO. It is seen that the signal after detection is modified due to the impulse-response of the receiver bandwidth f_c, which defines the total number of sub-pulses contributing to the current sampling instant as $k - 1 = (T_c - T)/T$.

Finally, the intensity (normalized with respect to the peak power of SUT, P) of the reconstituted SUT $\overline{I(\tau)}$ is obtained by integrating (II.23) over the interval $t \in [0; T_S]$. This normalized intensity is given by (II.24), in which the variable τ in this equation corresponds to the position of samples. The first line represents the low level of the SUT, while the second line represents the high level. It is worthwhile to point out that there are two main contributions to $\overline{I(\tau)}$: a) the ER of the symbol under test; and b) the product between neighboring symbols of the SUT and the ER of the sampling signal ER_{LO}.

$$\overline{I(\tau)} = \begin{cases} \left[\frac{1}{ER_S} + \frac{1}{ER_{LO}}(k-1)\right] \mathrm{sech}^2\left(\frac{\tau}{T_1}\right), & \text{if} \quad \tau \in \left[-\frac{T}{2}, \frac{T}{2}\right) \\ \sum_{l=1}^{k-1} \left[\frac{1}{ER_S ER_{LO}} + 1 + \frac{1}{ER_{LO}}(k-2)\right] \mathrm{sech}^2\left(\frac{\tau - lT}{T_1}\right), & \text{if} \quad \tau \in \left[\frac{T}{2}, T_S - \frac{T}{2}\right] \end{cases}. \tag{II.24}$$

The achievable ER of the reconstructed signal ER_{out}, can be specified as a figure of merit for the sampling system. It is defined as the ratio of the high level to the low level, represented in (II.20) at $\tau = T$ and $\tau = 0$, respectively, and is given by

$$ER_{out} = \frac{1 + ER_S ER_{LO} + (k-2)ER_S}{ER_{LO} + (k-1)ER_S}, \tag{II.25}$$

which puts in evidence the impact of ER_{LO} in the reconstruction of the SUT as it will be seen in following results.

Results and discussion

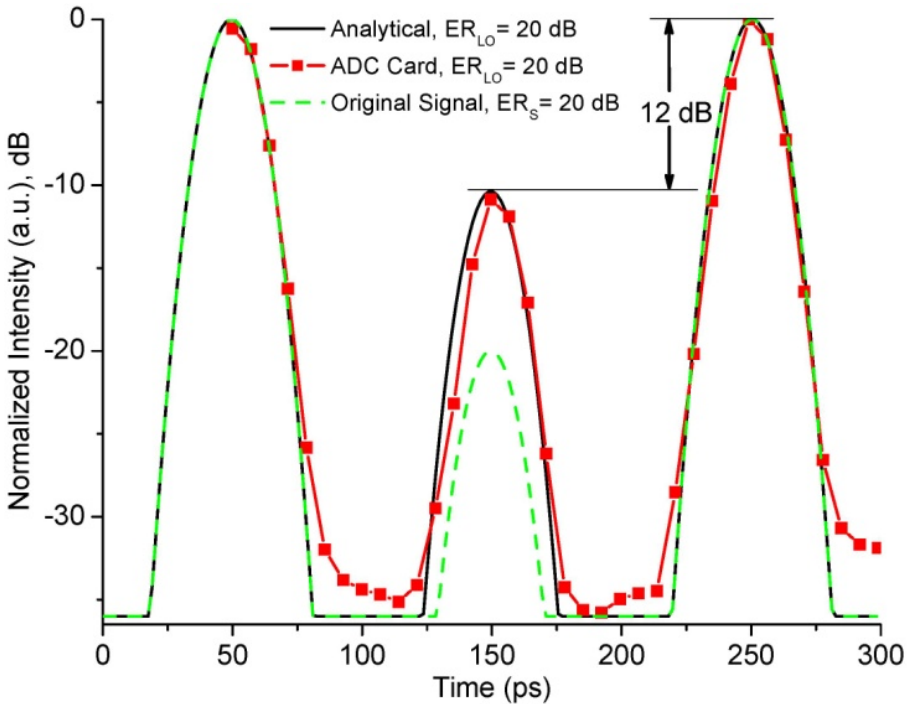


Figure II.37: Analytical prediction of $\overline{I(\tau)}$, with $ER_{LO} = 20$ dB, validated by experimental data.

The intensity of the reconstructed signal for the sequence of 1, 0, 1, as expressed by (II.24), is represented in Fig. II.37 for ER_{LO} corresponding to 20 dB. Also in the figure, experimental data of the sampled sequence have been included for comparison. The dash-line represents the analytical calculation of SUT with the assumption of an intrinsic ER of pulsed-LO at -35 dB, whereas the continuous line corresponds to the analytical calculation of the reconstructed SUT through the LOS. Experimental result is represented by square symbols. The good matching of the numerical and experimental results, shows that numerical simulations can give a good prediction of ER_{out}. Indeed both give a reconstructed ER_{out} of 12 dB. The small difference in noise floor between the experimental measurements and the theoretical calculations is due to the limited dynamic-range of the ADC card used

to sample the electrical signals delivered by the balanced-photodetector in the experimental case. Thanks to this agreement, the validation of our simulation model and analytical calculation are confirmed.

To understand the impact of ER_{LO} in the reconstruction of the sampled signal, ER_{out} is evaluated from (II.25) using the following parameters: ER_S is changed from 10 to 25 dB with 5 dB steps, while ER_{LO} varies from 0 to 60 dB. $(k-1)$, representing the number of sub-pulses contributing to the sample instant of the symbol under test, as schematically shown in the inset of Fig. II.38, is estimated at a value of 11 from $k-1 = (T_c-T)/T = 1.1ns/0.1ns$. In other words, the contributing sub-pulses fall within the electrical detection bandwidth shown as the dashed line in the inset of Fig. II.38. To validate this statement, a numerical simulation including the effect of the limited-bandwidth (either the photodiodes or the ADCs) has been carried out.

The evolution of the reconstructed signal extinction ratio ER_{out} as a function of ER_{LO} based on the validated model is plotted in Fig. II.38 for different values of SUT extinction ratio ER_S. In this graph, the circles represent the analytical calculation and the triangles the numerical simulation. Numerical simulation and analytical calculation reveal negligible differences. From the figure, it can be observed that the sampled signal is completely reconstructed when ER_{LO} goes above 35 dB, whereas for lower values, a less accurate representation of the SUT is obtained. For ER_S below 10 dB, the ER_{LO} requirement relaxes to about 20 dB. The stringent requirements for ER_{LO} are due to the additional contribution to the sampled symbol, which comes from the interaction between neighboring symbols and the corresponding sub-pulses of the pulsed-LO with magnitude $1/ER_{LO}$ (as shown in the inset of Fig. II.38).

The requirement of pulsed-LO ER is unfortunately limited by the MZM ER which is about 20 dB. As a consequence, the repetition rate down-conversion solution for the pulsed-LO can lead to ER values of the reconstructed signal varying between 9 and 12 dB when the ER of the SUT varies between 10 and 25 dB. This hard ER requirement could be relaxed by using *e.g.* an electro-absorption modulator (EAM) with ER better than 30 dB, or possibly with a second MZM stage. In this case, it would be possible to properly reconstruct the analyzed signal with ER levels up to 20 dB. This analytical model presents a useful and simple tool for predicting the operational limits of a linear optical sampling technique, in terms of extinction-ratio. The study of pulsed-LO extinction-ratio supplies an additional important requirement on the optical part with respect to earlier works [204] in the implementation of linear optical sampling system.

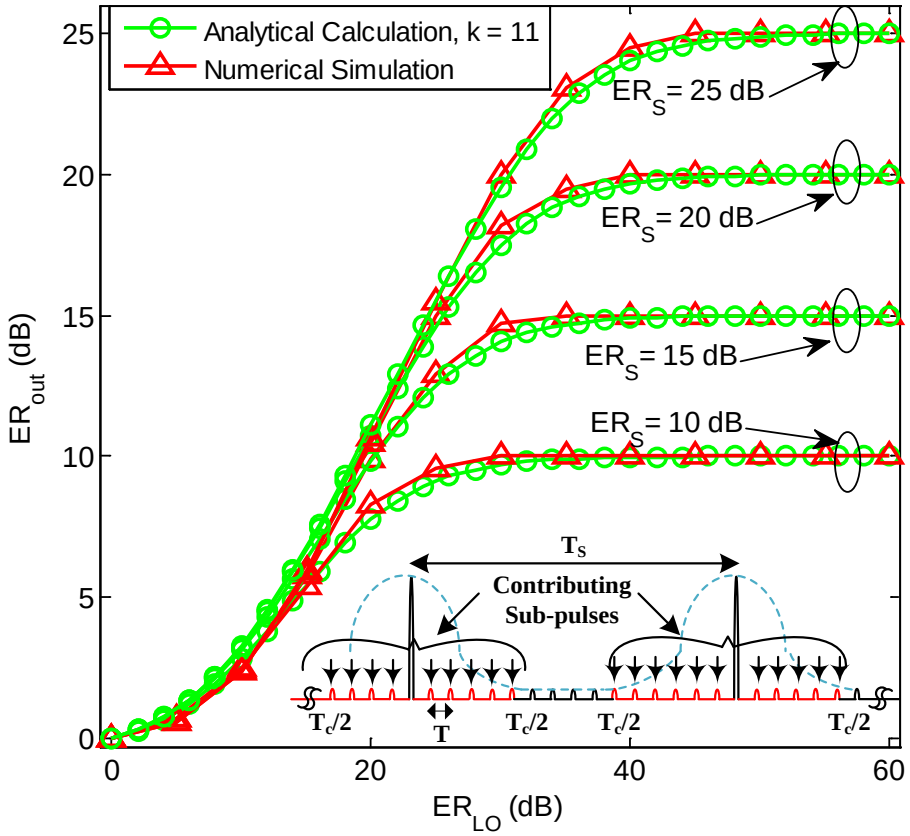


Figure II.38: ER_{out} evolution as a function of ER_{LO} for the different values of ER_S.

5. Conclusion

In this part, linear optical sampling (LOS) has been studied and shown as a promising technique for monitoring very high bit rate complex optical signals with low cost components comparing to current commercialized products. The idea behind this technique is the use of a short-pulse train, namely pulsed-LO, at low repetition rate to sample the high bit rate optical signal (i.e. $M-$PSK, $M-$QAM). These two signals are then mixed into a 90° optical hybrid which creates two components (in-phase and quadrature) in each state of polarization. Based on these two components, the full picture of data signals can be reconstructed in terms of eye diagram and constellation, after a digitization (ADC) and signal processing (DSP) stage in an equivalent time process.

The built prototype used as sampling source, an optical frequency comb generator based short pulse train at 11.4 GHz presenting 5 ps pulses and a low timing jitter (order of tens fs). This pulse train is then down-converted to a lower repetition rate of 714 MHz using a Mach-Zehnder modulator (MZM), to form the pulsed-LO. This technique offers the possibility to use relatively high repetition rate sampling pulse train with better stability than lower repetition rate sources together with relaxed constraints on optoelectronic converters and ADC bandwidths thanks to the down-conversion. The choice of certain DSPs is justified concretely in this part with additional DSPs for signal representation. The prototype is validated using several kinds of optical signals from the simplest form (OOK) to more complex ones (QPSK, 16-QAM). The successful reconstruction of data signal demonstrates the effectiveness of the proposed LOS system.

Due to the imperfection in recovering the data signal, several parameters in both optical and electrical parts are investigated for their impacts. Particularly, the impacts of limited pulsed-LO extinction-ration (ER), OSNR, timing jitter in the optical part are studied, pointing out its significant influence on the reconstructed signals. In current LOS configuration, the pulsed-LO ER inherent to the limited ER of the MZM has been proved for its significant impact on the signal reconstruction. The impact of pulsed-LO ER is analytically, numerically and experimentally demonstrated in a simple homodyne case. The results show that at least 35 dB pulsed-LO ER is required to be able to completely recover the signals. This cannot unfortunately be obtained with the current MZM ER (in order of 20 dB). An electro-absorption modulator (EAM) could be a good candidate with potential ER better than 30 dB, however, it is presently unavailable on the market for high operation speed.

Another possibility could be explored, involving a second MZM stage. Furthermore, several parameters in designing the electrical part, in which the ADCs are the heart, is found to have a significant impact on the recovered signal's quality. More specifically, the impacts of the limited-BW (induced by the opto-electronic interfaces and ADC), the ADC integration time and ADC effective number of bits (ENOB) are experimentally and numerically investigated with OOK and QPSK signals. It is found that 0.2 ns integration time of ADC (maximum 5 GS/s equivalent), 6 bits ENOB and at least 2 GHz BW are needed to be able to get a good 10 Gbaud signal reconstruction with the chosen pulsed-LO. In future, the very high bit rate signal and high modulation level will be used to investigate the LOS system limitation in which the effects of jitter and ENOB become more critical.

In the next steps, DSPs in LOS are also needed to be optimized to ensure the equivalent time operation. Some of developed DSPs for LOS application gave rise to solutions for high bit rate signal transmission that will be studied in the next part. More specifically, the solutions for IQ imbalance compensation in single carrier optical coherent transmission are proposed and investigated. The algorithms for carrier recovery, which are the indispensable part in current optical coherent systems, are also discussed for their performance and implementation complexity. Finally, the application of these algorithms in an optically regenerated link is studied and experimentally demonstrated in the next part.

Part III

DIGITAL SIGNAL PROCESSING FOR HIGH BIT RATE SIGNAL TRANSMISSION

Digital signal processing (DSP) is required in the coherent detection-based high bit-rate transmission systems. Thanks to DSP, the linear and possibly nonlinear impairments can be completely compensated for [97]. As stated earlier, our study is focused on the compensation of linear impairments which come from either the imperfection of devices (i.e. electrical signal generator, modulator) or transmission media (i.e. fiber). In this part, three kinds of impairment, composed of the IQ imbalance, the carrier frequency offset (CFO) and the laser phase noise, will be studied in the context of optical coherent communications. Several proposals for these impairments compensation will also be introduced and validated.

Firstly, two new solutions for the IQ imbalance compensation are proposed and discussed in Section 1. More specifically, the first method is based on the introduction of a new metric which allows us to estimate the phase imbalance and then to compensate for this imperfection (Section 1.1). The second one (Section 1.2) is suggested to integrate the IQ compensator into an equalizer to simultaneously activate several linear impairments compensation (i.e. IQ imbalance, timing skew, chromatic dispersion, polarization mode dispersion). To validate these proposals, the analytical, numerical and experimental studies will be carried out in each section.

Secondly, the algorithm for carrier recovery (both CFO compensation and carrier phase estimation (CPE)) will be investigated in Section 2 with the notable interest on feedforward structure that facilitates the real-time processing implementation. Particularly, recent works on feedforward carrier recovery (FFCR) will be summarized in Section 2.1. Then Section 2.2 will be dedicated to the proposed carrier recovery method based on the circular harmonic expansion (CHE) [231]. This method is explored for the first time in the optical coherent communication context and numerically validated in this section. Some additional improved algorithms are also proposed to be integrated with the CHE method to achieve better carrier recovery performance.

In Section 3, the developed DSP tools are applied, as a case study, in an all-optical regenerative coherent transmission system in which the nonlinear phase noise (NPN) is mitigated using a photonic-crystal-based power limiting function. This innovative solution is shown to preserve the phase of the signal and is hence compatible with phase encoded modulation formats; it is experimentally validated with QPSK signal showing the effectiveness of the proposed power limiter.

1. IQ imbalance compensation in optical fiber communications

Optical fiber transmission provides an exceptional advantage for long-haul communication systems to cope with the increasing global information exchange. For instance, WDM optical transmission systems at 100 Gbit/s per channel above, using polarization division-multiplexed quadrature phase-shift-keying (PDM-QPSK) and coherent detection, have recently been the object of intensive investigations and are already commercialized [232]. As far as the data bit-rate is increased, the system performance is more sensitive to the impairments. Among those, the imperfection of equipments for the advanced modulation format signal generation and reception, resulting in the in-phase/quadrature (I/Q) imbalance, can lead to a drastically reduced performance. As in I/Q down-conversion radio architecture [233], the I and Q components of the optical field should be ideally orthogonal to each other in an optical QPSK coherent system. However, hardware implementation imperfections and finite tolerances of the front-end components such as incorrect bias-points settings in the modulator, imperfect splitting ratio of couplers, unbalanced photodiodes responsivities and non ideal polarization splitters can create amplitude and phase imbalance, known as quadrature imbalance (or IQ imbalance), which destroys the orthogonality of the received signal [73].

In the following studies, the typical works for IQ imbalance compensation in optical communications are summarized in Section 1.1. Our first proposal for the IQ imbalance compensation, based on the introduction of a new metric, is then investigated in Section 1.2. While this solution can work independently of other compensation stage, another IQ imbalance compensation method is proposed to be integrated with the equalizer and studied in Section 1.3. Both proposed methods are numerically and experimentally validated to confirm their effectiveness in optical coherent communication systems.

1.1 State of the art of IQ imbalance compensations in optical communications

Since digital signal processing (DSP) circuits are becoming increasingly faster, providing simple and efficient compensation of linear and, possibly, non-linear impairments, it is im-

portant to assess their potential for the compensation of this detrimental loss of orthogonality in the receiver. Some effort has been dedicated to the compensation of IQ imbalance with the help of DSP. IQ imbalance causing inter-carrier interference (ICI) due to imperfect image rejection in multicarrier direct-detection systems has been analytically and numerically investigated [233]. In multicarrier coherent-detection systems, several frequency domain compensation methods for IQ imbalance have been reported, both for wireless and optical transmission. Those methods include the joint transmitter (Tx) and receiver (Rx) IQ imbalance compensation [234, 235] for the blind compensation class (in the sense that no known training symbols are required), the pilot-assisted method [236], the use of a novel training symbol structure [237], or the joint compensation of phase noise and IQ imbalance [238]. For single carrier optical coherent detection systems, some works exploiting time-domain compensation have been numerically and experimentally carried out. More specifically, IQ imbalance has been corrected in optical coherent quadrature phase-shift keying (QPSK) systems by applying different methods such as the Gram-Schmidt orthogonalization procedure (GSOP) [74], the ellipse correction method (EC) [75], and IQ compensations based on the constant modulus algorithm (CMA) [76] or the statistical properties of received signals [77]. In this thesis, we concentrate on the IQ imbalance compensation in single carrier optical fiber communications. Although the IQ imbalance problem in optical domain can be modeled exactly as in the radio domain, it is necessary to assess the potential of IQ imbalance compensation algorithms, in terms of robustness and performance, in the context of optical communications.

IQ imbalance compensation was proposed to work as either an independent DSP block cascaded with other compensation blocks or as a combination with equalization for a computational simplification. Note that the equalization stage alone cannot compensate for IQ imbalance [76]. The idea of combining IQ imbalance compensation with the equalization stage, which customarily includes polarization demultiplexing, chromatic dispersion compensation and timing recovery, was firstly suggested in [239]. As far as higher modulation format signals (i.e. $M-$QAM) and pulse shaping techniques (i.e. Nyquist filtering) were concerned, the IQ imbalance compensation integrated into an equalizer became an interesting solution. More particularly, the new equalizer structure was proposed in Ref. [239] and numerically validated up to 256-QAM signals. Shortly after that, a nearly similar structure was experimentally demonstrated with PDM-16QAM signal for the compensation in presence of Nyquist filtering [240]. Recently, an optimized version for this equalizer structure has been proposed to well operate in long-haul non-dispersion managed PDM-16QAM coherent system [241, 242]. Other approaches based on the indirect learning architecture (applied to root-raised-cosine (RRC) Nyquist pulses $M-$QAM) [243] or on the use of Turbo demodulation [244] were also studied. Tab. III.1 lists some typical works on IQ imbalance compensation.

In this paragraph, we firstly propose an alternative method for IQ imbalance compensation based on the definition and estimation of a suitable signal-to-noise ratio (SNR) metric

Table III.1: Some typical IQ imbalance compensation proposed in single carrier optical coherent communication systems.

Ref.	Equalizer integration	Modulation format	Year
[74]	No	QPSK	2008
[75]	No	QPSK	2009
[76]	Yes	QPSK	2009
[77]	No	QPSK	2012
[239]	Yes	$M-$QAM	2013
[240]	Yes	Nyquist pulse PDM-16QAM	2013
[78]	No	QPSK	2014
[241, 242]	Yes	PDM-16QAM	2014/2015
[243]	Yes	Nyquist pulse $M-$QAM	2015
[245]	Yes	$M-$QAM	2015

for the detected signal. The first solution, working independently of the equalization step, is theoretically, numerically and experimentally validated in optical QPSK coherent systems. After that, the second solution based on a joint structure of a butterfly equalizer and an IQ imbalance compensator is proposed and experimentally demonstrated in an optical 16-QAM coherent transmission system. It should be noted that we focus only on IQ phase imbalance in our study since amplitude imbalance can be corrected at the hardware level (such as the use of automatic gain controlled trans-impedance amplifiers) [246].

1.2 First proposed method: IQ imbalance compensation based on MSEM

The aim of our research is to develop and analyze a technique for enhancing performance in coherent QPSK optical communication systems in the presence of IQ imbalance. This approach, called Maximum SNR Estimation Method (MSEM), provides an attractive alternative to existing algorithms thanks to its reduced complexity (as shown in Section 1.2.1). Indeed, the proposed method requires simple mathematical functions such as exponentiation or division, whereas the GSOP method requires other more complex mathematical functions such as square root, which makes its implementation in field-programmable gate array (FPGA) circuits more complex. This feature enables the proposed algorithm to be suitable for real-time signal processing. Along with the EC method, our method can predict the phase mismatch between I and Q components, which is not possible with other published approaches [74, 76]. Section 1.2.2 is dedicated to the numerical validation of proposed method. We also experimentally compare the accuracy of our method to the GSOP approach by evaluating the bit-error-rate (BER) and the error vector magnitude (EVM) on the compensated constellations (as shown in Section 1.2.3). The performance of the proposed MSEM method matches that of the GSOP, while its implementation complexity

is reduced.

1.2.1 Principle and analytical study of MSEM

In order to demonstrate how the maximization of the signal to noise ratio metric can lead to IQ imbalance compensation, we first define and calculate the analytical expression of the SNR parameter for a QPSK signal. Without any loss of generality, the QPSK signal at the transmitter is assumed to have unit power. ϕ_S is the information carrying phase of QPSK signal which takes on the values $(2k+1)\cdot\pi/4$, $k=0,1,2,3$ with the same probability. During the transmission over the optical channel, this signal is corrupted by amplified spontaneous emission (ASE) noise, $n = n_C + j\cdot n_S$, that can be modeled as an additive white Gaussian noise (AWGN). The QPSK signal is then detected by mixing with a local oscillator, in a coherent receiver, to extract the in-phase (I) and quadrature (Q) components. The resulting two baseband electrical components are obtained by the sum of quadratic detection in the balanced photodiodes. To simplify our analysis, the carrier frequency offset (CFO) between the transmitter and receiver lasers is assumed to be zero; other noises (i.e. shot noise, thermal noise) are assumed to be negligible; the power of the received samples are normalized to one. We can express the I and Q terms by the following equations

$$I \propto \Re\left\{E_S E_{LO}^*\right\}, \tag{III.1}$$

$$Q \propto \Im\left\{E_S E_{LO}^* \cdot \mathrm{e}^{j\phi_{mis}}\right\}, \tag{III.2}$$

where E_S and E_{LO} represent the fields of the signal (S) and local oscillator (LO) at the inputs of the 90° hybrid in the receiver, $\Re$ and $\Im$ denote the real and imaginary parts of the beating products between S and LO, respectively. ϕ_{mis} represents the phase imbalance which cancels for an ideal dual drive IQ modulator. Imperfections in the implementation of the QPSK modulator can lead to $\phi_{mis} \neq 0$ and consequently to a loss of orthogonality. It should be noted that ϕ_{mis} lies in the range $(-90°, 90°)$ since the maximum phase difference between the projection of the I and Q components on the complex plane is 180°.

The I and Q components can be derived from equations (III.1) and (III.2) as follows

$$\begin{cases} I = \cos\phi_S + n_C \\ Q = \sin\left(\phi_S + \phi_{mis}\right) + n_C \sin\phi_{mis} + n_S \cos\phi_{mis} \end{cases}, \tag{III.3}$$

where n_C and n_S are random Gaussian variables with the same variance σ^2 and assumed to be decorrelated. The MSEM method consists in modifying the complex received signal, $r_x = I + j\cdot Q$, by adding a phase shift, ϕ_{var}, to form a new quantity $Q_n = \Im\left\{r_x \cdot \exp\left(j\cdot\phi_{var}\right)\right\}$ and consider as a new quadrature component. To differentiate with other definition of SNR

(i.e. SNR definition in Section 2.4.3 of Part I), the relevant SNR_r is defined by

$$SNR_r = \frac{\mathbf{E}^2\left(|r|^2\right)}{\sigma^2_{|r|^2}}, \tag{III.4}$$

where $\mathbf{E}(\cdot)$ and $|\cdot|$ are the mean and modulus operators, respectively. $\sigma^2_{|r|^2}$ represents the variance of the square modulus of the modified signal, $r = I + j \cdot Q_n$.

The expected value of $|r|^2$ (calculated in appendix A) is derived by

$$\mathbf{E}\left(|r|^2\right) = \left(\frac{1}{2} + \sigma^2\right) \cdot \left(1 + \alpha^2 + \beta^2\right), \tag{III.5}$$

in which α, β are defined by

$$\begin{cases} \alpha = \sin\phi_{var} + \sin\phi_{mis} \cdot \cos\phi_{var} \\ \beta = \cos\phi_{mis} \cdot \cos\phi_{var} \end{cases}. \tag{III.6}$$

The variance of $|r|^2$ is given by (appendix B)

$$\sigma^2_{|r|^2} = \alpha^2\beta^2 + 2\left(1 + 2\alpha^2 + \left(\alpha^2 + \beta^2\right)^2\right) \cdot \left(1 + \sigma^2\right) \cdot \sigma^2. \tag{III.7}$$

Finally, by substituting (III.5) and (III.7) into (III.4) the expression of SNR_r is achieved

$$SNR_r = \frac{\left(\frac{1}{2} + \sigma^2\right)^2 \cdot \left(1 + \alpha^2 + \beta^2\right)^2}{\alpha^2\beta^2 + 2\left(1 + 2\alpha^2 + (\alpha^2 + \beta^2)^2\right) \cdot (1 + \sigma^2) \cdot \sigma^2}. \tag{III.8}$$

In the noiseless case ($\sigma^2 = 0$), and introducing the expressions of α and β, given by (III.6), the $SNR_{r(wo)}$ is given by

$$SNR_{r(wo)} = \left(\frac{1 + \sin\phi_{var} \cdot \cos\phi_{var} \cdot \sin\phi_{mis}}{\cos\phi_{mis} \cdot \cos\phi_{var} \cdot (\sin\phi_{var} + \sin\phi_{mis} \cdot \cos\phi_{var})}\right)^2. \tag{III.9}$$

Eq. (III.9) shows that $SNR_{r(wo)}$ versus ϕ_{var} exhibits several maxima. In practical implementations, the IQ imbalance due to receiver imperfections should be sufficiently well controlled to remain in the range $[-30°, 30°]$. In this range, $SNR_{r(wo)}$ has only one maximum corresponding to $(\sin\phi_{var} + \sin\phi_{mis} \cdot \cos\phi_{var}) = 0$ or $\sin\phi_{mis} = -\tan\phi_{var}$. When the phase imbalance is small, ϕ_{mis} is close to $-\phi_{var}$.

Since this observation, the MSEM method hence relies on introducing a new parameter ϕ_{var} in the received signal; and the value of ϕ_{var} which maximizes the SNR_r (Eq. (III.4)) will gives the corresponding opposite phase imbalance value. By correcting the received signal with the deduced phase imbalance value ($\hat{\phi}_{mis} = -\phi_{var}$), the IQ imbalance can be compensate for. The following paragraph will evaluate the accuracy of the proposed algorithm.

Fig. III.1 depicts the evolution of the estimated phase imbalance based on the MSEM method as a function of a predefined phase imbalance in the noiseless case. A slight deviation of the estimated phase imbalance compared to the actual one is observed, especially when

the phase imbalance modulus becomes larger than 15°; below this value these estimation error is negligible. The estimated phase imbalance error is only 3.5° at the phase imbalance of ±30°. Note that, due to the deterministic of the algorithm bias at high phase imbalance value, we can correct this issue by simply adding a specific value based on the analytical results.

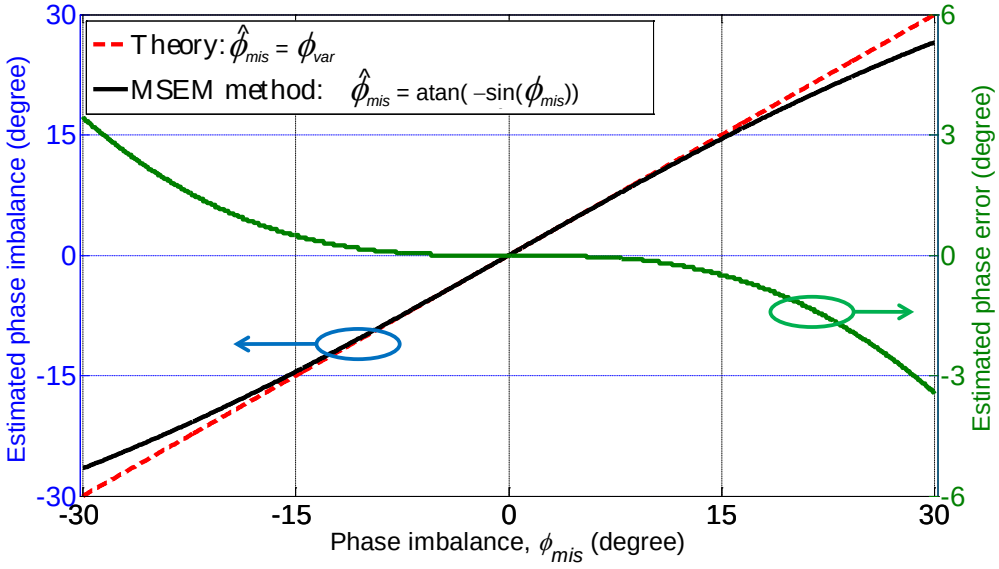


Figure III.1: Analytical prediction of the estimated phase imbalance values for different predefined phase imbalance values using the proposed MSEM method and their corresponding estimated phase error.

1.2.2 Numerical study of the proposed method

In the presence of noise, Eq. (III.8) the derivation of an analytical solution is tedious, we expect to derive a closed-form expression in future work. Actually, if ϕ_0 is a phase value associated to the maximum value of SNR_r in Eq. (III.8), a phase close to this value can be written as $\phi_0 + \epsilon$, where ϵ is small. By using the fist-order of Taylor series expansion, we found that $(SNR_r|_{\phi_{var}=\phi_0} - SNR_r|_{\phi_{var}=\phi_0+\epsilon})$ is not a constant. As a consequence, the maximum value of SNR_r and the corresponding estimated phase imbalance are dependent on the input received samples SNR (defined as the ratio between the received signal power and the noise power).

For this reason, we numerically study the proposed method based on Eq. (III.8). To this aim, the phase imbalance, ϕ_{mis}, is set to $-15°$ and assumed to be unknown at the receiver. Because the phase imbalance in optical coherent detection was assumed to be inside the range of $[-30°, 30°]$, the added phase value, ϕ_{var}, used to estimate the phase imbalance is also varied in this range. The noise is represented by its variance, σ^2, in Eq. (III.8). Considering the unit power of the received signal, the signal SNR (as the ratio between the signal power and the noise power) can be directly linked to σ^2. As a consequence, we can

simply deduce the evolution of SNR_r (Eq. (III.8)) as the function of the added phase, ϕ_{var}, as shown in Fig. III.2, corresponding to different received signal SNR (or noise equivalent). Even though the noise level is varied, the evolution of SNR_r still exhibits one extreme in the considered range of $[-30°, 30°]$, similar to the previous finding in the case of no noise.

More importantly, the added phase, ϕ_{var}, corresponding to the maximum value of SNR_r always happens around the opposite value of predefined phase imbalance, ϕ_{mis}, confirming the criteria used for the phase imbalance estimation (i.e. $\hat{\phi}_{mis} = -\phi_{var}$ which ϕ_{var} makes the SNR_r be maximum). Even in the presence of much noise (SNR = 4 dB), the maximum value of SNR_r still occurs at the added phase value, ϕ_{var}, of 15° which is the opposite value of the phase imbalance, $-\phi_{mis}$, confirming the robustness of our proposed criteria for IQ phase imbalance estimation.

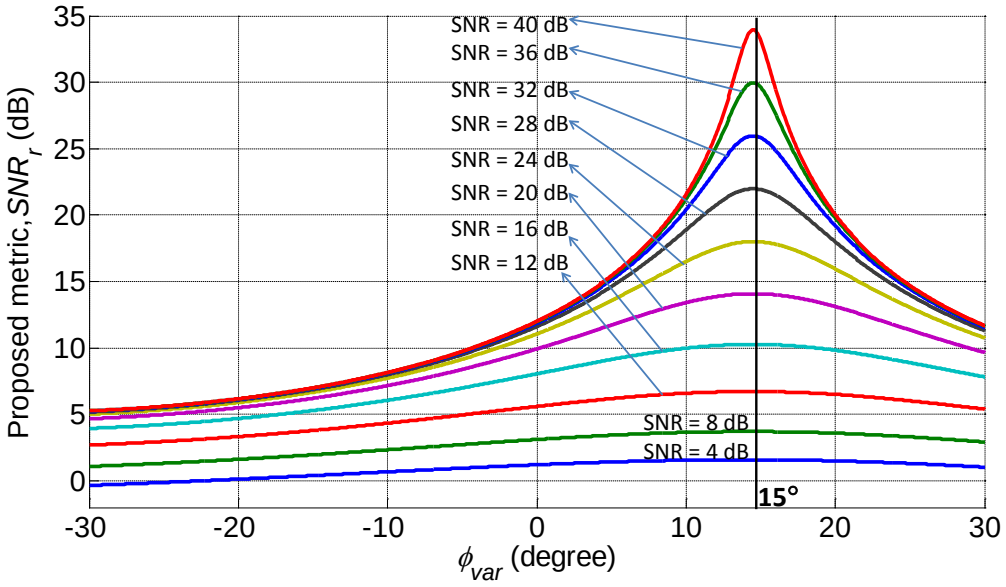


Figure III.2: Numerical calculation the proposed metric, SNR_r, as the function of the variable added phase ϕ_{var} at the $-15°$ phase imbalance.

The robustness of the proposed algorithm (in the presence of noise) is further investigated with different predefined phase imbalances, ϕ_{mis}, based on Eq. (III.8). Fig. III.3 presents the estimated phase imbalance, $\hat{\phi}_{mis}$, as the evolution of the input received samples' SNRs (linked to the σ^2 in Eq. (III.8)), for three predefined phase imbalances of 10°, 20° and 30°.

It can be observed that the estimated phase imbalance exhibits an asymptotical limit (or a fixed value) as the input SNR increases. At 10° phase imbalance, the impact of input SNR on the proposed algorithm is negligible, resulting in no estimation error of the phase imbalance value. As the phase imbalance increases to 20°, an input SNR of 16 dB is required to reach the asymptotical limit. However, the difference between the estimated phase imbalance at low input SNR (i.e. 4 dB) and that at high input SNR (i.e. 20 dB) is small (about 1°). For a phase imbalance of 30° (which is the maximum considered value), up to 20 dB input SNR is needed to achieve the asymptotical limit level. For this high phase

imbalance, the predicted phase imbalance at low input SNR is about 2.5° different from the converged estimated one. Note that, due to the deterministic of the algorithm bias at high phase imbalance value, we can correct this issue by simply adding a specific value based on the analytical results (as aforementioned in previous section).

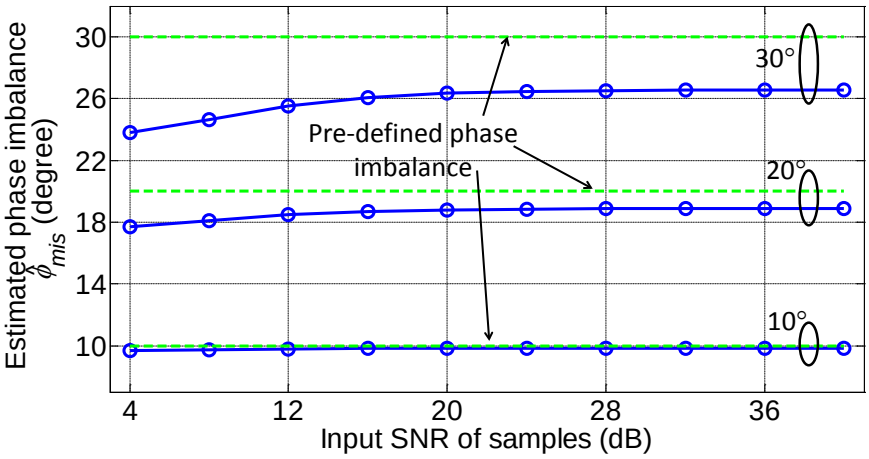


Figure III.3: Estimated phase imbalance under the impact of AWGN. Dashed lines: pre-defined phase imbalances of 10°, 20° and 30°. Solid lines: estimate phase imbalance by using the algorithm.

The proof-of-concept of proposed method will be experimentally validated in optical communication context in the following section. The proposed algorithm is also compared to the Gram-Schmidt orthogonalization procedure (GSOP - a frequent-used method in optical communication systems) with a 20 Gbaud QPSK signal.

1.2.3 Experimental study of the proposed method

a) Setup description

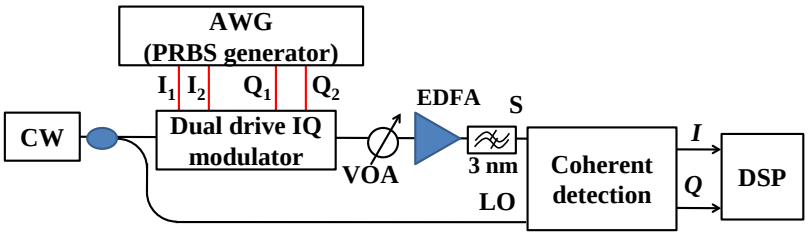


Figure III.4: Experimental setup for characterizing the quadrature imbalance compensation in a QPSK coherent system.

The impact of non-orthogonality between I and Q components is then experimentally investigated using the optical QPSK coherent system shown in Fig. III.4. To simplify the setup and avoid any impact from other functionalities implemented in the digital signal processing (DSP), the laser used as a transmitter is also the LO at the receiver in order

to avoid the carrier frequency offset compensation. The estimated linewidth of this optical source tuned at a wavelength of 1540 nm is about 100 kHz. Two pseudo-random binary sequences (PRBSs) with lengths of $2^{15}-1$ and $2^{23}-1$ are used as inputs to an IQ modulator, resulting in a 10 Gbaud non return-to-zero (NRZ)-QPSK signal at the modulator output. The bit sequences are synthesized using arbitrary waveform generators (AWG). An adjustable phase imbalance can be easily introduced by tuning the voltage applied to the phase-shifter controlling the relative phase between the two arms of the IQ modulator. The use of a variable optical attenuator (VOA) followed by an erbium-doped fiber amplifier (EDFA) and a 3 nm optical bandpass filter (OBPF) allows the adjustment of the optical signal-to-noise ratio (OSNR).

At the receiver side, an optical 90° hybrid (100 Gbit/s DP-QPSK integrated receiver) mixes the QPSK signal and the LO. After the detection by balanced photodiodes with a bandwidth of 32 GHz, I and Q are deduced. Finally, the electrical output signals are acquired by a real time oscilloscope with electrical bandwidth of 16 GHz. After data acquisition at 20 GS/s, post-processing is performed offline using the Matlab environment as in aforementioned procedures in simulation. Note that, for the first experimental step, we focus only on the algorithm validation. The algorithms for IQ imbalance compensation are applied on blocks of 10000 samples. Further study on the block length impact to the algorithm performance will be carried out in future. Moreover, the phase ambiguity is removed by processing the first 5000 samples to minimize the BER. Finally, the decoded bit sequence is compared to the transmitted one to determine the BER over 4 millions samples.

b) Results and discussion

Fig. III.5(a) shows the experimental constellation without IQ imbalance when OSNR is 12 dB (in 0.1 nm). Fig. III.5(b) represents the constellation with 17° phase IQ imbalance. This signal degradation leads to the increase of error probability, as it will be shown later. This degraded signal is processed with the same DSP procedure and IQ imbalance is compensated either using the GSOP or the proposed MSEM method, resulting in the constellations in Fig. III.5(c) and Fig. III.5(d), respectively. The retrieved constellations are similar to the one without IQ imbalance which proves the efficiency of the quadrature imbalance correction. In the next step, our method is experimentally validated by comparing its performance to that of the GSOP method in terms of BER and EVM.

Fig. III.6 depicts the measured BER as a function of received OSNR in different cases. The theoretical curve of an ideal QPSK signal (diamonds) without IQ imbalance is plotted based on the analysis in [25]. The measurement without IQ imbalance (asterisks) matches the theoretical trace within experimental errors. Next, the case of a phase mismatch of 17° without compensation (circles) is plotted in the same figure. As expected, the OSNR is degraded, the penalty being around 1.7 dB at 10^{-3}. BER after phase mismatch compensation using the GSOP (downward-pointing triangles) and the MSEM methods (upward-pointing triangles) is also plotted. In both cases, the IQ imbalance is well compensated, reducing the

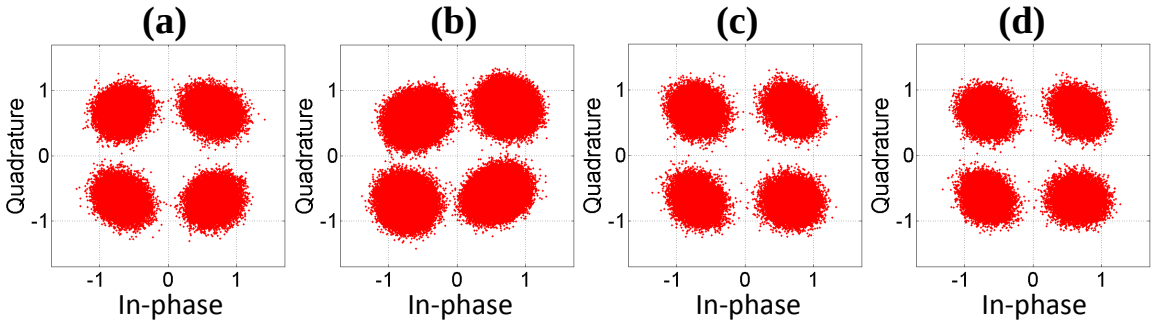


Figure III.5: Experimental QPSK constellations at 12 dB OSNR: (a) without IQ imbalance, (b) with IQ imbalance of 17°, (c) recovered using the GSOP method, (d) recovered using the proposed MSEM method.

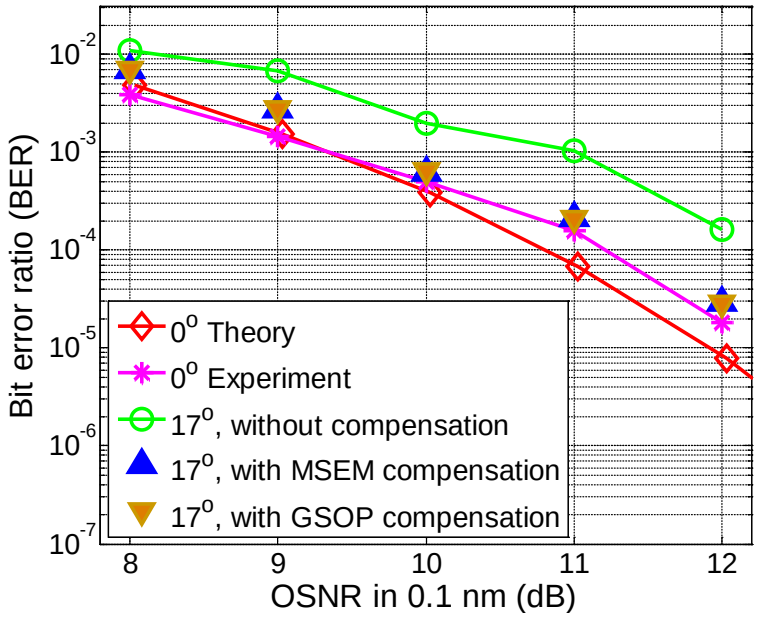


Figure III.6: BER measurement as a function of OSNR (in 0.1 nm) for phase misalignments of 0° and 17° without any correction and with compensation using the GSOP and MSEM methods.

power penalty close to the experimental case without IQ imbalance. The comparison of results using both compensation methods reveals their good agreement. To further investigate the accuracy of the proposed algorithm, the error vector magnitude (EVM) is calculated versus ϕ_{mis} at different OSNR values (Fig. III.7). It can be observed that, as the IQ imbalance increases, and when no compensation is applied (circles), the EVM increases by 40% in the worst case, representing an important deviation from the optimal constellation. With both correction methods - MSEM (stars) and GSOP (diamonds) - and with an OSNR higher than 10 dB, the EVM remains almost constant for a phase misalignment lower than 17°. Both methods can partially compensate for higher misalignments with a reduction of the EVM variation of about 10%. Finally, for an OSNR of 8 dB, the EVM starts to increase

Table III.2: Summary of operations used in two IQ imbalance compensation algorithms (GSOP and MSEM).

Algorithms	**Adder**	**Multiplier**	**Trigonometric function**	**Square-root**
GSOP	Yes	Yes	No	Yes
MSEM	Yes	Yes	Yes	No

above a phase imbalance of 9°.

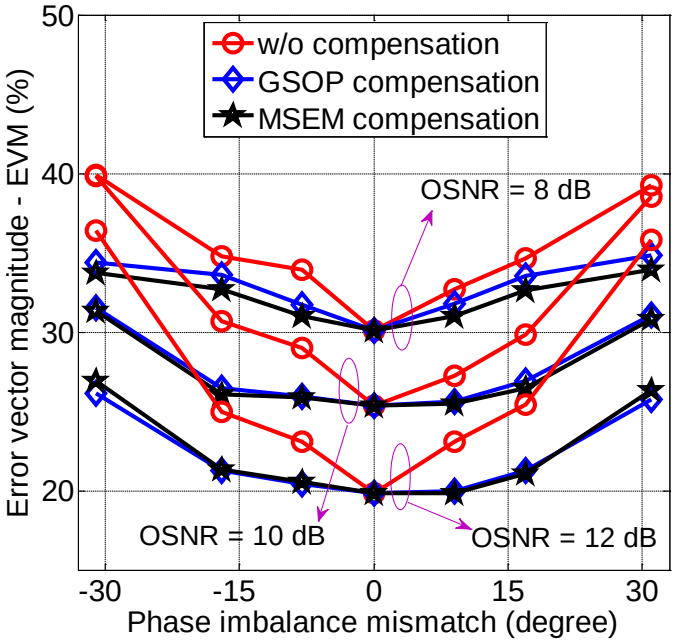


Figure III.7: EVM calculation under the impact of IQ imbalance without (w/o) and with compensation by the GSOP and MSEM methods.

As a conclusion, by theoretical, numerical and experimental studies, we have shown a promising IQ imbalance compensation method in optical QPSK coherent systems. The new method provides a good correction with lower implementation complexity even if the phase imbalance reaches up to 30°. To qualitatively compare the implementation complexity, Tab. III.2 provides some essential operations for both GSOP and the proposed MSEM method.

As far as higher modulation formats are used, the equalizer in DSP is a mandatory part. The following section is dedicated to a proposed joint IQ imbalance compensation and equalization method as a less computational solution.

1.3 Second proposed method: Joint IQ imbalance compensation and equalization

In high bit rate transmission, inter-symbol interference (ISI) is unavoidable due to bandwidth limitations at the Tx/Rx or linear and nonlinear propagation effects during optical fiber transmission. An equalizer stage is therefore required to cancel the ISI. As aforementioned, the equalization stage alone cannot completely compensate for IQ imbalance [73], especially at high IQ imbalance value. The association of IQ imbalance compensation with the equalization stage, which customarily includes polarization demultiplexing, chromatic dispersion compensation and timing recovery, was suggested in [239] as a computational simplification. The proposed solution was a modified version of the conventional adaptive finite-impulse-response (FIR) filters in a butterfly configuration structure. However, the required number of butterfly FIR filter coefficients-sets in this configuration is twice the conventional one, thereby significantly increasing the implementation complexity.

In this section, a novel simple blind adaptive IQ imbalance compensation is proposed based on a decision-directed least-mean-square (DD-LMS) algorithm integrated to a modified butterfly FIR filter configuration, as shown in Section 1.3.1. This method is blind in the sense that no known training symbols are required [233]. As shown later on, only 2 FIR filter coefficients-sets are used in the proposed method, instead of 4 in the existed equalizer based method [239], the time for updating the coefficients and the hardware resources (such as coefficient memories and number of look-up tables) in real time field-programmable gate array (FPGA) platforms is then reduced using this method. The method is firstly validated using a 16-QAM signal in this work (Section 1.3.2), however it can be applied to any single-carrier advanced modulation format, which is a desirable feature in the context of flexible optical transceivers [247]. As the $M-$QAM signal composes of several amplitude levels, the previously used Viterbi-Viterbi carrier phase recovery (usually applied for the $M-$PSK signal with constant amplitude) does not work properly. In this study, another technique for carrier phase recovery is simultaneously achieved during the adaptive coefficients update, thanks to a digital phase-locked loop (DPLL) based on a second-order loop filter [248]. The performance of the proposed IQ imbalance compensation method is experimentally evaluated in terms of bit error rate (BER) measurements (Section 1.3.2) and numerically investigated with optical fiber transmission up to 1200 km in the presence of group velocity dispersion (Section 1.3.3).

1.3.1 Analysis of the joint method proposal

a) Proposed method for IQ imbalance compensation

It should be reminded that we focus only on IQ phase imbalance in our study since amplitude imbalance can be corrected at the hardware level (such as the use of automatic gain controlled trans-impedance amplifiers) [246]. If I_0 and Q_0 are the transmitted in-phase

and quadrature components without IQ imbalance and no noise is considered at the receiver side, the physical (and the real) received signal (after the low-pass filter) in the presence of phase imbalances ϕ_1 (at the transmitter) and ϕ_2 (at the receiver) has the received in-phase (I_1) and quadrature (Q_1) components as follows [249]

$$\begin{cases} I_1 &= I_0 - Q_0 \sin\phi_1 \\ Q_1 &= Q_0 \cos(\phi_1 - \phi_2) - I_0 \sin\phi_2 \end{cases}. \tag{III.10}$$

Considering the IQ imbalance at the transmitter only, so $\phi_2 = 0$, the relation between the transmitted and received signals in the matrix form is represented by

$$\begin{bmatrix} I_1 \\ Q_1 \end{bmatrix} = \begin{bmatrix} 1 & -\sin\phi_1 \\ 0 & \cos\phi_1 \end{bmatrix} \begin{bmatrix} I_0 \\ Q_0 \end{bmatrix} = A \begin{bmatrix} I_0 \\ Q_0 \end{bmatrix}. \tag{III.11}$$

By inverting A matrix, we can write the transformation to be applied to the distorted constellation to restore it

$$\begin{bmatrix} I_0 \\ Q_0 \end{bmatrix} = \frac{1}{\cos\phi_1} \begin{bmatrix} \cos\phi_1 & \sin\phi_1 \\ 0 & 1 \end{bmatrix} \cdot \begin{bmatrix} I_1 \\ Q_1 \end{bmatrix} = \begin{bmatrix} 1 & \tan\phi_1 \\ 0 & (\cos\phi_1)^{-1} \end{bmatrix} \cdot \begin{bmatrix} I_1 \\ Q_1 \end{bmatrix}. \tag{III.12}$$

Fig. III.8(a) and (b) show the two transmitter IQ compensator structures based on (III.12). It is turned out that we should modify the received in-phase (I_1) component based on the received quadrature (Q_1) component to be able to compensate for the transmitter IQ imbalance.

If only IQ imbalance at the receiver is considered, $\phi_1 = 0$ in this case and (III.10) can be represented in the following matrix form

$$\begin{bmatrix} I_1 \\ Q_1 \end{bmatrix} = \begin{bmatrix} 1 & 0 \\ -\sin\phi_2 & \cos\phi_2 \end{bmatrix} \begin{bmatrix} I_0 \\ Q_0 \end{bmatrix} = B \begin{bmatrix} I_0 \\ Q_0 \end{bmatrix}. \tag{III.13}$$

Similar calculated as for the IQ imbalance at the transmitter, the resulting inverse B matrix can lead to the following form

$$\begin{bmatrix} I_0 \\ Q_0 \end{bmatrix} = \frac{1}{\cos\phi_2} \begin{bmatrix} \cos\phi_2 & 0 \\ \sin\phi_2 & 1 \end{bmatrix} \cdot \begin{bmatrix} I_1 \\ Q_1 \end{bmatrix} = \begin{bmatrix} 1 & 0 \\ \tan\phi_2 & (\cos\phi_2)^{-1} \end{bmatrix} \cdot \begin{bmatrix} I_1 \\ Q_1 \end{bmatrix}. \tag{III.14}$$

The relation in (III.14) presenting the two receiver IQ compensator structures is plotted in Fig. III.8(c) and (d). It is observed that to be able to compensate for the receiver IQ imbalance, the received quadrature (Q_1) should be modified based on the received in-phase (I_1) component. Note that, the samples of two received components are used to digitally compensate for the IQ imbalance. Particularly, the inputs of the compensators in Fig. III.8 are presented at the $n-$th sample, with the corresponding outputs $I_1'(n)$ and $Q_1'(n)$. In the case of no noise, $I_1'(n)$ and $Q_1'(n)$ become $I_0(n)$ and $Q_0(n)$ as the samples of the transmitted components.

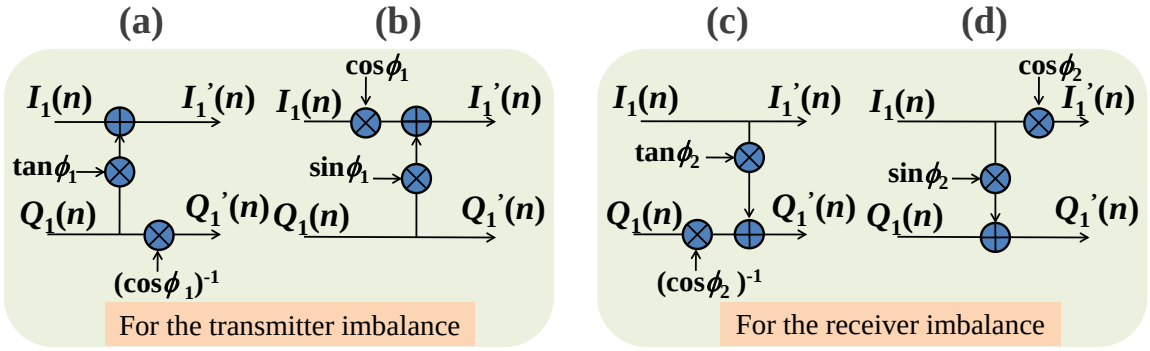


Figure III.8: IQ imbalance compensators for (a), (b) the transmitter imbalance and (c), (d) the receiver imbalance.

Among the state-of-the-art of IQ imbalance compensators in the optical communication context (among the one compensating for IQ imbalance independently of the equalizer stage), the method based on the discussed compensators showed better performance compared to other methods for large phase imbalance values, for example the one in [77].

Moreover, the previously mentioned integration of the IQ imbalance compensator of Fig. III.8 to the equalizer is feasible with low complexity by placing the IQ compensator after the equalizer. The detailed integrated configuration and its proof-of-concept operation are studied in the following sections.

b) Joint IQ imbalance compensation and equalizer

As pointed out in Ref. [239], the conventional equalizer with only 2 coefficient-sets (1 complex coefficient-set equivalent) cannot compensate for the IQ imbalance. In our study, we compare the case where IQ imbalance compensation and equalization are performed successively (henceforth referred to as case 1) with our proposed method where both are performed simultaneously (case 2). In case 1, the structure of Fig. III.8(d) is used to compensate for the IQ imbalance at the receiver side and is followed by conventional butterfly-structured FIR filters for equalization (Fig. III.9(a)). The separate implementation of the IQ compensator could result in increased computational complexity. In particular, the calculation of the values of the amplitude and phase imbalance compensation coefficients requires some trigonometric and square-root operations [77], which can make the implementation in FPGAs more complex. Moreover, the algorithmic error, inherent to the IQ compensator, can be transmitted to the second equalizer stage, leading to the misalignments of filter coefficient-sets.

To overcome this problem, we propose to integrate a new IQ imbalance compensator (Fig. III.9(c)) into the modified butterfly structured-FIR filters (case 2, represented in Fig. III.9(b)). Actually, the structure in Fig. III.9(c) is similar to the structures in Fig. III.8(b) and (c), in the sense that two parameters (K_1 and K_2 in Fig. III.9(c)) are introduced to be able to modify the I or Q components, as done by the trigonometric functions in Fig. III.8(b)

and (c). Based on the adaptive algorithm, the parameters (K_1, K_2) in the compensator (Fig. III.9(c)) can asymptotically converge towards the values deduced by the trigonometric functions in Fig. III.8(b) and (c), depending on where the IQ imbalance is generated.

Furthermore, in contrast to case 1 where the IQ compensator is placed before the equalizer, the additional algorithmic noise is removed in case 2 where the IQ compensator is placed after the equalizer. The parameters C_{in1} and C_{in2} are the inputs of the compensator, whereas the output of the compensator is given by

$$C_{out} = K_1 \cdot C_{in1} + K_2 \cdot C_{in2}, \tag{III.15}$$

where the values of K_1 and K_2 are adaptively updated.

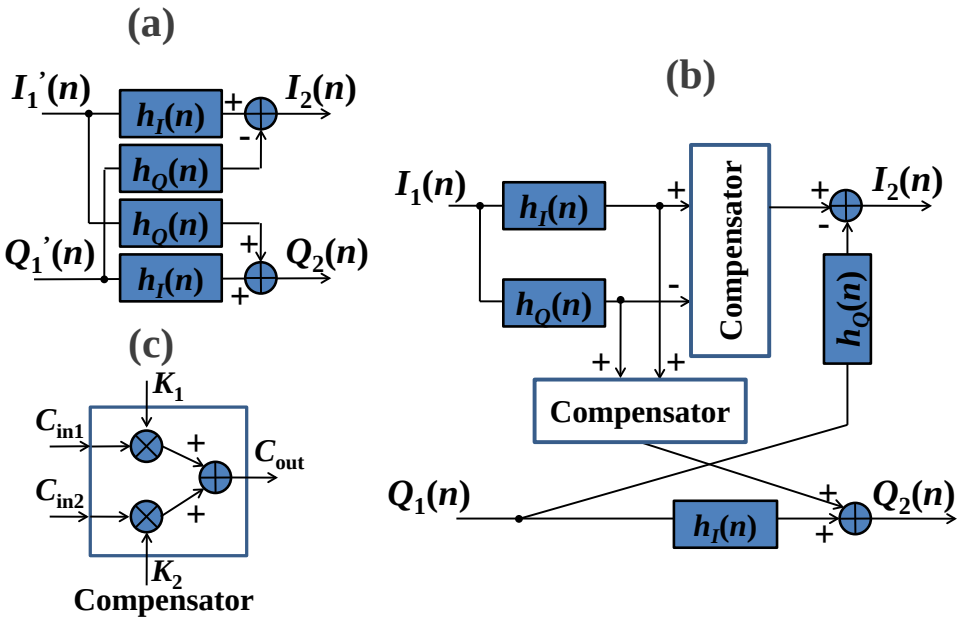


Figure III.9: (a) Conventional butterfly structured-FIR filters. (b) Proposed adaptive FIR filters. (c) IQ compensator structure.

The updating rules for the proposed IQ imbalance compensation are given by

$$K_2(n+1) = K_2(n) + \mu_1 \cdot \Delta K_2(n), \tag{III.16}$$

$$K_1(n+1) = \sqrt{1 - K_2^2(n+1)}, \tag{III.17}$$

in which μ_1 is a constant step-size parameter. ΔK_2 is calculated according to

$$\begin{aligned}\Delta K_2(n) = 2\Re\{ & e_1(n) \cdot [I_1(n) \otimes (-h_Q(n) + j \cdot h_I(n)) \\ & - \tfrac{K_2(n)}{K_1(n)} I_1(n) \otimes (h_I(n) + j \cdot h_Q(n))]^* \},\end{aligned} \tag{III.18}$$

where $\otimes$ and $*$ denote the convolution and complex conjugate operators, respectively. Note that, when the asymptotic convergence is achieved, K_1 and K_2 can be deduced approximately to the trigonometric functions in Fig. III.8(b) and (c) with respect to the phase imbalance. In practical implementations, the phase imbalance should be sufficiently well controlled so that its value remains in the range of $[-30°, 30°]$. This range ensures that a positive value is obtained in the argument of the square root in (III.17).

The real-valued column vectors $I_1(n)$ and $Q_1(n)$ are the inputs to 2 ports of the filters, representing the real and imaginary part of the input signal samples, respectively. If the number of the filter coefficients (the elements in $h_{I(Q)}$) is named as N_c, the corresponding outputs of the butterfly structured-FIR filters, $I_2(n)$ and $Q_2(n)$, are given by

$$I_2(n) = [K_1 \cdot h_I - K_2 \cdot h_Q]^T \cdot I_{1(N_c)}(n) - [h_Q]^T \cdot Q_{1(N_c)}(n), \tag{III.19}$$

$$Q_2(n) = [K_2 \cdot h_I + K_1 \cdot h_Q]^T \cdot I_{1(N_c)}(n) + [h_I]^T \cdot Q_{1(N_c)}(n), \tag{III.20}$$

where $[\cdot]^T$ denotes the transpose operator; $I_{1(Nc)}(n) = [I_1(n), I_1(n+1), ..., I_1(n+N_c-1)]$ and $Q_{1(Nc)}(n) = [Q_1(n), Q_1(n+1), ..., Q_1(n+N_c-1)]$. The outputs of FIR filters are then sent to the direct decision circuit to calculate the error for the adaptive algorithm.

The error after direct decision, $e_1(n)$, is given as follows

$$e_1(n) = d(n) - [I_2(n) + j \cdot Q_2(n)] \cdot \mathrm{e}^{-j \cdot \hat{\theta}(n)}, \tag{III.21}$$

where $d(n)$ represents the direct-decision symbol and $\hat{\theta}(n)$ is the carrier phase estimation obtained from the DPLL, as described in the following section. The filter coefficients are updated in order to minimize the mean square error (MSE), $\mathbf{E}(|e_1^2(n)|)$, after decision.

The tap weights of the proposed structure are then updated according to

$$\begin{aligned} h_I(n+1) = h_I(n) + \mu_2 \cdot \Re\Big\{ & e_1(n) \cdot \mathrm{e}^{j \cdot \hat{\theta}(n)} \\ & \cdot [K_1 \cdot I_1(n) + j \cdot (K_2 \cdot I_1(n) + Q_1(n))]^* \Big\}, \end{aligned} \tag{III.22}$$

$$\begin{aligned} h_Q(n+1) = h_Q(n) + \mu_2 \cdot \Re\Big\{ & e_1(n) \cdot \mathrm{e}^{j \cdot \hat{\theta}(n)} \\ & \cdot [(-K_2 \cdot I_1(n) - Q_1(n)) + j \cdot K_1 \cdot I_1(n)]^* \Big\}, \end{aligned} \tag{III.23}$$

where μ_2 is another step-size parameter. $\Re$ denotes the real part operator and $j = \sqrt{-1}$ is the imaginary unit.

The proposed IQ imbalance compensator can be implemented using 4 multiplications and 2 additions, which adds a small complexity (along with an extra complexity inherent to the update operation in (III.22) and (III.23)) compared to case 1 (4 multiplications and 1 addition only in Fig. III.8). However, as far as the equalization stage is concerned, case 2 brings simplification compared to case 1, because the IQ compensator coefficients in case 2 are adaptively calculated instead of using complex trigonometric functions as in case 1. Moreover, the IQ compensator in case 2 is placed after the equalizer, leading to no

Table III.3: Hardware complexity and computational effort for various IQ imbalance compensation methods.

Methods	**IQ compensator**	**Equalizer part**	**Coefficients-sets number to be updated**
Case 1 (successive structure)	4 MUL; 1 ADD; 2 trigonometric functions	$(4N_c)$ MUL; $(4(N_c\text{-}1))$ ADD	$2N_c$ +2
Case 2 (joint structure)	4 MUL; 2 ADD	$(4N_c)$ MUL; $(4(N_c\text{-}1))$ ADD	$2N_c$+2
Faruk's method [239]	0	$(4N_c)$ MUL; $(4(N_c\text{-}1))$ ADD	$4N_c$

N_c - number of coefficients for each FIR filter; ADD - adder operator; MUL - multiplier operator.

additional algorithmic noise transmitted to the equalization stage as in the case 1. Note that our modified FIR filters can integrate the IQ imbalance compensator because their updating rules both rely on LMS algorithms [250]. While our method is fully adaptive, the coefficients K_1 and K_2 estimated from the first processed block of samples can be applied without change to the following blocks to further reduce the computational effort in case of slowly varying imbalance values. The adaptive estimation of the imbalance value can be reactivated after an amount of time if necessary.

The hardware complexities of case 1 and case 2 as well as another recently reported method providing IQ imbalance compensation and equalization [239] are summarized in Tab. III.3. In this comparison, it is assumed that all equalizer structures have to compensate for the same channel impairments and can therefore be described by the same number of coefficients, N_c, for each FIR filter. Tab. III.3 shows that the hardware complexity (total number of adders and multipliers) of case 2 remains nearly similar to that of case 1 with the advantage of no use of trigonometric functions. Moreover, the coefficients-sets number required in both cases is reduced by a factor 2 in comparison to the one required in the method of [239], bringing less computational effort and saving the hardware resources in FPGA implementation. The following sections are aiming at numerical and experimental validation of proposed algorithm.

1.3.2 Robustness of joint algorithm in the presence of ASE noise (experimental case)

The discussed joint algorithm for the IQ imbalance compensation is experimentally validated in the presence of the amplified spontaneous emission (ASE) noise. As experimentally the phase imbalance of the coherent receiver can not be modified, we adjust the IQ phase imbalance at the transmitter side by modifying the bias voltage controlling the phase difference between the two arms of the IQ modulator. Although the proposed algorithm was developed in the case of IQ imbalance at the receiver side, it can be shown that this adaptive algorithm

can although compensate a default at the transmitter side. The following paragraphs will discuss the experimental setup and the obtained results in detail.

a) Experimental setup

The impact of non-orthogonality between I and Q channels is experimentally investigated in an optical 16-QAM coherent system. The setup is similar as for previous study in the first proposed IQ imbalance compensation (Fig. III.4). In order to allow a fair comparison between the aforementioned cases 1 and 2, the same laser is used at the transmitter and as local oscillator (LO) at the receiver. In this way, no carrier frequency offset compensation is required. In this experiment, the estimated linewidth of this optical source is of 100 kHz. At the transmitter, two 4-level pulse amplitude modulation (PAM) sequences are constituted from two PRBSs with lengths of $2^{11}-1$ and $2^{13}-1$ bits, to generate the 10-GSymbol/s data streams applied to a dual drive IQ modulator. The symbol sequences are generated with an arbitrary waveform generator (AWG).

The 4-PAM sequences applied to the I and Q inputs of the modulator are decorrelated through a 64-symbol delay. The received power is adjusted by means of a variable optical attenuator (VOA). The signal is then boosted by an erbium-doped fiber amplifier (EDFA) followed by a 3-nm optical bandpass filter (OBPF). At the receiver side, an optical 90° hybrid (DP-QPSK integrated receiver) mixes the 16-QAM signal and the LO. The signal and LO are first split. The split signal and LO are then cross-combined with proper phase shifts to produce two beating terms, namely I and Q. The 90° phase shift present in the lower branch of the splitting coupler for the LO results in the detection of the quadrature term, whereas the upper branch results in the detection of the in-phase term. The I and Q components are detected by balanced photodiodes and acquired by a real time oscilloscope with electrical bandwidth of 16 GHz at a sampling rate of 40 GS/s. After data acquisition, post-processing is performed offline using the Matlab environment.

To focus on the compensation of IQ imbalance in a 16-QAM system, polarization (de)multiplexing and chromatic dispersion effects due to transmission are ignored. Fig. III.10(a) represents the schematic of the DSP blocks at the receiver side. In the first step of DSP, the proposed FIR filter operating at four times the symbol rate is applied to blocks of 200 000 symbols. The received samples are then decimated to a symbol rate of 10 GS/s before being sent to the symbol-directed detector to calculate the mean square error. Moreover, a phase synchronization based on a second-order loop filter is digitally performed and acted as the DPLL [251]. Fig. III.10(b) presents the structure of the second-order loop filter, in which α and β are the loop parameters. Based on the error achieved from the direct-decision, $e_1(n)$, and the decimated signal, $r_{dec}(n)$, the phase error [252] is calculated by

$$e_2(n) = \Im\left\{e_1^*(n)\cdot r_{dec}(n)\cdot \mathrm{e}^{-i\cdot\hat{\theta}(n)}\right\}, \tag{III.24}$$

where $\Im$ denotes the imaginary part operator. Finally, the error is fed-back along with the carrier phase estimation to update the IQ compensators and FIR filters parameters. A

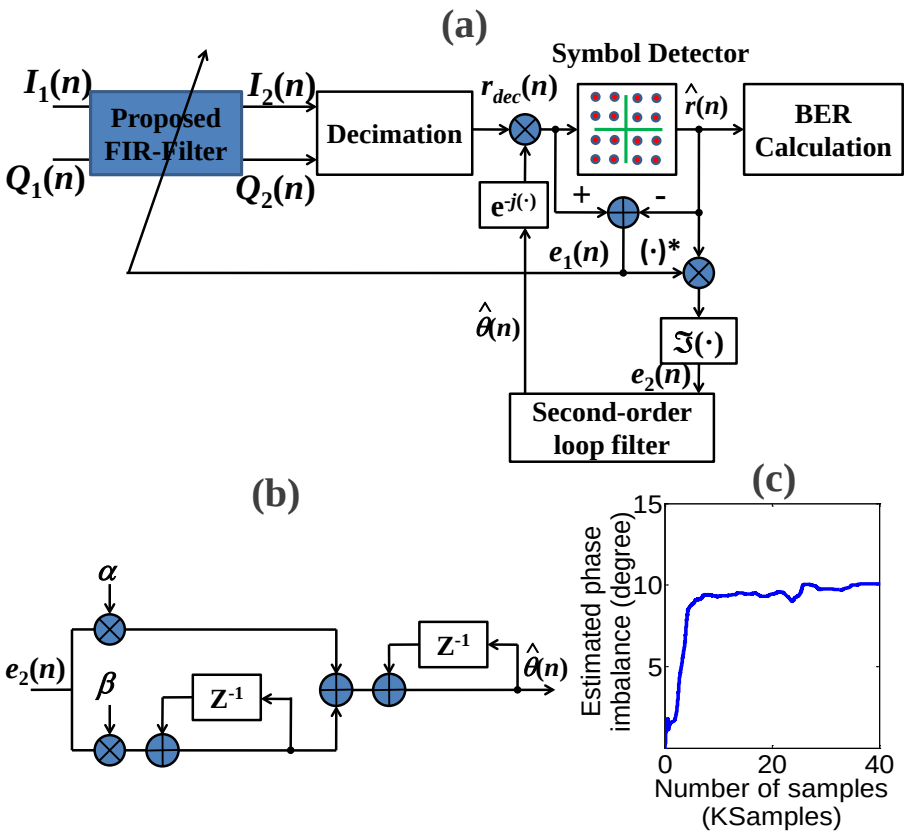


Figure III.10: (a) Schematic of DSP blocks for the received samples. (b) Second-order loop filter structure. (c) Convergence of the estimated phase imbalance.

comparison between the decoded and transmitted bit sequences is performed to determine the BER over 1 million samples. Fig. III.10(c) shows an example of the estimated phase imbalance based on the proposed algorithm. The fast convergence of the estimated phase imbalance after processing of ∼5000 symbols appears clearly.

b) Experimental B2B results

Fig. III.11(a) presents the results of BER measurements as a function of received power in different cases. The case without IQ imbalance (back-to-back curve, B2B) is plotted as a reference. Note that BER measurements are considered down to 10^{-5} only due to the limited number of acquired symbols. This BER level is however sufficiently lower than the BER of 10^{-3} at which the hard forward error correction (FEC) can be implemented to retrieve a BER of 10^{-9}. In the presence of 10° phase imbalance, the BER is degraded, resulting in a power penalty of 7 dB at a BER of 10^{-3}. By using the proposed compensation (referred to as case 2), the BER curve matches the reference case again, leading to a 7 dB power penalty reduction. Experimental constellations obtained at -26 dBm received power are presented in Fig. III.11(b) and (c) for the distorted and the retrieved constellations, respectively, showing the compensation efficiency. The proposed method is compared to the

case where IQ imbalance compensation and equalization are performed separately (referred to as case 1). The excellent match between both BER curves demonstrates the effectiveness of the proposed algorithm, which exhibits a significantly reduced computational and hardware complexity without any performance loss.

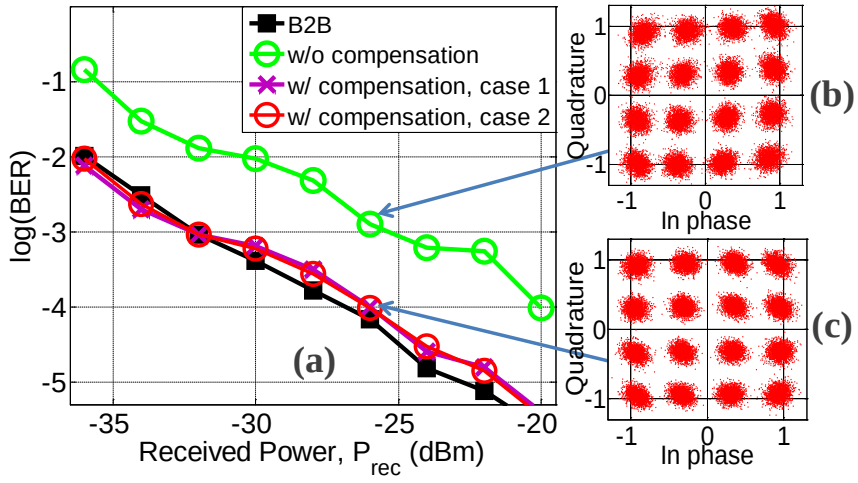


Figure III.11: BER measurement versus received power for 10° phase imbalance.

The phase imbalance is further increased to assess the effectiveness of the algorithms with a large range of the phase imbalance. More specifically, the phase imbalances of 10°, 15° and 21° are used to calculate the power penalty without (w/o) and with (w/) the help of IQ compensation algorithms. Fig. III.12 shows the power penalty at a BER of 10^{-3} with respect to the back-to-back case measured without and with compensation in case 1 and 2. Without compensation a power penalty of 12 dB is observed for a phase imbalance of 15°, indicating the high sensitivity of the system to this kind of impairment. In contrast, a power penalty reduction of 11 dB is measured at 15° phase imbalance using either case 1 compensation or our simplified approach (case 2).

In the next step, the proposed algorithm is verified in the optical fibre transmission context. In this case, the robustness of equalizer in integrated structure is tested with other impairments and more precisely to chromatic dispersion.

1.3.3 Robustness of joint algorithm in the presence of chromatic dispersion (numerical case)

Group-velocity dispersion (GVD) is a transmission impairment caused the frequency dependent phase (or group delay) over the optical fiber channel. This leads to pulse spreading and ISI if not compensated. We have so far validated the effectiveness of our IQ imbalance compensator in the absence of ISI. In this section, we numerically validate that the proposed joint IQ imbalance compensation and equalization does not affect the effectiveness of the equalizer in the presence of ISI induced by GVD. Note that, the IQ imbalance is now numerically generated at the receiver side by adjusting the phase difference between the two

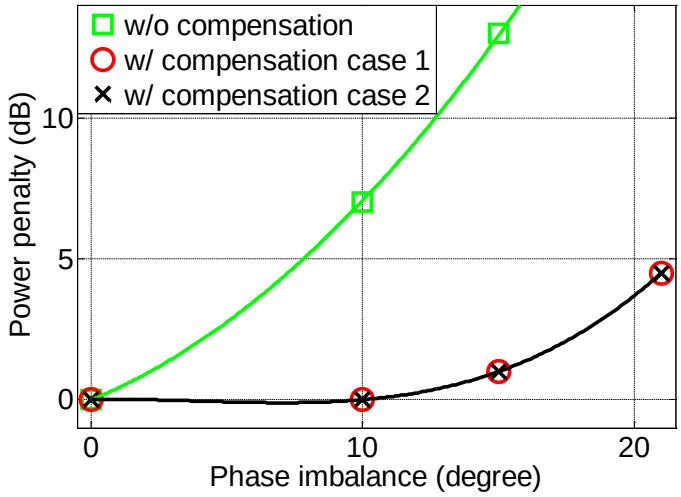


Figure III.12: Experimental power penalty at a BER of 10^{-3} versus phase imbalance. Solid lines: fitted curves corresponding to the measured values, represented with symbols.

branches in the coherent receiver.

To this aim, we simulate the transmission of a 10-Gbaud optical 16-QAM signal presenting 20° phase imbalance in the telecommunication wavelength window around 1550 nm. This signal is evaluated after the propagation over 1200 km standard single mode fiber (SSMF), with a dispersion parameter $D = 17$ ps/nm·km [253]. Note that the quantization noise of the analog-to-digital converter (ADC) is not considered in the simulation. In this case, it would be expected that the numerical results may exhibit no penalty after compensation and equalization, as pointed out in [239].

Fig. III.13 presents the BER calculated as a function of the optical signal to noise ratio (OSNR). The BER is evaluated over 65000 symbols and the calculation is repeated 10 times with different noise seeds for each OSNR value in order to calculate an average BER value. The BER curves depict the cases without (w/o) and with (w/) IQ imbalance compensation in case 2 (where IQ imbalance and equalization are handled simultaneously) after 1200 km optical fiber transmission. In the presence of such a strong IQ imbalance, the signal cannot be recovered (as depicted by the dashed lines) regardless of the transmission distance if the IQ imbalance is not compensated. With the proposed compensation, the BER curves are brought back to the B2B one with no noticeable penalty, as depicted by the dotted lines. The disappearance of penalty compared to the about 4 dB penalty in experimental results (Fig. III.12) is due to the ignored ADC quantization noise, as aforementioned, and due to the IQ imbalance generated at the receiver in the simulation cases. It is also to be noted that the required ADC resolution is relatively high as the IQ imbalance increases [239]. Finally, these results confirm the effectiveness of the equalizer in the joint compensation configuration.

To confirm our statement on the ADC ENOB impact, we have carried out similar simulations, excepted that the outputs I and Q are numerically quantized with ENOBs of 6 and

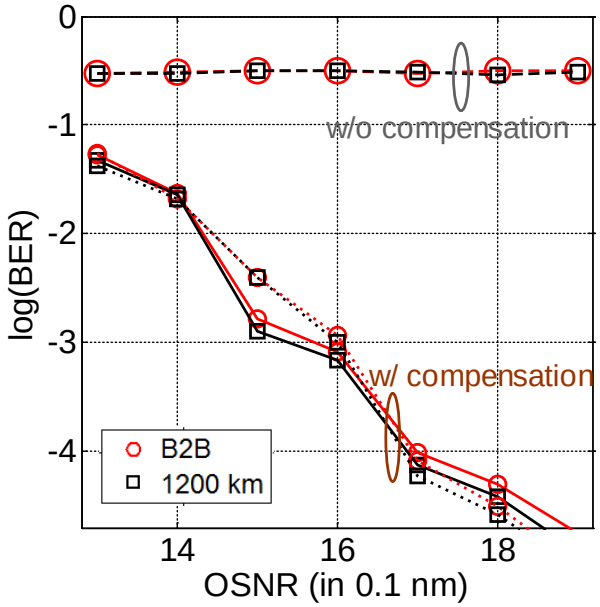


Figure III.13: BER versus OSNR under the impacts of chromatic dispersion and IQ imbalance. Solid lines: no IQ imbalance and with compensation. Dotted lines: with IQ imbalance of 20° and with compensation. Dashed lines: with IQ imbalance of 20° and without compensation.

4 bits, respectively. The different ENOB selection comes from the fact that: to fill the I and Q components into the full-scale range of the oscilloscope, different amplification (inherent to the oscilloscope channels) is applied, resulting in the different thermal noise between the two components. To quick assess this different noise, we simply change the ENOB (that also creates the random Gaussian noise process) between the I and Q components. The calculated BER in this case is compared to that in the case without quantization noise. Fig. III.14 presents the evolution of BER as the function of OSNR (in 0.1 nm) with and without impact of ADC ENOB. A 1-dB penalty is observed at a BER of 10^{-3}, confirming the impact of quantization noise to the calculated results. In the experimental case, this kind of noise can be worse due to the influence of other additional noises coming from the environment or equipments.

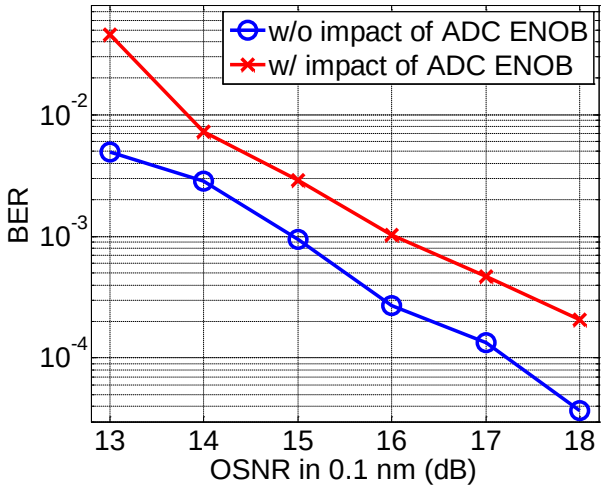


Figure III.14: Influence of ADC ENOB (6 and 4 bits for the I and Q components, respectively) on the calculated BER in systems with IQ imbalance.

2. Carrier recovery in optical coherent communications

The demand for very high data rate in next generation networks has induced a renewed interest for coherent detection and advanced modulation formats such as $M-$ary quadrature amplitude modulation ($M-$QAM) thanks to its high spectral efficiency [254, 255]. Carrier recovery (CR) is required in such coherent receivers, in which the random phase shift and rotation induced by the carrier frequency offset (CFO) between the transmitter laser and the local oscillator, as well as the laser phase noise, need to be compensated for. In a real implementation, huge parallelization and pipelining are required for feedback CR at 100 Gb/s or higher data rate transmission. Blind feedforward CR (FFCR) techniques are more suited for practical implementation since they do not require a feedback loop [256]. Section 2.1 will present some FFCR techniques (including both feedforward CFO and feedforward carrier phase estimation (CPE)) up to date in optical coherent communications. The carrier recovery based on circular harmonic expansion (CHE) is then introduced in Section 2.2. Some additional algorithms supported to improve the CHE algorithm performance are also presented. The numerical validation is finally carried out to confirm the effectiveness of investigated CR algorithm in optical coherent communication context.

2.1 State of the art of feedforward carrier recovery (FFCR)

2.1.1 Feedforward CFO compensation

Coherent detection is usually based on the intradyne detection scheme with unlocked transmitter (Tx) and local oscillator (LO) lasers. In such a scheme, the carrier frequency offset (CFO) between the Tx and LO can reach values as high as a few GHz [88], which does not allow proper recovery of the signal if not compensated. Frequency offset estimation (FOE) is hence required in the digital signal processing (DSP) at the receiver (Rx). Substantial efforts have been dedicated to the design of FOE solutions that do not require training symbols in either feedback [30] or feedforward [85] manners and using time domain [257] or frequency domain [90] approaches. Among those, feedforward FOE provides a better laser phase noise tolerance and is more hardware-efficient than feedback FOE [256]. Moreover, the use of periodograms in frequency domain analysis allows quickly estimating the CFO

with a smaller number of required symbols compared to the time domain approach [90].

The well-known Viterbi-Viterbi fourth power estimator (VV4PE) used for the FOE of $M-$ary phase shift keying ($M-$PSK) signals [85] is no longer valid for $M-$QAM, especially for cross $M-$QAM signals (e.g. 32-QAM). Several feedforward FOE methods based on the maximization of symbols periodograms using the fast-Fourier transform (FFT) have been proposed so far [90], including a solution for widening the FOE range [258]. However, the applicability of these methods to cross $M-$QAM has not been discussed in detail. Recently, the Viterbi-Viterbi monomial FOE (VVMFOE) method has been reported in [259], with an extension for cross $M-$QAM constellations. The idea behind this method is to assign weight coefficients to symbols with different amplitude levels, usually with negative power for cross $M-$QAM signal. However, the choice of this negative power value is empirical and the negative power may make the implementation in field programmable gate arrays (FPGAs) more complex and require more computational efforts.

2.1.2 Feedforward CPE

Several feedforward CPE methods have been proposed so far, including the family of minimum distance blind-phase-search (BPS) methods [256], however at the cost of a high complexity. Modified BPS versions targeting complexity reduction and/or performance improvement [260, 261], and references therein, have also been proposed. Another CPE family based on QPSK partitioning [262, 263, 264, 265, 266], and references therein, could increase the complexity when applied to high levels of $M-$QAM. Furthermore, its performance is degraded when working with cross $M-$QAM. The Viterbi-Viterbi monomial-based and maximum likelihood estimator (VVMPE-ML) was proposed as an alternative candidate for CPE [222] with significant complexity reduction in comparison to the BPS method by using the power operator to weight the symbol amplitudes. This weighting method improves the CPE estimator, albeit with an increased computational effort. Moreover, adding a maximum likelihood (ML) estimator as a second stage allows refining the recovered constellation, leading to an improved estimation [222]. However, the possibility to apply VVMPE-ML to cross $M-$QAM signals has not been discussed so far. Recently, a joint CR method has been proposed [267] based on Kalman filters, whose structure contains some feedback loops.

Tab. III.4 summarizes some recent works on feedforward CFO compensation and CPE. A lot of efforts have been carried out for feedforward compensation, confirming its interest in current high-speed transmission systems. In the next section, we exploit a recent new algorithm for FFCR, proposed in Ref. [231], and we validate it in the context of optical coherent communications.

2.2 Carrier recovery based on circular harmonic expansion

Along with carrier recovery (CR), phase ambiguity problem is critical in high-order modulation formats such as $M-$QAM, due to the symmetrical nature of the constellation. To solve

Table III.4: Some typical works on feedforward carrier recovery in optical communications.

Ref.	Compensation type	Operation based	Modulation format	Year
[85]	CFO	TD	QPSK	2007
[262]	CPE	QPSK partitioning	$M-$PSK and $M-$QAM	2008
[257]	CFO	TD	QPSK	2008
[268]	CFO	TD	QPSK	2008
[256]	CPE	MD	$M-$QAM	2009
[90]	CFO	FD	$M-$QAM	2009
[269]	CPE	MD and ML	$M-$QAM	2010
[270]	CPE	QPSK partitioning	16-QAM	2010
[271]	CFO	TD and FD	QPSK	2010
[272]	CFO	FD	$M-$PSK	2010
[273]	CPE	MD	$M-$QAM	2011
[274]	CFO	FD	$M-$QAM	2011
[275]	CFO	TD	16-QAM	2011
[276]	CFO	TD	$M-$PSK and $M-$QAM	2012
[91]	CFO	FD	$M-$QAM	2012
[222]	CPE	Viterbi-Viterbi monomial	$M-$QAM	2013
[260]	CPE	QPSK partitioning	16-QAM	2013
[277]	CFO	TD	QPSK and 16-QAM	2013
[261]	CPE	MD	$M-$QAM	2014
[265]	CPE	QPSK partitioning	64-QAM	2014
[278]	CPE	QPSK partitioning	16-QAM	2014
[259]	CFO	TD partitioning	$M-$QAM	2014
[279]	CFO	TD	16-QAM	2015
[266]	CPE	Constellation transformation	64-QAM	2015
[280]	CPE	Constellation transformation	$M-$QAM	2015

TD: time domain; FD: frequency domain; MD: minimum distance; ML: maximum likelihood.

this problem, several methods have been proposed so far [281, 94, 282]. Among them, the differential encoding/decoding without using preamble or data-aided synchronization are of interest thanks to its simplicity and good performance [282]. It should be noted that this differential encoding/decoding can also prevent cycle slips [283]. Although the goal of this study is focused on the CR, it is more meaningful and direct to study the CR algorithm in the differential encoding optical $M-$QAM coherent transmission systems.

In this section, we investigate an improved blind CR method for differentially angle encoding square and cross $M-$QAM signals in optical coherent systems where the impact of laser phase noise is troublesome. The proposed method utilizes the circular harmonic expansion (CHE) of loglikelihood functions (LLFs) [231] that will be briefly introduced in Section 2.2.1. The block diagram of proposed improved CR algorithm is then presented in Section 2.2.2. For CFO compensation, CHE is proposed to cascade to another gradient-algorithm step which can provide a similar accuracy with a fewer used-samples for the estimation, compared to the case without using the gradient-algorithm step. Whereas for CPE step, CHE is combined to a maximum likelihood estimator in order to refine the constellation as in VVMPE-ML [222]. Note that, the use of a look-up table (LUT) based on optimum weighting functions in our proposed CPE distinguishes our method (CHE-ML) from the VVMPE-ML method, resulting in not only a better laser phase noise estimation but also a reduction in overall computational effort. The CHE method alone has been studied for $M-$QAM in [231], but is, to the best of our knowledge, explored here for the first time in the context of optical coherent communication systems with a potential for efficient hardware implementation and good laser linewidth tolerance. Finally, the proposed method is numerically investigated with respect to the CFO and laser linewidth tolerance for cross and square $M-$QAM up to 128-QAM in Section 2.2.3.

2.2.1 Theoretical analysis of the method

The detail analysis of CHE method was reported in [284, 285, 231]. In the following paragraphs, we will summarize several major steps to deduce the CHE algorithm. Let's call the received sampled signal at the baud rate, $x(k) = c(k) \cdot exp(j \cdot \varphi(k)) + n(k)$, in which $k = 1, ..., K$; $c(k)$ presents the complex symbols corresponding to every possible symbol on the constellation (i.e. 16 possible symbols for 16-QAM signal); $n(k)$ denotes the samples of Gaussian noise being independent to each other with the same variance σ^2; $\varphi(k) = \varphi_0 + k \cdot \varphi_f$ is the phase rotation at the instance k due to the frequency synchronization error between the transmitter (Tx) and receiver (Rx) lasers. φ_0 denotes laser phase noise while $\varphi_f = 2\pi \cdot \Delta f \cdot T_B$ denotes the rotation due to the CFO, namely Δf, where T_B is the symbol duration. In the following, we denote $\mathbf{X}$ as the observed sequence $x(k)$ composed of K samples.

The idea of CHE algorithm is to provide an estimation of the CFO, Δf, and laser phase noise, φ_0, based on the maximum likelihood criteria. In other words, the values of φ_f and φ_0 can be conditionally estimated based on the observation of samples $x(k)$. It leads to

the calculation of conditional probability $\Pr(\varphi|\mathbf{X}=\{x(k)\})$. It is equivalent to find the probability of φ conditionally to a received observation vector $\mathbf{X}=(\mathbf{x_1},\mathbf{x_2},...,\mathbf{x_K})$. Because the successive noise samples are independent, this conditional probability can be represented by

$$\Pr(\varphi|\{x(k)\}) = \prod_{k=1}^{K} \Pr(\varphi|x_k = x(k)). \tag{III.25}$$

It is turned out that we calculate the probability of each sample, one after the other. Based on the compound probability law, maximizing $\Pr(\varphi|x_k=x(k))$ is equivalent to maximizing $\Pr(x_k=x(k)|\varphi)\cdot\Pr(\varphi)$, in which the first term can be written as

$$\Pr(x_k=x(k)|\varphi) = \frac{1}{M}\sum_{m=1}^{M}\Pr(x_k=x(k)||\varphi\,, c(k)=C_m), \tag{III.26}$$

where C_m belongs to the alphabet of M possible symbols of the constellation which have the same *a priori* probability. Due to the natural Gaussian noise, the conditional probability density of x_k (conditional to the transmission of symbol C_m in the presence of phase noise φ) can be written as

$$\frac{1}{2\pi\sigma^2}\exp\left(-\frac{\left|x-C_m e^{j\varphi}\right|^2}{2\sigma^2}\right) = \frac{1}{2\pi\sigma^2}\exp\left(-\frac{\left|xe^{-j\varphi}-C_m\right|^2}{2\sigma^2}\right). \tag{III.27}$$

The expression of the sample probability $x(k)$ conditionally assumed of the derivation of certain frequency offset, φ_f, and initial phase noise, φ_0, can be deduced as follows

$$\Pr(x_k=x(k)\,|\,\varphi_f,\varphi_0) = \frac{1}{2\pi\sigma^2 M}\sum_{m=1}^{M}\exp\left(-\frac{\left|x(k).e^{-j\left(\varphi_0+k\varphi_f\right)}-C_m\right|^2}{2\sigma^2}\right). \tag{III.28}$$

By using the logarithm, the relation in (III.25) can be transformed to a sum for the convenient calculation. By this way, the loglikelihood function (LLF) of $\mathbf{X}$ conditionally to $x(k)$ can be written by

$$\begin{aligned} &LLF(\mathbf{X}=\{x(k)\}\,|\,\varphi_f,\varphi_0) = \sum_{k=1}^{K} LLF(x_k=x(k)\,|\varphi_f,\varphi_0) \\ &= \sum_{k=1}^{K}\log\left(\Pr(x_k=x(k)\,|\varphi_f,\varphi_0)\right) = \sum_{k=1}^{M}\log\left(\frac{1}{2\pi\sigma^2 M}\sum_{m=1}^{M}\exp\left(-\frac{\left|x(k)\cdot e^{-j\left(\varphi_0+k\varphi_f\right)}-C_m\right|^2}{2\sigma^2}\right)\right). \end{aligned} \tag{III.29}$$

We suppose that the phase noise, φ_0, is equally distributed over $[0,2\pi]$. The CFO is firstly derived by the calculation of the likelihood of φ_f. By maximizing this likelihood

function (LF), we can retrieve the CFO value corresponding to φ_f

$$\begin{aligned} LF\left(\mathbf{X}=\{x\left(k\right)\}|\varphi_f\right) &= \tfrac{1}{2\pi}\int_0^{2\pi} LF\left(\mathbf{X}=\{x\left(k\right)\}\mid\varphi_f,\varphi_0\right)\cdot d\varphi_0, \\ LF\left(\mathbf{X}=\{x\left(k\right)\}|\varphi_f\right) &= \tfrac{1}{2\pi}\int_0^{2\pi} \exp\left[LLF\left(\mathbf{X}=\{x\left(k\right)\}\mid\varphi_f,\varphi_0\right)\right]\cdot d\varphi_0. \end{aligned} \tag{III.30}$$

Or

$$LF\left(\mathbf{X}=\{x\left(k\right)\}|\varphi_f\right)=\frac{1}{2\pi}\int_0^{2\pi}\exp\left[\sum_{k=1}^{K}LLF\left(x_k=x\left(k\right)\mid\varphi_f,\varphi_0\right)\right]\cdot d\varphi_0. \tag{III.31}$$

The calculation of this LLF is still complicate. By re-writing the $LLF(x_k|\varphi_f,\varphi_0)$ into polar co-ordinate as $LLF(r\cdot e^{j\cdot\phi}|\varphi_f,\varphi_0)$, where r and ϕ are the module and argument of x_k, respectively, the calculation simplification can be achieved by developing the Fourier series over phase ϕ. The expression of the conditional likelihood function of the received sequence is then presented by [284]

$$LF\left(\mathbf{X}=\{x\left(k\right)\}\mid\varphi_f\right)=\frac{1}{2\pi}\int_0^{2\pi}\exp\left[\mathrm{Re}\sum_{n=0}^{\infty}\left(e^{-jn\varphi_0}\right)\cdot F_n\left(n\varphi_f\right)\right]\cdot d\varphi_0, \tag{III.32}$$

in which F_n is the function depending on the harmonic coefficients of the Fourier series. Due to the angular symmetry of the QAM constellation, only harmonics with the index of multiple of 4 are nonzero. The harmonic ranked 0 is a constant and hence is omitted. By retaining the first nonzero harmonic (the 4-th harmonic), the LF approximation is obtained as follows

$$LF\left(\mathbf{X}=\{x\left(k\right)\}\mid\varphi_f\right)\approx\frac{1}{2\pi}\int_0^{2\pi}\exp\left[\mathrm{Re}\left\{\left(e^{-4j\varphi_0}\right).F_4\left(4\varphi_f\right)\right\}\right].d\varphi_0. \tag{III.33}$$

The right hand term is $I_0(|F_4(4\varphi_f)|)$ where I_0 is the zeroth-order modified Bessel function. Since this function is monotonously increasing, maximizing the LF (which is represented by the Bessel function) is equivalent to maximizing the argument inside the Bessel function. The resulting CFO estimator is as follows [284]

$$\widehat{\varphi_f}=\frac{1}{4}\arg\max_{\varphi_f}\left|F_4\left(\varphi_f\right)\right|. \tag{III.34}$$

In fact, $F_4(4\varphi_f)$ is the spectrum of the nonlinearly transformed samples sequence whose magnitude can be implemented using a lookup table (LUT), bringing a reduced computational effort [284]. After the CFO compensation based on (III.34), the LUT can be re-used to estimate and compensate for the laser phase noise. This LUT will be schematically located

in the general algorithm blocks in next section. The simple rule for CPE was introduced in [285] as follows

$$\widehat{\varphi_0} = \frac{1}{4} \arg F_4 \left(4\widehat{\varphi_f}\right). \tag{III.35}$$

It should be noted that the optimum weighting function for the nonlinearly transformed samples sequence [231] is used in this work to improve the performance of estimators in (III.34) and (III.35). In the following section, we investigate the robustness of CHE algorithm. The improved algorithm is proposed by combining the CHE algorithm with other algorithms for a better estimation of both CFO and laser phase noise.

2.2.2 Proposed improved CHE algorithm for CR

Fig. III.15 presents the configuration for $M-$QAM CR using aforementioned CHE algorithm, in which 2 main stages for CFO compensation (stage 1) and CPE (stage 2) are discussed in the following parts. For CFO compensation, the estimator rule in (III.34) is used which results in the efficiently zero-padded FFT implementation. We call this step as a raw CFO estimation with the help of a lookup table (LUT1) for the nonlinear transformation (represented for CHE algorithm). Actually, the estimation accuracy depends on the number of samples, N, used for the estimation and the block length effect will be studied in next section. To improve the estimation performance, another step, named as a fine CFO estimation, can be either the gradient-descent algorithm [90] or chirp-Z transformation [91]. In our case, the original CHE is proposed to cascade to another step using gradient-descent algorithm, referred to as CHEFOE, because it has already been developed in Section 3.4.2 of Part I for the linear optical sampling technique. By this way, the number of samples used for FFT operation can be reduced while the estimation accuracy is still remained.

For CPE, the CHE algorithm (stage 2a in Fig. III.15) is combined to another ML estimator (stage 2b in Fig. III.15) in order to refine the constellation. To this way, the error probability can be reduced at the detection. Particularly, the procedure for the raw phase noise estimator over N_1 symbols is based on the rule in (III.35), in which the nonlinear transformation based on LUT1 is used (represented for CHE algorithm). The output symbols in the stage 2a, $x_1(k)$, are fed to the final step with the ML operation over N_2 symbols to refine the phase estimation. For this reason, the improved CPE is named as CHE-ML algorithm. According to Ref. [25, 269], the ML phase is calculated by $\widehat{\varphi_{ML}} = \arg\left[\sum_{k=1}^{N_2} DD\left(x_1\left(k\right)\right)^* x_1\left(k\right)\right]$, where DD is the direct-detection operation for QAM symbol detector . This direct-detection operation is implemented via another look-up table, called LUT2 in stage 2b of Fig. III.15. The detail effect of block lengths, N_1 and N_2, used in this estimation will be further discussed in next paragraphs.

It should be reminded that the weighting function for the received symbols' amplitude implementing in LUT1 is simultaneously utilized for CPE and CFO compensation, leading to less computational effort in the joint configuration.

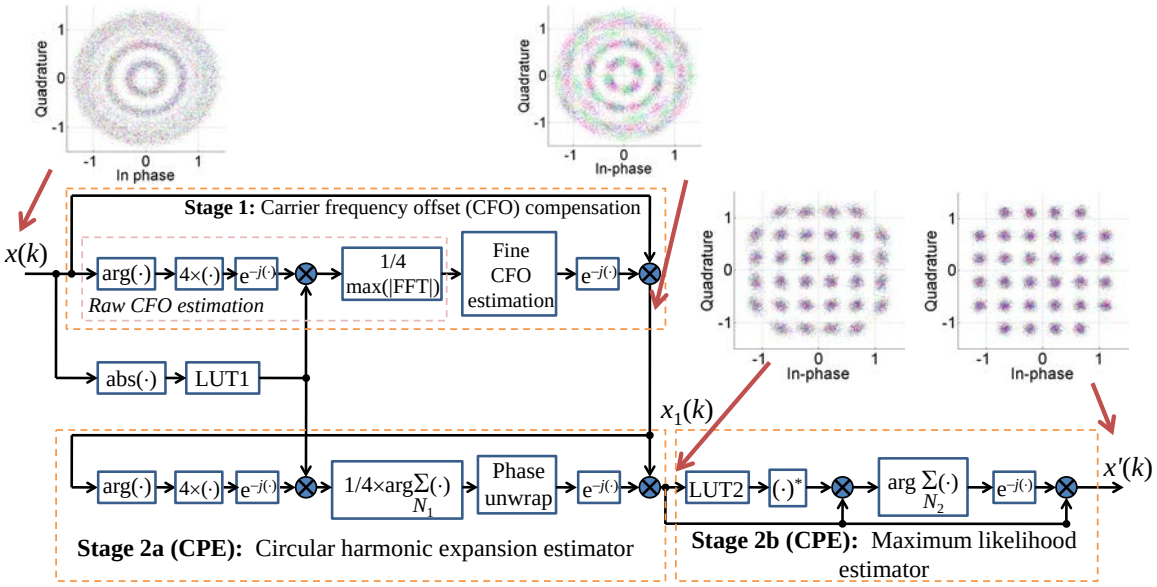


Figure III.15: Joint blind CR configuration based on CHE-ML using the first nonzero harmonic component. The insets show the 32-QAM constellations at each stages with SNR = 21 dB, $\Delta\nu \cdot T_B = 10^{-5}$, and normalized CFO of 0.025; LUT: lookup table.

The following subsection is dedicated to numerically validate the proposed algorithm in optical coherent communication context. For simplicity, the CFO compensation and CPE will be studied separately.

2.2.3 Algorithm validation

In order to evaluate the performance of the proposed joint CR method, the transmission of 16-, 32-, 64- and 128-QAM signals is simulated and the impact of the laser sources is studied. Fig. III.16 presents a simplified schema used in the simulation. For signal encoding, $s(k)$, the square $M-$QAM signal is generated by angle differential encoding [282] (more details in Appendix C) a PRBS with a length of $2^{13}-1$ onto the constellation, whereas the differentially Gray encoding [256] with the same PRBS length is used for cross $M-$QAM as discussed before. About 130 000 symbols are transmitted. The symbols are then corrupted by AWGN noise, represented as the amplitude noise loading (Fig. III.16) to form the distorted signal, $s_1(k)$. The noise is specified by the SNR in the electrical domain (the ratio between the signal power and the noise power assumed to AWGN with infinite bandwidth). The SNR values are chosen for each signal so that it leads to 1 dB penalty on the received SNR compared to the theoretical SNR values [25], at a BER of 10^{-3} corresponding to the soft forward-error correction (FEC) BER limit [286]. These SNRs values are equal to 18.4 dB, 20.8 dB, 24.5 dB and 26.6 dB for 16-, 32-, 64- and 128-QAM signals, respectively.

Concerning the laser, the phase noise caused by the laser linewidth, $\Delta\nu$, is modeled as a discrete time random walk $\varphi_n = \varphi_{n-1} + \Delta n$, in which Δn is a Gaussian random variable with zero mean and variance $2\pi \cdot \Delta\nu \cdot T_B$, where T_B is the QAM symbol duration. The laser

phase noise effect is then introduced to $s_1(k)$ to form a new corrupted signal, $s_2(k)$. To focus on the carrier recovery algorithms, no transmission link is considered in this model. At the receiver, the CFO effect (inherent to the frequency difference between the transmitter and receiver laser) is inserted by CFO loading block (Fig. III.16). The impairment effects introduced chromatic dispersion, polarization mode dispersion, timing clock error are completely removed for simplicity. The signal $x(k)$ after the coherent detection is assumed to be the discrete received samples at the baud rate and used for the CR algorithms evaluation (as discussed in Sections 2.2.1 and 2.2.2).

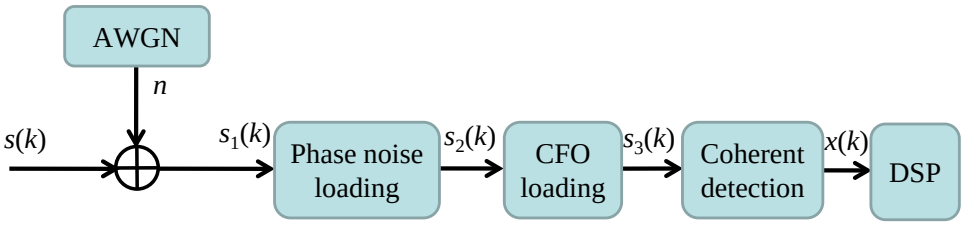


Figure III.16: Schema used in the simulations for characterizing the carrier recovery algorithms.

In the following studies, the proposed improved CHE algorithm for the carrier recovery is compared to the existed solutions. More specifically, for the CFO compensation, the proposed improved method is compared to the 4-th power [90] and Viterbi-Viterbi monomial frequency offset estimation (VVMFOE) methods [259].

For the CPE, the proposed improved CHE algorithm is evaluated in comparison to the Viterbi-Viterbi monomial based and maximum likelihood phase estimator (VVMPE-ML) [222] and the blind phase search (BPS) method [256]. Note that, according to Ref. [256], the benchmarked performance of the single-stage BPS is done with 64 test phase values for 16- and 32-QAM and with 128 test phase values for 64- and 128-QAM, to get the sufficient phase angle resolutions.

Validation of CFO compensation

In Stage 1, the CFO compensation depicted in Fig. III.15 is investigated with two cascaded steps. The proposed improved CFO estimator is evaluated based on 500 runs of simulation and compared to the 4-th power [90] and VVMFOE methods [259]. To simplify the investigation and to give the idea of how the CFO estimation accuracy is, 10 Gbaud 16- and 32-QAM signals are considered with the CFO of 0.5 and 0.25 GHz, respectively.

In the first step, the raw CFO estimations of three algorithms are compared and the fine CFO estimation is not activated for the fair comparison. Fig. III.17 presents examples of normalized spectra of 16- and 32-QAM signals using 512 and 1024 symbols, respectively. As expected, the frequency indices associated with the maximum values in the normalized spectra correspond to the four-times of predefined CFOs, confirming the effectiveness of this CFO estimation. All three algorithms can work for 16-QAM, whereas the 4-th power method does not function for 32-QAM. It can be seen that the CHEFOE and VVMFOE methods

provide a better periodogram than the 4-th power method. However, the periodogram obtained by CHEFOE is less noisy than that of VVMFOE, indicating a better estimator.

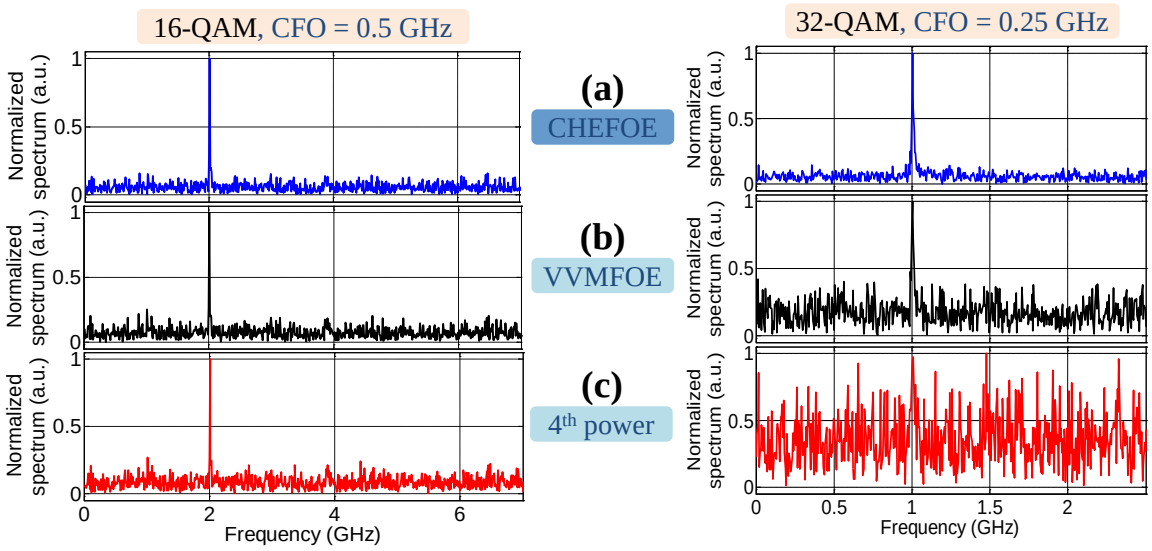


Figure III.17: Examples of normalized spectra of 16- and 32-QAM signals with the CFOs of 0.25 GHz (first column) and 0.5 GHz (second column), respectively, using (a) circular harmonic expansion frequency offset estimation (CHEFOE); (b) Viterbi-Viterbi monomial frequency offset estimation (VVMFOE); (c) 4-th power methods.

In the next step, the CFO estimation error (the difference between the predefined CFO and the estimated one) is evaluated as a function of number of utilized symbols, N (the total symbol numbers used for the FFT operation in periodogram representation). The mean value (upper row) and the corresponding standard deviation (STD) (lower row) of the CFO estimation error are investigated for 16-QAM (Fig. III.18(a)) and 32-QAM (Fig. III.18(b)) signals. For 16-QAM signals, the three methods give similar performance as the number of symbols exceeds 2^8, resulting in mean value and standard estimation of estimation error smaller than 4 MHz and 2 MHz, respectively. For 32-QAM signals, the required number of symbols for CHEFOE, VVMFOE and 4-th power methods required to achieve similar mean value and standard deviation as for 16-QAM signals are 2^9, 2^{10} and 2^{13}, respectively. It means that the proposed method requires less than half the number of symbols for the CFO estimation compared to VVMFOE method and 8 times less than the 4-th power method, indicating the robustness of the CHEFOE method.

The laser linewidth tolerance of the three methods is further studied (Fig. III.19) with symbol lengths of 2^9 and 2^{10} for 16-QAM and 32-QAM signals, respectively. For 16-QAM signals, the tolerable normalized linewidths can take on values as high as $2.5 \cdot 10^{-3}$, 10^{-3} and $5 \cdot 10^{-4}$ using the CHEFOE, VVMFOE and 4-th power methods, respectively, in order to obtain a mean of the estimation errors less than 5 MHz. For 32-QAM signals, the 4-th power method does not work, whereas the normalized linewidth tolerance of the VVMFOE method reduces to 10^{-4}. The CHEFOE method still allows a normalized linewidth tolerance

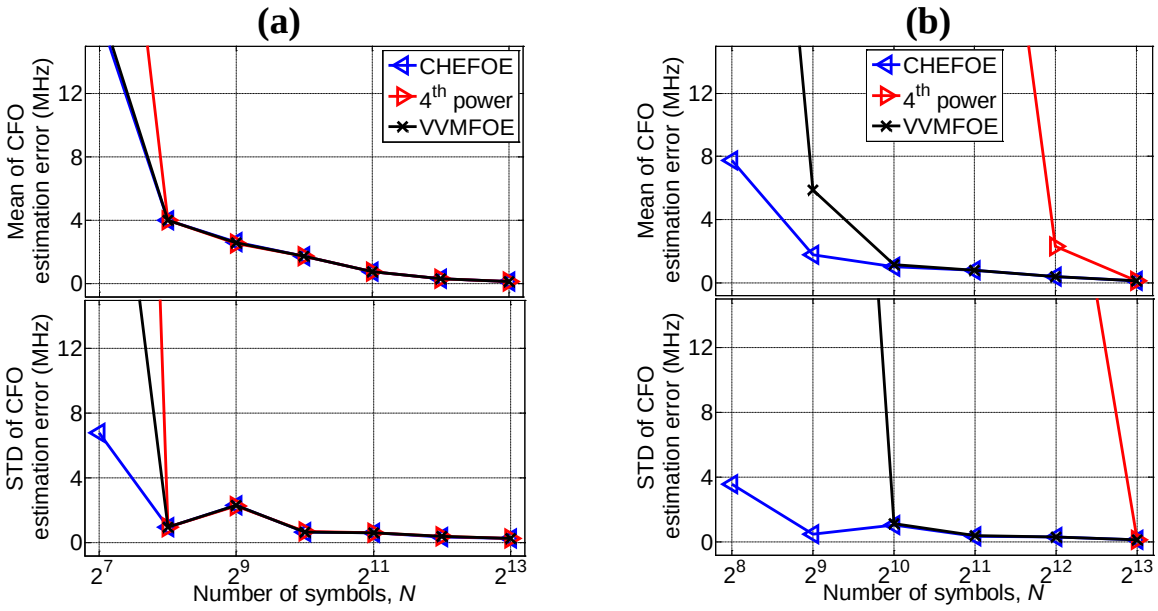


Figure III.18: Average and STD values of the CFO estimation error as the function of the number of symbols, N, used for the FFT operation of (a) 16-QAM and (b) 32-QAM signals.

up to $2.5 \cdot 10^{-3}$ for an estimation error below 5 MHz, confirming the effectiveness of the proposed method.

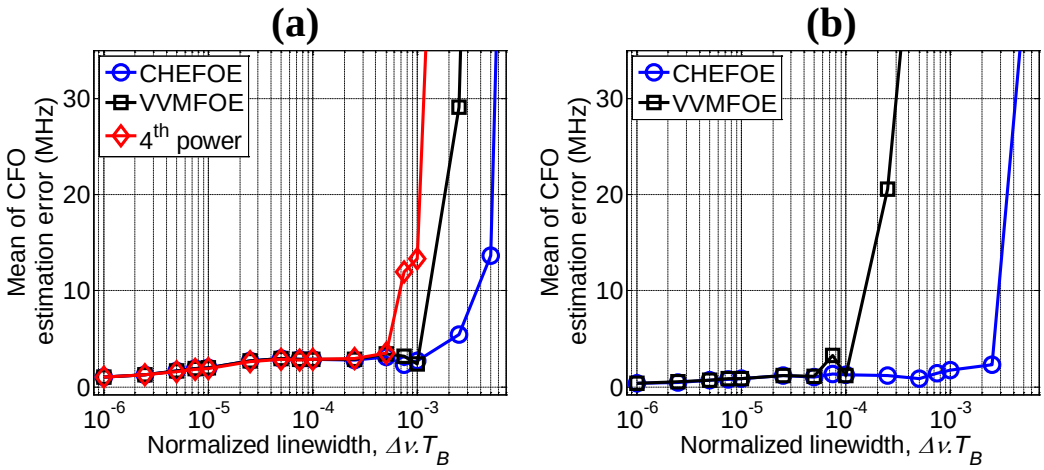


Figure III.19: CFO estimation error versus normalized linewidth for (a) 16-QAM and (b) 32-QAM signals. CFOs/ FFT block lengths for 16- and 32-QAM are set to 0.5 GHz/ 2^9 and 0.25 GHz/ 2^{10}, respectively. The 4-th power method for 32-QAM is not plotted due to the error worse than 30 MHz.

Finally, the steepest-descent algorithm combined with CHEFOE is activated and considered only for 16-QAM signals in comparison to the VVMFOE method with $N = 256$. The extrema of periodogram are chosen such that $4 \cdot \varphi_f \cdot T_B$ lies in two adjacent FFT points. Fig. III.20 presents the mean value and standard deviation of the estimation error as a function of frequency offset, using the CHEFOE and VVMFOE methods before and

after applying the gradient-descent algorithm. It can be observed that the combination of FOE with gradient descent algorithm reduces up to a factor two the CFO estimation error compared to FOE alone, indicating the accuracy of the proposed combination estimator.

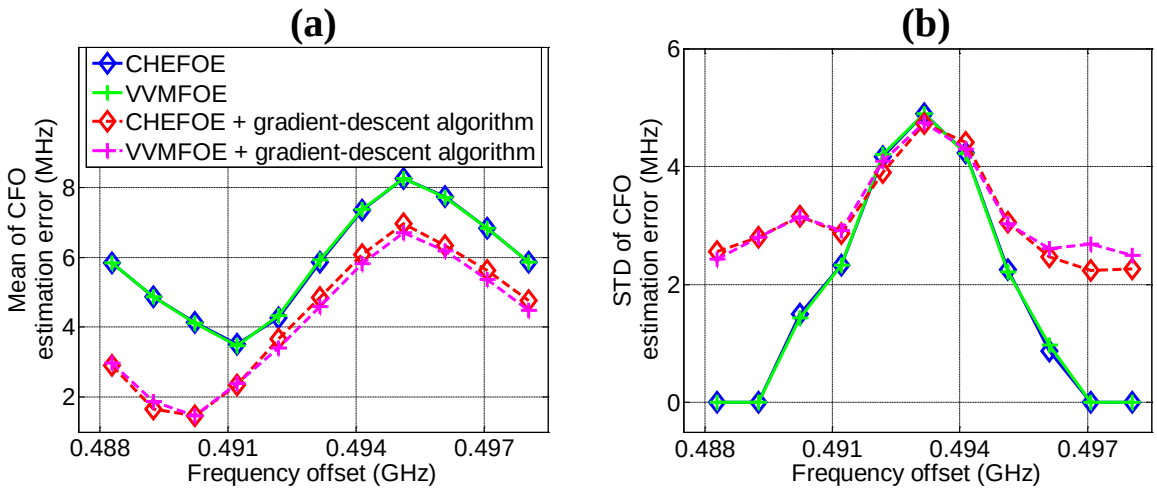


Figure III.20: Mean and STD of the estimation errors for 16-QAM in a FFT interval.

Since the proposed improved CFO compensation is validated, the next paragraphs are dealt with the validation of the proposed improved CPE based on CHE method. To focus on this CPE, the effect of CFO is disabled in the simulation blocks (Fig. III.16).

Validation of CPE compensation

a) Optimized block lengths for CPE

In this part, we will study the proposed improved CPE in Fig. III.15 (Stage 2). As in the case of CFO compensation, the block lengths, N_1 and N_2, are the important parameters which degrade the system performance in terms of BER. It is then crucial to determine the optimum block lengths for each $M-$QAM signal. The numerical simulations are carried out with variable block lengths under the different linewidth impacts for a 1 dB SNR penalty at the hard FEC threshold of 10^{-3}. Fig. III.21 shows the results obtained with 16-QAM (Fig. III.21(a)) and 32-QAM (Fig. III.21(b)) signals. The calculated BER corresponding to the variable block lengths in the first CPE step of the proposed CHE-ML are compared to those of VVMPE-ML and BPS.

BERs for 16-QAM signal, indicated in the first row of Fig. III.21(a), are calculated with the normalized linewidth of 10^{-4}, whereas BERs, in the second row of Fig. III.21(a), are achieved with the normalized linewidth of 10^{-5}. It can be seen that VVMPE-ML requires more symbols to reach to the optimum BER. BPS and the proposed CHE-ML quickly reach to optimum block length value (specified by the shortest block length value at the minimum achievable BER) with nearly similar speed. When the phase noise is increased (normalized linewidth from 10^{-5} to 10^{-4}), the BPS slightly degrades the linewidth tolerance compared to the VVMPE-ML and CHE-ML methods.

Table III.5: Optimum results of block lengths for 1 dB penalty at the hard FEC limit of 10^{-3} for the first CPE step.

Methods	16-QAM	32-QAM	64-QAM	128-QAM
VVMPE-ML	24	–	70	–
BPS	16	20	40	100
CHE-ML	16	60	50	220

In the case of 32-QAM signal, the normalized linewidths of 10^{-5} and 10^{-6} are used in the first and the second rows of Fig. III.21(b), respectively. According to Ref. [231], the VVMPE-ML does not work with cross $M-$QAM because the weighting function (inherent to the power elevation) does not provide the negative weighting change as in CHE method. The BPS in this case is quickly reached to the optimum block length than the proposed CHE-ML, however, at the cost of more complexity in implementation (as discussed later on).

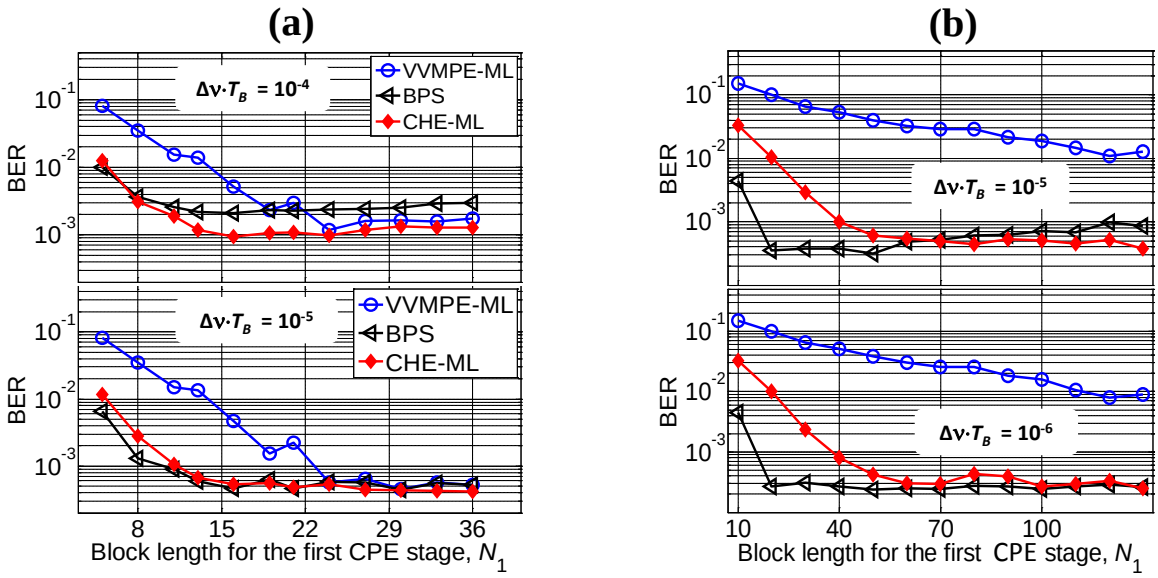


Figure III.21: Calculated BER versus the block length for the first CPE step of (a) 16-QAM and (b) 32-QAM with the signal SNRs corresponding to 1 dB penalty at the BER of 10^{-3}. Normalized linewidths, $\Delta\nu \cdot T_B$, of 10^{-4} and 10^{-5} in the first and second rows of 16-QAM, respectively. Normalized linewidths, $\Delta\nu \cdot T_B$, of 10^{-5} and 10^{-6} in the first and second rows of 32-QAM, respectively.

Although the phase noise impacts are different, the optimum block lengths are almost similar for both 16- and 32-QAM signals. More specifically, the optimum block lengths for 16-QAM are 24, 16, 16 corresponding to VVMPE-ML, CHE-ML, BPS algorithms. For 32-QAM, the VVMPE-ML algorithm is no longer working, while the optimized block lengths for CHE-ML and BPS are 60 and 20, respectively.

Similar investigation is carried out for 64- and 128-QAM signals. Tab. III.5 summarizes

the optimum block lengths of the first CPE stage, N_1, for different $M-$QAM signals. The optimized block lengths for the second CPE stage, N_2, of VVMPE-ML and CHE-ML algorithms have been studied in the same way but the results are not plotted to reduce the distraction. The obtained optimum block lengths, N_2, for 16-, 32-, 64- and 128-QAM signals are 16, 20, 24 and 30, respectively. In the next part, the robustness of proposed improved CPE algorithm is studied and compared to those of VVMPE-ML and BPS algorithms.

b) Linewidth-tolerance of CPE

The optimum block lengths for each method as studied before are applied in this investigation. BER as the function of the normalized laser linewidth for 16- and 32-QAM signals, calculated at the FEC threshold of 10^{-3} are represented in the first and second rows of Fig. III.22, respectively. As expected, BER increases with the increase of linewidth.

For 16-QAM signals (first row of Fig. III.22), the BPS provides a better BER for a low normalized linewidth ($\Delta\nu \cdot T_B \leq 9 \cdot 10^{-4}$) compared to the VVMPE-ML and CHE-ML methods. At high normalized linewidth ($\Delta\nu \cdot T_B > 9 \cdot 10^{-4}$), CHE-ML and VVMPE-ML methods show a slightly better BER than BPS, while the BER below 10^{-3} provided by CHE-ML is similar to that of VVMPE-ML.

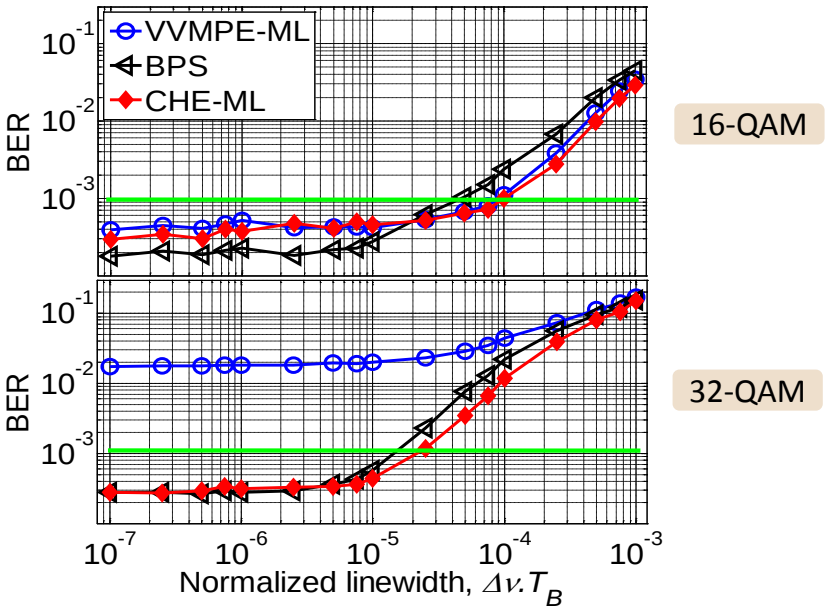


Figure III.22: Calculated BER versus laser linewidth for (a) 16-QAM and (b) 32-QAM signals and the SNRs of 1 dB penalty at the FEC threshold of 10^{-3}.

For 32-QAM signal (second row of Fig. III.22), the VVMPE-ML does not work properly, the error floor exceeds 10^{-3} whatever the normalized linewidth is. It is according to the finding in Ref. [231] that the VVMPE estimator based on the optimal nonlinear least-square (NLLS) is inferior to the CHE estimator, especially for cross $M-$QAM constellations, due to the sign-changing nature of the weighting function $A_4(r(k))$. For a low normalized linewidth, the performance of BPS and our proposed CHE-ML is almost similar. CHE-ML method

presents a better tolerance comparing to BPS method at the high region of normalized linewidth, while keeping less complexity (as shown in the next part) in comparison to BPS, showing the effectiveness of the proposed improved CPE method.

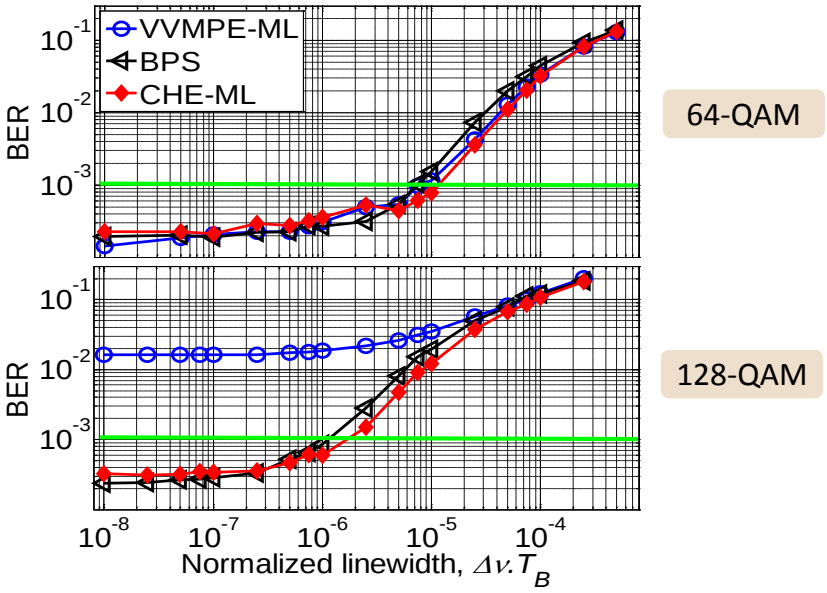


Figure III.23: Calculated BER versus laser linewidth for (a) 64-QAM and (b) 128-QAM signals and the SNRs of 1 dB penalty at the FEC threshold of 10^{-3}.

We carry out further investigation on 64- and 128-QAM signals at the hard FEC threshold as in Fig. III.23. For square 64-QAM (first row of Fig. III.23), the three algorithms are working properly. Furthermore, the BER evolutions are superimposed at the low normalized linewidth region and started to divergence at the high normalized linewidth region. For cross 128-QAM (second row of Fig. III.23), VVMPE-ML does not operate again, as similar to the case 32-QAM signal. BPS indicates a better calculated BER compared to CHE-ML method at the low normalized linewidth, while CHE-ML shows the better tolerance at the high normalized linewidth with less complexity.

It should be reminded that the VVMPE-ML and BPS algorithms compensate for only the phase noise effect, so they should require an extra step before CPE in presence of CFO. However, in our case, the CFO using the aforementioned CHE method can be easily integrated with CPE to reduce the computational effort. Therefore, in real transmission systems where the CFO and laser phase noise are unavoidable; our method provides a simplified solution for these impairments compensation.

The normalized linewidth tolerance for 1 dB penalty of different CPE methods is summarized in Tab. III.6. Based on this analysis, the proposed improved CPE method can tolerate a linewidth times symbol duration product ($\Delta\nu \cdot T_B$) equal to $1.04 \cdot 10^{-4}$, $2.31 \cdot 10^{-5}$, $1.24 \cdot 10^{-5}$, $1.71 \cdot 10^{-6}$ for 16-, 32-, 64- and 128-QAM, respectively. At 40 Gbaud, all of these linewidth requirements can be met using commercial external-cavity laser.

Table III.6: Normalized linewidth tolerance for 1 dB penalty at the hard FEC limit of 10^{-3} for various CPE methods.

Methods	16-QAM	32-QAM	64-QAM	128-QAM
VVMPE-ML	$9.24 \cdot 10^{-5}$	–	$8.04 \cdot 10^{-6}$	–
BPS	$4.83 \cdot 10^{-5}$	$1.52 \cdot 10^{-5}$	$7.78 \cdot 10^{-6}$	$1.13 \cdot 10^{-6}$
CHE-ML	$1.04 \cdot 10^{-4}$	$2.31 \cdot 10^{-5}$	$1.24 \cdot 10^{-5}$	$1.71 \cdot 10^{-6}$

Table III.7: Hardware and computational complexity for different CPE methods.

Methods	Real multipliers	Real adders	Comparators and decisions	Lookup table
VVMPE-ML	$(l/4+16)N_1+$ $10N_2+1$	$8N_1+6N_2$	N_2	1
BPS	$6BN_1+4N_1$	$6BN_1 - B+$ $2N_1+2$	$BN_1 + N_1 + B$	-
CHE-ML	$2N_1+8N_2$ $+2$	$2N_1+5N_2+1$	$N_1 + N_2$	2

l: raising power level of sample amplitude [222]; N_1, N_2: block lengths of the first and second CPE stages, respectively.

c) Hardware complexity comparison

The hardware complexities of the various CPE algorithms are presented in Tab. III.7. For clarity, the hardware implementation in the CFO stage of proposed joint CFO compensation and CPE method is ignored for a fair comparison. According to Ref. [260], the optimum implementation of the fourth power operation of a complex number leads to 6 real multipliers and 2 real adders. Moreover, within the scope of this work, other algorithms, for example CORDIC [287], transformation to polar co-ordinates [288], are not considered.

Based on the optimum block lengths and parameters of each algorithm, an example of the calculated values of each operation according to 16-QAM are indicated in Tab. III.8. In summary, in the form of number of real multipliers/adders, the proposed improved CHE method always brings a less computational effort in comparison to the VVMPE-ML and BPS methods, showing the significant advantage especially in the real-time system implementation. More specifically, in comparison to BPS algorithm, the proposed improved CHE method provides a complexity reduction by factors of about 54/38, 34/27, 69/52 and 65/56 (in the forms of adders/multipliers) for 16-, 32-, 64- and 128-QAM, respectively. Thanks to the use of another lookup table (LUT), the proposed method reduces the complexities compared to the VVMPE-ML method by factors of about 2/4 and 3/5 (in the forms of adders/multipliers) for 16- and 64-QAM, respectively.

In conclusion, we have proposed several new algorithms (for IQ imbalance compensation, CPE and CFO compensation) and validated for the first time in optical coherent system context in this section. For the IQ imbalance compensation, analytical, numerical and experimental investigations have been carried out. The first proposed IQ imbalance com-

Table III.8: Example of calculated hardware complexity for different CPE methods with 16-QAM signal.

Methods	**Real multipliers**	**Real adders**	**Comparators and decisions**	**Lookup table**
VVMPE-ML	641	288	16	1
BPS	6208	6114	1104	-
CHE-ML	162	113	32	2

pensation has been introduced based on a new metric definition and shown to be a good alternative solution compared to the existed solutions with less complexity and a given accuracy. While the second proposed IQ imbalance compensation has been integrated into an equalizer bringing an advantage of the simultaneous compensation of several impairments. Also, the modified equalizer structure gives a less computational effort compared to the current solutions.

For the carrier recovery (CR - both CFO compensation and CPE), we have improved the circular harmonic expansion (CHE) algorithm to obtain a better compensation for CFO and laser phase noise. Particularly, the proposed CFO compensation is enhanced by cascading to another fine CFO estimation stage to increase the accuracy while still using fewer symbols for the estimation. Additionally, the CHE algorithm for CPE is proposed to combine with another maximum likelihood (ML) estimator in order to refine the constellation for a better bit error probability. The proposed improved CHE algorithm for the CR has been numerically validated with a number of modulation formats levels (from 16- to 128-QAM signals). These algorithms globally show similar performance to the best results of state of the art but with a reduced complexity.

All these algorithms which were firstly developed for the linear optical sampling technique are notably very useful for the optical coherent transmission experiments. In the next section, these DSP stages will be used in an experiment involving in an all-optical signal processing function and allowing to limit the accumulation of nonlinear phase noise.

3. DSP application to all-optical signal regeneration in coherent systems

All-optical signal processing, and more precisely optical regeneration is one of the topics of interest in FOTON laboratory. It notably led to a thesis work on optical signal processing using photonic crystal devices [289]. This work was carried out using OOK modulation formats only; I had hence the opportunity to combine results of both our works in a common experiment during my PhD allowing me to validate the tools developed during my work in an optically regenerated coherent link.

3.1 Context of the study

As mentioned in Part I, the bi-dimensional modulation format signals such as $M-$PSK signals are nowadays widely used for long optical transmission distance at very high bit rate signals. All-optical signal processing to avoid noise accumulation in the link could be an attractive solution for improving the performance of $M-$PSK transmission systems at the condition that at least it preserves the phase of the signal and at best it reduces the signal phase noise. Unfortunately, main techniques developed before the 2000's years were sensitive to the signal intensity variations as developed for ASK transmissions and can not be used for $M-$PSK transmission links. Therefore, the study on novel all-optical functions for $M-$PSK signal processing is a key issue.

Besides, one of the limiting impairment of $M-$PSK transmission is the accumulation of nonlinear phase noise (NPN) coming from the conversion of amplified spontaneous emission (ASE) noise into phase noise by the Kerr nonlinearity of the transmission fiber [290]. NPN could be compensated in the digital domain, albeit at the cost of increased complexity in coherent receivers. In the optical domain, some solutions leading to simultaneous phase and amplitude regeneration were proposed [291, 292]. An alternative, and maybe a simpler solution, is the amplitude fluctuation limitation which was shown to reduce the accumulation of NPN along fiber links [293]. Several techniques for phase-preserving power limiter have been experimentally demonstrated using four-wave mixing (FWM) in fiber [294], a nonlinear

optical loop mirror (NOLM) [295, 296], or a microcavity based saturable absorber [293]. Some of these methods, when they are based on optical fibers, are generally limited by either a weak integration capacity or a high power requirement. More recently it has been demonstrated during the PhD work of K. Lengle [289] that a compact regeneration scheme could be promising for allowing very large integration with low operating power. It is using the switching of a photonic crystal microcavity on an Indium Phosphide (InP) over silicon-on-insulator (SOI) hybrid technology.

During my work, I have studied the possibility to use this device to limit the NPN accumulation in a QPSK transmission link.

3.1.1 Presentation of the device

First of all, InP over SOI hybrid technology is an extremely promising solution for future photonic circuits as it combines CMOS compatibility with the optoelectronic properties of III-V materials. This technology is now sufficiently mature to allow the demonstration of main optical functions (lasers [297], amplifiers [298], modulators, flip-flops [299], wavelength converters [300], modulation format converters [301] and 2R-regenerators, including power-limiters [302]). Secondly, thanks to their small achievable size with strong optical confinement and enhanced nonlinearity originating from their resonant behavior, photonic crystal (PhC) nanocavities are considered to be promising building blocks for high-density photonic integrated circuits. In particular, all-optical switching has been recently demonstrated using an InP on SOI PhC nanocavity, and applied to wavelength conversion up to 20 Gbit/s [303].

The passive device used in my work and presented in Fig. III.24, consists of a single-mode SOI wire waveguide evanescently coupled to an InP-based PhC nanocavity. The cavity is of the "nanobeam" type obtained by drilling holes in a single mode InP wire waveguide. The cavity is realized by varying the spacing between holes of the same diameter, resulting in a quality factor of the order of 850. A carrier lifetime of 30 ps is furthermore ensured by the use of surface quantum wells. The cavity is fully encapsulated in SiO_2 for efficient heat-sinking. Grating couplers are used at each extremity of the tapered SOI waveguide to enable coupling to cleaved standard single-mode fibers, leading to a total fiber-to-fiber insertion loss (away from resonances) of the device of 12 dB. The device is fully described in [304]. A resonance with a depth of 17 dB is measured on this cavity as depicted in Fig. III.24(c). We will play with this resonance to generate the power limiting function.

3.1.2 Principle of the power limiter

The cavity resonance wavelength depends on the incident power (as a consequence of a change of the carrier density and hence of the refractive index). This wavelength shift is schematically represented in Fig. III.25(a) to illustrate the principle. If the signal exhibits intensity fluctuations, the dynamic shift will be different depending on the instantaneous

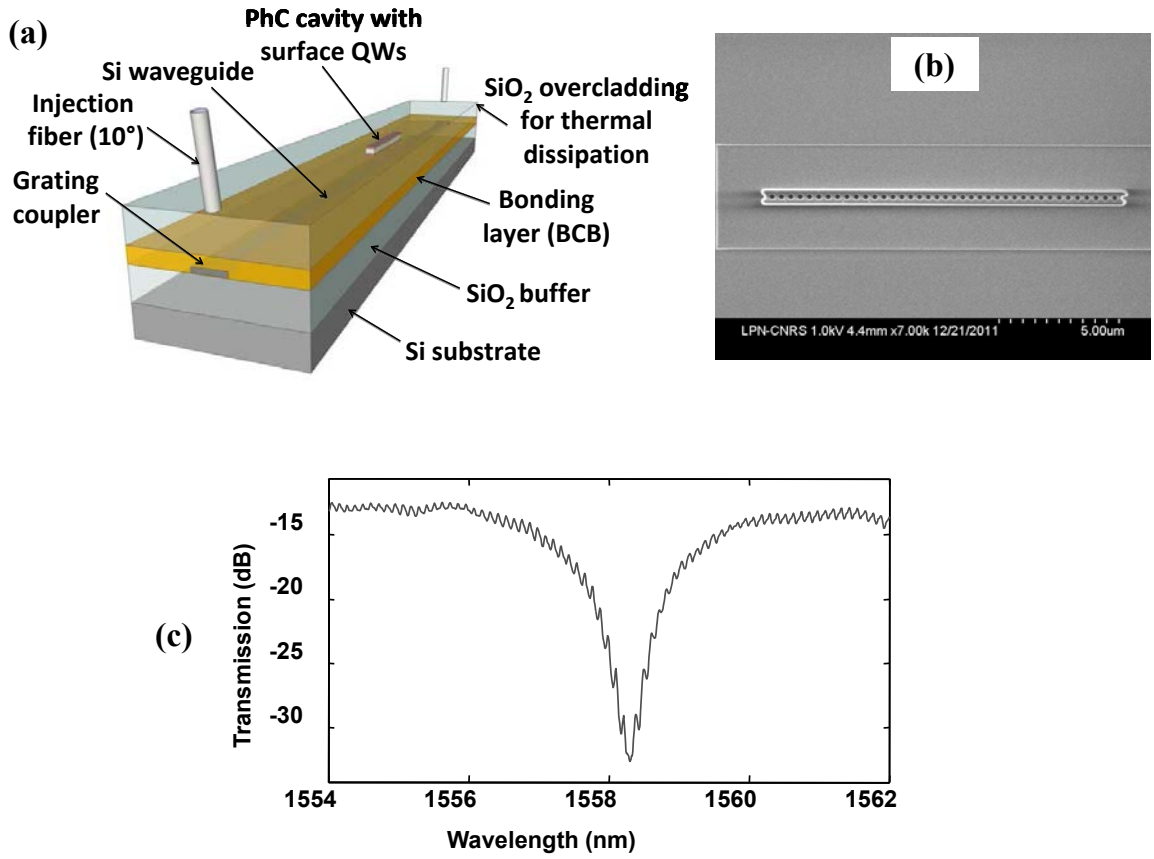


Figure III.24: (a) Device structure and (b) scanning electron microscope picture of the fabricated component. (c) Measured transmission of the cavity (resolution 0.01 nm).

intensity of the pulse. The wavelength shift is estimated to be less than 1 nm under our experimental conditions and enables power limitation, provided that the signal is slightly blue shifted compared to the resonance. The shifted resonance is actually also deeper compared to the initial static resonance, emphasizing the transmission loss [303]. By tuning the signal to a suitable wavelength, a transmission function such as the one represented in Fig. III.25(b) can be obtained, providing the intensity limitation of the input signal. This power limiting function was demonstrated to operate with an OOK signal in [305].

During my work, I have demonstrated the possibility to use this limiter to limit the NPN accumulation.

3.2 Demonstration of phase preservation of the power limiter

A first step before considering the possibility to reduce the NPN accumulation was to study if the device would modify the phase of the signal; if this was the case, it would be detrimental for the use with $M-$PSK signals. To this aim, we assessed the power limiter in an experiment using a non return-to-zero (NRZ)-QPSK signals at 20 Gbit/s exhibiting amplitude noise and estimated the bit error ratio (BER) and phase distribution of the signal.

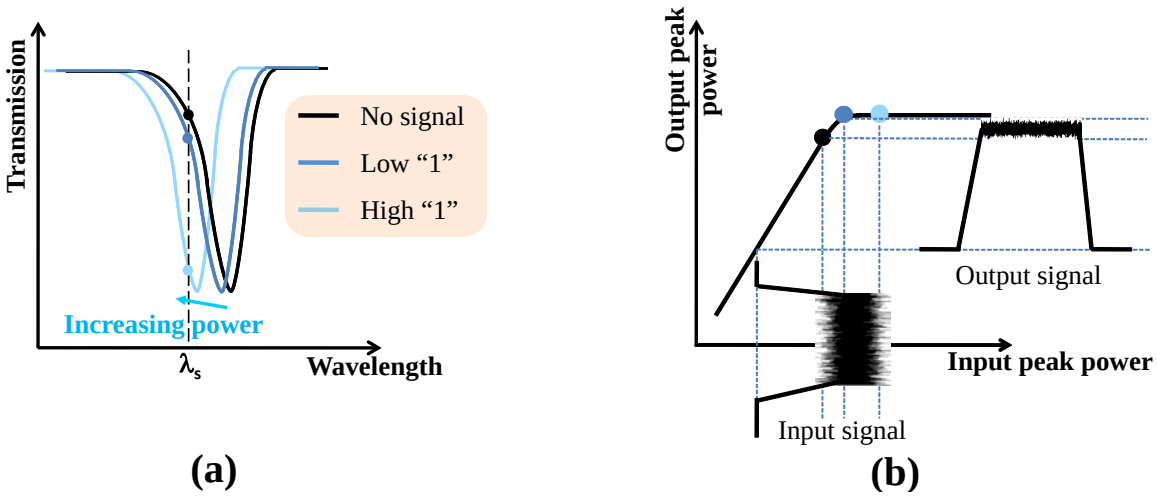


Figure III.25: (a) Principle of the power limiter function. (b) Example of the transmission function.

3.2.1 Experimental setup

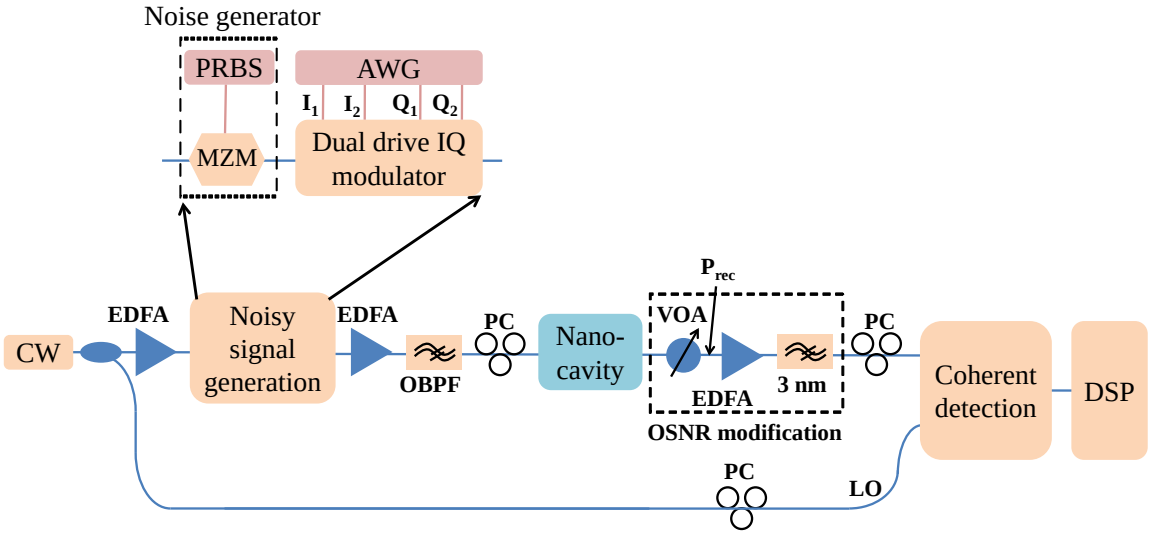


Figure III.26: Experimental setup for power-limitation of a 20-Gbit/s QPSK signal.

The power-limiter function was demonstrated using the implementation of Fig. III.26. To evaluate the potential of the device as a power limiter, intensity fluctuations were added to a 10-Gbaud QPSK signal. Intensity noise was emulated by externally modulating the output of a CW laser with a pseudo-random binary sequence (PRBS) of length $2^7 - 1$ at 10 Gbit/s, hence generating two levels of amplitude with an adjustable extinction ratio in order to tune the amplitude of the emulated noise. This signal was then modulated in an IQ modulator driven by two decorrelated PRBS sequences with lengths of $2^{15} - 1$ and $2^{23} - 1$ obtained from arbitrary waveform generators (AWGs), resulting in a 10-Gbaud NRZ-QPSK signal, each symbol point of the constellation being split into two levels of amplitude. The

artificial generation of amplitude noise may appear strange here compared to a real case, however, this first study is focused on the ability of the device to reduce amplitude noise without degrading the phase. As it will be seen later, the presence of the two amplitude levels will clearly help us to observe the power limiting function. Amplitude noise generation by OSNR degradation will be studied in the second study which is focused on the non-linear phase noise reduction in the presence of the device.

The laser wavelength is adjusted at a slightly blue shifted wavelength compared to the cavity resonance and the signal polarisation is aligned to the TE mode of the input waveguide (through a polarization controller) before being injected into the component. A variable optical attenuator (VOA) followed by an erbium-doped fiber amplifier (EDFA) and a 3 - nm optical bandpass filter (BPF) allow the adjustment of the optical signal-to-noise ratio (OSNR) at the receiver input. An optical 90° hybrid (100-Gbit/s DP-QPSK integrated receiver) mixes the QPSK signal and the local oscillator (LO). To simplify the setup, a homodyne configuration was used, with the same laser (linewidth of about 100 kHz) used at the transmitter and as LO in the receiver. The in-phase and quadrature components are then detected by balanced photodiodes with a bandwidth of 32 GHz. Finally, the electrical output signals are measured by a real-time oscilloscope with an electrical bandwidth of 16 GHz. After data acquisition at 20 GSample/s, post-processing is performed offline using the Matlab environment.

Re-timing of the samples was realized with an adaptive finite impulse response (FIR) filter [25] acting as an equalizer. After convergence of the feedback loop of the equalizer, the following processes were performed with one sample per symbol after decimating the symbol rate to 10 GSymbol/s. The offline processing was applied to blocks of $2 \cdot 10^5$ samples. The Viterbi and Viterbi algorithm for carrier phase estimation was performed on blocks of 50 samples, enabling to reconstruct the constellation. Moreover, the phase ambiguity was alleviated by processing the first 5000 samples to minimize the BER. Finally, the decoded bit sequence was compared to the transmitted one to determine the BER over 4 millions samples.

3.2.2 Results and discussions

Fig. III.27 shows examples of constellations of the received QPSK signal for an OSNR of 13 dB (defined over a 0.1-nm noise bandwidth). Compared to the reference constellation in Fig. III.27(a), the effect of the added amplitude level appears as a splitting of each phase modulation state into two lobes in the constellation diagram, as shown in Fig. III.27(b). After passing through the power-limiter, the regenerated constellation (Fig. III.27(c)) clearly indicates the effect of intensity noise suppression by merging the split lobes again, even though some residual intensity noise remains as compared to the reference constellation.

In order to investigate quantitatively the impact of the noise level, the phase modulation was removed by elevating the processed complex signal samples to the fourth power,

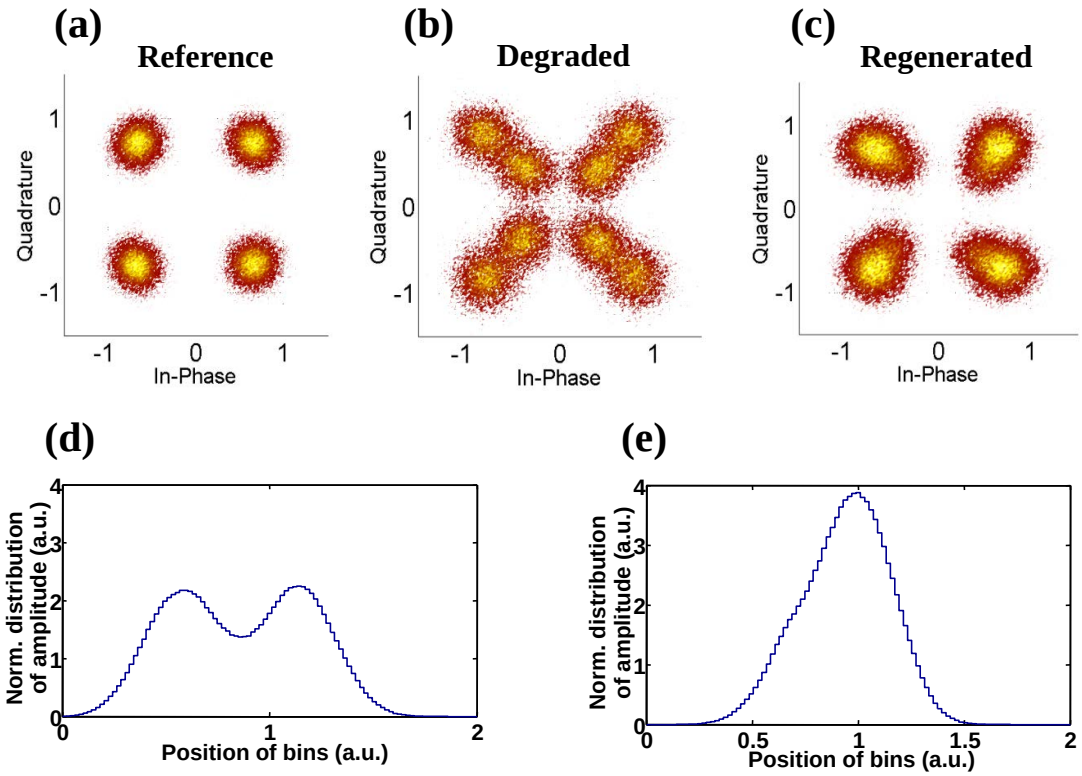


Figure III.27: Experimental constellation diagrams for OSNR at the receiver of 13 dB: (a) Reference without additional noise. (b) Degraded signal with additional noise. (c) Regenerated signal through the nanocavity. Amplitude distributions of (d) the degraded signal and (e) the regenerated signal.

so that the phase distributions of all symbols are superimposed at the same angle. The noise magnification induced by the 4^{th} power exponentiation was then compensated for by inverse operations (division by four for the phase noise and one-fourth power operation for the amplitude noise). The amplitude and phase distributions of the samples can then be calculated.

The amplitude distributions are plotted in Fig. III.27(d), in the case of the degraded signal and in Fig. III.27(e) in the regenerated case. Performance is evaluated through the introduction of the new metric $SNR_{est} = 10{\cdot}\log(\mathrm{SNR}_x^2)$, where $SNR_x = \mu_x/\sigma_x$ (as discussed in Section 2.4.3 of Part I), μ and σ are the average and standard deviation of the squared modulus of the processed signal samples, x. SNR_{est} is calculated to be 9.8 dB before regeneration and 12.2 dB in the regenerated case, showing an amplitude noise reduction of 2.4 dB.

The impact of the regenerator on the phase of the signal was investigated next for an OSNR at the receiver of 13 dB and for the same input noise level of SNR_{est} = 9.8 dB. The phase variation was evaluated by the standard deviation of the phase distribution relatively to the average value. The resulting histograms of the phase distribution obtained before and after regeneration using $2 \cdot 10^5$ symbols are depicted in Fig. III.28(a) and (b),

respectively. Fig. III.28(c) shows the evolution of the phase distribution standard deviation as a function of amplitude SNR_{est} based noise level, without regeneration in grey and with regeneration in black. It can be seen that the added amplitude noise level induces an increase of the phase noise variance. However, the standard deviation of the phase noise after the cavity is only marginally lower (about 0.02 at high amplitude noise levels) than that of the non-regenerated signal, which proves the phase-preservation of the regenerated signal. The amplitude-to-phase noise transfer induced by the amplitude noise reduction process is therefore very small.

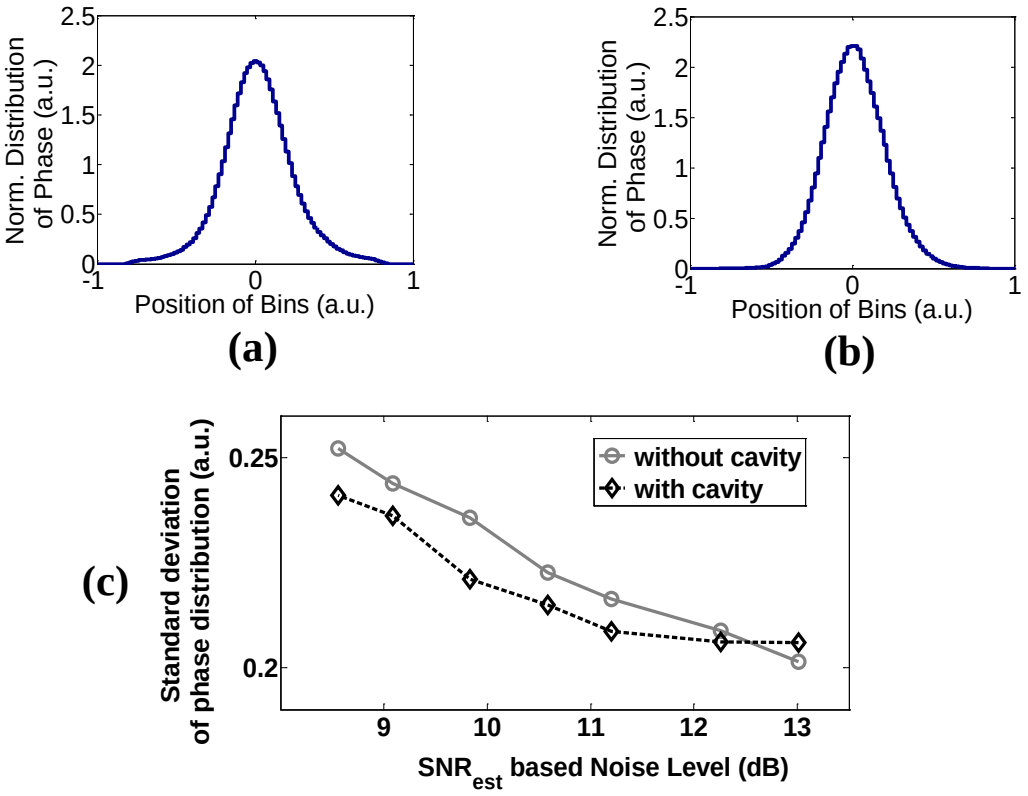


Figure III.28: Impact of the limiter on the phase (for OSNR at the receiver of 13 dB). (a) Phase histogram of the degraded signal. (b) Phase histogram of the regenerated signal. (c) Evolution of the standard deviation of the phase with the imposed amplitude noise level.

To assess this quality improvement, BER measurements were performed on signals with the same amplitude noise level as in Fig. III.28. The theoretical BER curve of a QPSK signal is plotted in Fig. III.29 (green diamonds) based on the analysis in [25]. The experimental back-to-back measurement (blue stars) matches the theoretical curve with minor differences. First, BER measurements were performed when the transmitter was tuned away from the resonance without additional amplitude noise (red empty circles). This result demonstrates that the transmission through the component does not have any impact on the signal compared to the back-to-back case. Next, the impact of the device away from its resonance on a signal with added amplitude noise was assessed by comparing the resulting BER curve (red

filled circles) with that obtained by replacing the device with an attenuator having the same insertion loss (grey filled triangles). Both curves are quite similar, which implies that the effect of the device on the BER performance is negligible when the signal wavelength is tuned away from the resonance. Finally, the measurement was performed on the degraded signal after being switched through the cavity resonance (black cross symbols). This result points out a penalty reduction of up to 6 dB at a BER of 10^{-3} compared to the degraded signal, demonstrating the efficiency of the amplitude noise limiter for phase encoded modulation formats. These results were obtained with a sub-milliwatt coupled peak power.

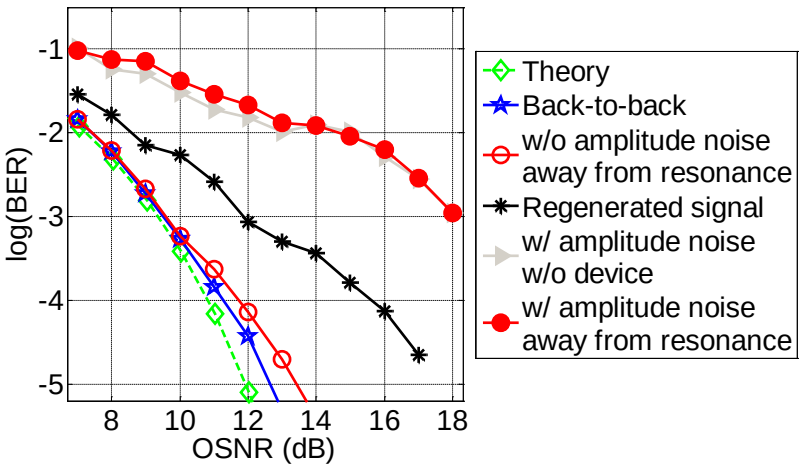


Figure III.29: BER curves of the power-limiter for 20-Gbit/s QPSK (for artificial amplitude noise level SNR_{est}=9.8 dB).

Finally, the efficiency of the device was investigated as a function of amplitude noise level. BER measurements were performed for different amplitude noise levels, as shown in Fig. III.30, with (black diamond), and without (grey circle) the device. The received OSNR is set at 10 dB corresponding to the BER of 10^{-3} in the back-to-back case and without noise. In this way, we can point out the amplitude noise level at which the device will achieve the best efficiency (by bringing back the BER to the 10^{-3} level).

As shown in Fig. III.30, the BER is severely degraded at high-amplitude noise levels compared to low noise levels. However it can be noticed that over the studied noise level range, the BER is improved by one order of magnitude after the cavity and that the improvement remains constant regardless of the input amplitude noise level. At a noise level $SNR_{est} = 13$ dB, performance similar to the back-to-back case is obtained after regeneration , confirming the effectiveness of the power-limiter.

After having demonstrated that our power limiter does not affect the phase of the signal, it is necessary to test its functionality in an optical transmission link in which the nonlinear phase noise is a major limiting factor.

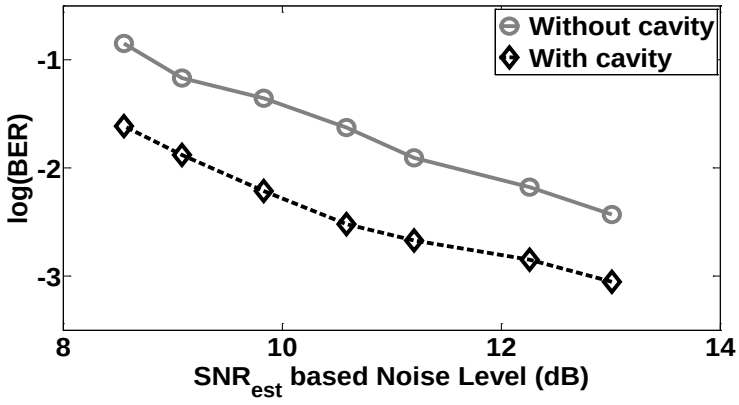


Figure III.30: Evolution of the BER as a function of the amplitude noise level for a 20 Gbit/s QPSK signal with and without power limitation (for an OSNR at the receiver of 10 dB).

3.3 Demonstration of NPN reduction in optical coherent transmission systems

In order to validate the non linear phase noise limitation performed by our power limiter we generate artificially a link in which NPN is dominant. This configuration, although not realistic from a system point of view, is a first step to study the possibility to reduce the phase noise of an optical coherent transmission system. A 10 Gbaud NRZ-QPSK link is considered in this experiment. The limiter performance is estimated in terms of BER measurements. The improvement in receiver sensitivity resulting from the use of the intensity limitation function prior to highly-nonlinear transmission demonstrates the effectiveness of the scheme for 20 Gbit/s QPSK signals.

3.3.1 Experimental setup

The experimental setup is represented in Fig. III.31. By using the same way as in Section 3.2, a NRZ-QPSK signal at 10 Gbaud is generated by applying 2 PRBS sequences to an IQ modulator. The IQ modulator output signal is then amplified by an EDFA1 and bandpass filtered. Intensity noise is added prior to nonlinear transmission by degrading the OSNR of the modulated signal. This is achieved by noise loading the signal with the output of an amplified spontaneous emission (ASE) source followed by a 1-nm OBPF and a variable optical attenuator (VOA). This noise loading is different from the previous discussion in Section 3.2 (where amplitude fluctuations were generated through an amplitude modulation by a PRBS), however, this noise loading now allows us to emulate closely the effect happening in the optical transmission link where a lot of optical amplifiers are used. At the input of the regeneration stage, the power of the signal is adjusted to 9 dBm by EDFA2 followed by a VOA. The degraded QPSK signal then enters the nanocavity-based intensity limiter with its state-of-polarization (SOP) aligned on the TE mode of the waveguide thanks to a polarization controller. The center wavelength of the signal is slightly blue-shifted with respect

to the linear cavity resonance in order to enable the previously described intensity limiting function. To be able to fairly compare the transmission performances of the noise-loaded and intensity-limited signals, a polarizer aligned with the signal SOP is used in place of the nanocavity in the former case.

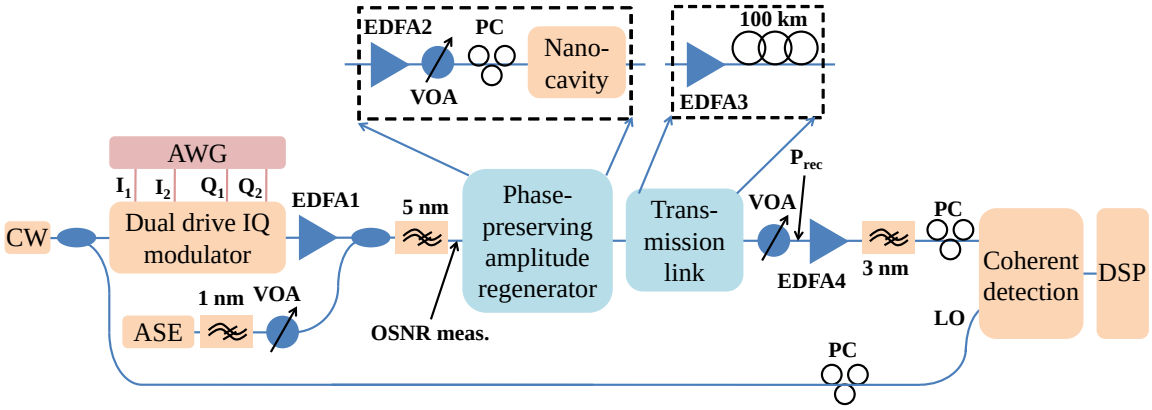


Figure III.31: Experimental setup for evaluation of NPN reduction in coherent optical transmission link.

The OSNR degradation at the transmitter side allows the generation of NPN after injecting the signal with a high power to the subsequent optical fiber link. The signal power is boosted up to 17 dBm by EDFA3 before being launched to 100-km non-zero-dispersion-shifted fiber (NZDSF, chromatic dispersion of 4 ps/(nm·km) at 1550 nm), in order to emulate the nonlinearities accumulation of a long distance transmission.

At the receiver side, another VOA followed by EDFA4 and a 3-nm OBPF are used in order to adjust the received OSNR for BER measurements. The QPSK signal and the local oscillator (LO) are mixed in an optical 90° hybrid DP-QPSK integrated coherent receiver. The in-phase and quadrature components are then detected by balanced photodiodes and acquired by a real-time oscilloscope with electrical bandwidth of 16 GHz. Finally, post-processing is performed offline using the Matlab environment after data acquisition at 20 GS/s. It should be noted that the same laser, operating at 1557 nm with a linewidth of 100 kHz, is utilized at the transmitter and as the LO in order to simplify the setup by avoiding any impact from other functionalities implemented in the DSP. In particular, carrier frequency offset compensation is not necessary.

In the first step of digital processing, an adaptive FIR filter [25] operating at twice the symbol rate is used as equalizer and applied to blocks of 20000 symbols. After stabilization of the feedback loop of the equalizer, the received samples are decimated to a symbol rate of 10 GS/s for the following processes. Phase estimation is performed by applying the widely-used Viterbi-Viterbi algorithm on blocks of 10 samples. Moreover, the first 5000 samples are processed by adding the phase rotations of (0°; 90°; 180°; 270°). The phase rotation associated to the minimum BER among four rotations is applied to all the samples, in order to remove the 4-fold phase ambiguities inherent to the unknown rotation of the constellation.

A comparison between the decoded bit sequence and the transmitted one is then performed to determine the BER over 4 million samples. The impact of NPN on the phase information is also characterized through phase distribution analysis.

3.3.2 Results and discussions

Fig. III.32 represents the constellations of the received samples, as well as the corresponding normalized distributions of the phase obtained by elevating the processed complex signal samples to the fourth power in order to suppress the information carrying phase and to superimpose all symbols at the same phase angle. Fig. III.32(a) and (d) correspond to the back-to-back (B2B) case (no transmission and no intensity limitation) for a received OSNR (over 0.1 nm) of 18 dB. Fig. III.32(b) and (e) are obtained after transmission over 100 km without the intensity limiter for an OSNR at the link input of 18 dB and a received power of -20 dBm. The observed dispersion of the constellations and broadening of the phase distributions are due to NPN. Finally, Fig. III.32(c) and (d) are obtained after transmission over 100 km in the regenerated case under the same input OSNR and power conditions, showing a less dispersed constellation and a narrower phase distribution.

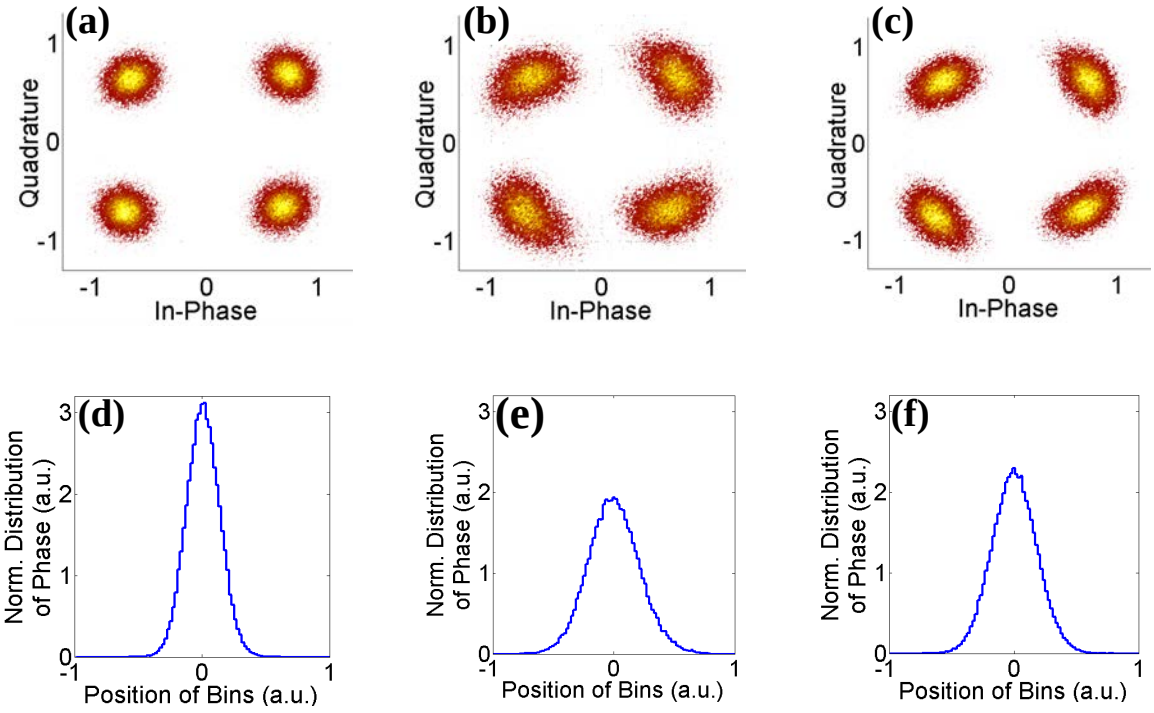


Figure III.32: Constellations and phase distributions at a transmitted OSNR of 18 dB for (a), (d): back-to-back; (b), (e): 100 km transmission without intensity limitation, and (c), (f): 100 km transmission with intensity limitation.

Fig. III.33 presents the results of BER measurements as a function of received power in different cases. Back-to-back curves were measured for transmitter OSNR values of 18 dB and 33 dB. Linear phase noise due to ASE is dominant in the former case, as shown by

the power penalty of 3.4 dB at a BER of 10^{-3}. After transmission without prior intensity limitation, an error floor at a BER of 10^{-3} is obtained when the input OSNR is 18 dB, showing that the link is indeed limited by NPN. When the intensity limiter is applied, the BER floor for an input OSNR of 18 dB is reduced by two orders of magnitude. This demonstrates that NPN is reduced, proving the efficiency of the device for limiting the impact of intensity fluctuations due to OSNR degradation before non-linear transmission.

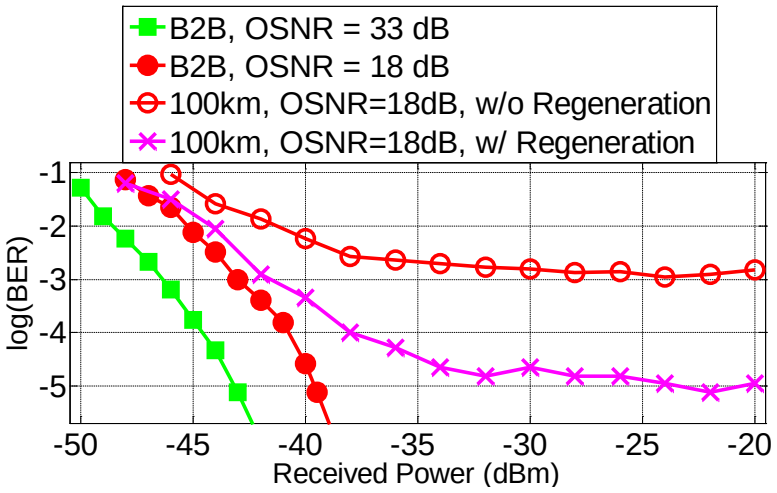


Figure III.33: BER curves back-to-back and after transmission without and with intensity limitation for input OSNR values of 18 dB and 33 dB.

Finally, Fig. III.34 shows the results of BER measurements as a function of the transmitter OSNR for a constant received power of -20 dBm with (circles) and without (squares) regeneration, showing a BER improvement over the entire considered OSNR range. Moreover, the required OSNR for a BER of 10^{-3} is relaxed by more than 3.5 dB thanks to the device.

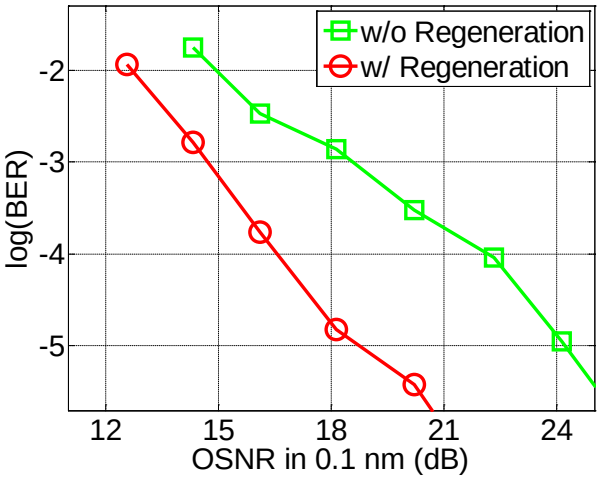


Figure III.34: BER versus input OSNR (P_{rec} = -20 dBm).

4. Conclusion

In this part, we have proposed several alternative solutions for DSP in both LOS and high bit rate coherent transmission systems . Particularly, two IQ imbalance compensation methods have been proposed and validated in a typical IQ imbalance range of $[-30°, 30°]$. One method, called maximum SNR estimation method (MSEM), is operating independently from other DSP steps and is experimentally validated with 10 Gbaud QPSK signal. This method was compared to the existed GSOP method, showing the similar performance while the implementation complexity of the proposed method is reduced. The second IQ imbalance compensation method relies on a compensator which can be integrated in the equalizer to reduce the complexity. This method is experimentally studied with 16-QAM signals and can be extended to any $M-$QAM signals. The comprehensive theoretical analysis of the IQ imbalance problem is carried out and numerically characterized with the optical transmission systems where the chromatic dispersion effects are dominant.

An improved carrier recovery based on circular harmonic expansion (CHE) algorithm possibly functioning with any kind of bi-dimensional modulation format signals is proposed and numerically validated up to 128-QAM. More specifically, the carrier frequency offset (CFO) compensation is proposed to cascade CHE algorithm with another gradient-descent algorithm to improve the estimation. Sharing the same CHE-based lookup table with CFO compensation, CPE is proposed to combine with another maximum likelihood (ML) estimator stage to refine the constellation. This proposed method is then compared to the Viterbi-Viterbi monomial phase estimation (VVMPE-ML) and blind phase search (BPS) methods. It is shown that the proposed improved method provides less complexity and computational efforts than the two other methods while keeping the similar laser linewidth tolerance as for BPS method (normally the benchmark for the comparisons).

The discussed DSPs have been used to characterize an all-optical regeneration transmission system. The phase preserving and power limiting function based on a photonic crystal nanocavity is proposed and experimentally investigated in detail. The validation of the power limiter is carried out with a 10 Gbaud QPSK signal, showing the effectiveness of the regenerating component. Moreover, the capability of nonlinear phase noise reduction in an optical transmission link is also studied. The results show that the proposed power limiter function is a promising solution for all-optical signal regeneration. Some perspectives and future work are also discussed.

CONCLUSION

Optical coherent communications play an important role in telecommunication networks to deal with future capacity demands. Especially, thanks to the recent offered possibilities of the high speed digital circuits, the coherent detection in conjunction with bi-dimensional modulation formats and digital signal processing (DSP) have become an attractive solution to achieve high spectral efficiency and high overall bit rate per channel. In this case, the technical challenges have been transferred to the limitations in electrical devices, in which the analog-to-digital converter (ADC) at the receiver side is the major bottleneck due to its limited bandwidth, sampling rate and the quantization accuracy. In order to work with 100 Gb/s and beyond, the development of faster ADCs and suitable algorithms used in DSPs is still a challenging issue. Developing an optical sampling technique allowing to relax the ADC bandwidth requirement and associated algorithms for DSP were the main objectives of my thesis. Due to the pluridisciplinary nature of this task, my PhD thesis was conducted both at FOTON and CAIRN IRISA/INRIA laboratories.

To overcome this bandwidth limitation, the linear optical sampling (LOS) technique was chosen in my work. This technique indeed happened to be of double interest in both teams as LOS was also to be implemented in the frame of a national research program (OCELOT project), which was aiming at developing a linear optical sampling oscilloscope for optical signal visualization. I had hence the chance to contribute to this project by being involved in the experimental setup implementation and validation.

My work can be classified into two major categories. Firstly, I have contributed to the implementation and validation of the linear optical sampling prototype setup in the frame of OCELOT project. Secondly, all the DSP algorithms developed for the prototype have been improved and opened to other applications in high-speed optical communication context. The detail contributions are summarized as follows

Linear optical sampling prototype implementation and validation

Signals to be sampled were first needed to be generated. Each typical modulation format has been generated at 10 Gbaud, for example, the optical OOK signal (typical format of ASK signals), the optical QPSK signal (typical format of PSK signals) and the optical 16-QAM signal (typical format of QAM signals). Although there is still a few impairments in

the signal generation (due to the limited bandwidth of devices), it should be noted that the optical 16-QAM signals has been successfully generated for the first time in our laboratory.

Based on these available signals, the LOS setup has been then implemented and validated. The idea behind the LOS technique is the use of a short-pulse train with low timing jitter (in the order of tens of femtoseconds), named pulsed-LO, at low repetition rate to sample the high bit rate optical signal (i.e. $M-$PSK, $M-$QAM). After that, these two signals are mixed into a 90° optical hybrid which creates two components (in-phase and quadrature) in each state of polarization. Based on these two components, the full picture of data signals can be reconstructed in terms of eye diagram and constellation diagram with the help of DSP stage. This technique relaxed limitations of optoelectronic converters and ADC bandwidths thanks to the undersampling process. The LOS prototype has been successfully validated with 10 Gbaud NRZ-OOK, QPSK and 16-QAM signals. The proposal for improving the setup chain performance has also been made.

Several degradations in the recovered signal have been observed, and diverse hypothesis in order to improve the signal quality were then investigated in both optical and electrical parts. More specifically, the influence of the ADC parameters (which is the heart of the electrical part) in this technique has been comprehensively assessed for some important parameters that may be helpful for the system design. The impacts of the ADC bandwidth, integration time and effective number of bits (ENOB) were experimentally and numerically investigated with OOK and QPSK signals. It was found that 0.2 ns integration time of ADC (5 GS/s equivalent), effective number of bit (ENOB) of 6 bits and at least 2 GHz BW are needed to be able to get a good 10 Gbaud signal reconstruction with the chosen pulsed-LO.

Then, the impact of the pulsed-LO parameters (namely the timing jitter, the OSNR and the extinction ratio (ER) of the LO-source) in the current configuration have been studied in details. Whereas it was shown numerically that timing jitter and OSNR should not affect the reconstructed signal in our setup, the pulsed-LO extinction ratio happens to be at the origin of the limited quality of our reconstructed signal. The limited ER, inherent to the use of a Mach-Zehnder modulator (MZM) to decrease the LO repetition rate, has been proved for its significant impact on the signal reconstruction. The impact of pulsed-LO ER is analytically, numerically and experimentally demonstrated in a simple homodyne case. The results show that at least 35 dB pulsed-LO ER is required to be able to completely recover the signals. This cannot unfortunately be obtained with the current MZM ER (in order of 20 dB). An electro-absorption modulator (EAM) could be a good candidate with potential ER better than 30 dB.

Some developed DSPs for LOS application, in turn, become interesting solutions for high bit rate signal transmission that have constituted the second major contribution of my PhD work.

DSP algorithms for high speed optical communication and their applications

DSP is indispensable in the coherent detection-based high bit-rate transmission systems. Thanks to DSP, the linear and possibly nonlinear impairments can be completely compensated for. During this work, our concern was focused on the compensation of linear impairments which come from either the imperfection of devices (i.e. electrical signal generator, modulator) or transmission media (i.e. fiber). More particularly, three kinds of impairment, composed of the IQ imbalance, the carrier frequency offset (CFO) and the laser phase noise, have been numerically and experimentally studied in the context of optical coherent communications, in conjunction with the proposed algorithms for these impairments compensation.

For IQ imbalance compensation, two new IQ imbalance compensation methods have been proposed and validated in a typically practical IQ phase imbalance range of $[-30°, 30°]$. The first original method, called the maximum SNR estimation method (MSEM), operates independently compared to other DSP steps and this method was experimentally validated with 10 Gbaud QPSK signal. The comprehensive theoretical analysis of the IQ imbalance problem has also been carried out. Based on this analysis, the proposed MSEM method can perfectly compensate for the IQ imbalance with a phase imbalance inferior to 15°. However, the phase estimation error of 3.5° was observed when the phase imbalance was increased to 30°. Fortunately, this small residual phase estimation error (in the case of the high phase imbalance value) can be compensated by simply adding a deterministic value to the estimated phase imbalance, based on the analytical results (i.e. Fig. III.1). The second IQ compensation method concerned the integration of an IQ compensator (being placed after the finite impulse response (FIR) filters) into an equalizer to reduce the complexity. Compared to the current IQ compensation-based equalizer method, the proposed method avoids the use of trigonometric and square-root functions, providing simplification in the FPGA implementation. Moreover, the IQ compensator is placed after the FIR filters, yielding no algorithmic noise to be transmitted to the FIR coefficient updates, as compared to the case where IQ imbalance is placed before FIR filters. This method was experimentally studied with 10 Gbaud 16-QAM signals (but it possibly works with any $M-$QAM signal) and numerically characterized with an optical transmission system limited by chromatic dispersion (CD) effects. The proposed equalizer still remained other functions (i.e. CD compensation) after the integration with the IQ compensator. At 10° phase imbalance, a 7 dB power penalty can be completely compensated for. When the phase imbalance increased to 20°, the proposed structure can be experimentally compensated for with fewer than 5 dB power penalty. The residual power penalty could be due to the IQ imbalance experimentally generated at the transmitter side. This penalty disappeared in the numerical validation with the IQ imbalance generated at the receiver side.

For the carrier recovery in coherent optical communication, an improved method based on circular harmonic expansion (CHE) algorithm possibly functioning with any kind of bi-

dimensional modulation format signal has been proposed and numerically validated up to 128-QAM, for the first time, in optical coherent communications context. More specifically, the improved proposed carrier frequency offset (CFO) compensation consists in cascading CHE algorithm (acting as the coarse compensation) with the gradient-descent algorithm (acting as the fine compensation) to improve the estimation. Compared to the existing algorithms, the proposed CFO compensation has improved the laser linewidth tolerance of the system (Fig. III.19) and the required samples for the CFO estimation are fewer than in other methods (Fig. III.18) while keeping the similar estimation accuracy.

Sharing the same CHE-based lookup table with CFO compensation, CPE is proposed to be combined with another maximum likelihood (ML) estimator stage to refine the constellation. This proposed method is then compared to the Viterbi-Viterbi monomial phase estimation (VVMPE-ML) and blind phase search (BPS) methods. It is shown that the proposed improved method provides less complexity and computational efforts than the two other methods while keeping the similar laser linewidth tolerance as for BPS method (normally the benchmark for the comparisons). The tolerable laser linewidth is falling into the linewidth range of available commercial external cavity lasers (ECLs), thus confirming the effectiveness of the proposed carrier recovery method.

The developed DSPs have then been used to characterize an all-optical regeneration transmission system where the nonlinear phase noise is normally dominant. Benefitting from the PhD work of [289] in the laboratory, the phase preserving and power limiting function based on a photonic crystal nanocavity has been proposed and experimentally investigated in detail with the phase modulated signals. The validation of the power limiter was carried out with a 10 Gbaud QPSK signal, showing the effectiveness of the regenerating component. The capability of nonlinear phase noise reduction in an optical transmission link has been also demonstrated after 100 km transmission of a 10 Gbaud QPSK signal. The results show that the proposed power limiter function is a promising solution for all-optical signal regeneration.

All the studies dedicated in this thesis provide some perspectives and future works with respect to each aforementioned contribution.

Perspectives

- *For linear optical sampling technique:* besides the visualization of high bit-rate optical signals, inline optical performance monitoring (in terms of OSNR, chromatic dispersion) will be also expected by using this technique; the recovered signal quality will be expected to be further improved by solving the limited extinction ratio issue of pulsed-LO (i.e. using EAM instead of MZM); the higher bit rate signal (order of hundreds Gbaud) and the higher modulation level ($>$ 16-QAM) could be used to investigate the LOS system limitation in which the effects of jitter and ENOB would now become more critical; DSPs in LOS would also need to be optimized to ensure

the equivalent time operation with shorter refresh rates (order of ms per acquisition).

- *For the proposed algorithms used in the optical communication:* the MSEM-based IQ imbalance compensation is expected to work with more complex modulation formats ($M-$QAM): this is to be validated. The joint IQ imbalance compensation and equalizer need to extend in the presence of polarization mode dispersion (PMD), timing jitter; the carrier recovery based on CHE algorithm should be experimentally validated using more harmonics to achieve a better estimation; the integration of IQ imbalance compensation and CHE-based carrier recovery could also be investigated.

Part IV

Appendices

A. Expected value calculation of modified received QPSK signal in MSEM algorithm for IQ imbalance compensation

We should remind that QPSK signal at the transmitter is assumed to have unit power and ϕ_S is the information carrying phase which takes on the values $(2k+1)\pi/4$, $k = 0, 1, 2, 3$ with the same probability. The transmitted QPSK signal is then detected by the coherent receiver and transformed to the baseband by the low-pass filter. ϕ_{mis} represents the phase imbalance which cancels for an ideal orthogonality between the projection of I and Q components on the complex plane.

We would recall the expression of the I and Q components as follows

$$\begin{cases} I = \cos\phi_S + n_C \\ Q = \sin\left(\phi_S + \phi_{mis}\right) + n_C \sin\phi_{mis} + n_S \cos\phi_{mis} \end{cases}, \tag{A.1}$$

where n_C and n_S are random Gaussian variables with the same variance σ^2 and assumed to be decorrelated. The MSEM method consists in modifying the complex received signal, $r_x = I + j \cdot Q$, by adding a phase shift, ϕ_{var}, to form a new quantity $Q_n = \Im r_x \cdot exp(j \cdot \phi_{var})$ and consider as a new quadrature component. The relevant SNR_r is defined by

$$SNR_r = \frac{\mathbf{E}^2\left(|r|^2\right)}{\sigma^2_{|r|^2}}, \tag{A.2}$$

where $\mathbf{E}(\cdot)$ and $|\cdot|$ are the mean and modulus operators, respectively. $\sigma^2_{|r|^2}$ represents the variance of the square modulus of the modified signal, $r = I + j \cdot Q_n$.

After some mathematical manipulation, Q_n can be written as

$$\begin{aligned} Q_n = {} & \cos\phi_S \cdot \sin\phi_{\text{var}} + \sin\left(\phi_S + \phi_{mis}\right) \cdot \cos\phi_{\text{var}} \\ & + n_C \sin\phi_{\text{var}} + \left(n_C \sin\phi_{mis} + n_S \cos\phi_{mis}\right) \cdot \cos\phi_{\text{var}}. \end{aligned} \tag{A.3}$$

To simplify the calculations, the following quantities are defined

$$\begin{cases} U = \cos\phi_S \\ V = \alpha\cos\phi_S + \beta\sin\phi_S \\ X = n_C \\ Y = \alpha n_C + \beta n_S \\ \alpha = \sin\phi_{\text{var}} + \sin\phi_{mis}\cos\phi_{\text{var}} \\ \beta = \cos\phi_{mis}\cos\phi_{\text{var}} \end{cases}. \tag{A.4}$$

The modified signal is then rewritten as

$$r = I + j\cdot Q_n = (U+X) + j\cdot(V+Y). \tag{A.5}$$

Based on the definition of SNR_r metric in (A.2), the new random variable R^2 equal to the squared modulus of r needs to be considered

$$R^2 = (U+X)^2 + (V+Y)^2. \tag{A.6}$$

From (A.6), the expected value of R^2 is calculated as follows

$$\mathbf{E}\left\{(U+X)^2+(V+Y)^2\right\} = \mathbf{E}\left\{\left(U^2+V^2\right)\right\} + \mathbf{E}\left\{\left(X^2+Y^2\right)\right\} + 2\mathbf{E}\left(UX\right) + 2\mathbf{E}\left(VY\right). \tag{A.7}$$

It must be noted that the expected value of U, V, X and Y is zero. On the other hand, U and X, V and Y are uncorrelated so that the last two terms of (A.7) cancel. Moreover, ϕ_S is uniformly distributed over the four values $(2k+1)\pi/4$, $k=0,1,2,3$. Using the quantities defined in (A.4), the variances of U, V and their co-variance can be retrieved as

$$\mathbf{E}\left(U^2\right) = \frac{1}{2}, \quad \mathbf{E}\left(V^2\right) = \frac{1}{2}\left(\alpha^2+\beta^2\right), \quad \mathbf{E}\left(UV\right) = \frac{\alpha}{2}. \tag{A.8}$$

As mentioned, n_C and n_S are random Gaussian variables with the same variance σ^2. The variances of X, Y and their covariance are

$$\mathbf{E}\left(X^2\right) = \sigma^2, \quad \mathbf{E}\left(Y^2\right) = \sigma^2\left(\alpha^2+\beta^2\right), \quad \mathbf{E}\left(XY\right) = \alpha\sigma^2. \tag{A.9}$$

Finally, the expected value of R^2 is derived as in (III.5)

$$\mathbf{E}\left(R^2\right) = \left(\frac{1}{2}+\sigma^2\right)\cdot\left(1+\alpha^2+\beta^2\right). \tag{A.10}$$

B. Variance calculation of modified received QPSK signal in MSEM algorithm for IQ imbalance compensation

The variance of R^2 (defined in (A.6)) can be written as

$$\sigma^2_{|r|^2} = \mathbf{Var}\left(R^2\right) = \mathbf{E}\left(R^4\right) - \left[\mathbf{E}\left(R^2\right)\right]^2. \tag{B.1}$$

Due to the assumption of central and uncorrelated variables, some terms cancel and the expectation of R^4 can be written as

$$\begin{aligned}\mathbf{E}\left(R^4\right) = \mathbf{E}\left[\left(U^2+V^2\right)^2\right] + \mathbf{E}\left[\left(X^2+Y^2\right)^2\right] \\ + 2\mathbf{E}\left[\left(U^2+V^2\right).\left(X^2+Y^2\right)\right] + 4\mathbf{E}\left[\left(UX+VY\right)^2\right].\end{aligned} \tag{B.2}$$

Based on the definition of the QPSK signal, (U^2+V^2) is a random discrete variable taking on two equiprobable values, $1/2(1+(\alpha+\beta)^2)$ and $1/2(1+(\alpha-\beta)^2)$. The first term of (B.2) can then be derived as

$$\mathbf{E}\left[\left(U^2+V^2\right)^2\right] = \frac{1}{4}\left[\left(1+\alpha^2+\beta^2\right)^2 + 4\alpha^2\beta^2\right]. \tag{B.3}$$

The second term of (B.2) is calculated using the fact that all the moments of a Gaussian variable can be derived from its variance [306]. More specifically, the fourth order moments of (X,Y) can be written as

$$\begin{cases}\mathbf{E}\left[X^4\right] = 3\sigma^4 \\ \mathbf{E}\left[Y^4\right] = 3\left(\alpha^2+\beta^2\right)^2\sigma^4 \\ \mathbf{E}\left[X^2Y^2\right] = \mathbf{E}\left[n_C^2\left(\alpha n_C+\beta n_S\right)^2\right] = \left(3\alpha^2+\beta^2\right)\sigma^4\end{cases}. \tag{B.4}$$

Therefore, the second term of (B.2) is given by

$$\mathbf{E}\left\{\left(X^2+Y^2\right)^2\right\} = \left[3+2\left(3\alpha^2+\beta^2\right)+3\left(\alpha^2+\beta^2\right)^2\right]\sigma^4. \tag{B.5}$$

(U^2+V^2) and (Y^2+X^2) are independent random variables. The third term of (B.2) is then achieved

$$\begin{aligned}\mathbf{E}\left[\left(U^2+V^2\right).\left(X^2+Y^2\right)\right] &= \mathbf{E}\left[\left(U^2+V^2\right)\right]\cdot\mathbf{E}\left[\left(X^2+Y^2\right)\right] \\ &= \tfrac{\sigma^2}{2}\left(1+\alpha^2+\beta^2\right)^2.\end{aligned} \tag{B.6}$$

Due to the independence property between the variables (U,V) and (X,Y), the last term of (B.2) can be reformulated as

$$\mathbf{E}\left[(UX+VY)^2\right] = \mathbf{E}\left[U^2\right]\mathbf{E}\left[X^2\right] + 2\mathbf{E}\left[UV\right]\cdot\mathbf{E}\left[XY\right] + \mathbf{E}\left[V^2\right]\mathbf{E}\left[Y^2\right]. \tag{B.7}$$

The last term is expressed as

$$\mathbf{E}\left[(UX+VY)^2\right] = \left(\alpha^2 + \frac{1+\left(\alpha^2+\beta^2\right)^2}{2}\right)\cdot\sigma^2. \tag{B.8}$$

From (B.3), (B.5), (B.6) and (B.8), the variance of R^2 is finally derived as in (III.7)

$$\sigma^2_{|r|^2} = \mathbf{Var}\left(R^2\right) = \alpha^2\beta^2 + 2\left(1+2\alpha^2+\left(\alpha^2+\beta^2\right)^2\right)\cdot\left(1+\sigma^2\right)\cdot\sigma^2. \tag{B.9}$$

C. Angle differential coding and decoding for $M-$QAM signal

$M-$QAM signal is represented by M possible symbols on the constellation in which each symbol contains $m = log_2 M$ bits. In differential encoding, a group of m bits is mapped onto one of the M possible transitions between two consecutive symbols, $S(k-1)$ and $S(k)$. Although various differential encoding methods have been reported as in Ref. [281] and the references therein, the angle differential encoding/decoding scheme for square $M-$QAM [282] and the differentially Gray encoding/decoding for cross $M-$QAM [256] are used in this paper because of its easy employment and sufficient recovery of 4-fold ambiguity. The following subsections will discuss the differential encoding/decoding methods. The simulation is carried out over 130 000 symbols for the bit-error-rate (BER) calculations with a 20-loops for each calculation before taking the average values.

C.1 Square $M-$QAM

The angle differential encoding for square $M-$QAM is carried out by dividing each group of m bits into $m/2$ subgroups of 2 bits, namely dibit. After that $m/2$ differential angles $\{\Delta\theta_1, \Delta\theta_2, ..., \Delta\theta_{m/2}\}$ are used to express the transition between two consecutive symbols. The first dibit specifies the first differential angle $\Delta\theta_1$, whereas the second differential angle $\Delta\theta_2$ is determined by the second dibit and so on. The same mapping rule for each dibit to the differential angle is described in Tab. C.1.

In principle, each $M-$QAM complex symbol can be presented as a summation of $m/2$

Table C.1: Rule for mapping two bits to differential angle.

$b_1 b_2$	**Angle mapping**
00	0
01	$\pi/2$
10	$3\pi/2$
11	π

terms

$$S(k) = s_1(k) + s_2(k) + ... + s_{m/2}(k), \tag{C.1}$$

in which the terms are updated by the following differential encoding rules

$$\begin{array}{rcl} s_1(k) & = & s_1(k-1)\, e^{j\Delta\theta_1(k)} \\ s_2(k) & = & s_2(k-1)\, e^{j\Delta\theta_2(k)} \\ ... & & \\ s_{m/2}(k) & = & s_{m/2}(k-1)\, e^{j\Delta\theta_{m/2}(k)} \end{array}, \tag{C.2}$$

and each term is calculated as follows

$$s_n(k) = 2^{\left(\frac{m}{2}-n\right)} \cdot \sqrt{2} \cdot e^{j\frac{(2l-1)\pi}{4}} = R_n \cdot e^{j\frac{(2l-1)\pi}{4}}, \tag{C.3}$$

where $n = 1, 2, ..., m/2$ is the index of each term in (C.1) and $l = 1, 2, 3, 4$ corresponds to four possible positions of each dibit. Fig. C.1(a) shows an example for differentially encoding 64-QAM. In this case, $s_1(k)$ represents the center (star symbols) of the four 16-QAM constellation with the radius R_1 of $4\sqrt{2}$. Moreover, $s_2(k)$ is the displacement vector to specify the center (hexagonal symbols) of the four 4-QAM constellation with the radius R_2 of $2\sqrt{2}$. Finally, $s_3(k)$ is used to determine the differential encoding symbols with the radius R_3 of $\sqrt{2}$. The placement of each symbol is normally associated with an amplitude scaling factor, to get unity energy of the modulation scheme. For the square $M-$QAM, the scaling amplitude factor is calculated as $\sqrt{2/3(M-1)}$ (as shown in Appendix D).

After carrier recovery (CR), the received sample, $x(k)$ is affected by the unknown phase ambiguity, $\varphi \in \{0, \pi/2, \pi, 3\pi/2\}$ and distorted by the additive white Gaussian noise (AWGN). Fig. C.1(b) presents the block diagram of the multi-stage differential decoding scheme for square $M-$QAM. In the first step, the rotated quadrant center is found by using

$$\widehat{s}_1(k) = R_1 \cdot \{\mathrm{sgn}[\Re(x(k))] + j \cdot \mathrm{sgn}[\Im(x(k))]\}, \tag{C.4}$$

where *sgn* is the *signum* function. $\Re$ and $\Im$ represent the real and imaginary parts of samples, respectively. Based on two consecutive values, $\hat{s}_1(k-1)$ and $\hat{s}_1(k)$, the first differential angle $\Delta\hat{\theta}_1(k)$ corresponding to the first dibit is detected by the following rule

$$\Delta\widehat{\theta}_1(k) = \begin{cases} 0 & \text{if } \widehat{s}_1(k) \cdot \widehat{s}_1^*(k-1) = R_1 \\ \pi/2 & \text{if } \widehat{s}_1(k) \cdot \widehat{s}_1^*(k-1) = j \cdot R_1 \\ 3\pi/2 & \text{if } \widehat{s}_1(k) \cdot \widehat{s}_1^*(k-1) = -j \cdot R_1 \\ \pi & \text{if } \widehat{s}_1(k) \cdot \widehat{s}_1^*(k-1) = -R_1 \end{cases}, \tag{C.5}$$

where $*$ denotes the complex conjugate operator. In the next step, other displacement

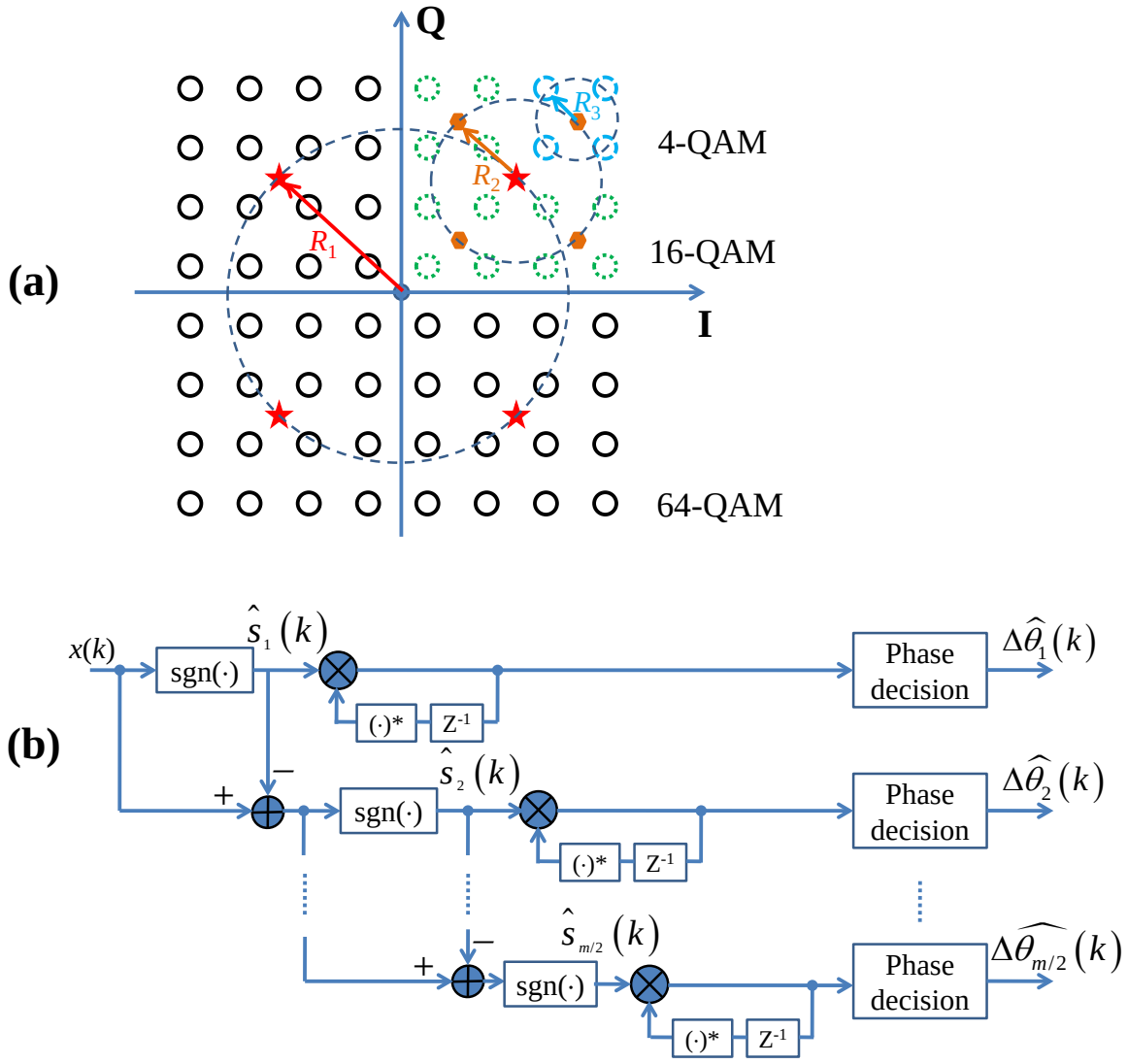


Figure C.1: (a) Angle differential multi-stage encoding scheme for 4-, 16-, 64-QAM. (b) Multi-stage decoding scheme of angle differential square $M-$QAM receiver.

vectors are calculated as follows

$$\hat{s}_t(k) = R_t \cdot \left\{ \text{sgn}\left[\Re\left(x(k) - \sum_{i=1}^{t-1} \hat{s}_i(k) \right) \right] + j \cdot \text{sgn}\left[\Im\left(x(k) - \sum_{i=1}^{t-1} \hat{s}_i(k) \right) \right] \right\}, \quad \text{(C.6)}$$

with $t = 2, 3, ..., m/2$. The differential angle $\Delta\hat{\theta}_t(k)$ and the respective dibit are similarly decided as in (C.5) using the corresponding R_t. Based on these differential angles, the corresponding dibits can be de-mapped using Tab. C.1. In consequence, the $M-$QAM received symbols can be correctly determined regardless of the phase ambiguity. Fig. C.2 shows the calculated BERs of the square $M-$QAM (16-, 64- and 256-QAM) symbols using differential encoding and Gray mapping under the corruption of AWGN. The signal to noise ratio (SNR) penalty of less than 1 dB is observed at the BER of 10^{-3}, showing the good

performance of the angle differential encoding.

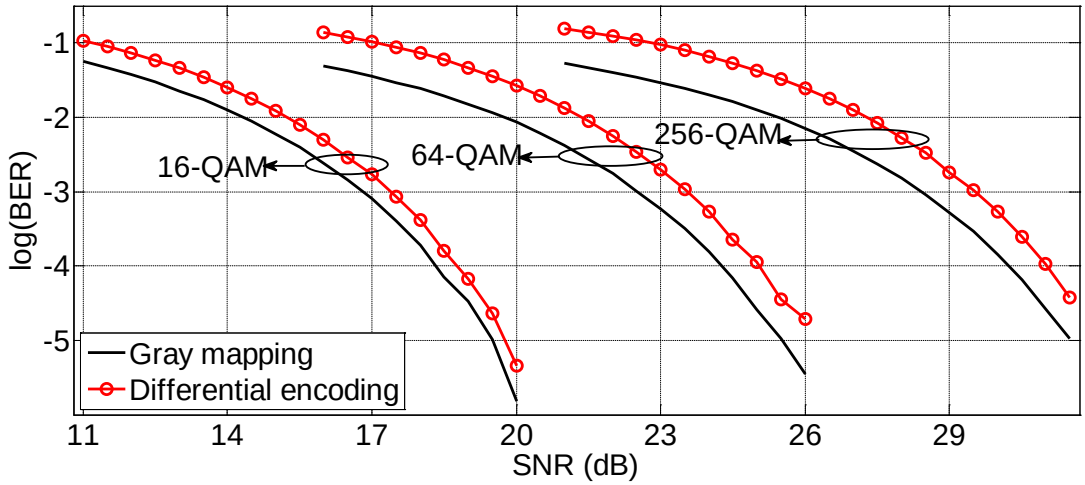


Figure C.2: BER calculation of square $M-$QAM (16-, 64- and 256-QAM) using Gray mapping and differential encoding.

C.2 Cross $M-$QAM

Cross $M-$QAM constellation used in this work is symmetric over the abscissa and the ordinate of the inphase/quadrature (IQ) plane, in which the number of bits, m, in each symbol can be presented as $m = 2 \cdot p + 1$, with $p \geq 2$. For cross $M-$QAM constellation, the angle differential encoding as aforementioned is no longer valid. However, the 4-fold ambiguity in cross $M-$QAM can be recovered by only differentially encoding the first dibit incorporating to Gray mapping the other bits [256]. Although it doesn't have any general formulation and also depends on each cross $M-$QAM constellation, this method can be used to validate and to compare the different CR algorithms.

As in square $M-$QAM, a group of m bits is mapped onto M possible positions on the constellation, in which the first dibit are differentially encoded following the rule as in square $M-$QAM. This encoding is used to remove the 4-fold ambiguity by marking the quadrant in the complex plane based on the transition between two consecutive symbols. The other bits are then Gray mapped to specify the symbols position in each quadrant. Note that, the Gray mapping for cross $M-$QAM cannot be perfect with the minimum Hamming distance between 2 adjacent symbols due to the asymmetric of the cross $M-$QAM [25]. Fig. C.3 illustrates the bits to symbol assignment for 32-QAM signal, corresponding to the groups of 5 bits mapped onto 32 possible positions on the constellation based on the discussed rule. The normalized constellation to get the unity energy can be done with the scaling factor before the transmission. For the cross $M-$QAM, the scaling factor is calculated as $\sqrt{(M-2)/3 + 5 \cdot 2^{(\log_2 M - 4)}}$ (as shown in Appendix E).

At the detection, the first dibit in the group is firstly determined based on the rule as

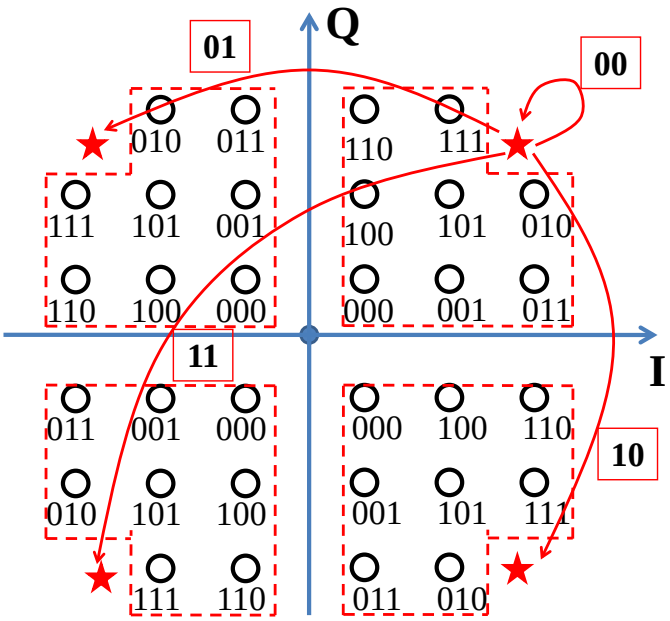


Figure C.3: Bits to symbol assignment of 32-QAM using the first 2 bits for differential encoding of the quadrant and Gray mapping the other bits.

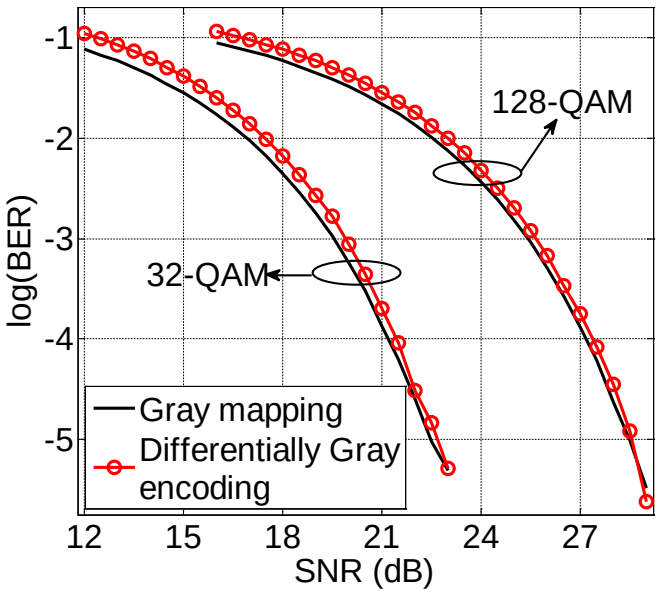


Figure C.4: BER calculation of cross $M-$QAM (32- and 128-QAM) using Gray mapping and differential encoding.

in square $M-$QAM. Finally, the other bits are Gray de-mapped to get the bit sequence. The similar simulations for 32- and 128-QAM are carried out with both Gray mapping and differentially Gray encoding. Fig. C.4 presents the BER calculation for the cross $M-$QAM signals corrupted by the AWGN. The results show a negligible SNR penalty of using differentially Gray encoding comparing to pure Gray mapping, while the capability of removing

the 4-fold ambiguity is still remained.

D. Energy of square $M-$QAM

In general, for any $M-$QAM modulation, the symbols are equidistantly placed to each other and divided equally between the four quadrants in its constellation diagram. Typically, the placement of each symbol is associated with an amplitude scaling factor, which is necessary to normalize the average energy of the modulation scheme to unity. The symbols are placed along the odd integer multiples of the amplitude scaling factor along both the abscissa and ordinate, with the even integer multiplies of the amplitude scaling factor acting as the decision boundaries for demodulation. The energy scaling factor is the reciprocal of the average symbol energy of a constellation diagram, and thus, the amplitude scaling factor becomes the square root of the energy scaling factor. The actual locations of each symbol are established by dividing the odd integers by the square root of the calculated average symbol energy.

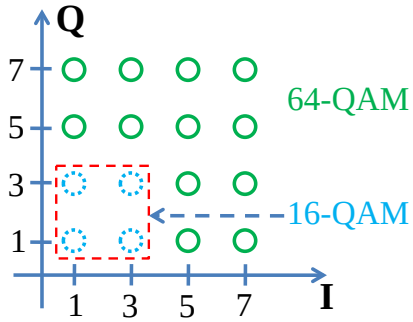


Figure D.1: Examples of the first quadrants for square (16- and 64-QAM) $M-$QAM.

Assuming that the square $M-$QAM symbols are independent and identically distributed (i.i.d) and have the equal Gaussian distribution. The alphabets of $M-$QAM is presented as follows

$$C_m = \{\pm(2u+1) \pm (2u+1) \cdot j\}, \tag{D.1}$$

in which $m = 1, 2, ..., M$ and $u = 0, 1, ..., \sqrt{M}/2 - 1$.

The energies of real and imaginary parts should be similar to each other due to the same

distribution between symbols. The energy of square $M-$QAM signal is then given by

$$\begin{aligned} E_{sM-QAM} &= \mathbf{E}\left[|C_m|^2\right] \\ &= \mathbf{E}\left[|\Re\{C_m\}|^2\right] + \mathbf{E}\left[|\Im\{C_m\}|^2\right] \\ &= 2\cdot\mathbf{E}\left[|\Re\{C_m\}|^2\right], \end{aligned} \tag{D.2}$$

where $\mathbf{E}(\cdot)$ is the expectation operator. $\Re$ and $\Im$ denote the real and imaginary parts of the signal, respectively. Because of symmetric constellation, each quadrant consists of $M/4$ constellation points. Moreover, the elements of each alphabet is used $\sqrt{M}/2$ times by both real and imaginary parts in each quadrant. Without loss the generality, the first quadrant is considered. Fig. D.1 show the examples of the first quadrants of 16- and 64-QAM constellation, where 2 and 4 elements of the alphabet are used in this quadrant, respectively. Based on this observation, (D.2) can be re-written as follows

$$\begin{aligned} E_{sM-QAM} &= 2\cdot\frac{\sqrt{M}/2}{M/4}\cdot\sum_{u=0}^{\sqrt{M}/2-1}(2u+1)^2 \\ &= \frac{16}{\sqrt{M}}\sum_{u=0}^{\sqrt{M}/2-1}[u\cdot(u+1)]+2. \end{aligned} \tag{D.3}$$

If S_n is called for the summation of 2 multiplied consecutive integer number, $S_n = 1\cdot2+2\cdot3+...+u\cdot(u+1)$, by multiplying a factor of 3 on both sides of S_n, we can obtain

$$\begin{aligned} 3\cdot S_n &= 1\cdot2\cdot3+2\cdot3\cdot3+3\cdot4\cdot3+...+u\cdot(u+1)\cdot3 \\ &= 1\cdot2\cdot3+2\cdot3\cdot(4-1)+3\cdot4\cdot(5-2)+... \\ &\quad +u\cdot(u+1)\cdot((u+2)-(u-1)) \\ &= u\cdot(u+1)\cdot(u+2). \end{aligned} \tag{D.4}$$

Therefore, we can deduce the expression of S_n as follows

$$\begin{aligned} S_n &= 1\cdot2+2\cdot3+3\cdot4+...+u\cdot(u+1) \\ &= \tfrac{u\cdot(u+1)\cdot(u+2)}{3}. \end{aligned} \tag{D.5}$$

Substituting (D.5) into (D.3), the energy of square $M-$QAM signal is given by

$$E_{sM-QAM} = \frac{2}{3}(M-1). \tag{D.6}$$

E. Energy of cross $M-$QAM

Considering the cross $M-$QAM symbols with $M = 2 \cdot (2p+1)$, the value of p is hence calculated as

$$p = \frac{1}{2}\left(\log_2 M - 1\right). \tag{E.1}$$

In this study, the M is chosen no less than 32, corresponding to $p \geq 2$. Taking the similar assumption and observation as in square $M-$QAM, the energy of cross $M-$QAM signal is as follows

$$E_{cM-QAM} = 2 \cdot \mathbf{E}\left[\left|\Re\left\{C_m\right\}\right|^2\right]. \tag{E.2}$$

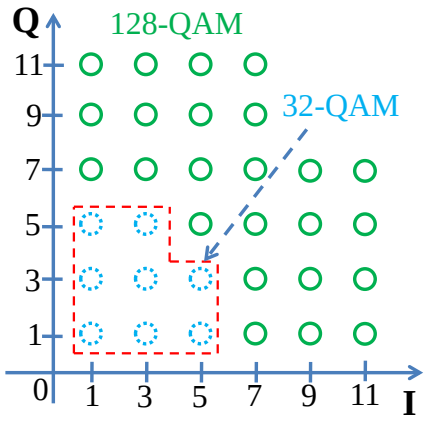


Figure E.1: Examples of the first quadrants for cross (32- and 128-QAM) $M-$QAM.

In each quadrant, there are always $M/4$ points due to the symmetry of constellation. It can be observed that we have $\left(\sqrt{M/8} + 2^{p-2}\right)$ elements of each alphabet in each quadrant. Considering the first quadrant, $2p-2$ biggest elements are appeared at the outermost corner of the constellation. If the energy of all elements appearing in one quadrant is taken into account, we should exclude the energy introduced by the $2p-2$ biggest elements to get the energy of cross $M-$QAM constellation. Fig. E.1 shows the examples of the first quadrants of 32- and 128-QAM, in which we have 3 and 6 elements of each alphabet with the outermost corner receiving the element $\{+5\}$ and $\{+9, +11\}$, respectively. In consequence, the energy

of cross $M-$QAM constellation is calculated by

$$E_{cM-QAM} = \frac{8}{M} \cdot \left[a \sum_{u=0}^{a-1} (2u+1)^2 - 2^{p-2} \sum_{u=b}^{a-1} (2u+1)^2 \right]. \tag{E.3}$$

with $a = \left(\sqrt{M/8} + 2^{p-2} \right)$ and $b = \sqrt{M/8}$.

Or the energy can be represented as

$$E_{cM-QAM} = \frac{8}{M} \cdot \left[\sqrt{\frac{M}{8}} a + 2^{p-2} b + \sqrt{2M} \sum_{u=0}^{a-1} u\,(2u+1) + 2^n \sum_{u=b}^{a-1} u\,(2u+1) \right]. \tag{E.4}$$

Substituting a, b and (D.5) into (E.4), we can get the following result

$$E_{cM-QAM} = \frac{M-2}{3} + 5 \cdot 2^{(\log_2 M - 4)}. \tag{E.5}$$

List of Publications

Peer-reviewed journal articles

[1] **T. -H. Nguyen**, K. Lengle, A. Bazin, L. Bramerie, C. Peucheret, M. Gay, O. Sentieys, J. -C. Simon, R. Raj and F. Raineri, "Phase-preserving power limiting function using InP on SoI photonic crystal nanocavity," *IEEE Photon. Technol. Lett.*, vol. 25, no. 12, pp. 1215-1218, Jun. 2014.

[2] **T. -H. Nguyen**, F. Gomez-Agis, L. Bramerie, M. Gay, J. -C. Simon and O. Sentieys, "Impact of sampling-source extinction ratio in linear optical sampling," *IEEE Photon. Technol. Lett.*, vol. 25, no. 7, pp. 663-666, Apr. 2013.

Peer-reviewed conference proceeding

[1] **T. -H. Nguyen**, M. Joindot, P. Scalart, M. Gay, L. Bramerie, O. Sentieys, and J. -C. Simon, "Carrier phase recovery for optical coherent M-QAM communication systems using harmonic decomposition-based maximum loglikelihood estimators," in *Proc. of the Signal Processing in Photonics Communications (SPPcom2015)*, MA, USA, Jul. 2015, paper SpT4D.3.

[2] **T. -H. Nguyen**, M. Joindot, P. Scalart, M. Gay, L. Bramerie, O. Sentieys, and J. -C. Simon, "Carrier frequency offset estimation based on circular harmonic expansion for optical coherent M-QAM communication systems," in *Proc. of the IEEE Opto Electronics and Communications Conference (OECC2015)*, Shanghai, China, Jul. 2015.

[3] **T. -H. Nguyen**, P. Scalart, M. Joindot, M. Gay, L. Bramerie, C. Peucheret, A. Carer, O. Sentieys, and J. -C. Simon, "Joint simple blind IQ imbalance compensation and adaptive equalization for 16-QAM optical communications," in *Proc. of the IEEE International Conference on Communications (ICC 2015)*, UK, Jun. 2015, pp. 6529-6534.

[4] **T. -H. Nguyen**, M. Gay, L. Bramerie, K. Lengle, C. Peucheret, O. Sentieys, J. -C. Simon, A. Bazin, R. Raj, and F. Raineri, "Nonlinear phase noise reduction for

20-Gbit/s NRZ-QPSK signals using InP on SOI photonic crystal nanocavity," in *Proc. of Optical Fiber Communication (OFC 2015)*, CA, USA, Mar. 2015, paper Tu2F.3.

[5] **T. -H. Nguyen**, F. Gomez-Agis, M. Gay, L. Anet-Neto, P. Scalart, C. Peucheret, M. Joindot, O. Sentieys, J. -C. Simon, and L. Bramerie, "IQ imbalance compensation based on maximum SNR estimation in coherent QPSK systems," in *Proc. of the 16th International Conference on Transparent Optical Networks (ICTON2014)*, Graz, Austria, Jul. 2014, paper Tu.C1.3.

[6] **T. -H. Nguyen**, F. Gomez-Agis, L. Bramerie, M. Gay, J. -C. Simon, and O. Sentieys, "Impact of extinction ratio in linear optical sampling," in *Proc. of the 7th International Conference on Photonics and Applications (ICPA-7)*, Ho Chi Minh, Vietnam, Nov. 2012.

Peer-reviewed French conference proceeding

[1] **T. -H. Nguyen**, M. Gay, F. Gomez-Agis, S. Lobo, E. Borgne, M. Joindot, O. Sentieys, J. -C. Simon, et L. Bramerie, "Limitation des convertisseurs analogique numériques pour les techniques d'échantillonnage optique linéaire," in *Proc. of Journée Nationales de l'Optique Guidée (JNOG 2015)*, Rennes, France, Jul. 2015.

[2] M. Gay, F. Gomez-Agis, **T. -H. Nguyen**, A. O'Hare, L. Bramerie, S. Lobo, E. Borgne, C. Peucheret, et J. -C. Simon, "Autocorrelateur optique linéaire," in *Proc. of Journée Nationales de l'Optique Guidée (JNOG 2015)*, Rennes, France, Jul. 2015.

[3] **T. -H. Nguyen**, M. Gay, L. Bramerie, K. Lengle, C. Peucheret, O. Sentieys, J. -C. Simon, A. Bazin, R. Raj et F. Raineri, "Réduction du bruit de phase non-linéaire d'un signal NRZ-QPSK à 20 Gbit/s grâce à une nanocavité à cristal photonique," in *Proc. of Journée Nationales de l'Optique Guidée (JNOG 2014)*, Nice, France, Oct. 2014.

[4] **T. -H. Nguyen**, F. Gomez-Agis, M. Gay, L. Anet-Neto, J. -C. Simon, P. Scalart, O. Sentieys, and L. Bramerie, "Nouvelle méthode de compensation du déséquilibre en quadrature pour des systèmes QPSK," in *Proc. of Journée Nationales de l'Optique Guidée (JNOG 2013)*, Paris, France, Oct. 2013.

To be submitted

[1] **T. -H. Nguyen**, M. Joindot, P. Scalart, M. Gay, L. Bramerie, F. Gomez-Agis, C. Peucheret, O. Sentieys and J. -C. Simon, "Analytical and experimental demonstration of maximum SNR estimation-based IQ imbalance compensation in coherent QPSK systems," *aiming to submit to J. Lightw. Technol.*, 2015.

[2] **T. -H. Nguyen**, M. Gay, L. Bramerie, C. Peucheret, O. Sentieys, J. -C. Simon, P. Scalart and M. Joindot, "Joint blind feedforward carrier recovery for quadrature-amplitude modulation using the circular harmonic expansion-based maximum loglikelihood estimators," *aiming to submit to J. Lightw. Technol.*, 2015.

[3] **T. -H. Nguyen**, M. Gay, L. Bramerie, C. Peucheret, O. Sentieys, J. -C. Simon, P. Scalart and M. Joindot, "Block and sliding window averaging CPE for M-QAM using harmonic expansion-based maximum loglikelihood estimators," *aiming to submit to IEEE Photon. Technol. Lett.*, 2015.

[4] **T. -H. Nguyen**, M. Gay, F. Gomez-Agis, S. Lobo, E. Borgne, C. Peucheret, M. Joindot, O. Sentieys, J. -C. Simon, and L. Bramerie, "Experimental investigation of ADC parameters impacts on linear optical sampling systems," *aiming to submit to IEEE Photon. Technol. Lett.*, 2015.

Bibliography

[1] G. Agrawal, *Applications of nonlinear fiber optics*. Academic press, 2001.

[2] E. Desurvire, *Erbium-doped fiber amplifiers : principles and applications*. Hoboken, N.J: Wiley-Interscience, 2002.

[3] M. Joindot and S. Gosselin, "Optical fiber transport systems and networks: fundamentals and prospects," *Comptes Rendus Physique*, vol. 9, no. 9-10, pp. 914–934, Nov. 2008.

[4] C. Laperle, B. Villeneuve, Z. Zhang, D. McGhan, H. Sun, and M. O'Sullivan, "Wavelength division multiplexing (WDM) and polarization mode dispersion (PMD) performance of a coherent 40Gbit/s dual-polarization quadrature phase shift keying (DP-QPSK) transceiver," in *Optical Fiber Communication Conference*. Optical Society of America, 2007, p. PDP16.

[5] [Online]. Available: http://www.oiforum.com/public/documents/OIF_DPC_RX-01.0.pdf.

[6] S. J. Savory, "Digital filters for coherent optical receivers," *Opt. Express*, vol. 16, no. 2, pp. 804–817, Jan 2008.

[7] [Online]. Available: http://www.fujitsu.com/emea/news/pr/fseu-en_20130312-1054-fujitsu-adc-28nmcmos-converter.html

[8] P. Pupalaikis and M. Schnecker, "A 30 GHz bandwidth, 80 GS/s sample rate real-time waveform digitizing system," in *Optical Fiber Communication (OFC), collocated National Fiber Optic Engineers Conference, 2010 Conference on (OFC/NFOEC)*, March 2010, pp. 1–3.

[9] G. Raybon, B. Guan, A. Adamiecki, P. Winzer, N. Fontaine, S. Chen, P. Pupalaikis, R. Delbue, K. Doshi, B. Bhat, A. Blankman, A. Konczykowska, J.-Y. Dupuy, and F. Jorge, "160-Gbaud coherent receiver based on 100-GHz bandwidth, 240-GS/s analog-to-digital conversion," in *Optical Fiber Communications Conference and Exhibition (OFC), 2015*, March 2015, pp. 1–3.

[10] G. C. Valley, "Photonic analog-to-digital converters," *Opt. Express*, vol. 15, no. 5, pp. 1955–1982, Mar 2007.

[11] C. Dorrer, D. Kilper, H. Stuart, G. Raybon, and M. Raymer, "Linear optical sampling," *Photonics Technology Letters, IEEE*, vol. 15, no. 12, pp. 1746–1748, Dec 2003.

[12] J. K. Fischer, R. Ludwig, L. Molle, C. Schmidt-Langhorst, C. C. Leonhardt, A. Matiss, and C. Schubert, "High-speed digital coherent receiver based on parallel optical sampling," *Journal of Lightwave Technology*, vol. 29, no. 4, pp. 378–385, Feb. 2011.

[13] C. Dorrer, C. Doerr, I. Kang, and R. Ryf, "High-sensitivity high-resolution linear sampling up to 640 Gb/s using 90°-waveguide optical hybrid," in *Lasers and Electro-Optics, 2004. (CLEO). Conference on*, vol. 2, May 2004, pp. 2 pp. vol.2–.

[14] C. Zhang, Y. Mori, K. Igarashi, K. Katoh, and K. Kikuchi, "Ultrafast operation of digital coherent receivers using their time-division demultiplexing function," *Journal of Lightwave Technology*, vol. 27, no. 3, pp. 224–232, Feb. 2009.

[15] J.-X. Cai, Y. Sun, H. G. Batshon, M. Mazurczyk, H. Zhang, D. G. Foursa, and A. N. Pilipetskii, "54 Tb/s transmission over 9150 km with optimized hybrid Raman-EDFA amplification and coded modulation," in *Optical Communication (ECOC), 2014 European Conference on*. IEEE, 2014, pp. 1–3.

[16] R. W. Tkach, "Scaling optical communications for the next decade and beyond," *Bell Labs Technical Journal*, vol. 14, no. 4, pp. 3–9, Feb. 2010.

[17] "Cisco visual networking index: Forecast and methodology, 2013-2018," in *white paper*, Jun. 2014. [Online]. Available: http://www.cisco.com/c/en/us/solutions/collateral/service-provider/ip-ngn-ip-next-generation-network/white_paper_c11-481360.pdf

[18] P. J. Winzer, "High spectral-efficiency optical modulation formats," *Journal of Lightwave Technology*, vol. 30, no. 24, pp. 3824–3835, Dec. 2012.

[19] A. E. Willner, S. Khaleghi, M. R. Chitgarha, and O. F. Yilmaz, "All-optical signal processing," *Journal of Lightwave Technology*, vol. 32, no. 4, pp. 660–680, Feb. 2014.

[20] H. Takara, A. Sano, T. Kobayashi, H. Kubota, H. Kawakami, A. Matsuura, Y. Miyamoto, Y. Abe, H. Ono, K. Shikama *et al.*, "1.01-Pb/s (12 SDM/222 WDM/456 Gb/s) crosstalk-managed transmission with 91.4-b/s/Hz aggregate spectral efficiency," in *European Conference and Exhibition on Optical Communication*. Optical Society of America, 2012, pp. Th–3.

[21] T. L. Nguyen, "Road to Terabit optical communications systems," in *IEEE Circuits and Systems Society seminar*, 2014. [Online]. Available: http://sites.ieee.org/scv-cas/files/2014/01/2014Nguyen.pdf

[22] I. Kaminow, *Optical fiber telecommunications IV*. San Diego: Academic Press, 2002.

[23] G. P. Agrawal, *Lightwave Technology Telecommunication Systems*. Hoboken, NJ: Wiley, 2005.

[24] G.-P. Agrawal, *Fiber-optic communication systems*. New York: Wiley, 2010.

[25] J. Proakis, *Digital communications*. Boston: McGraw-Hill, 2001.

[26] C. Fludger, T. Duthel, D. van den Borne, C. Schulien, E.-D. Schmidt, T. Wuth, J. Geyer, E. De Man, Khoe Giok-Djan, and H. de Waardt, "Coherent equalization and POLMUX-RZ-DQPSK for robust 100-GE transmission," *Journal of Lightwave Technology*, vol. 26, no. 1, pp. 64–72, Jan. 2008.

[27] P. C. Becker, *Erbium-doped fiber amplifiers fundamentals and technology*. San Diego: Academic Press, 1999.

[28] W. Shieh, X. Yi, Y. Ma, and Q. Yang, "Coherent optical OFDM: has its time come?[invited]," *Journal of Optical Networking*, vol. 7, no. 3, pp. 234–255, 2008.

[29] J.-X. Cai, "100G transoceanic length transmission with high spectral efficiency using bandwidth constrained PDM-QPSK," in *Optical Fiber Communication Conference*. Optical Society of America, 2011, p. OMI3.

[30] P. Winzer, A. Gnauck, C. Doerr, M. Magarini, and L. Buhl, "Spectrally efficient long-haul optical networking using 112-Gb/s polarization-multiplexed 16-QAM," *Journal of Lightwave Technology*, vol. 28, no. 4, pp. 547–556, Feb. 2010.

[31] Y. Koizumi, K. Toyoda, M. Yoshida, and M. Nakazawa, "1024 QAM (60 Gbit/s) single-carrier coherent optical transmission over 150 km," *Optics express*, vol. 20, no. 11, pp. 12 508–12 514, 2012.

[32] S. Beppu, K. Kasai, M. Yoshida, and M. Nakazawa, "2048 QAM (66 Gbit/s) single-carrier coherent optical transmission over 150 km with a potential SE of 153 bit/s/Hz," *Optics Express*, vol. 23, no. 4, p. 4960, Feb. 2015.

[33] J.-X. Cai, C. R. Davidson, A. Lucero, H. Zhang, D. G. Foursa, O. V. Sinkin, W. W. Patterson, A. N. Pilipetskii, G. Mohs, and N. S. Bergano, "20 Tbit/s transmission over 6860 km with sub-Nyquist channel spacing," *Journal of Lightwave Technology*, vol. 30, no. 4, pp. 651–657, Feb. 2012.

[34] C. R. Davidson, C. J. Chen, M. Nissov, A. Pilipetskii, N. Ramanujam, H. D. Kidorf, B. Pedersen, M. A. Mills, C. Lin, M. I. Hayee, and others, "1800 Gb/s transmission of one hundred and eighty 10 Gb/s WDM channels over 7000 km using the full EDFA C-band," in *Optical Fiber Communication Conference*. Optical Society of America, 2000, p. PD25.

[35] A. H. Gnauck, G. Raybon, S. Chandrasekhar, J. Leuthold, C. Doerr, L. Stulz, A. Agarwal, S. Banerjee, D. Grosz, S. Hunsche, and others, "2.5 Tb/s (64x42.7 Gb/s) transmission over 40x100 km NZDSF using RZ-DPSK format and all-Raman-amplified spans," in *Optical Fiber Communication Conference*. Optical Society of America, 2002, p. FC2.

[36] G. P. Agrawal, *Fiber-optic communication systems*. New York: Wiley-Interscience, 2002.

[37] H. C. H. Mulvad, M. Galili, L. K. Oxenløwe, H. Hu, A. T. Clausen, J. B. Jensen, C. Peucheret, and P. Jeppesen, "Demonstration of 5.1 Tbit/s data capacity on a single-wavelength channel," *Optics Express*, vol. 18, no. 2, pp. 1438–1443, 2010.

[38] J. Zhang, Z. Dong, H.-C. Chien, Z. Jia, Y. Xia, and Y. Chen, "Transmission of 20× 440-Gb/s super-Nyquist-filtered signals over 3600 km based on single-carrier 110-GBaud PDM QPSK with 100-GHz grid," in *Optical Fiber Communication Conference*. Optical Society of America, 2014, pp. Th5B–3.

[39] J.-X. Cai, O. Sinkin, H. Zhang, Y. Sun, A. Philipetskii, G. Mohs, and N. Bergano, "ISI compensation up to Nyquist channel spacing for strongly filtered PDM-RZ-QPSK using multi-tap CMA," in *National Fiber Optic Engineers Conference*. Optical Society of America, 2012, pp. JW2A–47.

[40] M. Salsi, C. Koebele, P. Tran, H. Mardoyan, E. Dutisseuil, J. Renaudier, M. Bigot-Astruc, L. Provost, S. Richard, P. Sillard *et al.*, "Transmission of 96× 100gb/s with 23% super-FEC overhead over 11680 km, using optical spectral engineering," in *Optical Fiber Communication Conference*. Optical Society of America, 2011, p. OMR2.

[41] R. Cigliutti, A. Nespola, D. Zeolla, G. Bosco, A. Carena, V. Curri, F. Forghieri, Y. Yamamoto, T. Sasaki, and P. Poggiolini, "Ultra-long-haul transmission of 16x112 Gb/s spectrally-engineered DAC-generated Nyquist-WDM PM-16QAM channels with 1.05x(symbol-rate) frequency spacing," in *Optical Fiber Communication Conference*. Optical Society of America, 2012, pp. OTh3A–3.

[42] G. Colavolpe, T. Foggi, A. Modenini, and A. Piemontese, "Faster-than-Nyquist and beyond: how to improve spectral efficiency by accepting interference," *Optics express*, vol. 19, no. 27, pp. 26 600–26 609, 2011.

[43] J. Yu, Z. Dong, X. Xiao, Y. Xia, S. Shi, C. Ge, W. Zhou, N. Chi, and Y. Shao, "Generation, transmission and coherent detection of 11.2 Tb/s (112× 100 Gb/s) single source optical OFDM superchannel," in *Optical Fiber Communication Conference and Exposition (OFC/NFOEC), 2011 and the National Fiber Optic Engineers Conference*. IEEE, 2011, pp. 1–3.

[44] J. Yu, Z. Dong, H.-C. Chien, Z. Jia, M. Gunkel, and A. Schippel, "Field trial Nyquist-WDM transmission of 8× 216.4 Gb/s PDM-CSRZ-QPSK exceeding 4 b/s/Hz spectral efficiency," in *National Fiber Optic Engineers Conference*. Optical Society of America, 2012, pp. PDP5D–3.

[45] X. Zhou, L. Nelson, P. Magill, R. Issac, B. Zhu, D. Peckham, P. Borel, and K. Carlson, "4000 km transmission of 50 GHz spaced, 10×494.85-Gb/s hybrid 32-64 QAM using cascaded equalization and training-assisted phase recovery," in *National Fiber Optic Engineers Conference*. Optical Society of America, 2012, pp. PDP5C–6.

[46] S. L. Jansen, I. Morita, T. C. Schenk, and H. Tanaka, "Long-haul transmission of 16× 52.5 Gbits/s polarization-division-multiplexed OFDM enabled by MIMO processing," *Journal of Optical Networking*, vol. 7, no. 2, pp. 173–182, 2008.

[47] X. Liu, S. Chandrasekhar, P. Winzer, B. Zhu, D. Peckham, S. Draving, J. Evangelista, N. Hoffman, C. Youn, Y. Kwon *et al.*, "3× 485-Gb/s WDM transmission over 4800 km of ULAF and 12× 100-GHz WSSs using CO-OFDM and single coherent detection with 80-GS/s ADCs," opt. fiber commun. conf./nat," in *Fiber Opt. Eng. Conf*, 2011.

[48] A. J. Lowery, L. B. Du, and J. Armstrong, "Performance of optical OFDM in ultralong-haul WDM lightwave systems," *Journal of Lightwave Technology*, vol. 25, no. 1, pp. 131–138, Jan. 2007.

[49] D. Qian, M.-F. Huang, S. Zhang, P. N. Ji, Y. Shao, F. Yaman, E. Mateo, T. Wang, Y. Inada, T. Ogata *et al.*, "Transmission of 115×100G PDM-8QAM-OFDM channels with 4 bits/s/Hz spectral efficiency over 10181 km," in *European Conference and Exposition on Optical Communications*. Optical Society of America, 2011, p. Th13.

[50] W. Shieh, "OFDM for flexible high-speed optical networks," *Journal of Lightwave Technology*, vol. 29, no. 10, pp. 1560–1577, May 2011.

[51] S. Zhang, M.-F. Huang, F. Yaman, E. Mateo, D. Qian, Y. Zhang, L. Xu, Y. Shao, I. Djordjevic, T. Wang *et al.*, "40×117.6 Gb/s PDM-16QAM OFDM transmission over 10181 km with soft-decision LDPC coding and nonlinearity compensation," in *National Fiber Optic Engineers Conference*. Optical Society of America, 2012, pp. PDP5C–4.

[52] S. Chandrasekhar, X. Liu, B. Zhu, and D. W. Peckham, "Transmission of a 1.2-Tb/s 24-carrier no-guard-interval coherent OFDM superchannel over 7200-km of ultra-large-area fiber," *ECOC 2009*, 2009.

[53] Y.-K. Huang, M.-F. Huang, D. Qian, Y. Shao, E. Ip, T. Inoue, Y. Inada, T. Ogata, Y. Aoki, and T. Wang, "4×1.15-Tb/s DP-QPSK superchannel transmission over 10181-km of EDFA amplified hybrid large-core/ultra low-loss fiber spans with 2-dB

FEC margin," in *Communications and Photonics Conference and Exhibition, 2011. ACP. Asia.* IEEE, 2011, pp. 1–6.

[54] H. Masuda, E. Yamazaki, A. Sano, T. Yoshimatsu, T. Kobayashi, E. Yoshida, Y. Miyamoto, S. Matsuoka, Y. Takatori, M. Mizoguchi *et al.*, "13.5-Tb/s (135 × 111-Gb/s/ch) no-guard-interval coherent OFDM transmission over 6,248 km using SNR maximized second-order DRA in the extended L-band," in *National Fiber Optic Engineers Conference.* Optical Society of America, 2009, p. PDPB5.

[55] J.-X. Cai, Y. Cai, Y. Sun, C. Davidson, D. Foursa, A. Lucero, O. Sinkin, W. Patterson, A. Pilipetskii, G. Mohs *et al.*, "112×112 Gb/s transmission over 9360 km with channel spacing set to the baud rate (360% spectral efficiency)," in *Optical Communication (ECOC), 2010 European Conference on.* IEEE, 2010, pp. 1–3.

[56] Jin-Xing Cai, Yi Cai, C. R. Davidson, D. G. Foursa, A. Lucero, O. Sinkin, W. Patterson, A. Pilipetskii, G. Mohs, and N. S. Bergano, "Transmission of 96×100-Gb/s bandwidth-constrained PDM-RZ-QPSK channels with 300% spectral efficiency over 10610 km and 400% spectral efficiency over 4370 km," *Journal of Lightwave Technology*, vol. 29, no. 4, pp. 491–498, Feb. 2011.

[57] J.-X. Cai, H. G. Batshon, H. Zhang, C. Davidson, Y. Sun, M. Mazurczyk, D. Foursa, O. Sinkin, A. Pilipetskii, G. Mohs *et al.*, "25 Tb/s transmission over 5530 km using 16QAM at 5.2 b/s/Hz spectral efficiency," *Optics express*, vol. 21, no. 2, pp. 1555–1560, 2013.

[58] H. Zhang, J.-X. Cai, H. G. Batshon, C. R. Davidson, Y. Sun, M. Mazurczyk, D. G. Foursa, A. Pilipetskii, G. Mohs, and N. S. Bergano, "16QAM transmission with 5.2 bits/s/Hz spectral efficiency over transoceanic distance," *Opt. Express*, vol. 20, no. 11, pp. 11 688–11 693, May 2012.

[59] B. Zhu, T. Taunay, M. Fishteyn, X. Liu, S. Chandrasekhar, M. F. Yan, J. M. Fini, E. M. Monberg, and F. V. Dimarcello, "112-Tb/s Space-division multiplexed DWDM transmission with 14-b/s/Hz aggregate spectral efficiency over a 76.8-km seven-core fiber," *Opt. Express*, vol. 19, no. 17, pp. 16 665–16 671, Aug 2011.

[60] B. Puttnam, W. Klaus, Y. Awaji, N. Wada, A. Kanno, T. Kawanishi, K. Imamura, H. Inaba, K. Mukasa, R. Sugizaki *et al.*, "19-core fiber transmission of 19×100×172-Gb/s SDM-WDM-PDM-QPSK signals at 305 Tb/s," in *Proc. Opt. Fiber Commun./Nat. Fiber Opt. Eng. Conf*, 2012.

[61] T. Mizuno, T. Kobayashi, H. Takara, A. Sano, H. Kawakami, T. Nakagawa, Y. Miyamoto, Y. Abe, T. Goh, M. Oguma *et al.*, "12-core × 3-mode dense space division multiplexed transmission over 40 km employing multi-carrier signals with

parallel MIMO equalization," in *Optical Fiber Communication Conference*. Optical Society of America, 2014, pp. Th5B–2.

[62] R. Ryf, N. K. Fontaine, B. Guan, R.-J. Essiambre, S. Randel, A. Gnauck, S. Chandrasekhar, A. Adamiecki, G. Raybon, B. Ercan *et al.*, "1705-km transmission over coupled-core fibre supporting 6 spatial modes," in *2014 The European Conference on Optical Communication (ECOC)*, 2014.

[63] M. Salsi, C. Koebele, P. Tran, H. Mardoyan, S. Bigo, and G. Charlet, "80× 100-Gbit/s transmission over 9000 km using erbium-doped fibre repeaters only," in *36th European Conference and Exhibition on Optical Communication*, 2010.

[64] H. Zhang, H. G. Batshon, D. Foursa, M. Mazurczyk, J.-X. Cai, C. Davidson, A. Pilipetskii, G. Mohs, and N. Bergano, "30.58 Tb/s transmission over 7230 km using PDM half 4D-16QAM coded modulation with 6.1 b/s/Hz spectral efficiency," in *Optical Fiber Communication Conference*. Optical Society of America, 2013, pp. OTu2B–3.

[65] S. Chandrasekhar, X. Liu, P. J. Winzer, T. Lotz, C.-J. Youn, Y.-H. Kwon, and E.-S. Nam, "Field Demonstration of 3×341-Gb/s PDM-OFDM-256 iterative polar modulation signals with a record 11.0-b/s/Hz intrachannel spectral efficiency," in *Optical Fiber Communication Conference*. Optical Society of America, 2014, pp. Th5A–8.

[66] H. Takara, T. Mizuno, H. Kawakami, Y. Miyamoto, H. Masuda, K. Kitamura, H. Ono, S. Asakawa, Y. Amma, K. Hirakawa *et al.*, "120.7-Tb/s (7 SDM/180 WDM/95.8 Gb/s) MCF-ROPA unrepeatered transmission of PDM-32QAM channels over 204 km," in *Optical Communication (ECOC), 2014 European Conference on*. IEEE, 2014, pp. 1–3.

[67] M.-K. Siu and P. Tong, "Generation of some de Bruijn sequences," *Discrete Mathematics*, vol. 31, no. 1, pp. 97–100, 1980.

[68] E. L. Wooten, K. M. Kissa, A. Yi-Yan, E. J. Murphy, D. Lafaw, P. F. Hallemeier, D. Maack, D. V. Attanasio, D. J. Fritz, G. J. McBrien *et al.*, "A review of Lithium Niobate modulators for fiber-optic communications systems," *Selected Topics in Quantum Electronics, IEEE Journal of*, vol. 6, no. 1, pp. 69–82, 2000.

[69] M. Seimetz, *High-order modulation for optical fiber transmission*. Dordrecht; New York: Springer, 2009.

[70] M. Nakazawa, K. Kikuchi, and T. Miyazaki, *High spectral density optical communication technologies*. Berlin; London: Springer, 2010.

[71] R. Nagarajan, C. Doerr, and F. Kish, "Semiconductor photonic integrated circuit transmitters and receivers," *Optical Fiber Telecommunications, vol. VIA, I. Kaminow*, pp. 25–98, 2013.

[72] B. Zhang, C. Malouin, and T. J. Schmidt, "Design of coherent receiver optical front end for unamplified applications," *Opt. Express*, vol. 20, no. 3, pp. 3225–3234, Jan 2012.

[73] X. Liu, "Receiver sensitivity improvement in optical DQPSK and DQPSK/ASK through data-aided multi-symbol phase estimation," in *2006 European Conference on Optical Communications*, 2006.

[74] I. Fatadin, S. J. Savory, and D. Ives, "Compensation of quadrature imbalance in an optical QPSK coherent receiver," *IEEE Photonics Technology Letters*, vol. 20, no. 20, pp. 1733–1735, Oct. 2008.

[75] Sun Hyok Chang, Hwan Seok Chung, and Kwangjoon Kim, "Impact of quadrature imbalance in optical coherent QPSK receiver," *IEEE Photonics Technology Letters*, vol. 21, no. 11, pp. 709–711, Jun. 2009.

[76] C. Petrou, A. Vgenis, I. Roudas, and L. Raptis, "Quadrature imbalance compensation for PDM QPSK coherent optical systems," *IEEE Photonics Technology Letters*, vol. 21, no. 24, pp. 1876–1878, Dec. 2009.

[77] Y. Q. Yaojun Qiao, Y. X. Yanfei Xu, L. L. Lujiao Li, and Y. J. Yuefeng Ji, "Quadrature imbalance compensation algorithm based on statistical properties of signals in CO-QPSK system," *Chinese Optics Letters*, vol. 10, no. 12, pp. 120 601–120 604, 2012.

[78] T.-H. Nguyen, F. Gomez-Agis, M. Gay, L. Anet-Neto, P. Scalart, C. Peucheret, M. Joindot, O. Sentieys, J.-C. Simon, and L. Bramerie, "IQ imbalance compensation based on maximum SNR estimation in coherent QPSK systems," in *Transparent Optical Networks (ICTON), 2014 16th International Conference on*. IEEE, 2014, pp. 1–4.

[79] S. Verdu, "Maximum likelihood sequence detection for intersymbol interference channels: a new upper bound on error probability," *IEEE Transactions on Information Theory*, vol. 33, no. 1, pp. 62–68, 1987.

[80] M. Schmidt and G. P. Fettweis, "Fractionally-spaced prefiltering for reduced state equalization," in *Global Telecommunications Conference, 1999. GLOBECOM'99*, vol. 5. IEEE, 1999, pp. 2291–2295.

[81] P. S. R. Diniz, *Adaptive Filtering*. Boston, MA: Springer US, 2008.

[82] D. George, R. R. Bowen, J. Storey, and others, "An adaptive decision feedback equalizer," *Communication Technology, IEEE Transactions on*, vol. 19, no. 3, pp. 281–293, 1971.

[83] S. Chandramouli, "A novel analog decision-feedback equalizer in CMOS for serial 10-Gb/sec data transmission systems," 2007.

[84] M. Morelli and U. Mengali, "Feedforward frequency estimation for PSK: a tutorial review," *European Transactions on Telecommunications*, vol. 9, no. 2, pp. 103–116, 1998.

[85] A. Leven, N. Kaneda, U.-V. Koc, and Y.-K. Chen, "Frequency estimation in intradyne reception," *IEEE Photonics Technology Letters*, vol. 19, no. 6, pp. 366–368, Mar. 2007.

[86] J. C. M. Diniz, J. de Oliveira, E. S. Rosa, V. B. Ribeiro, V. E. S. Parahyba, R. da Silva, E. P. da Silva, L. H. H. de Carvalho, A. F. Herbster, and A. C. Bordonalli, "Simple feedforward wide-range frequency offset estimator for optical coherent receivers," *Optics express*, vol. 19, no. 26, pp. B323–B328, 2011.

[87] M. Qiu, Q. Zhuge, X. Xu, M. Chagnon, M. Morsy-Osman, and D. V. Plant, "Simple and efficient frequency offset tracking and carrier phase recovery algorithms in single carrier transmission systems," *Optics Express*, vol. 21, no. 7, p. 8157, Apr. 2013.

[88] M. Funabashi, H. Nasu, T. Mukaihara, T. Kimoto, T. Shinagawa, T. Kise, K. Takaki, T. Takagi, M. Oike, T. Nomura, and A. Kasukawa, "Recent advances in DFB lasers for ultradense WDM applications," *IEEE Journal of Selected Topics in Quantum Electronics*, vol. 10, no. 2, pp. 312–320, Mar. 2004.

[89] P. Ciblat and L. Vandendorpe, "Blind carrier frequency offset estimation for non-circular constellation-based transmissions," *IEEE Transactions on Signal Processing*, vol. 51, no. 5, pp. 1378–1389, May 2003.

[90] M. Selmi, Y. Jaouën, and P. Ciblat, "Accurate digital frequency offset estimator for coherent PolMux QAM transmission systems," *ECOC 2009*, 2009.

[91] H. Leng, S. Yu, X. Li, M. Lan, P. Liao, T. Wang, and W. Gu, "Frequency offset estimation for optical coherent M-QAM detection using chirp Z-transform," *IEEE Photonics Technology Letters*, vol. 24, no. 9, pp. 787–789, May 2012.

[92] A. Viterbi, "Nonlinear estimation of PSK-modulated carrier phase with application to burst digital transmission," *Information Theory, IEEE Transactions on*, vol. 29, no. 4, pp. 543–551, 1983.

[93] D.-S. Ly-Gagnon, S. Tsukamoto, K. Katoh, and K. Kikuchi, "Coherent detection of optical quadrature phase-shift keying signals with carrier phase estimation," *Journal of Lightwave Technology*, vol. 24, no. 1, pp. 12–21, Jan. 2006.

[94] W. J. Weber III, "Differential encoding for multiple amplitude and phase shift keying systems," *Communications, IEEE Transactions on*, vol. 26, no. 3, pp. 385–391, 1978.

[95] Yan Wang, E. Serpedin, and P. Ciblat, "Optimal blind carrier recovery for MPSK burst transmissions," *IEEE Transactions on Communications*, vol. 51, no. 9, pp. 1571–1581, Sep. 2003.

[96] G. Li, "Recent advances in coherent optical communication," *Advances in Optics and Photonics*, vol. 1, no. 2, p. 279, Apr. 2009.

[97] S. J. Savory, "Digital coherent optical receivers: Algorithms and subsystems," *IEEE Journal of Selected Topics in Quantum Electronics*, vol. 16, no. 5, pp. 1164–1179, Sep. 2010.

[98] M. G. Taylor, "Phase estimation methods for optical coherent detection using digital signal processing," *Journal of Lightwave Technology*, vol. 27, no. 7, pp. 901–914, Apr. 2009.

[99] M. Oerder and H. Meyr, "Digital filter and square timing recovery," *IEEE Transactions on communications*, vol. 36, pp. 605–612, 1988.

[100] S. J. Lee, "A new non-data-aided feedforward symbol timing estimator using two samples per symbol," *Communications Letters, IEEE*, vol. 6, no. 5, pp. 205–207, 2002.

[101] F. M. Gardner, "A BPSK/QPSK timing-error detector for sampled receivers," *IEEE Transactions on communications*, vol. 34, pp. 423–429, 1986.

[102] D. N. Godard, "Passband timing recovery in an all-digital modem receiver," *Communications, IEEE Transactions on*, vol. 26, no. 5, pp. 517–523, 1978.

[103] F. M. Gardner, "Interpolation in digital modems. I. Fundamentals," *Communications, IEEE Transactions on*, vol. 41, no. 3, pp. 501–507, Mar 1993.

[104] L. Erup, F. M. Gardner, and R. Harris, "Interpolation in digital modems. II. Implementation and performance," *Communications, IEEE Transactions on*, vol. 41, no. 6, pp. 998–1008, Jun 1993.

[105] G. P. Agrawal, *Nonlinear fiber optics*. San Diego: Academic Press, 2001.

[106] A. Leven, N. Kaneda, and S. Corteselli, "Real-time implementation of digital signal processing for coherent optical digital communication systems," *IEEE Journal of Selected Topics in Quantum Electronics*, vol. 16, no. 5, pp. 1227–1234, Sep. 2010.

[107] S. Haykin, *Adaptive filter theory*. Upper Saddle River, N.J: Prentice Hall, 2002.

[108] K.-P. Ho and J. Kahn, "Electronic compensation technique to mitigate nonlinear phase noise," *Journal of Lightwave Technology*, vol. 22, no. 3, pp. 779–783, Mar. 2004.

[109] A. P. T. Lau and J. M. Kahn, "Signal design and detection in presence of nonlinear phase noise," *Journal of Lightwave Technology*, vol. 25, no. 10, pp. 3008–3016, Oct. 2007.

[110] K. V. Peddanarappagari and M. Brandt-Pearce, "Volterra series approach for optimizing fiber-optic communications system designs," *Lightwave Technology, Journal of*, vol. 16, no. 11, pp. 2046–2055, 1998.

[111] Y. Gao, F. Zhang, J. Li, L. Liu, Z. Chen, L. Zhu, L. Li, and A. Xu, "Experimental demonstration of nonlinear electrical equalizer to mitigate intra-channel nonlinearities in coherent QPSK systems," *ECOC 2009*, 2009.

[112] C. Paré, N. Doran, A. Villeneuve, and P.-A. Bélanger, "Compensating for dispersion and the nonlinear Kerr effect without phase conjugation," *Optics letters*, vol. 21, no. 7, pp. 459–461, 1996.

[113] S. J. Savory, G. Gavioli, E. Torrengo, and P. Poggiolini, "Impact of interchannel nonlinearities on a split-step intrachannel nonlinear equalizer," *IEEE Photonics Technology Letters*, vol. 22, no. 10, pp. 673–675, May 2010.

[114] E. Ip and J. M. Kahn, "Compensation of dispersion and nonlinear impairments using digital backpropagation," *Journal of Lightwave Technology*, vol. 26, no. 20, pp. 3416–3425, Oct. 2008.

[115] D. Millar, S. Makovejs, V. Mikhailov, V. Mikhailov, R. Killey, P. Bayvel, and S. Savory, "Experimental comparison of nonlinear compensation in long-haul PDM-QPSK transmission at 42.7 and 85.4 Gb/s," *ECOC 2009*, 2009.

[116] D. S. Millar and S. Savory, "Nonlinear digital processing for uncompensated systems," in *Signal Processing in Photonic Communications*. Optical Society of America, 2010, p. SPWB6.

[117] I. Shake, H. Takara, and S. Kawanishi, "Simple measurement of eye diagram and BER using high-speed asynchronous sampling," *Journal of Lightwave Technology*, vol. 22, no. 5, pp. 1296–1302, May 2004.

[118] M. Chagnon, M. Osman, M. Poulin, C. Latrasse, J.-F. Gagne, Y. Painchaud, C. Paquet, S. Lessard, and D. Plant, "Experimental study of 112 Gb/s short reach transmission employing PAM formats and SiP intensity modulator at 1.3 μm," *Optics Express*, vol. 22, no. 17, p. 21018, Aug. 2014.

[119] M. D. McKinley, K. A. Remley, M. Myslinski, J. S. Kenney, D. Schreurs, and B. Nauwelaers, "EVM calculation for broadband modulated signals," in *64th ARFTG Conf. Dig*, 2004, pp. 45–52.

[120] R. Schmogrow, B. Nebendahl, M. Winter, A. Josten, D. Hillerkuss, S. Koenig, J. Meyer, M. Dreschmann, M. Huebner, C. Koos, J. Becker, W. Freude, and J. Leuthold, "Error vector magnitude as a performance measure for advanced modulation formats," *IEEE Photonics Technology Letters*, vol. 24, no. 1, pp. 61–63, Jan. 2012.

[121] R.-J. Essiambre, G. Kramer, P. J. Winzer, G. J. Foschini, and B. Goebel, "Capacity limits of optical fiber networks," *Journal of Lightwave Technology*, vol. 28, no. 4, pp. 662–701, Feb. 2010.

[122] S. Smith, *Digital signal processing : a practical guide for engineers and scientists.* Amsterdam Boston: Newnes, 2003.

[123] E. Ip, A. P. T. Lau, D. J. F. Barros, and J. M. Kahn, "Coherent detection in optical fiber systems," *Opt. Express*, vol. 16, no. 2, pp. 753–791, Jan 2008.

[124] M. A. Taubenblatt, "Optical interconnects for high-performance computing," *Journal of Lightwave Technology*, vol. 30, no. 4, pp. 448–457, 2012.

[125] J. Leuthold, C. Koos, and W. Freude, "Nonlinear silicon photonics," *Nature Photonics*, vol. 4, no. 8, pp. 535–544, 2010.

[126] [Online]. Available: http://www.ieee802.org/3/bs/index.html

[127] B. Shoop, *Photonic Analog-to-Digital Conversion.* Berlin, Heidelberg: Springer Berlin Heidelberg Imprint Springer, 2001.

[128] T. Ellermeyer, R. Schmid, A. Bielik, J. Rupeter, and M. Moller, "DA and AD converters in SiGe technology: Speed and resolution for ultra high data rate applications," in *Proc. ECOC*, vol. 10, 2010.

[129] J. Proakis, *Digital signal processing : principles, algorithms, and applications.* Upper Saddle River, N.J: Prentice Hall, 1996.

[130] M. Waltari, "Integration of high-speed CMOS sample-and-hold circuits," *Licentiate's thesis, Helsinki University of Technology, Finland*, 1999.

[131] A. Carlson, *Communication systems : an introduction to signals and noise in electrical communication.* Boston: McGraw-Hill Higher Education, 2010.

[132] W. Kester, *Analog-digital conversion.* Analog Devices, 2004.

[133] R. H. Walden, "Performance trends for analog to digital converters," *Communications Magazine, IEEE*, vol. 37, no. 2, pp. 96–101, 1999.

[134] R.-H. Walden, "Analog-to-digital conversion in the early twenty-first century," *Wiley Encyclopedia of Computer Science and Engineering*, 2008.

[135] B. Le, T. W. Rondeau, J. H. Reed, and C. W. Bostian, "Analog-to-digital converters," *Signal Processing Magazine, IEEE*, vol. 22, no. 6, pp. 69–77, 2005.

[136] P. B. Kenington and L. Astier, "Power consumption of A/D converters for software radio applications," *Vehicular Technology, IEEE Transactions on*, vol. 49, no. 2, pp. 643–650, 2000.

[137] R. H. Walden, "Analog-to-digital converter survey and analysis," *Selected Areas in Communications, IEEE Journal on*, vol. 17, no. 4, pp. 539–550, 1999.

[138] C. Laperle and M. OSullivan, "Advances in high-speed DACs, ADCs, and DSP for optical coherent transceivers," *Journal of Lightwave Technology*, vol. 32, no. 4, pp. 629–643, Feb. 2014.

[139] [Online]. Available: http://www.wirelessdesignonline.com/doc/14-b-ad-0001

[140] [Online]. Available: http://www.ti.com/lit/ds/symlink/ads5546.pdf

[141] H. Sun, K.-T. Wu, and K. Roberts, "Real-time measurements of a 40 Gb/s coherent system," *Opt. Express*, vol. 16, no. 2, pp. 873–879, Jan 2008.

[142] M. Birk, P. Gerard, R. Curto, L. E. Nelson, X. Zhou, P. Magill, T. J. Schmidt, C. Malouin, B. Zhang, E. Ibragimov, S. Khatana, M. Glavanovic, R. Lofland, R. Marcoccia, R. Saunders, G. Nicholl, M. Nowell, and F. Forghieri, "Real-time single-carrier coherent 100 Gb/s PM-QPSK field trial," *Journal of Lightwave Technology*, vol. 29, no. 4, pp. 417–425, Feb. 2011.

[143] N. Kaneda, T. Pfau, H. Zhang, J. Lee, Y.-K. Chen, C. J. Youn, Y. H. Kwon, E. S. Num, and S. Chandrasekhar, "Field demonstration of 100-Gb/s real-time coherent optical OFDM detection," in *Optical Communication (ECOC), 2014 European Conference on*, Sept 2014, pp. 1–3.

[144] P. Schvan, J. Bach, C. Fait, P. Flemke, R. Gibbins, Y. Greshishchev, N. Ben-Hamida, D. Pollex, J. Sitch, S.-C. Wang, and J. Wolczanski, "A 24GS/s 6b ADC in 90nm CMOS," in *Solid-State Circuits Conference, 2008. ISSCC 2008. Digest of Technical Papers. IEEE International*, Feb 2008, pp. 544–634.

[145] R. Plassche, *CMOS Integrated Analog-to-Digital and Digital-to-Analog Converters*. Boston, MA: Springer US, 2003.

[146] S. Gupta, M. Choi, M. Inerfield, and J. Wang, "A 1GS/s 11b time-interleaved ADC in 0.13 μm CMOS," in *Solid-State Circuits Conference, 2006. ISSCC 2006. Digest of Technical Papers. IEEE International*, Feb 2006, pp. 2360–2369.

[147] [Online]. Available: http://www.datasheetarchive.com/dl/Datasheet-025/DSA00435782.pdf

[148] [Online]. Available: http://www.rsc.rockwell.com/highspeed/files/PB_0040XA1-1104.pdf

[149] C. Schiller and P. Byrne, "A 4-GHz 8-b ADC system," *Solid-State Circuits, IEEE Journal of*, vol. 26, no. 12, pp. 1781–1789, Dec 1991.

[150] [Online]. Available: http://www.rsc.rockwell.com/highspeed/files/PB_0032XA1-1104.pdf

[151] K. Poulton, R. Neff, B. Setterberg, B. Wuppermann, T. Kopley, R. Jewett, J. Pernillo, C. Tan, and A. Montijo, "A 20 GSa/s 8b ADC with a 1 MB memory in 0.18 μm CMOS," in *Solid-State Circuits Conference, 2003. Digest of Technical Papers. ISSCC. 2003 IEEE International*, Feb 2003, pp. 318–496 vol.1.

[152] P. Schvan, D. Pollex, S.-C. Wang, C. Falt, and N. Ben-Hamida, "A 22GS/s 5b ADC in 0.13 μ SiGe BiCMOS," in *Solid-State Circuits Conference, 2006. ISSCC 2006. Digest of Technical Papers. IEEE International*, Feb 2006, pp. 2340–2349.

[153] R. Kertis, J. Humble, M. Daun-Lindberg, R. Philpott, K. Fritz, D. Schwab, J. Prairie, B. Gilbert, and E. Daniel, "A 35 GS/s 5-bit SiGe BiCMOS flash ADC with offset corrected exclusive-or comparator," in *Bipolar/BiCMOS Circuits and Technology Meeting, 2008. BCTM 2008. IEEE*, Oct 2008, pp. 252–255.

[154] [Online]. Available: http://www.micram.com/attachments/030_VEGA%20ADC30%20two-page.pdf

[155] S. Shahramian, S. Voinigescu, and A. Carusone, "A 35-GS/s, 4-bit flash ADC with active data and clock distribution trees," *Solid-State Circuits, IEEE Journal of*, vol. 44, no. 6, pp. 1709–1720, June 2009.

[156] Y. Greshishchev, J. Aguirre, M. Besson, R. Gibbins, C. Falt, P. Flemke, N. Ben-Hamida, D. Pollex, P. Schvan, and S.-C. Wang, "A 40GS/s 6b ADC in 65nm CMOS," in *Solid-State Circuits Conference Digest of Technical Papers (ISSCC), 2010 IEEE International*, Feb 2010, pp. 390–391.

[157] M. Chu, P. Jacob, J.-W. Kim, M. LeRoy, R. Kraft, and J. McDonald, "A 40 Gs/s time interleaved ADC using SiGe BiCMOS technology," *Solid-State Circuits, IEEE Journal of*, vol. 45, no. 2, pp. 380–390, Feb 2010.

[158] I. Dedic, "56Gs/s ADC: Enabling 100GbE," in *Optical Fiber Communication (OFC), collocated National Fiber Optic Engineers Conference, 2010 Conference on (OFC/NFOEC)*, March 2010, pp. 1–3.

[159] G. Raybon, P. Winzer, A. Adamiecki, A. Gnauck, A. Konczykowska, F. Jorge, J. Dupuy, A. Sureka, C. Scholz, R. Delbue, P. Pupalaikis, L. Buhl, C. Doerr, S. Chandrasekhar, B. Zhu, and D. Peckham, "8 $\times$ 320-Gb/s transmission over 5600 km using all-ETDM 80-Gbaud polarization multiplexed QPSK transmitter and coherent receiver," in *Optical Fiber Communication Conference and Exposition (OFC/NFOEC), 2012 and the National Fiber Optic Engineers Conference*, March 2012, pp. 1–3.

[160] F. Kartner, A. Khilo, and A. Nejadmalayeri, "Progress in photonic analog-to-digital conversion," in *Optical Fiber Communication Conference and Exposition and the National Fiber Optic Engineers Conference (OFC/NFOEC), 2013*, March 2013, pp. 1–3.

[161] D. Esman, A. Wiberg, M.-H. Yang, L. Liu, B.-P. Kuo, N. Alic, and S. Radic, "Photonic parametric sampled analog-to-digital conversion at 100 GHz and 6 ENOBs," in *Optical Communication (ECOC), 2014 European Conference on*, Sept 2014, pp. 1–3.

[162] D. Esman, A. Wiberg, N. Alic, and S. Radic, "Highly linear broadband photonic-assisted Q-band ADC," *Lightwave Technology, Journal of*, vol. 33, no. 11, pp. 2256–2262, June 2015.

[163] H. F. Taylor, M. J. Taylor, and P. W. Bauer, "Electro-optic analog-to-digital conversion using channel waveguide modulators," *Applied Physics Letters*, vol. 32, no. 9, p. 559, 1978.

[164] P. W. Juodawlkis, J. C. Twichell, G. E. Betts, J. J. Hargreaves, R. D. Younger, J. L. Wasserman, F. J. Donnell, K. G. Ray, and R. C. Williamson, "Optically sampled analog-to-digital converters," *Microwave Theory and Techniques, IEEE Transactions on*, vol. 49, no. 10, pp. 1840–1853, 2001.

[165] C. Pala, L. Thylen, M. Mokhtari, and U. Westergren, "A high-speed electro-optical analog-to-digital converter principle," in *Circuits and Systems, 2001. ISCAS 2001. The 2001 IEEE International Symposium on*, vol. 1, May 2001, pp. 432–435 vol. 1.

[166] J. Stigwall and S. Galt, "Analysis of the resolution-bandwidth-noise trade-off in wavelength-based photonic analog-to-digital converters," *Applied optics*, vol. 45, no. 18, pp. 4310–4318, 2006.

[167] H. Taylor, "An electrooptic analog-to-digital converter," *Proceedings of the IEEE*, vol. 63, no. 10, pp. 1524–1525, 1975.

[168] I. A. Goncharenko, A. K. Esman, V. K. Kuleshov, and V. A. Pilipovich, "Optical broadband analog-digital conversion on the base of microring resonator," *Optics Communications*, vol. 257, no. 1, pp. 54–61, Jan. 2006.

[169] J. Chou, O. Boyraz, D. Solli, and B. Jalali, "Femtosecond real-time single-shot digitizer," *Applied Physics Letters*, vol. 91, no. 16, p. 161105, 2007.

[170] Y. Miyoshi, S. Takagi, S. Namiki, and K. Kitayama, "Resolution-enhanced ultrafast ADC using optical multi-period transfer functions of NOLMs," in *Optical Fiber Communication (OFC), collocated National Fiber Optic Engineers Conference, 2010 Conference on (OFC/NFOEC)*, March 2010, pp. 1–3.

[171] H. Chi, Z. Li, X. Zhang, S. Zheng, X. Jin, and J. Yao, "Proposal for photonic quantization with differential encoding using a phase modulator and delay-line interferometers," *Optics letters*, vol. 36, no. 9, pp. 1629–1631, 2011.

[172] T. Satoh, K. Takahashi, H. Matsui, K. Itoh, and T. Konishi, "10-GS/s 5-bit real-time optical quantization for photonic analog-to-digital conversion," *Photonics Technology Letters, IEEE*, vol. 24, no. 10, pp. 830–832, May 2012.

[173] T. Satoh, T. Nagashima, K. Itoh, and T. Konishi, "Power-saving approach toward 7-bit optical quantization for photonic analog-to-digital conversion," in *Lasers and Electro-Optics Pacific Rim (CLEO-PR), 2013 Conference on*, June 2013, pp. 1–2.

[174] P. Jiang, Y. Chai, I. White, R. Penty, J. Heaton, A. Kuver, S. Clements, C. Leburn, A. McWilliam, A. Lagatsky, C. Brown, and W. Sibbett, "80 GSPS photonic analogue to digital conversion system using broadband continuous wave source," in *Lasers and Electro-Optics, 2005. (CLEO). Conference on*, vol. 2, May 2005, pp. 874–876 Vol. 2.

[175] H. Wen, H. Wang, and Y. Ji, "All-optical quantization and coding scheme for ultrafast analog-to-digital conversion exploiting polarization switches based on nonlinear polarization rotation in semiconductor optical amplifiers," *Optics Communications*, vol. 285, no. 18, pp. 3877–3885, 2012.

[176] Y. Han and B. Jalali, "Photonic time-stretched analog-to-digital converter: fundamental concepts and practical considerations," *Lightwave Technology, Journal of*, vol. 21, no. 12, pp. 3085–3103, Dec 2003.

[177] [Online]. Available: http://www.calmarlaser.com/docs/FPL_White_Rev1.3010109.pdf

[178] [Online]. Available: http://www.u2t.de/pdf/Datasheet_TMLL1550_V42.pdf

[179] [Online]. Available: http://www.optocomb.com/files/9014/2303/8264/eng_wtec_01.pdf

[180] C. Schmidt-Langhorst and H.-G. Weber, "Optical sampling techniques," *Journal of Optical and Fiber Communications Reports*, vol. 2, no. 1, pp. 86–114, Mar. 2005.

[181] J. S. Orcutt, B. Moss, C. Sun, J. Leu, M. Georgas, J. Shainline, E. Zgraggen, H. Li, J. Sun, M. Weaver, S. Urošević, M. Popović, R. J. Ram, and V. Stojanović, "Open foundry platform for high-performance electronic-photonic integration," *Opt. Express*, vol. 20, no. 11, pp. 12 222–12 232, May 2012.

[182] X. Zheng, D. Patil, J. Lexau, F. Liu, G. Li, H. Thacker, Y. Luo, I. Shubin, J. Li, J. Yao, P. Dong, D. Feng, M. Asghari, T. Pinguet, A. Mekis, P. Amberg, M. Dayringer, J. Gainsley, H. F. Moghadam, E. Alon, K. Raj, R. Ho, J. E. Cunningham, and A. V.

Krishnamoorthy, "Ultra-efficient 10Gb/s hybrid integrated silicon photonic transmitter and receiver," *Opt. Express*, vol. 19, no. 6, pp. 5172–5186, Mar 2011.

[183] C. Gunn, "CMOS photonics for high-speed interconnects," *Micro, IEEE*, vol. 26, no. 2, pp. 58–66, March 2006.

[184] A. Khilo, S. J. Spector, M. E. Grein, A. H. Nejadmalayeri, C. W. Holzwarth, M. Y. Sander, M. S. Dahlem, M. Y. Peng, M. W. Geis, N. A. DiLello, and others, "Photonic ADC: overcoming the bottleneck of electronic jitter," *Optics express*, vol. 20, no. 4, pp. 4454–4469, 2012.

[185] B. Murmann, "ADC performance survey 1997-2014." [Online]. Available: http://web.stanford.edu/~murmann/adcsurvey.html.

[186] A. Agoston, S. Pepper, R. Norton, J. Ebner, and K. Schoen, "100 GHz through-line sampler system with sampling rates in excess of 10 Gsamples/second," in *Microwave Symposium Digest, 2003 IEEE MTT-S International*, vol. 3, June 2003, pp. 1519–1521 vol.3.

[187] N. Yamada, S. Nogiwa, and H. Ohta, "640-Gb/s OTDM signal measurement with high-resolution optical sampling system using wavelength-tunable soliton pulses," *Photonics Technology Letters, IEEE*, vol. 16, no. 4, pp. 1125–1127, April 2004.

[188] M. Westlund, H. Sunnerud, M. Karlsson, and P. Andrekson, "Software-synchronized all-optical sampling for fiber communication systems," *Journal of Lightwave Technology*, vol. 23, no. 3, pp. 1088–1099, Mar. 2005.

[189] X. Chen, I. Kim, G. Li, H. Zhang, and B. Zhou, "Coherent detection using optical time-domain sampling," in *Optical Fiber communication/National Fiber Optic Engineers Conference, 2008. OFC/NFOEC 2008. Conference on*, Feb 2008, pp. 1–3.

[190] M. Westlund, H. Sunnerud, M. Karlsson, and P. A. Andrekson, "Software-synchronized all-optical sampling," in *Optical Fiber Communication Conference*. Optical Society of America, 2003, p. WP6.

[191] C. Dorrer, "Monitoring of optical signals from constellation diagrams measured with linear optical sampling," *Journal of Lightwave Technology*, vol. 24, no. 1, pp. 313–321, Jan. 2006.

[192] S. Watanabe, R. Okabe, F. Futami, R. Hainberger, C. Schmidt-Langhorst, C. Schubert, and H.-G. Weber, "Novel fiber Kerr-switch with parametric gain: Demonstration of optical demultiplexing and sampling up to 640 Gb/s," *Proc. 30th ECOC 2004*, pp. 1–27, 2004.

[193] P. J. Maguire, L. P. Barry, T. Krug, M. Lynch, A. L. Bradley, J. F. Donegan, and H. Folliot, "Highly-efficient optical sampling based on two-photon absorption in a semiconductor micro-cavity device," in *Conference on Lasers and Electro-Optics*. Optical Society of America, 2005, p. CTuAA5.

[194] J. Van Erps, F. Luan, M. D. Pelusi, T. Iredale, S. Madden, D.-Y. Choi, D. A. Bulla, B. Luther-Davies, H. Thienpont, and B. J. Eggleton, "High-resolution optical sampling of 640-Gb/s data using four-wave mixing in dispersion-engineered highly nonlinear As_2S_3 planar waveguides," *Journal of Lightwave Technology*, vol. 28, no. 2, pp. 209–215, Jan. 2010.

[195] P. Andrekson, "Picosecond optical sampling using four-wave mixing in fibre," *Electronics Letters*, vol. 27, no. 16, pp. 1440–1441, Aug 1991.

[196] C. Dorrer, C. Doerr, I. Kang, R. Ryf, J. Leuthold, and P. Winzer, "Measurement of eye diagrams and constellation diagrams of optical sources using linear optics and waveguide technology," *Journal of Lightwave Technology*, vol. 23, no. 1, pp. 178–186, Jan. 2005.

[197] C. Dorrer, J. Leuthold, and C. R. Doerr, "Direct measurement of constellation diagrams of optical sources," in *Optical Fiber Communication Conference*. Optical Society of America, 2004, p. PD33.

[198] K. Okamoto and F. Ito, "Dual-channel linear optical sampling for simultaneously monitoring ultrafast intensity and phase modulation," *Lightwave Technology, Journal of*, vol. 27, no. 12, pp. 2169–2175, June 2009.

[199] H. Sunnerud, M. Skold, M. Westlund, and P. Andrekson, "Characterization of complex optical modulation formats at 100 Gb/s and beyond by coherent optical sampling," *Lightwave Technology, Journal of*, vol. 30, no. 24, pp. 3747–3759, Dec 2012.

[200] M. Skold, G. Raybon, A. L. Adamiecki, P. J. Winzer, H. Sunnerud, M. Westlund, A. Konczykowska, F. Jorge, J. Dupuy, L. L. Buhl *et al.*, "Quasi-real-time optical sampling scheme for high-speed signal acquisition and processing," *Photonics Technology Letters, IEEE*, vol. 25, no. 5, pp. 504–507, 2013.

[201] X. Chen, X. Xie, I. Kim, G. Li, H. Zhang, and B. Zhou, "Coherent detection using optical time-domain sampling," *Photonics Technology Letters, IEEE*, vol. 21, no. 5, pp. 286–288, March 2009.

[202] K. Kikuchi, K. Igarashi, Y. Mori, and C. Zhang, "Demodulation of 320-Gbit/s optical quadrature phase-shift keying signal with digital coherent receiver having time-division demultiplexing function," in *Optical Fiber Communication Conference*. Optical Society of America, 2008, p. OTuO4.

[203] C. Zhang, Y. Mori, K. Igarashi, K. Katoh, and K. Kikuchi, "Demodulation of 480-Gbit/s 8PSK OTDM signal with digital coherent receiver," in *2008 34th European Conference on Optical Communication*, 2008.

[204] I. Kim, C. Kim, and G. Li, "Requirements for the sampling source in coherent linear sampling," *Optics express*, vol. 12, no. 12, pp. 2723–2730, 2004.

[205] S. Kray, F. Spöler, T. Hellerer, and H. Kurz, "Electronically controlled coherent linear optical sampling for optical coherence tomography," *Opt. Express*, vol. 18, no. 10, pp. 9976–9990, May 2010.

[206] H. Ohta, S. Nogiwa, N. Oda, and H. Chiba, "Highly sensitive optical sampling system using timing-jitter-reduced gain-switched optical pulse," *Electronics Letters*, vol. 33, no. 25, pp. 2142–2144, 1997.

[207] H. Ohta, S. Nogiwa, and H. Chiba, "Highly sensitive optical sampling system with 100 GHz bandwidth," in *Optical Communication, 1998. 24th European Conference on*, vol. 1. IEEE, 1998, pp. 503–504.

[208] S. Nogiwa, H. Ohta, Y. Kawaguchi, and Y. Endo, "Improvement of sensitivity in optical sampling system," *Electronics Letters*, vol. 35, no. 11, pp. 917–918, 1999.

[209] J. Lepley, J. Ellison, S. Edirisinghe, A. Siddiqui, and S. Walker, "Excess penalty impairments of polarisation shift keying transmission format in presence of polarisation mode dispersion," *Electronics Letters*, vol. 36, no. 8, p. 736, 2000.

[210] S. Nogiwa, Y. Kawaguchi, H. Ohta, and Y. Endo, "Highly sensitive and time-resolving optical sampling system using thin PPLN crystal," *Electronics Letters*, vol. 36, no. 20, pp. 1727–1728, 2000.

[211] C. Dorrer, D. Kilper, H. Stuart, and G. Raybon, "Ultra-sensitive optical sampling by coherent-linear detection," in *Optical Fiber Communication Conference*. Optical Society of America, 2002, p. FD5.

[212] A. Otani, T. Otsubo, and H. Watanabe, "A turn-key-ready optical sampling oscilloscope by using electro-absorption modulators," in *Proc. 25th Europ. Conf. Opt. Commun*, 1999, pp. 374–375.

[213] J. Veselka and S. Korotky, "Pulse generation for soliton systems using lithium niobate modulators," *Selected Topics in Quantum Electronics, IEEE Journal of*, vol. 2, no. 2, pp. 300–310, 1996.

[214] H. Hu, H. C. H. Mulvad, C. Peucheret, M. Galili, A. Clausen, P. Jeppesen, and L. K. Oxenlowe, "10 GHz pulse source for 640 Gbit/s OTDM based on phase modulator and self-phase modulation," *Optics express*, vol. 19, no. 26, pp. B343–B349, 2011.

[215] F. Lelarge, B. Dagens, J. Renaudier, R. Brenot, A. Accard, F. v. Dijk, D. Make, O. L. Gouezigou, J.-G. Provost, F. Poingt, J. Landreau, O. Drisse, E. Derouin, B. Rousseau, F. Pommereau, and G.-H. Duan, "Recent advances on InAs/InP quantum dash based semiconductor lasers and optical amplifiers operating at 1.55 μm," *IEEE Journal of Selected Topics in Quantum Electronics*, vol. 13, no. 1, pp. 111–124, 2007.

[216] R. Ludwig and A. Ehrhardt, "Turn-key-ready wavelength-, repetition rate-and pulsewidth-tunable femtosecond hybrid modelocked semiconductor laser," *Electronics Letters*, vol. 31, no. 14, pp. 1165–1167, 1995.

[217] S. Xiao, L. Hollberg, N. R. Newbury, and S. A. Diddams, "Toward a low-jitter 10 GHz pulsed source with an optical frequency comb generator," *Opt. Express*, vol. 16, no. 12, pp. 8498–8508, Jun 2008.

[218] "1550 nm tunable picoseconds laser source (TMLL1550)." [Online]. Available: http://www.u2t.de/pdf/Datasheet_TMLL1550_V42.pdf

[219] T. Saitoh, S. Mattori, S. Kinugawa, K. Miyagi, A. Taniguchi, M. Kourogi, and M. Ohtsu, "Modulation characteristic of waveguide-type optical frequency comb generator," *Journal of lightwave technology*, vol. 16, no. 5, p. 824, 1998.

[220] R. Ludwig, W. Pieper, N. A. Jahn, and A. Ehrhardt, "10 GHz all-optical clock recovery using a mode-locked semiconductor laser in a 40 Gbit/s, 100-km transmission experiment," 1996.

[221] [Online]. Available: http://www.optoplex.com/download/coherent_detection_and_optical_hybrid.pdf

[222] S. Dris, P. Bakopoulos, I. Lazarou, C. Spatharakis, and H. Avramopoulos, "$M-$QAM carrier phase recovery using the viterbi-viterbi monomial-based and maximum likelihood estimators," in *Optical Fiber Communication Conference and Exposition and the National Fiber Optic Engineers Conference (OFC/NFOEC), 2013*, March 2013, pp. 1–3.

[223] L. Noirie, F. Cérou, G. Moustakides, O. Audouin, and P. Peloso, "New transparent optical monitoring of the eye and ber using asynchronous under-sampling of the signal," in *28th European Conference on Optical Communication, 2002 (ECOC'02)*, vol. 5, 2002, pp. PD2–2.

[224] C. Gosset, I. Aldaya, C. Wang, H. Huang, X. You, J. Even, G. Campuzano, and F. Grillot, "Self-referenced technique for monitoring and analysing the non-linear dynamics of semiconductor lasers," *Optics Express*, vol. 22, no. 13, p. 16528, Jun. 2014.

[225] M. Hart, C. Duff, and S. Hinch, "Firmware measurement algorithms for the HP 83480 digital communications analyzer," *Hewlett-Packard J*, vol. 47, pp. 13–21, 1996.

[226] W. A. Finke, *Algorithm for finding the eye crossing level of a multilevel signal.* Google Patents, Sep. 2003, uS Patent 6,614,434. [Online]. Available: http://www.google.com/patents/US6614434

[227] A. Ramachandran, "Nonlinearity and noise modeling of operational transconductance amplifiers for continuous time analog filters," Ph.D. dissertation, Texas A&M University, 2006.

[228] T.-H. Nguyen, F. Gomez-Agis, L. Bramerie, M. Gay, J. Simon, and O. Sentieys, "Impact of sampling-source extinction ratio in linear optical sampling," *Photonics Technology Letters, IEEE*, vol. 25, no. 7, pp. 663–666, April 2013.

[229] I. Koll'ar and J. J. Blair, "Improved determination of the best fitting sine wave in ADC testing," *Instrumentation and Measurement, IEEE Transaction on*, vol. 54, no. 5, pp. 1978–1983, 2005.

[230] W. Kester, "MT-003: Understand SINAD, ENOB, SNR, THD, THD+ N, and SFDR so you don't get lost in the noise floor," pp. 1–3, 2005.

[231] A. V. Petrov and A. B. Sergienko, "Optimal blind biharmonic feedforward phase offset estimation for QAM signals," in *Communications (ICC), 2013 IEEE International Conference on.* IEEE, 2013, pp. 4756–4760.

[232] G. Raybon, A. Adamiecki, P. J. Winzer, S. Randel, L. Salamanca, A. Konczykowska, F. Jorge, J.-Y. Dupuy, L. L. Buhl, S. Chandrashekhar, C. Xie, S. Draving, M. Grove, K. Rush, and R. Urbanke, "High symbol rate coherent optical transmission systems: 80 and 107 Gbaud," *Journal of Lightwave Technology*, vol. 32, no. 4, pp. 824–831, Feb. 2014.

[233] M. Valkama, M. Renfors, and V. Koivunen, "Advanced methods for I/Q imbalance compensation in communication receivers," *Signal Processing, IEEE Transactions on*, vol. 49, no. 10, pp. 2335–2344, 2001.

[234] T. C. Schenk, P. F. Smulders, and E. R. Fledderus, "Estimation and compensation of frequency selective Tx/Rx IQ imbalance in MIMO OFDM systems," in *Communications, 2006. ICC'06. IEEE International Conference on*, vol. 1. IEEE, 2006, pp. 251–256.

[235] C.-H. Liu, "Joint Tx and Rx IQ imbalance compensation of OFDM transceiver in mesh network," in *Global Telecommunications Conference, 2008. IEEE GLOBECOM 2008. IEEE.* IEEE, 2008, pp. 1–5.

[236] W. Chung, "Transmitter IQ mismatch compensation in coherent optical OFDM systems using pilot signals," *Optics express*, vol. 18, no. 20, pp. 21 308–21 314, 2010.

[237] X. Ma, K. Li, and Y. Bai, "Novel training symbol structure for transmitter IQ mismatch compensation for coherent optical OFDM," *IEEE Photonics Technology Letters*, vol. 25, no. 21, pp. 2047–2049, Nov. 2013.

[238] S. Cao, C. Yu, and P. Y. Kam, "Decision-aided joint compensation of transmitter IQ mismatch and phase noise for coherent optical OFDM," *Photonics Technology Letters, IEEE*, vol. 24, no. 12, pp. 1066–1068, 2012.

[239] M. S. Faruk and K. Kikuchi, "Compensation for in-phase/quadrature imbalance in coherent-receiver front end for optical quadrature amplitude modulation," *IEEE Photonics Journal*, vol. 5, no. 2, pp. 7 800 110–7 800 110, Apr. 2013.

[240] M. Paskov, D. Lavery, and S. J. Savory, "Blind equalization of receiver in-phase/quadrature skew in the presence of Nyquist filtering," *IEEE Photonics Technology Letters*, vol. 25, no. 24, pp. 2446–2449, Dec. 2013.

[241] R. . Rios-Muller, J. Renaudier, and G. Charlet, "Blind receiver skew compensation for long-haul non-dispersion managed systems," in *Optical Communication (ECOC), 2014 European Conference on*. IEEE, 2014, pp. 1–3.

[242] R. Rios Muller, J. Renaudier, and G. Charlet, "Blind receiver skew compensation and estimation for long-haul non-dispersion managed systems using adaptive equalizer," *Journal of Lightwave Technology*, vol. 33, no. 7, pp. 1315–1318, Apr. 2015.

[243] G. Khanna, S. Calabro, B. Spinnler, E. D. Man, and N. Hanik, "Joint adaptive precompensation of transmitter I/Q skew and frequency response for high order modulation formats and high baud rates," in *Optical Fiber Communication Conference*. Optical Society of America, 2015, pp. M2G–4.

[244] T. Koike-Akino, D. S. Millar, K. Kojima, K. Parsons, T. Yoshida, K. Ishida, Y. Miyata, W. Matsumoto, and T. Mizuochi, "Turbo demodulation for LDPC-coded high-order QAM in presence of transmitter angular skew," in *Optical Communication (ECOC), 2014 European Conference on*. IEEE, 2014, pp. 1–3.

[245] T.-H. Nguyen, P. Scalart, M. Joindot, M. Gay, L. Bramerie, C. Peucheret, A. Carer, J.-C. Simon, and O. Sentieys, "Joint simple blind IQ imbalance compensation and adaptive equalization for 16-QAM optical communications," in *IEEE International Conference on Communications*, 2015.

[246] B. Razavi, "Design considerations for direct-conversion receivers," *Circuits and Systems II: Analog and Digital Signal Processing, IEEE Transactions on*, vol. 44, no. 6, pp. 428–435, 1997.

[247] C. Rottondi, M. Tornatore, A. Pattavina, and G. Gavioli, "Routing, modulation level, and spectrum assignment in optical metro ring networks using elastic transceivers," *Journal of Optical Communications and Networking*, vol. 5, no. 4, p. 305, Apr. 2013.

[248] F. Gardner, *Phaselock techniques*. Hoboken, NJ: John Wiley, 2005.

[249] T. Schenk and J.-P. Linnartz, *RF imperfections in high-rate wireless systems impact and digital compensation*. Dordrecht; London: Springer, 2008.

[250] W. Nam, H. Roh, J. Lee, and I. Kang, "Blind adaptive I/Q imbalance compensation algorithms for direct-conversion receivers," *Signal Processing Letters, IEEE*, vol. 19, no. 8, pp. 475–478, Aug 2012.

[251] A. Metref, "Contribution to the study of the carrier recovery problem in the cognitive radio context," Theses, Université Rennes 1, Mar. 2010. [Online]. Available: https://tel.archives-ouvertes.fr/tel-00534856

[252] I. Fatadin, D. Ives, and S. J. Savory, "Compensation of frequency offset for differentially encoded 16- and 64-QAM in the presence of laser phase noise," *IEEE Photonics Technology Letters*, vol. 22, no. 3, pp. 176–178, Feb. 2010.

[253] "ITU-T G.652 Characteristics of a single-mode fibre and cable." [Online]. Available: http://www.itu.int/rec/T-REC-G.652-200911-I/en

[254] P. Winzer, "Beyond 100G Ethernet," *Communications Magazine, IEEE*, vol. 48, no. 7, pp. 26–30, July 2010.

[255] E. Lach and W. Idler, "Modulation formats for 100G and beyond," *Optical Fiber Technology*, vol. 17, no. 5, pp. 377–386, Oct. 2011.

[256] T. Pfau, S. Hoffmann, and R. Noe, "Hardware-efficient coherent digital receiver concept with feedforward carrier recovery for M-QAM constellations," *Journal of Lightwave Technology*, vol. 27, no. 8, pp. 989–999, Apr. 2009.

[257] L. Li, Z. Tao, S. Oda, T. Hoshida, and J. C. Rasmussen, "Wide-range, accurate and simple digital frequency offset compensator for optical coherent receivers," in *Optical Fiber Communication Conference*. Optical Society of America, 2008, p. OWT4.

[258] Y. Cao, S. Yu, Y. Chen, Y. Gao, W. Gu, and Y. Ji, "Modified frequency and phase estimation for M-QAM optical coherent detection," *Proc. ECOC 2010*, pp. 1–3, 2010.

[259] C. Spatharakis, N. Argyris, S. Dris, and H. Avramopoulos, "Frequency offset estimation and carrier phase recovery for high-order QAM constellations using the Viterbi-Viterbi monomial estimator," in *Communication Systems, Networks & Digital Signal Processing (CSNDSP), 2014 9th International Symposium on*. IEEE, 2014, pp. 781–786.

[260] K. P. Zhong, J. H. Ke, Y. Gao, and J. C. Cartledge, "Linewidth-tolerant and low-complexity two-stage carrier phase estimation based on modified QPSK partitioning

for dual-polarization 16-QAM systems," *Journal of Lightwave Technology*, vol. 31, no. 1, pp. 50–57, Jan. 2013.

[261] X. Zhou, C. Lu, A. P. T. Lau, and K. Long, "Low-complexity carrier phase recovery for square M-QAM based on S-BPS algorithm," *IEEE Photonics Technology Letters*, vol. 26, no. 18, pp. 1863–1866, Sep. 2014.

[262] M. Seimetz, "Laser linewidth limitations for optical systems with high-order modulation employing feed forward digital carrier phase estimation," in *optical fiber communication conference*. Optical Society of America, 2008, p. OTuM2.

[263] S. M. Bilal, C. R. Fludger, and G. Bosco, "Multi-stage CPE algorithms for 64-QAM constellations," in *Optical Fiber Communication Conference*. Optical Society of America, 2014, pp. M2A–8.

[264] S. M. Bilal, A. Carena, C. Fludger, and G. Bosco, "Dual stage CPE for 64-QAM optical systems based on a modified QPSK-partitioning algorithm," *IEEE Photonics Technology Letters*, vol. 26, no. 3, pp. 267–270, Feb. 2014.

[265] S. M. Bilal, C. R. S. Fludger, V. Curri, and G. Bosco, "Multistage carrier phase estimation algorithms for phase noise mitigation in 64-quadrature amplitude modulation optical systems," *Journal of Lightwave Technology*, vol. 32, no. 17, pp. 2973–2980, Sep. 2014.

[266] S. M. Bilal, G. Bosco, J. Cheng, A. P. T. Lau, and C. Lu, "Carrier phase estimation through the rotation algorithm for 64-QAM optical systems," *Journal of Lightwave Technology*, vol. 33, no. 9, pp. 1766–1773, May 2015.

[267] T. Inoue and S. Namiki, "DSP-implementable block processing of carrier-phase recovery for M-QAM signals," in *Optical Fiber Communications Conference and Exhibition (OFC), 2014*, March 2014, pp. 1–3.

[268] S. Hoffmann, S. Bhandare, T. Pfau, O. Adamczyk, C. Wordehoff, R. Peveling, M. Porrmann, and R. Noe, "Frequency and phase estimation for coherent QPSK transmission with unlocked DFB lasers," *IEEE Photonics Technology Letters*, vol. 20, no. 18, pp. 1569–1571, Sep. 2008.

[269] X. Zhou, "An improved feed-forward carrier recovery algorithm for coherent receivers with M-QAM modulation format," *IEEE Photonics Technology Letters*, vol. 22, no. 14, pp. 1051–1053, Jul. 2010.

[270] I. Fatadin, D. Ives, and S. J. Savory, "Laser linewidth tolerance for 16-QAM coherent optical systems using QPSK partitioning," *IEEE Photonics Technology Letters*, vol. 22, no. 9, pp. 631–633, May 2010.

[271] S. Zhang, L. Xu, J. Yu, M.-F. Huang, P. Y. Kam, C. Yu, and T. Wang, "Dual-stage cascaded frequency offset estimation for digital coherent receivers," *IEEE Photonics Technology Letters*, vol. 22, no. 6, pp. 401–403, Mar. 2010.

[272] Y. Cao, S. Yu, J. Shen, W. Gu, and Y. Ji, "Frequency estimation for optical coherent M-PSK system without removing modulated data phase," *IEEE Photonics Technology Letters*, vol. 22, no. 10, pp. 691–693, May 2010.

[273] J. Li, Z. Tao, H. Zhang, W. Yan, T. Hoshida, and J. C. Rasmussen, "Spectrally efficient quadrature duobinary coherent systems with symbol-rate digital signal processing," *Journal of Lightwave Technology*, vol. 29, no. 8, pp. 1098–1104, Apr. 2011.

[274] T. Nakagawa, M. Matsui, T. Kobayashi, K. Ishihara, R. Kudo, M. Mizoguchi, and Y. Miyamoto, "Non-data-aided wide-range frequency offset estimator for QAM optical coherent receivers," in *Optical Fiber Communication Conference*. Optical Society of America, 2011, p. OMJ1.

[275] M. Li and L.-K. Chen, "Blind carrier frequency offset estimation based on eighth-order statistics for coherent optical QAM systems," *IEEE Photonics Technology Letters*, vol. 23, no. 21, pp. 1612–1614, Nov. 2011.

[276] X. Zhou, X. Chen, and K. Long, "Wide-range frequency offset estimation algorithm for optical coherent systems using training sequence," *IEEE Photonics Technology Letters*, vol. 24, no. 1, pp. 82–84, Jan. 2012.

[277] D. Huang, T.-H. Cheng, and C. Yu, "Accurate two-stage frequency offset estimation for coherent optical systems," *IEEE Photonics Technology Letters*, vol. 25, no. 2, pp. 179–182, Jan. 2013.

[278] I. Fatadin, D. Ives, and S. J. Savory, "Carrier-phase estimation for 16-QAM optical coherent systems using QPSK partitioning with Barycenter approximation," *Journal of Lightwave Technology*, vol. 32, no. 13, pp. 2420–2427, Jul. 2014.

[279] M. Li, J. Zhao, and L.-K. Chen, "Multisymbol QPSK partitioning for improved frequency offset estimation of 16-QAM signals," *IEEE Photonics Technology Letters*, vol. 27, no. 1, pp. 18–21, Jan. 2015.

[280] X. Su, L. Xi, X. Tang, Z. Zhang, S. Bai, W. Zhang, and X. Zhang, "A multistage CPE scheme based on crossed constellation transformation for M-QAM," *IEEE Photonics Technology Letters*, vol. 27, no. 1, pp. 77–80, Jan. 2015.

[281] E. Cacciamani and C. Wolejsza, "Phase-ambiguity resolution in a four-phase PSK communications system," *Communication Technology, IEEE Transactions on*, vol. 19, no. 6, pp. 1200–1210, December 1971.

[282] J.-K. Hwang, Y.-L. Chiu, and C.-S. Liao, "Angle differential-QAM scheme for resolving phase ambiguity in continuous transmission system," *International Journal of Communication Systems*, vol. 21, no. 6, pp. 631–641, Jun. 2008.

[283] E. Ip and J. M. Kahn, "Feedforward carrier recovery for coherent optical communications," *Journal of Lightwave Technology*, vol. 25, no. 9, pp. 2675–2692, Sep. 2007.

[284] A. B. Sergienko and A. V. Petrov, "Blind carrier frequency offset estimation for QAM signals based on weighted 4-th power of signal samples," in *Design & Test Symposium (EWDTS), 2010 East-West.* IEEE, 2010, pp. 278–281.

[285] A.-B. Sergienko and A. V. Petrov, "Joint blind estimation of carrier phase and frequency offset for QAM signals using circular harmonic decomposition," in *Acoustics, Speech and Signal Processing (ICASSP), 2011 IEEE International Conference on.* IEEE, 2011, pp. 3460–3463.

[286] T. Mizuochi, "Recent progress in forward error correction and its interplay with transmission impairments," *IEEE Journal of Selected Topics in Quantum Electronics*, vol. 12, no. 4, pp. 544–554, Jul. 2006.

[287] J. E. Volder, "The CORDIC trigonometric computing technique," *Electronic Computers, IRE Transactions on*, no. 3, pp. 330–334, 1959.

[288] T. Pfau, R. Peveling, V. Herath, S. Hoffmann, C. Wördehoff, O. Adamczyk, M. Porrmann, and R. Noe, "Towards real-time implementation of coherent optical communication," ser. Proceedings of OFC/NFOEC 2009, 2009.

[289] K. Lenglé, "Traitement tout optique du signal à base de composants à cristaux photoniques en matériaux semiconducteurs III-V," Ph.D. dissertation, Université de Rennes 1, 2013.

[290] J. P. Gordon and L. F. Mollenauer, "Phase noise in photonic communications systems using linear amplifiers," *Optics letters*, vol. 15, no. 23, pp. 1351–1353, 1990.

[291] G. Li, K. Croussore, C. Kim, Y. Han, and I. Kim, "All-optical phase and amplitude regeneration of DPSK signals based on phase-sensitive amplification," in *Optical Fiber Communication Conference.* Optical Society of America, 2006, p. OFH7.

[292] R. Slavik, F. Parmigiani, J. Kakande, C. Lundstrom, M. Sjodin, P. A. Andrekson, R. Weerasuriya, S. Sygletos, A. D. Ellis, L. Gruner-Nielsen, D. Jakobsen, S. Herstrom, R. Phelan, J. O'Gorman, A. Bogris, D. Syvridis, S. Dasgupta, P. Petropoulos, and D. J. Richardson, "All-optical phase and amplitude regenerator for next-generation telecommunications systems," *Nature Photonics*, vol. 4, no. 10, pp. 690–695, Oct. 2010.

[293] L. Bramerie, Quang Trung Le, M. Gay, A. O'Hare, S. Lobo, M. Joindot, J. Simon, Hoang-Trung Nguyen, and J. Oudar, "All-optical 2R regeneration with a vertical microcavity-based saturable absorber," *IEEE Journal of Selected Topics in Quantum Electronics*, vol. 18, no. 2, pp. 870–883, Mar. 2012.

[294] M. Matsumoto and K. Sanuki, "Performance improvement of DPSK signal transmission by a phase-preserving amplitude limiter," *Opt. Express*, vol. 15, no. 13, pp. 8094–8103, Jun 2007.

[295] K. Cvecek, K. Sponsel, C. Stephan, G. Onishchukov, R. Ludwig, C. Schubert, B. Schmauss, and G. Leuchs, "Phase-preserving amplitude regeneration for a WDM RZ-DPSK signal using a nonlinear amplifying loop mirror," *Optics express*, vol. 16, no. 3, pp. 1923–1928, 2008.

[296] S. Boscolo, R. Bhamber, and S. Turitsyn, "Design of Raman-based nonlinear loop mirror for all-optical 2R regeneration of differential phase-shift-keying transmission," *IEEE Journal of Quantum Electronics*, vol. 42, no. 7, pp. 619–624, Jul. 2006.

[297] Y. Halioua, A. Bazin, P. Monnier, T. J. Karle, G. Roelkens, I. Sagnes, R. Raj, and F. Raineri, "Hybrid III-V semiconductor/silicon nanolaser," *Optics express*, vol. 19, no. 10, pp. 9221–9231, 2011.

[298] H. Park, A. W. Fang, O. Cohen, R. Jones, M. J. Paniccia, and J. E. Bowers, "A hybrid AlGaInAs-Silicon evanescent amplifier," *IEEE Photonics Technology Letters*, vol. 19, no. 4, pp. 230–232, 2007.

[299] D. Van Thourhout, T. Spuesens, S. K. Selvaraja, L. Liu, G. Roelkens, R. Kumar, G. Morthier, P. Rojo-Romeo, F. Mandorlo, P. Regreny, O. Raz, C. Kopp, and L. Grenouillet, "Nanophotonic devices for optical interconnect," *IEEE Journal of Selected Topics in Quantum Electronics*, vol. 16, no. 5, pp. 1363–1375, Sep. 2010.

[300] R. Kumar, T. Spuesens, P. Mechet, P. Kumar, O. Raz, N. Olivier, J.-M. Fedeli, G. Roelkens, R. Baets, D. Van Thourhout *et al.*, "Ultrafast and bias-free all-optical wavelength conversion using III-V-on-silicon technology," *Optics letters*, vol. 36, no. 13, pp. 2450–2452, 2011.

[301] R. Kumar, T. Spuesens, P. Mechet, N. Olivier, J.-M. Fedeli, P. Regreny, G. Roelkens, D. van Thourhout, and G. Morthier, "10Gbit/s all-optical NRZ-OOK to RZ-OOK format conversion in an ultra-small III-V-on-silicon microdisk fabricated in a CMOS pilot line," *Opt. Express*, vol. 19, no. 24, pp. 24 647–24 656, Nov 2011.

[302] P. Mechet, T. Spuesens, S. Werquin, K. Vandoorne, N. Olivier, J.-M. Fedeli, P. Regreny, D. Van Thourhout, G. Roelkens, and G. Morthier, "All-optical low-power 2R regeneration of 10-Gb/s NRZ signals using a III-V on SOI microdisk laser," *IEEE Photonics Journal*, vol. 5, no. 6, pp. 7 802 510–7 802 510, Dec. 2013.

[303] K. Lenglé, T. N. Nguyen, M. Gay, L. Bramerie, J.-C. Simon, A. Bazin, F. Raineri, and R. Raj, "Modulation contrast optimization for wavelength conversion of a 20 Gbit/s data signal in hybrid InP/SOI photonic crystal nanocavity," *Optics letters*, vol. 39, no. 8, pp. 2298–2301, 2014.

[304] A. Bazin, K. Lengle, M. Gay, P. Monnier, L. Bramerie, R. Braive, G. Beaudoin, I. Sagnes, R. Raj, and F. Raineri, "Ultrafast all-optical switching and error-free 10 Gbit/s wavelength conversion in hybrid InP-silicon on insulator nanocavities using surface quantum wells," *Applied Physics Letters*, vol. 104, no. 1, p. 011102, 2014.

[305] K. Lengle, M. Gay, A. Bazin, I. Sagnes, R. Braive, P. Monnier, L. Bramerie, N. Nguyen, C. Pareige, R. Madec, and others, "Fast all-optical 10 Gb/s NRZ wavelength conversion and power limiting function using hybrid InP on SOI nanocavity," in *European Conference and Exhibition on Optical Communication*. Optical Society of America, 2012, pp. We–2.

[306] W. Magnus, *Formulas and theorems for the special functions of mathematical physics*. Berlin,New York: Springer-Verlag, 1966.

List of symbols and abbreviations

$A(B)_m$ - m^{th} order Bessel polynomials, 85
A_{eff} - optical mode effective area, 9
A_{mid} - intensity average value, 75
B - bandwidth of the sampling system, 64
BW_{ADC} - ADC bandwidth, 83
BW_{PD} - photodiode bandwidth, 83
B_{ref} - referent bandwidth, 34
C_m - alphabet of M possible symbol on the constellation, 136
$C_{in1(2)}$ - input of the IQ compensator, 123
C_{out} - output of the IQ compensator, 123
D - dispersion parameter, 29
$E_{S(LO)}$ - field of S (LO), 61
$E(z,t)$ - complex optical field, 8
ER_S - signal extinction-ratio, 101
ER_{LO} - pulsed-LO extinction-ratio, 85, 101
ER_{out} - extinction-ratio of the reconstructed signal, 102
E_s - energy per symbol, 34
$E_{S(LO)}$ - field of S(LO), 21, 112
F_n - function depending on the n^{th} harmonic of the Fourier series, 137
$H(f)$ - transfer function of a Bessel filter, 85
I - intensity of sampled data signal, 61
$I(Q)_0$ - transmitted in-phase (quadrature) component without IQ imbalance, 121
$I(Q)_1$ - received in-phase (quadrature) component with IQ imbalance and no noise, 121
$I(Q)_2$ - output of the FIR filter, 124
$I_{ideal(measure),r}$ - normalized voltage of ideal (measured) in-phase component for the r^{th} symbol, 33
$K_{1(2)}$ - parameters of the IQ compensator, 123
L - normalized impulse response of channel, 24
LF - likelihood function, 136
LLF - loglikelihood function, 136
M - number of symbols in a modulated alphabet, 10
N - number of symbols used for CFO estimation, 138
N_0 - power spectral density of the optical noise, 34
N_1 - number of symbols used for the first CPE stage, 138
N_2 - number of symbols used for the second CPE stage, 138
N_P - number of signal period, 74
N_c - number of the filter coefficients, 29, 124
P - peak power of the SUT, 101
$P(0/1)$ - conditional probability of receiving symbol 0 when sending the symbol 1, 31
$P(1/0)$ - conditional probability of receiving symbol 1 when sending the symbol 0, 31
$P(z,t)$ - signal power, 9
P_e - error probability, 31
P_s - average optical signal power, 34
$P_{1(0)}$ - probability that the symbol 1(0) is transmitted, 31
$P_{I(Q)}$ - average energy of the I(Q) compo-

nent, 23

P_{LO} - pulsed-LO power, 85

P_{diss} - power dissipation, 42

Q_n - modified quadrature component, 113

$Q_{ideal(measure),r}$ - normalized voltage of ideal (measured) quadrature component for the r^{th} symbol, 33

R - photodiode responsivity, 61

R_B - baud rate (symbol rate), 10, 25, 34

R_b - bit rate, 10

SNR_r - new definition of SNR for signal r, 113

$S_m(f)$ - periodogram, 73

T - pulse time-slot, 85

T_0 - half-width of the full-width at half maximum, 85

T_B - symbol duration, 24, 34, 135, 139

T_D - data signal period, 73

T_S - pulsed-LO period, 85

T_S - sampling period, 26, 29

T_S - sampling period of pulsed-LO, 61

T_{LO} - time period between sampling pulses, 57

T_{int} - integration time, 83

$V(t)$ - applied voltage, 17

V^{th} - optimum decision threshold, 32

V_π - half-wave voltage (π phase shift), 17

V_{FS} - full-scale voltage, 43

$[\cdot]^T$ - transpose operator, 124

ΔE - uncertainty of energy, 43

$\Delta\nu$ - a Gaussian random variable, 139

$\Delta\omega$ - difference between the pulsation of interest and ω_0, 29

$\Delta\phi(t)$ - phase shift in PM, 17

$\Delta\varphi$ - phase shift between 2 consecutive samples, 26

Δf - CFO, 26, 135

Δ - quantization step-size, 38

$\Im$ - imaginary part operator, 21, 61, 112, 127

$\Re$ - real part operator, 21, 61, 112, 124

Θ - temperature in Kelvin, 42

$\mathbf{E}(\cdot)$ - ensemble average operator, 23, 113, 124

$\mathbf{X}$ - observed sequence $\{x(k)\}$ composed of K samples, 135

δT - fraction of T_D, 73

γ - Kerr nonlinear coefficient, 9

$\hat{\phi}_{mis}$ - estimated phase imbalance, 113, 115

$\hat{\theta}(n)$ - carrier phase estimation by DPLL, 124

λ_0 - optical carrier wavelength, 29

$\lfloor a \rfloor$ - floor function returning to the largest integer less than or equal to a, 38

$\mu_{0(1)}$ - mean of the symbol 0(1) distributions, 32

μ - step size parameter, 74, 123

ω_0 - optical carrier angular frequency, 61

ϕ_{mis} - phase imbalance value, 112

ϕ_{var} - added phase shift, 112

ϕ_1 - phase imbalance at the transmitter, 121

ϕ_2 - phase imbalance at the receiver, 121

ρ_k - amplitude component of k-th received sample, 26

ρ - percentage of selected intensity, 75

σ^2 - variance of noise, 112, 135

$\sigma_{0(1)}$ - standard deviation of the symbol 0(1) distributions, 32

τ_{FWHM} - FWHM of the pulsed-LO, 64

τ - time delay between adjacent taps, 24

τ_a - (aperture jitter) timing jitter, 43

τ_n - time delay of the pulsed-LO, 57

θ_k - phase component of k-th received sample, 26

$\varepsilon_{S(LO)}$ - complex electric field of S (LO), 61

$\varphi(k)$ - phase rotation at the instance k, 135

φ_0 - laser phase noise, 135

φ_f - rotation due to the CFO, 135

φ_m - modulated signal phase, 26

φ_n - laser phase noise, 26

$\widehat{\varphi_0}$ - estimated laser phase noise, 137

$\widehat{\varphi_f}$ - estimated CFO, 137

ξ - correlation coefficient in GSOP, 23
$a(b)_i$ - coefficients of Bessel polynomial, 86
a_k - k-th tap coefficient, 29
c - speed of light, 29
$c(k)$ - complex symbols corresponding to every possible symbol on the constellation, 135
$d(n)$ - direct detection symbol, 124
$e_1(n)$ - error after direct detection, 124
$e_2(n)$ - phase error after DPLL, 127
$erfc$ - complementary error function, 32
$f(t)$ - pulse envelop waveform, 85
f_S - sampling rate, 42
f_T - current gain of transistor, 43
$h(t)$ - impulse response, 61, 101
$h_{I(Q)}$ - FIR filter, 124
$i_{1(2)}$ - photocurrents of the I component, 21
$j = \sqrt{-1}$ - imaginary number, 17, 19, 124
k - down-conversion rate, 85
m - number of encoded bit on one symbol, 35
mod - *modulo* operator, 74
$n(k)$ - samples of Gaussian noise, 135
$n(z,t)$ - fiber refractive index, 9
n_L - conventional refractive index, 9
$n_{C(S)}$ - random Gaussian variable, 112
n_{NL} - nonlinear refractive index, 9
$p_{1(0)}$ - probability density function (PDF) of symbol 1(0), 32
$q_{1(2)}$ - photocurrents of the Q component, 21
r - modified r_x signal, 113
r_k - k-th received sample, 26
r_x - complex received signal, 112
s_k - sampled data, 73
$sgn(\cdot)$ - signum function, 38
$x(k)$ - received symbol at baud rate, 135
z - distance of propagation, 29

ADC - analog-to-digital converter, 2, 6, 36, 37, 40, 42, 44, 47, 56, 82, 83, 129
AGC - automatic gain control, 37
ASE - amplified spontaneous emission, 8, 27, 33, 56, 86, 112, 150, 158
ASIC - application-specific integrated circuit, 44
ASK - amplitude shift keying, 10
AWG - arbitrary waveform generator, 117, 126, 153
AWGN - additive white Gaussian noise, 12, 31, 33, 42, 86, 112

BER - bit error ratio, 31, 33, 112, 120, 151, 157
BPS - blind phase search, 133, 140
BW - bandwidth, 13, 83, 84, 90

CD - chromatic dispersion, 2, 8, 29, 30
CFO - carrier frequency offset, 4, 21, 25, 108, 112, 132, 133, 135, 140, 141
CHE - circular harmonic expansion, 4, 108, 132, 135, 140
CMA - constant modulus algorithm, 24, 30, 110
CMOS - complementary-metal-oxide semiconductor, 36, 37, 44, 150
CO - central office, 8
CPE - carrier phase estimation, 4, 21, 26, 108, 132, 135, 140
CR - carrier recovery, 132, 135, 140
CW - continuous wave, 68

DA - data-aided, 24
DBI - digital bandwidth interleaving, 2, 47
DBP - digital backward propagation, 30
DD - decision-directed, 30
DD-LMS - decision-directed least-mean-square, 120
DFB - distributed feedback, 25, 65
DFE - decision feedback equalization, 24
DFG - difference frequency generation, 55
DPLL - digital phase-locked loop, 120

DSO - digital sampling oscilloscope, 83, 84
DSP - digital signal processing, 2, 6, 10, 21, 25, 26, 28, 30, 36, 37, 56, 59, 84, 108, 110, 117

EAM - electro-absorption modulator, 55
EC - ellipse correction, 110
EDFA - erbium-doped fiber amplifier, 1, 13, 68, 86, 117, 126, 153, 158
ENOB - effective number of bit, 4, 40, 42, 64, 82, 83
EVM - error vector magnitude, 21, 31, 33, 74, 84, 112

FFCR - feedforward carrier recovery, 108, 132
FFE - feedforward equalization, 24
FFT - fast Fourier transform, 26, 29, 85, 133
FIR - finite impulse response, 24, 30, 120, 153
FMC - FPGA mezzanine card, 72
FOE - frequency offset estimation, 133, 141
FOM - figure of merit, 42, 44
FPGA - field programmable gate array, 59, 72, 112, 120, 133
FSR - free spectrum range, 68
FWHM - full-width at half maximum, 85, 99
FWM - four wave mixing, 10, 55, 150

GRIN - gradient index, 70
GSOP - Gram-Schmidt orthogonalization procedure, 110, 112
GVD - group-velocity dispersion, 129

HD - high definition, 6

ICI - inter-carrier interference, 110
IMDD - intensity modulation/direct detection, 7
InP - Indium Phosphide, 150
IP - Internet protocol, 6
ISI - inter-symbol interference, 8, 21, 24, 80, 90, 120, 129

LAN - local area network, 8
LLF - loglikelihood function, 135
LMS - least mean square, 24, 30
LO - local oscillator, 4, 133, 153
LOS - linear optical sampling, 4, 55, 60, 64, 82, 83, 99
LPF - low pass filter, 83, 85
LSB - least significant bit, 44
LUT - look-up table, 135

MAN - metro area network, 8
MAP - maximum a posteriori probability, 15
MIMO - multiple input multiple output, 30
ML - maximum likelihood, 133, 135
MLL - mode-locked laser, 65, 67, 99
MLSD - maximum-likelihood sequence detector, 24
MLSE - maximum-likelihood sequence estimation, 15, 30
MMSE - minimum mean square error, 24
MSB - maximum significant bit, 44
MSEM - maximum SNR estimation method, 112, 171
MZM - Mach-Zehnder modulator, 67

NDA - non-data-aided, 24
NLLS - nonlinear least-square, 146
NLSE - nonlinear Schrodinger equation, 8
NOLM - nonlinear optical loop mirror, 55, 150
NPN - nonlinear phase noise, 4, 108, 150, 151, 157, 158
NZDSF - non-zero-dispersion-shifted fiber, 158

OBPF - optical bandpass filter, 99, 117, 126, 153, 158
ODL - optical-delay line, 99
OFCG - optical frequency comb generator, 67
OFDM - orthogonal frequency division multiplexing, 10

OOK - on-off keying, 10
OP - operating point, 17
OSNR - optical signal-to-noise ratio, 33, 117, 153, 158
OSO - optical sampling oscilloscope, 70, 80

PAM - pulse amplitude modulation, 126
PDF - probability density function, 31
PhC - photonic crystal, 150
PIC - photonic integrated circuits, 36
PM - phase modulator, 16
PMD - polarization mode dispersion, 2, 8, 30
PPLN - periodically poled Lithium Niobate, 55
PRBS - pseudo random binary sequence, 16, 117, 153, 158
PSK - phase shift keying, 10, 12, 26

QAM - quadrature amplitude modulation, 10, 12, 26
QPSK - quadrature phase shift keying, 12, 110, 117, 171

RLS - recursive least square, 30
RRC - root-raised-cosine, 110
Rx - receiver, 8, 110, 133

SAR - successive approximation register, 44
SE - spectral efficiency, 7, 10
SFDR - spurious-free dynamic range, 42
SFG - sum frequency generation, 55
SNR - signal-to-noise ratio, 12, 21, 28, 31, 42, 110
SOI - silicon-on-insulator, 150
SoP - state of polarization, 7, 21, 30
SPM - self-phase modulation, 10
SSMF - standard single mode fiber, 129
STD - standard deviation, 141
STR - symbol timing recovery, 28
SUT - signal under test, 99

T/H - track-and-hold, 37, 83
TDM - time-division multiplexing, 7
TIA - transimpedance amplifier, 37, 75
TMLL - tunable mode-locked laser, 70
Tx - transmitter, 8, 110, 133

UNI - ultrafast nonlinear interferometer, 55

VOA - variable optical attenuator, 117, 126, 158
VoD - video on demand, 6
VV4PE - Viterbi-Viterbi fourth power estimator, 133
VVMFOE - Viterbi-Viterbi monomial FOE, 133, 140
VVMPE - Viterbi-Viterbi monomial phase estimation, 135
VVMPE-ML - Viterbi-Viterbi monomial-based and maximum likelihood estimator, 133, 140

WAN - wide area network, 8
WDM - wavelength division multiplexing, 1, 7, 30

XPM - cross phase modulation, 10, 30, 55